Chemical Vapour Deposition as a possible route for large-scale production of graphene

Università degli Studi di Torino
Scuola di Dottorato in Scienza e Alta Tecnologia

Tesi di Dottorato di Ricerca in Scienza e Alta Tecnologia

Chemical Vapour Deposition as a possible route for large-scale production of graphene

Marco Piazzi

Università degli Studi di Torino
Scuola di Dottorato in Scienza e Alta Tecnologia

Tesi di Dottorato di Ricerca in Scienza e Alta Tecnologia
Indirizzo di Fisica e Astrofisica

Chemical Vapour Deposition as a possible route for large-scale production of graphene

Author:
Marco Piazzi

Tutor:
Prof. Ettore Vittone
Co-tutor:
Dr. Giampiero Amato

External reviewer:
Prof. Luca Ottaviano

COLOPHON

This document was typeset with LaTeX using ArsClassica, a reworked version by Lorenzo Pantieri of the ClassicThesis style developed by André Miede (inspired by Robert Bringhurst's seminal book on typography *"The Elements of Typographic Style"*).

CONTACTS

Marco Piazzi: m.piazzi@inrim.it
marco.piazzi@unito.it

Venite gente vuota, facciamola finita:
voi preti che vendete a tutti un'altra vita;
se c'è come voi dite un Dio nell'infinito
guardatevi nel cuore, l'avete già tradito
e voi materialisti, col vostro chiodo fisso
che Dio è morto e l'uomo è solo in questo abisso,
le verità cercate per terra, da maiali,
tenetevi le ghiande, lasciatemi le ali;
tornate a casa nani, levatevi davanti,
per la mia rabbia enorme mi servono giganti.
Ai dogmi e ai pregiudizi da sempre non abbocco
e al fin della licenza io non perdono e tocco.
Io non perdono, non perdono e tocco!

"Cyrano" (F. Guccini)

To beloved Eleonora

ABSTRACT

Graphene is a 2D layer of carbon atoms arranged in a honeycomb lattice. Unlike usual semiconductors, charge carriers in graphene behave as massless Dirac particles, characterized by Fermi velocity $v_F \simeq 10^6\,m\,s^{-1}$, and exhibit a perfect electron/hole symmetry, making this material a gapless semiconductor. These astonishing features explain the most intriguing properties of graphene: charge carriers mobilities at room temperature up to $200\,000\,cm^2\,V^{-1}\,s^{-1}$, anomalous Quantum Hall Effect, weak localization providing minimal conductivity also for vanishing density of states, perfect tunneling through rectangular strong potential barriers, superior thermal conductivity ($5000\,W\,m^{-1}\,K^{-1}$ for suspended monolayer graphene), almost perfect transparency over a wide range of the electromagnetic spectrum. These peculiarities, combined with its inherent excellent mechanical properties (Young's modulus of 1 TPa) and the demonstrated possibility of gating graphene to fabricate Field Electron Transistors, make this material the most promising candidate for many applications, ranging from Nanoelectronics to Optoelectronics, Photonics, Spintronics and even Metrology.

However, a scalable, cost-effective and efficient method to grow monolayer graphene over large scale areas, as required by electronic industries, is still lacking. The "groundbreaking experiments" performed by the Nobel Prizes K. S. Novoselov and A. K. Geim in 2004 led for the first time to grow graphene on an insulating substrate, allowing to investigate its properties: nonetheless, the technique they have developed (micromechanical exfoliation of Highly Oriented Pyrolytic Graphite by means of adhesive tape), although quite straightforward and cost-effective, is messy (monolayer graphene flakes must be searched after deposition) and not up-scalable: therefore, though this method provides high quality and quite large graphene crystals, ideal for basic research, it is not suitable for industrial purposes. Various attempts have been carried out during the years to conceive more efficient graphene growth techniques and nowadays one of the most powerful methods to achieve the goal is the Chemical Vapour Deposition (CVD) through decomposition, activated by a catalytic substrate, of a carbon precursor. The interest for this technique stems from its suitability to match the requirements of device fabrication technologies and from the quite low temperatures ($T \sim 900\,°C$) required for graphene growth. However, it has some drawbacks related to the polycrystalline nature of the catalytic substrate limiting the growth of large graphene crystals and to the difficulties (mainly related to dewetting of the substrate) arising while processing thin film catalysts (especially Cu) at the temperatures needed.

In this thesis the results concerning the research about CVD processes performed at I.N.Ri.M. in the last three years will be presented. Emphasis will be devoted to the presentation of results concerning the deposition of graphene on Cu films, since in this field an *in situ* technique allowing for a real time control of dewetting occurring on Cu surface has been developed. Moreover, results concerning a laser induced etching technique to reduce the number of layers on top of Cu, discovered while characterizing the samples with Raman analysis, will be also reported.

Both the techniques represent good achievements towards a better control of CVD processes and therefore towards the full exploitation of this technique as a promising route to grow high quality monolayer graphene, over large scale areas.

SOMMARIO

Il grafene è un reticolo bidimensionale di atomi di carbonio disposti in un reticolo cristallino esagonale a nido d'ape. A differenza dei comuni semiconduttori, i portatori di carica nel grafene si comportano come particelle di Dirac a massa nulla, caratterizzate da velocità di Fermi $v_F \simeq 10^6\,\mathrm{m\,s^{-1}}$, e presentano una perfetta simmetria elettrone/lacuna: per questo motivo, il grafene è un semiconduttore a gap nulla. Queste strabilianti caratteristiche spiegano le più intriganti proprietà di questo materiale: mobilità massima dei portatori di carica a temperatura ambiente di $200\,000\,\mathrm{cm^2\,V^{-1}\,s^{-1}}$, effetto Hall quantistico anomalo, debole localizzazione dei portatori di carica che porta ad una conduttività minima finita anche per densità di stati nulla, probabilità di tunneling unitaria attraverso elevate barriere di potenziale, una elevata conduttività termica ($5000\,\mathrm{W\,m^{-1}\,K^{-1}}$ nel caso di un singolo strato sospeso di grafene), una trasparenza quasi perfetta a quasi tutte le frequenze della radiazione elettromagnetica. Queste caratteristiche peculiari, unite alle eccellenti proprietà meccaniche intrinseche al materiale (modulo di Young pari a 1 TPa) e alla possibilità sperimentale di fabbricare transistori a effetto di campo collegando elettrodi al grafene, rendono questo materiale il più promettente candidato per un gran numero di applicazioni, dalla Nanoelettronica, alla Optoelettronica, alla Fotonica, alla Spintronica e anche alla Metrologia.

Purtroppo, un metodo per la crescita di singoli strati di grafene di elevate dimensioni, che offra scalabilità, costi contenuti ed efficienza, come richiesto dalle industrie elettroniche, non è ancora stato sviluppato. Gli esperimenti pionieristici ideati nel 2004 dai Premi Nobel K. S. Novoselov e A. K. Geim hanno consentito, per la prima volta, di depositare grafene su substrati isolanti, permettendo così lo studio delle proprietà di questo materiale: tuttavia, la tecnica proposta, basata sull'esfoliazione micromeccanica di grafite pirolitica altamente orientata, sebbene abbastanza semplice e a basso costo, non offre scalabilità ed è complicata dal fatto di dover ricercare i singoli strati di grafene sul substrato isolante solo dopo la loro deposizione. Di conseguenza, sebbene il metodo permetta di depositare singoli cristalli di grafene di alta qualità e di dimensioni abbastanza elevate, ideali per la ricerca di base, esso non è adatto per scopi industriali. Nel corso degli anni si sono susseguiti vari tentativi per ideare tecniche di deposizione di grafene più efficienti e, attualmente, uno dei metodi più promettenti per raggiungere lo scopo di una industrializzazione nella produzione del grafene è la Deposizione Chimica da Fase Vapore (CVD), ottenuta mediante la decomposizione, attivata mediante un substrato catalizzatore, di gas precursori del carbonio. L'interesse per questa tecnica nasce dalla possibilità che essa fornisce di soddisfare le esigenze dettate dalle moderne tecnologie di fabbricazione di dispositivi elettronici e dal fatto di poter ottenere la crescita di grafene a temperature abbastanza basse ($T \sim 900\,^\circ\mathrm{C}$). Ovviamente, la tecnica presenta anche degli svantaggi, legati alla natura policristallina dei catalizzatori, che limita la possibilità di crescere cristalli di grafene di grandi dimensioni, e ad alcune difficoltà (principalmente legate al dewetting) che si riscontrano su film sottili catalizzatori (in particolare di Cu) alle temperature richieste dai processi di CVD.

In questa tesi verranno presentati i risultati riguardanti i processi CVD svolti negli ultimi tre anni presso I.N.Ri.M.. Particolare enfasi sarà data alla presentazione dei risultati riguardanti la deposizione di grafene su film di

Cu, in quanto in questo campo è stata sviluppata una tecnica *in situ* che permette il controllo in tempo reale di effetti di dewetting eventualmente in atto sulla superficie del Cu durante il processo CVD. Verranno inoltre riportati i risultati riguardanti una tecnica di etching indotta da fascio laser, capace di ridurre il numero di strati di grafene presenti sul Cu, scoperta durante la caratterizzazione mediante spettroscopia Raman dei campioni grafenici.

Entrambe le tecniche rappresentano degli importanti passi in avanti verso un maggiore controllo dei processi CVD e, di conseguenza, verso un pieno sfruttamento di questa tecnica come possibile strada verso la crescita di singoli strati di grafene, di dimensione elevata ed alta qualità.

CONTENTS

LIST OF FIGURES

LIST OF TABLES

ACKNOWLEDGEMENTS

The material of this thesis is based upon a research project involving the Solid State Physics Group of the University of Turin and the Quantum Research Group of the "Istituto Nazionale di Ricerca Metrologica" (I.N.Ri.M.) of Turin. The research has been performed by many people that I would like to acknowledge for their invaluable help.

First of all, I wish to express my deepest gratitude to my tutors, Prof. E. Vittone and Dr. G. Amato, for their aid: they helped me with their huge experience and competence during all my research, supporting my work with useful discussions and suggestions and guiding me into the world of research with their patience, passion and friendship.

Many thanks to Prof. L. Ottaviano (University of L'Aquila), who reviewed the whole manuscript addressing interesting comments and advices, and to Dr. T. Ohshima (Japan Atomic Energy Agency), who also read the text suggesting useful corrections and insights.

Secondly, I would like to thank a lot my teammate Dr. L. Croin for the great experimental work he performed everyday at the Quantum Research Laboratory of I.N.Ri.M., for the precious help he always gave me for achieving many of the results discussed in this thesis, for many useful and friendly discussions I had with him, for all the (many many) troubles he encountered and brilliantly solved with the experimental instrumentation used for the research. I am also very grateful to another colleague of mine, Dr. E. Enrico, who explained me the basic principles of Scanning Electron Microscopy and had always a reassuring presence in the Quantum Research Laboratory.

Then, I am also grateful to other colleagues, researchers, students that I met in these three years and that contributed in different ways to the successful completion of this work: Dr. L. Boarino for having hosted me in his office and for its helpful insights on the subject, Dr. A. Damin (NIS Centre - Turin) for the fundamental work he performed helping me with Raman Spectroscopy, Dr. F. Gregori and Dr. F. Caveglia Beatris for the work they performed about Chemical Vapour Deposition of graphene, Dr. M. Prato for the computerisation of the e-beam evaporation processes, Dr. A. Battiato (University of Turin) for his willingness with X-Ray Photoelectron Spectroscopy measurements, Dr. E. Olivetti for X-Ray Diffraction analyses, Dr. S. Gentiluomo for the setup of the thermal evaporator, Dr. N. De Leo for useful discussions about Metrology and Dr. F. Bosia (University of Turin) who taught me some notions about COMSOL Multiphysics software.

Finally, I wish to thank a lot my parents for the invaluable support they ensured me during my studies, always encouraging me with enthusiasm. A special thanks to all my friends, with whom I shared many amazing adventures and fun time: they helped me in overcoming difficulties and they withstood with great patience the long speeches about my research.

Lastly, let me thank with love Eleonora, the person who really made possible all this work with her unceasing support, her prompt suggestions, her endless patience, her lovely smiles and hugs, her fundamental presence accompanying every single moment of my research during these last three years, in particular the "darkest" periods I encountered along the way.

Marco Piazzi

Turin, March 7th, 2013

INTRODUCTION

The discovery of *p-n* junctions (diodes) made by Russell Ohl in 1939 while observing the photovoltaic effect when light was flashed onto a silicon rod ([138]), together with the physical theory explaining their working principles later developed by William Shockley in 1949 ([164]), can be considered a milestone in the recent history of Semiconductor Physics. Indeed, immediately after that discovery it was quite clear that a route towards the fabrication of a new class of electronic devices could be opened. The huge effort made in the direction of such a fabrication came finally to a success between 1947 and 1948 when Walter Brattain, John Bardeen and William Shockley, three researchers of Bell Laboratories (later awarded with the Nobel Prize in Physics in 1956 for their revolutionary invention) presented the first prototype of a transistor ever made. These devices became very soon fundamental elements of every electronic circuit and their presence in analogic and digital systems is nowadays unavoidable. During the last 60 years the intense research on this kind of semiconductor devices has allowed to make huge improvements both in the fabrication procedures (bringing to an enhancement of the performances) and, more important, in the miniaturization processes involving transistors, this way opening the era of Micro- and Nanoelectronics (a complete review about diodes and transistors, the underlaying physical principles and the fabrication issues can be found in [120] and [176]). From 1948 up to now, many tipologies of transistors have been built (mainly divided into two categories, the Bipolar Junction Transistors on one side and the Field Effect Transistors on the other side) and their typical size has been reduced of about 3 orders of magnitude, from few µm to tens of nm (Figure 1). This fact allowed to successfully satisfy the Moore's Law ([123]), according to which the number of transistors in integrated circuits doubles approximately every two years: this empirical law has become a paradigm of every electronic and informatic industry, whose aim is to fulfil the trend predicted by it.

Although Moore's Law has been met up to now (as depicted in Figure 2), a major problem is arisen in the last years: Si based transistors, the cheapest and better ones produced until now, are reaching their limiting performances and it is difficult to think that Si can continue to serve as basic element for the fabrication of Nanoelectronic devices in the future.

Therefore, new materials showing better properties with respect to Si are definitely needed to deal with the challenges of modern Nanoelectronics. Despite the efforts, none of the materials proposed in the past years succeeded to meet the requirements of industrial applications, all of them failing in some respects compared to Si (a list of some of these materials together with their properties is reported in Table 1).

Nevertheless, in 2004 another material appeared into the scene, reinforcing the expectations for a fully new paradigm to be used for Nanoelectronic devices' fabrication: *graphene*, a truly two-dimensional system of carbon atoms arranged in an honeycomb lattice. A group of researchers from Manchester University, headed by Prof. A. K. Geim and Prof. K. S.Novoselov (later awarded with the Nobel Prize in Physics in 2010), succeeded in that year in synthesizing such a one-atom thick membrane by mechanically exfoliating highly oriented pyrolitic graphite (HOPG) samples

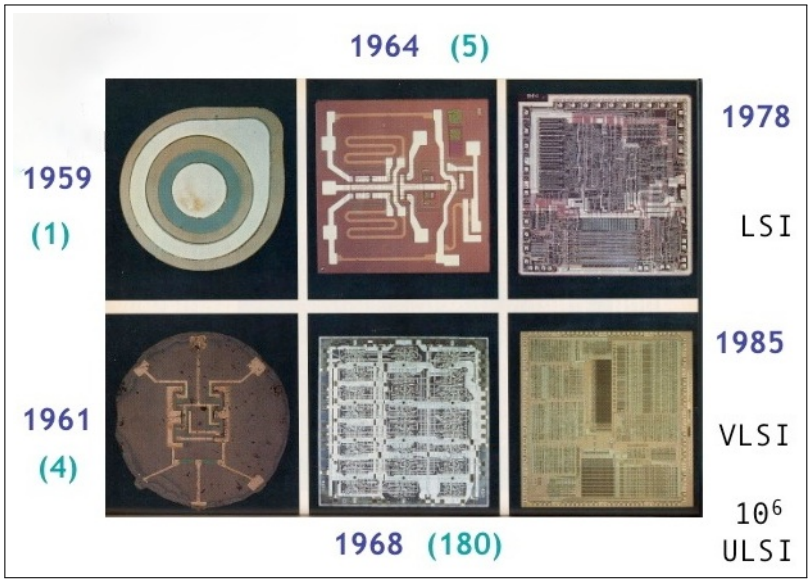

Figure 1: Evolution of transistors' average size. Increase in the number of transistors present as basic components in integrated circuits during the years: the decrease in transistors' average size is clearly visible.

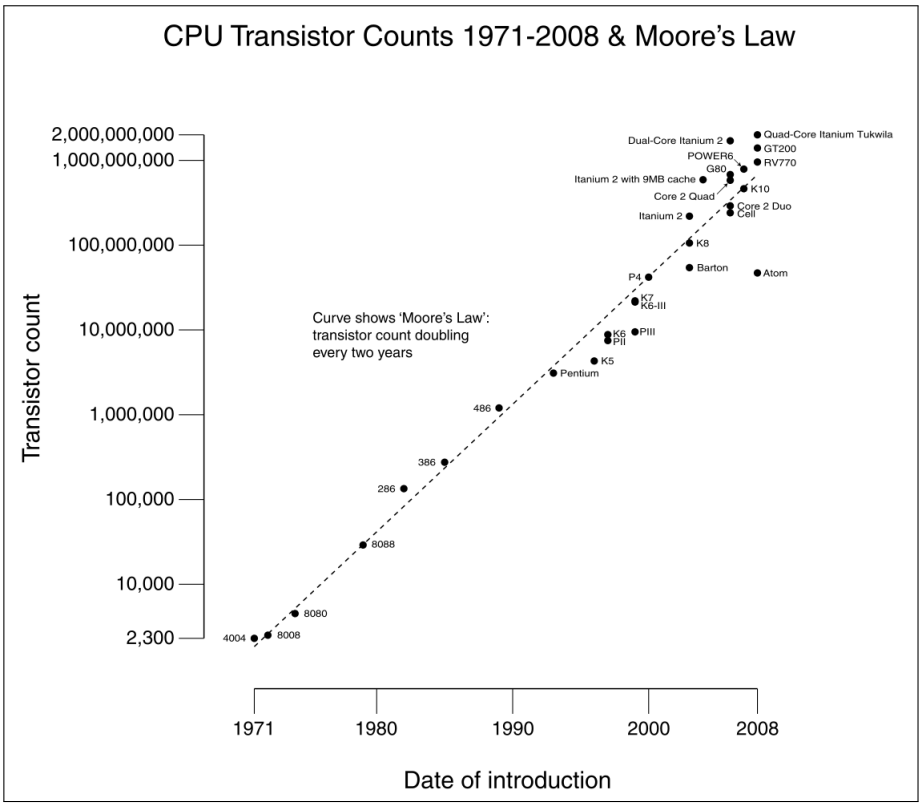

Figure 2: Moore's Law. Graph showing a nearly perfect agreement between realised and expected (according to Moore's Law) behaviours concerning the increase in the number of transistors present in integrated circuits per year. Courtesy of Wikipedia.

Typical values for *c*-Si: indirect gap, bandgap = 1.1242 eV, $\mu \sim 500$–$1200\,\mathrm{cm^2\,V^{-1}\,s^{-1}}$, $\rho = 10^5\,\Omega\,\mathrm{cm}$, thermal conductivity = $1.48\,\mathrm{W\,cm^{-1}\,K^{-1}}$

	Advantages	**Drawbacks**
GaAs	Direct gap $\mu \sim 4000$–$9000\,\mathrm{cm^2\,V^{-1}\,s^{-1}}$ $\rho = 10^9\,\Omega\,\mathrm{cm}$	Technology
SiC	Bandgap $\sim$ 2–3 eV High temperature operation	Price ($>$ 400 \$/wafer)
a-Si:H	Direct gap Bandgap = 1.75 eV High absorption coefficient Cheap	Degradation
Diamond	Bandgap = 5.47 eV $\mu = 2800\,\mathrm{cm^2\,V^{-1}\,s^{-1}}$ Thermal conductivity = $25\,\mathrm{W\,cm^{-1}\,K^{-1}}$	Price Technology

Table 1: Potential Si substitutes. Main semiconductors used in the last years to fabricate a new class of non Si-based Nanoelectronic devices.

with adhesive tape, thus sticking the thin carbon films this way obtained on an insulating SiO_2/Si substrate ([134]): they showed some of the incredibly astonishing properties owned by such a material because of its peculiar dimensionality and crystallographic arrangement (a detailed description of these properties will be reviewed in Chapter 1), emphasising in particular the presence of a zero band-gap in its electronic configuration and the possibility of measuring an ambipolar Electric Field Effect (meaning that charge carriers can be switched between 2D electron and hole gases by continuously tuning a gate potential V_g) by gating the system with an oxidized n^+-type Si substrate patterned as a multiterminal Hall device (the geometry of the device is shown in Figure 3). Mobilities of up to $10\,000\,\mathrm{cm^2\,V^{-1}\,s^{-1}}$ were measured even at room temperature, corresponding to charge carriers mean free paths of $\sim 0.4\,\mu\mathrm{m}$ (meaning ballistic transport in graphene): these are surprising huge values, given the two-dimensional nature of the material, much higher than those obtained in conventional Si-based transistors. Following these first remarkable results, in the last years many other exciting properties of graphene systems has been theoretically demonstrated and experimentally detected (some of them are briefly summarized in Table 2). Therefore graphene is today regarded as the most surprising, fascinating and extraordinary semi-metallic material one can deal with for a variety of amazing applications, including Nanoelectronics (Field-Effect Transistors at THz frequency, radiation detectors/modulators in the THz region of the electromagnetic spectrum, see [3, 140, 189] for more details), Optoelectronics and Photonics (transparent conductive electrodes for touch screens and photovoltaic cells, microcavities, fast photodetectors, ultra-fast lasers, see [3] for details), Thermal management of Electronics ([149]), Spintronics ([163]), Energy and Chemical Harvesting (for the development of solar and fuel cells and for the hydrogen storage, see [100] for details), gas sensing ([38]) and Metrology ([162]).

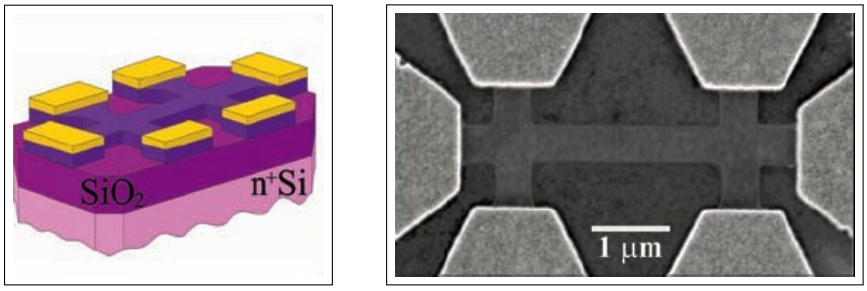

(a) (b)

Figure 3: Hall device's geometry for graphene systems. (a) Scanning Electron Microscope image of the device geometry implemented to measure Electric Field-Effect and charge carriers mobilities in graphene; (b) schematic view of the same geometry. Both adapted from [134].

Graphene physical properties	
Electronic	Giant intrinsic mobility $\mu \sim 2 \times 10^5\,\mathrm{cm^2\,V^{-1}\,s^{-1}}$ ([39])
	Large intrinsic electron mean free path $\ell \sim 1\,\mu\mathrm{m}$ ([39])
Thermal	Very high thermal conductivity $\sim 50\,\mathrm{W\,cm^{-1}\,K^{-1}}$ ([5])
Mechanical	Very high Young's modulus $\sim 0.5\,\mathrm{TPa}$ ([93])
Magnetic	High spin relaxation time $\tau_s \sim 150\,\mathrm{ps}$ and spin relaxation length $\lambda_s \sim 1.5$–$2\,\mu\mathrm{m}$ at room temperature ([180]), enhanced in bilayer graphene to $\tau_s \sim 2\,\mathrm{ns}$ ([204])
Optical	High optical transmittance $T \sim 97.7$ % from visible to near-infrared wavelengths ([127])

Table 2: Brief summary of graphene physical properties. A list of the main remarkable properties measured on mechanically exfoliated and suspended (apart from spintronics measurements) monolayer graphene, making it an ideal material for a wide range of applications. Adapted from [54].

Focusing on Metrology, it is worth reminding that a profound revision in the definition of the seven base units of the International System (SI) is ongoing from about two decades (for a review see [81, 147, 161]). This redefinition accomplishes a new paradigm of metrological research, according to which all the SI units' definitions will be related to fundamental constants of nature (whose values are specified and fixed by hand) through physical laws believed to hold exactly. As a consequence, the realization of units' standards will be more accurate and invariable over time. In particular, the definition of new quantum electrical standards (for current, resistance and voltage) is of a great importance: since 1980s is conventional to relate these standards to fundamental Laws' of Nature, namely the Josephson effect for the voltage standard, the Quantum Hall effect (QHE) for the resistance standard and the Single-Electron tunneling for the electrical current standard. The practical devices realising these standards are Josephson junctions, Quantum Hall bars and Single-Electron Transistors (SETs). According to this linking we have:

1. $U_J = nf_J/K_J$ for the voltage U_J produced by a Josephson junction operated at frequency f_J on the n-th voltage step;
2. $R_{QHR} = R_K/m$ for the resistance of a Quantum Hall bar operated on the m-th resistance plateau;
3. $I_{SET} = Q_S f_{SET}$ for the current generated by a Single-Electron tunneling device driving a charge quanta Q_S at frequency F_{SET}

where K_J, R_K and Q_S are "phenomenological constants", therefore considered here as empirical quantities to be determined experimentally and not fixed *a priori*. By means of the Ohm's Law $U_J = R_{QHR} I_{SET}$ it is possible to relate these constants as

$$K_J R_K Q_S = mn\,(f_J/f_{SET})\,. \tag{1}$$

The aim of metrological experiments exploiting Ohm' Law is conceived to test the consistency of the three quantum electrical effects described above by checking the validity of the relation 1 and, moreover, to search for possible deviations of the value of the phenomenological constants K_J, R_K, Q_S from the ideal case, represented by

$$\begin{aligned} K_J &= 2e/h; \\ R_K &= h/e^2; \\ Q_S &= e \end{aligned} \tag{2}$$

where e is the (absolute value of the) electron elementary charge and h is the Planck constant. Such experiments are known as Quantum Metrology Triangle (QMT) experiments (following the denomination introduced in [99] by the researchers that originally proposed them), since they compare (through Ohm's Law) three fundamental quantum effects and fundamental constants of nature, pictorially put at the vertices of a triangle (as in Figure 4). The idea is to close the triangle by comparing, thanks to the Ohm's Law, the voltage U_J delivered by a Josephson array voltage standard with the Hall voltage of a QHE sample operating on the m-th plateau of the Quantum Hall Resistance and across which the current I_{SET} flows from a SET device. In order to perform QMT measurements aimed to check the validity of 1 and 2 at the highest possible accuracy, the possibility of relying on

practical devices realising the quantum electrical standards with the lowest uncertainties achievable is needed. In this respect, it has been demonstrated in the seminal work by Tzalenchuk and co-workers ([184]) that graphene, being a truly 2D quantum gas of electrons, can be used for the definition of a new quantum resistance standard reaching better precision with respect to other devices previously employed: indeed, authors succeeded in determining the value of the R_K constant, by using monolayer epitaxial graphene patterned into Hall bars, with an accuracy of three parts per 10^9 at 300 mK, four order of magnitude better than ever reported.

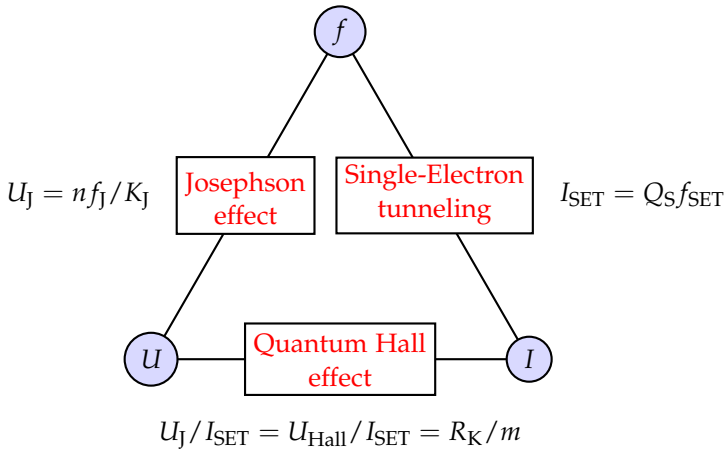

Figure 4: Quantum Metrology Triangle. Original version of the QMT experiment, as proposed in [99], connecting resistance, voltage and current standards.

Although, as mentioned above, graphene may represent a very promising material for a wide range of applications, a major and still unsolved problem is nowadays limiting its potential industrial use: the lack of a reproducible, efficient and cheap method allowing for a large-scale area production of high quality monolayer graphene, not affecting its remarkable properties. The micromechanical cleavage technique ideated by Geim and co-workers certainly offers the possibility of growing mono- and few-layer graphene flakes as big as $\sim 100\,\mu m$ or even more, of the best quality feasible up to now (a useful feature for experiments aiming to investigate the theoretical properties of such a material), but it is unsuitable for industrial purposes. The research for such a method is a great challenge involving a lot of industries, research groups and institutions around the world and many techniques (see Chapter 1 for a comprehensive discussion) has been proposed during the years, but further improvements are needed in order to make them really attractive for Nanotechnologies and other applications. It is enough here to mention that the most promising ones in order to achieve the aim are:

- the chemical reduction of graphene/graphite oxides;
- the epitaxial growth of graphene by thermal sublimation of *c*-SiC;
- the Chemical Vapour Deposition (CVD) of graphene by decomposition of a carbon precursor on a catalytic substrate.

The last method offers in particular many advantages: it has high accessibility (all is needed for a CVD process are an instrument, usually an e-beam evaporator, for the deposition of the catalyst and an heater equipped with

gas lines for graphene deposition), it does not require very high temperature for the growth process (in a typical CVD process $T_{CVD} \lesssim 900$–$950\,^{\circ}C$), it provides repeatability and it allows to obtain quite large graphene flakes (several μm^2 in size). On the other hand, some drawbacks still limit its exploitation: the need for a transfer of graphene from the catalyst to an insulating substrate for applications (a step for which a really smart and fully nondestructive technique has not been found yet) and the polycrystalline nature of the metal catalyst itself, making graphene grown by CVD usually quite defective (because of the grain boundaries it encounters during growth) and worsening its conduction properties (mainly in terms of the charge carriers mobility, decreasing of two order of magnitude with respect to the ideal suspended graphene case).

A better understanding of the physical mechanisms involved in CVD processes, a deep investigation of the response of different metallic catalysts to the carbon precursor used during graphene synthesis and a consequent optimization of the many parameters determining the quality and number of graphene layers grown by means of this technique is therefore crucial in order to make substantial progresses towards a fruitful use of the CVD method in many different fields, Nanoelectronics above all. In this thesis I report the results of the research performed on these topics at the Italian Metrological Institute (I.N.Ri.M.) of Turin.

I.N.Ri.M., performing the duties of primary metrological Institute of Italy, realises the primary standards for the base and derived units of the SI, ensures the maintenance of such standards and has research groups focused on the science of measurements and on the development of innovative technologies and devices. As already pointed out, graphene may offer interesting prospects both in metrology and in nanotechnology and for this reason I.N.Ri.M. has shown a natural interest for the development of a research about the fabrication of this material. In particular the possibility of take advantage of the outstanding properties of graphene for QMT experiments (through the implementation of graphene-based Hall devices) is of huge interest for I.N.Ri.M., given the fundamental rôle played by such experiments in metrological research. I.N.Ri.M. has an established experience and has already reached important results in the fabrication of Josephson junctions (Figure 5) and SETs (Figure 6) and therefore the investigation of graphene growth techniques gives a chance to test the validity of the Metrological Triangle.

Moreover, the instrumentation present at the Quantum Research Laboratory present at I.N.Ri.M. (a thermal and an e-beam evaporator suitable for the deposition of many metallic substrates, together with a Rapid Thermal Annealing-Oxidation System equipped with gas lines allowing for chemical growth of thin films at temperatures up to $1300\,^{\circ}C$) suggested to focus the research on the CVD technique carried out over different catalytic substrates.
After some processes performed on Ni films, not giving really exhaustive results, the research concentrated on Cu: indeed, the latter shows many advantages with respect to other metallic catalysts, mainly due to the different decomposition (of the carbon precursor molecules)/graphene growth mechanisms involved during CVD. As a consequence, growth on Cu should be self-limited (meaning that it should stop after one layer of graphene has been grown on the substrate) and should assure an easier transfer process because of the weak bonding between graphene and Cu. Graphene synthesis has been carried out both on thick Cu foil ($\sim 1\,mm$ thick) and, more

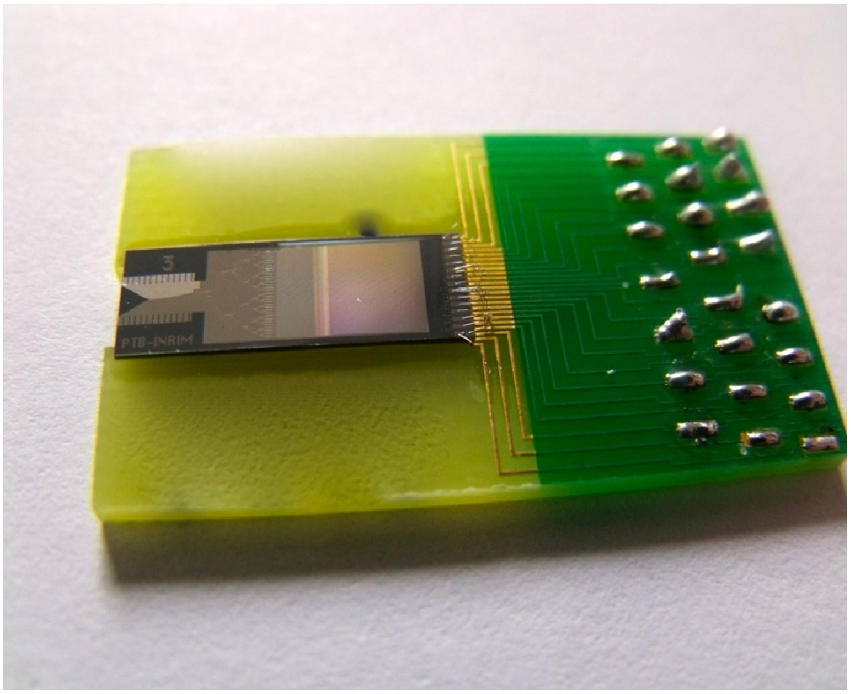

Figure 5: Josephson junction for Voltage Standard at I.N.Ri.M.. Programmable Josephson Voltage Standard for an output voltage of 1 V, based on binary-divided series arrays consisting of 8192 overdamped Superconductor-Normal metal-Insulator-Superconductor (SNIS) Josephson junctions fabricated at I.N.Ri.M. in collaboration with Physikalish-Technische Bundesanstalt (PTB), Germany.

interesting, on thin films ($\lesssim 500\,\text{nm}$).
However, Cu films featured a major (and known) drawback, represented by its dewetting from the underlying SiO_2/Si sample at the temperatures reached during the CVD processes: dewetting, deeply changing the morphology of the surface by formation of droplets roughening and reducing the uniformity of the film, can affect in a significant way the quality and the possibility itself of synthesizing graphene. Therefore, an intense study of this phenomenon has been carried out during the research activity.
Finally, in order to characterize graphene, common tools proper of Surface Physics have been employed: mainly Scanning Electron Microscopy (SEM), X-Ray Photoelectron Spectroscopy (XPS) and Raman Spectroscopy. One of the most interesting result has been obtained while characterizing a graphene sample grown on a thin Cu film by Raman Spectroscopy: a laser-induced ablation effect locally etching away outermost graphene layers present on top of the substrate, and therefore lowering their number, has been observed. This effect (that will be explained in detail in Chapter 3) deeply relies on three factors:

- the high laser power (1 mW) used during the spectra acquisitions, locally enhancing the temperature of the sample;

- the finite size and terraces-like shape of the graphene flakes present on Cu, limiting the heat conduction of the outermost graphene layers with respect to the ideal free-standing case;

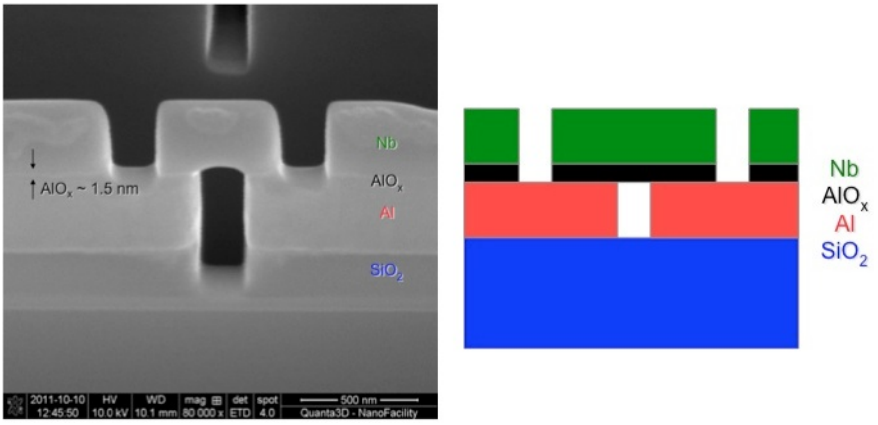

(a)

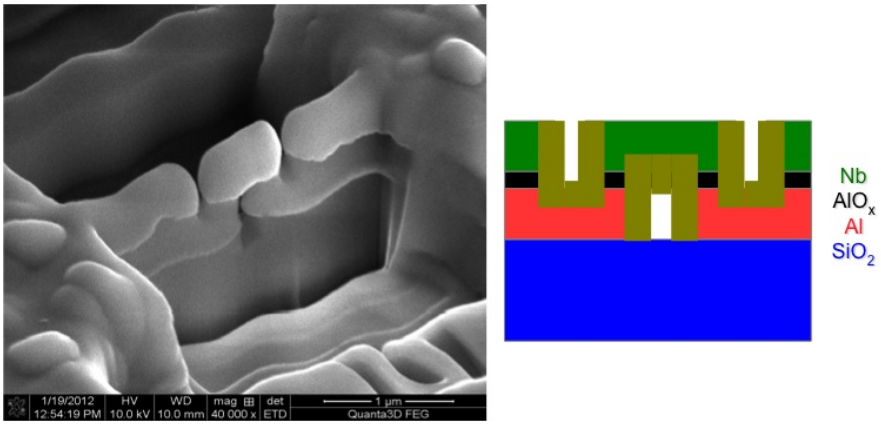

(b)

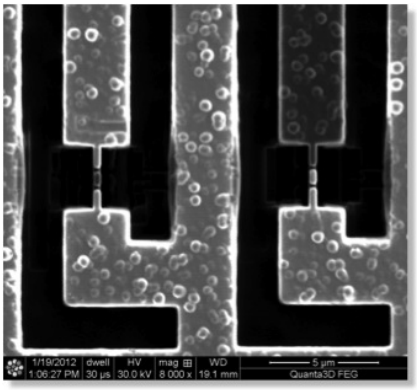

(c)

Figure 6: Hybrid SET for Current Standard at I.N.Ri.M.. (a) Scanning Electron Microscopy (SEM) image and schematic view of an Hybrid NISIN SET for Current Standard fabricated by Focus Ion Beam (FIB) lithography at I.N.Ri.M.; (b) SEM image and schematic view of the same Hybrid SET after the anodizing process; (c) FIB image of the same Hybrid SET integrated in a testing array.

- the presence of a metal substrate with high thermal conductivity, acting as an heat sink and thus preserving the innermost layer from etching.

The thesis is organized as follows:

1. in Chapter 1 an extensive review of the theoretical properties of graphene will be reported, together with a description and a comparison among the main methods proposed during the years for graphene growth;
2. Chapter 2 will be devoted to the description of the experimental apparatus and procedure used at I.N.Ri.M. for the deposition of Cu thin films, showing the samples obtained, and a detail explanation of the dewetting phenomenon and of the insights gained in this field will be provided;
3. in Chapter 3 the results concerning graphene deposition on different substrate (Ni, Cu foils and Cu films) and its transfer will be presented, focusing in particular on the Raman characterization of the samples and on the laser-induced etching effect experimentally observed;
4. finally, in the Conclusions I will summarize the results highlighting the main criticalities encountered and I will mention possible steps for the development and improvement of the research in the future.

1 GRAPHENE: "FLATLAND" IN THEORY AND IN PRACTICE

In this chapter I will introduce the main concepts about graphene: after introducing its molecular crystalline structure (Sec. 1.1), I will illustrate in detail its properties from a theoretical point of view (Sec. 1.2), focusing in particular on the description of its electronic transport features, on the introduction of the main concepts related to the appearance of the Quantum Hall Effect in graphene systems and on a very brief review about Klein paradox and weak localization in graphene. In Sec. 1.3 I will instead describe different techniques developed up to now to grow graphene, focusing a bit more on the CVD method since it is the technique I have employed to deposit few-layer graphene during my studies on the subject.

1.1 A BRIEF PRIMER ABOUT CARBON CRYSTALLOGRAPHY

1.1.1 Carbon and its allotropic forms

Carbon (chemical symbol C) is an element of the Periodic Table with atomic number $Z = 6$ and electronic configuration (in terms of quantum hydrogen-like eigenstates) $1s^2 2s^2 2p^2$ (it has therefore four valence electrons). The ground-state atomic configuration is characterized by total spin angular momentum $S = 1$, total orbital angular momentum $L = 1$ and total angular momentum $J = 0$: the single C atom ground-state is therefore the multiplet $^3P_0$. The first excited state, with $J = 1$, represented by the multiplet $^3P_1$, has an energy $E \approx 2\,\text{meV}$ ([151]): this value gives an estimate of the strength of the spin-orbit coupling in the carbon atom. It is well known from antiquity and it occurs in nature in three isotopes (two stable, ^{12}C, ^{13}C, and the last one,^{14}C, radioactive and often used for dating objects). Together with oxygen (O), hydrogen (H) and nitrogen (N), it is one of the most important chemical species for living being, forming hydrocarbons when bonded with H in long chains, appearing (in combination with O and H) in many important organic compounds like sugars, lignans, chitins, alcohols, fats, being present with N in alkaloids and, with the addiction of sulfur (S), also in antibiotics and amino acids and finally being involved in many biological processes like the photosynthesis occurring in plants. As a consequence, it is at the basis of organic chemistry and it is present in all known organic life.

From a crystallographic point of view, carbon appears in nature both in ordered crystal lattices and in amorphous form. As a crystal, it organizes itself in several allotropic forms, different one each other for their space dimension and for the kind of 2s-2p orbitals hybridization and chemical bonding involved. The most important and known allotropes of carbon are listed in Table 3 and their geometrical structures are shown in Figure 7.

Fullerene C_{60}, also known as *buckyball* or *buckminsterfullerens* is the 0D allotropic form of carbon: it has a truncated-icosahedric geometric structure,

Space dimension	Allotropic form	Hybridization	Bonding	Crystal system - class
0D	Fullerenes (C_{60})	sp^2	σ	Cubic - hexoctahedral
1D	Nanotubes	sp^2	σ	//
2D	Graphene	sp^2	σ in-plane, π between p_z orbitals	(2D) Hexagonal
3D	Graphite	sp^2 (in each plane)	σ in-plane, van der Waals out-of-plane	Hexagonal - dihexagonal dipyramidal
	Diamond	sp^3	σ	Cubic - hexoctahedral

Table 3: Allotropic forms of carbon. List of the most important C allotropes in any space dimension, showing the kind of sp hybridization, the chemical bonds between C atoms and the crystal symmetry involved in each system.

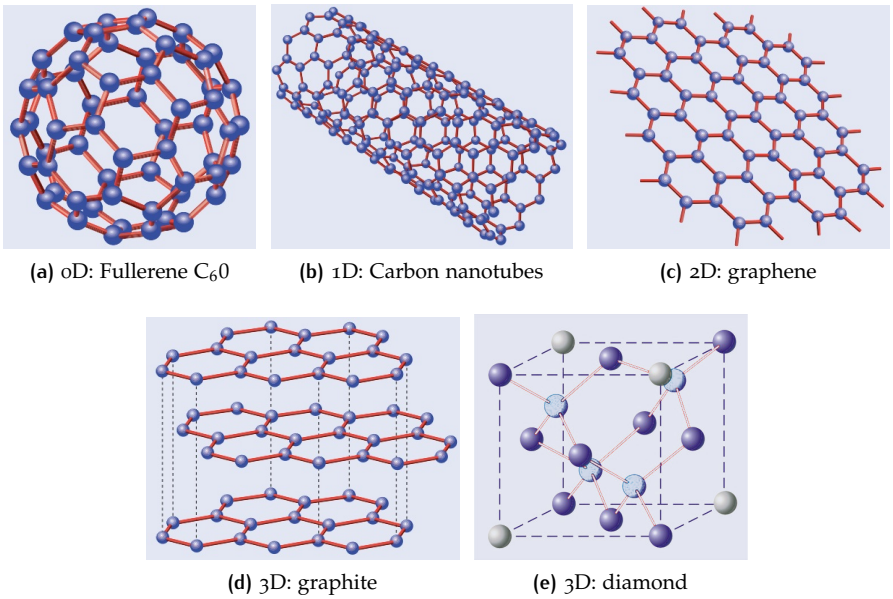

(a) 0D: Fullerene C_60 **(b)** 1D: Carbon nanotubes **(c)** 2D: graphene

(d) 3D: graphite **(e)** 3D: diamond

Figure 7: Crystal structure of carbon allotropes. Schematic view of the geometry of carbon allotropic forms in any space dimension. Adapted from [23].

resembling a soccer ball. It has been first intentionally prepared in 1985 by H. W. Kroto, J. R. Heath, S. C. O'Brien, R. F. Curl and R. E. Smalley from Rice University and the University of Sussex ([89]): three of them (H. W. Kroto, R. F. Curl and R. E. Smalley) have been awarded with the Nobel prize in Chemistry in 1996 for their key rôle in the discovery. Fullerenes can be obtained by wrapping-up a 2D structure of sp^2 hybridized C atoms arranged in hexagons and pentagons. Because of their properties, in particular their large internal space, possible applications concern hydrogen harvesting, photovoltaic cells and medicine.

Carbon nanotubes, the 1D allotropes of carbon, are cylindrical nanostructures of entirely sp^2 hybridized C atoms. In these structures, one dimension is much larger than the other two: nanotubes with a length to diameter ratio of up to 1.32×10^8:1 has been synthesized ([196]). Although a large percentage of the academic literature attributes the first synthesis of nanometre size C nanotubes to S. Iijima from NEC Corporation (Japan) in 1991, the history of their discovery is much more complex: indeed, it has been ascertained that nanotubes have been synthesized already in 1952 by a team of Russian researchers, L. V. Radushkevich and V. M. Lukyanovich. The fact that the article showing clear images of 50 nm diameter tubes was published in Russian language on a Soviet journal let the news unnoticed for many years. Later on, many other evidences of the synthesis of nanotubes by different scientists have been reported and can be found in literature. The misleading opinion of assigning S. Iijima the leadership in the discovery of carbon nanotubes is probably due to the incredible acceleration that followed Iijima's report on Nature of 1991 ([69]), to the innovative technique he employed for their synthesis and, most important, to the widespread habit of not distinguishing between single- and multi-walled carbon nanotubes: while for the latter the timeline of the discovery is quite ambiguous, for the former there is no doubt that the discovery should be attributed to S. Iijima' research group, that first reported the formation of this structure on Nature in 1993[1] ([70]). A full description of the history of nanotubes' discovery is beyond the scopes of this thesis and for more details I suggest the interested reader to refer to the comprehensive editorial [122], written in 2006 by M. Monthioux and V. Kuznetsov for the journal *Carbon*.

From the structural point of view, carbon nanotubes are categorized as single-, double- and multi-walled carbon nanotubes (SWCNs, DWCNs and MWCNs respectively) according to the number of concentric cylindrical graphitic fibres composing them (only one for SWCNs, two for DWCNs and multiple in the case of MWCNs). DWCNs form a special class of nanotubes because they have a morphology and many properties resembling those of SWCNs, but their resistance to chemicals is greatly improved. SWCNs can be obtained by rolling up along certain specific discrete angles (i.e. directions) a 2D single layer of graphite and joining the edges: according to the wrapping direction and the subsequent kind of edges obtained, they can be divided into *zigzag*, *armchair* and *chiral* nanotubes (Figure 8). This distinction is very important because the rolling angle (therefore the kind of edges) and the diameter of the tubes deeply affect their properties, in particular their band structure and electrical conductivity, that can show a metallic or semi conductive behaviour. Another important feature of nanotubes is their unique strength, resulting from the sp^2 hybridization of the C atoms form-

1 To be more precise, from a scientific and not merely a chronological point of view the discovery of single-walled carbon nanotubes should be shared between Iijima's and Bethune's groups, since also the latter reported the successful synthesis of these structures exactly in the same issue of Nature, see [11]

ing their structure, making them one of the strongest and stiffest material in nature in terms of tensile strength and elastic (Young's) modulus.
Due to the briefly described properties, carbon nanotubes find a place in a large number of applications. First of all they are employed as basic building blocks in Nanoelectronic engineering, in particular for the development of intermolecular FETs (SWCTs FETs have been reported in [111]): the main obstacle to nanotubes based electronics is the lack of a mass production technology (similar to what is happening for graphene). Moreover, because of their superior mechanical properties, carbon nanotubes are often used also for structural engineering applications, ranging from everyday life items like clothes or sport gear to more advanced issues (space elevators, bio-mimetic composite materials, ...). Finally, possible applications of nanotubes for photovoltaic cells, hydrogen storage, radar absorption, textile industry and medicine have been reported in the last years.

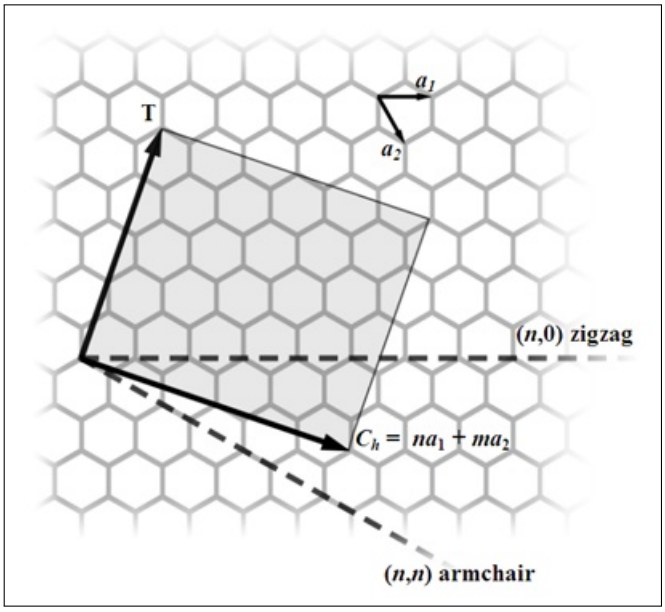

(a)

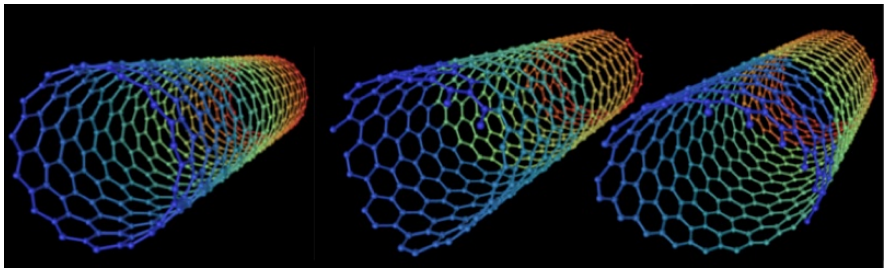

(b)

Figure 8: Carbon nanotubes edges. (a) Schematic description of carbon nanotubes formation from an (ideally) infinite single layer of graphite (i.e. graphene): the pair of integer indices (n,m) denotes the number of real pace graphene unit vectors $\mathbf{a}_1, \mathbf{a}_2$ to be summed up in order to obtain the vector $\mathbf{C}_\mathrm{h}$. The vector $\mathbf{T}$, orthogonal to $\mathbf{C}_\mathrm{h}$, is the tube axis: C_h is therefore the direction along which graphene must be rolled up to get the carbon nanotube; (b) Examples of different kinds of carbon nanotubes edges: zigzag, armchair and chiral (from left to right respectively). Courtesy of Wikipedia.

The allotropic forms of carbon in 3D, diamond and graphite (Figure 9), are the most known and studied since ancient times. Diamond have been probably recognized in India already 3000 years ago and it is nowadays a very popular mineral because of its widespread commercial use as gemstone. Carbon atoms in diamond are arranged in a cubic-hexoctahedral crystal lattice, a variation of the face-centered cubic structure, with crystal space group (in Hermann-Mauguin notation) Fd3m. Its hardness and thermal conductivity, the highest known among natural bulk materials, represent the most peculiar characteristics shown by this mineral and are closely related to the strong covalent bonding between the sp^3 hybridized C atoms constituting the lattice. Formation of diamonds can occur only at specific pressure and temperature conditions ($P \sim 4.5$–$6\,\mathrm{GPa}$, $T \sim 900$–$1300\,^\circ\mathrm{C}$), found in meteorites and in the Earth's lithospheric mantle; typical growth age varies from 1 to 3.3 thousand million years. Diamonds are famous also for their excellent optical dispersion, responsible for their lustre. Industrial applications range from electronics to high pressure experiments (for example for building diamond anvil cells) and use in cutting and grinding tools. A complete description of the physical principles and of the properties of diamond is far beyond the scope of this thesis and I refer the interested reader to specialized texts.
Graphite is the most common carbon allotrope: used already during the Neolithic Age (4^{th} Millennium B.C.) in southeastern Europe for painting pottery, it is the building block of pencils and its formation is the result of the reduction of sedimentary carbon compounds during metamorphism. It occurs in metamorphic rocks, igneous rocks and meteorites. Moreover, it is the most stable allotrope of carbon in standard conditions: also diamond is less stable than graphite, but the rate conversion from diamond to graphite is negligible in standard ambient conditions. Unlike diamond, usually an excellent electrical insulator, graphite is an electrical conductor: this is due to the geometrical structure of graphite, being composed by a stacking of 2D layers of sp^2 hybridized C atoms arranged in an honeycomb lattice. The conduction occurs primarily within each plane because of the delocalization of p_z electrons, those left unbounded after sp^2 orbital hybridization. The distance between planes is $3.35\,\text{Å}$ and their interaction occurs through van der Waals forces. Graphite is nowadays employed in refractories, batteries, steelmaking, foundry facings, lubricants and pencils. It is worth mentioning that HOPG, an high-quality synthetic form of graphite with an angular spread between sheets of less than 1°, is commonly used in scientific research and it has been indeed the first and essential element used by K. S. Novoselov, A. K. Geim and co-workers to synthesize graphene, as described in Sec. 1.3.

1.1.2 The 2D allotropic form: graphene

As described in the previous section, allotropic forms in space dimensions other than two are well known from decades (in certain cases, like for diamond and graphite, centuries): they have been successfully synthesized in laboratories and widely studied for many years. Nonetheless, until few years ago (2004) the 2D allotropic form of carbon, called *graphene*, was still missing: although P. R. Wallace had already predicted its band structure in 1947 ([192]) and some experiments opening the possibility of growing one-atom-thick graphitic forms of carbon appeared in the '70s and '80s ([117, 186]), no one before 2004 succeeded in growing monolayer graphene (MLG) in a way allowing for measuring its properties independently from the sub-

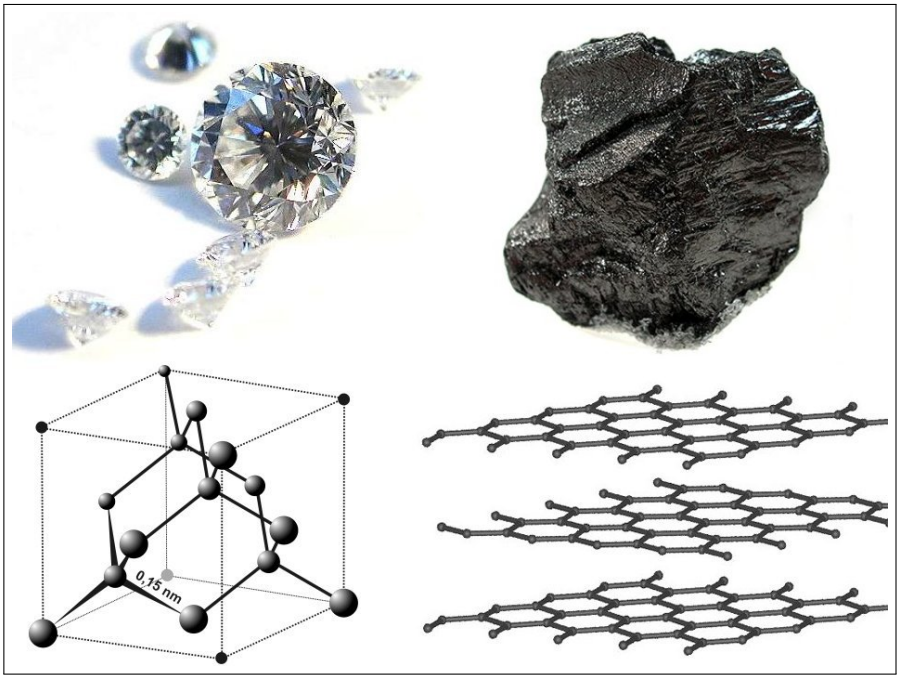

Figure 9: 3D allotropic forms of carbon: diamond and graphite. Image showing the oldest and best known allotropic forms of carbon: diamond and graphite. Lattice structures of both are also shown. Courtesy of Wikipedia.

strate. Only in 2004, as already mentioned in the Introduction, a research group from the Manchester University headed by K. S. Novoselov and A. K. Geim ([134]) had been able to do so, by successively peeling off layers of HOPG with adhesive tape and sticking them on a 300 nm-SiO_2/Si sample: among the flakes left on the substrate, visible on a common optical microscope, also MLG microrystals have been eventually detected. Because of the insulating properties of the SiO_2 layer, by gating opportunely monolayer graphene with n^+-type Si (Figure 3), the researchers could measure the sheet resistivity of MLG and few-layer graphene (FLG) as a function of the gate voltage applied, obtaining the evidence for a surprising behaviour typical of 2D zero-gap semimetals (completely different from the behaviour of graphite and thicker multilayer graphene) and extrapolating astonishing mobilities values of up to $10\,000\,\mathrm{cm^2\,V^{-1}\,s^{-1}}$. Moreover, QHE measurements in presence of an external magnetic field at temperature $T = 3\,\mathrm{K}$ were also performed, showing the characteristics plateaus in the behaviour of the Hall resistivity ρ_{xy} as a function of the magnetic field applied and providing clear evidence of the intrinsic 2D nature of charge carriers (that can be either electrons or holes) present in MLG and FLG.
These groundbreaking experiments has boosted immediately a very intense research on graphene, involving a great number of theoreticians and experimentalists around the world: indeed, the fact that a 2D membrane exists and is stable under ambient conditions is surprising and amizing by itself. Before 2004 the majority of scientists were sceptic about the possibility that such a truly two dimensional atomic crystal could really exist, mainly because of the Wagner-Mermin theorem ([118]), according to which no long-range order should be present in two dimensions. Finite temperature attempts indeed against the formation of any perfect 2D structure: in fact, because of the temperature atomic vibrations around nuclei equilibrium

positions turn out to be too large and to exceed the interatomic distance, thus provoking the rise of long-wavelength destructive bending fluctuations and the melt of the crystal. The reason why a truly one-atom-thick flexible membrane like graphene do really exist must be searched in anharmonic non-linear coupling between bending and stretching oscillatory modes, suppressing dangerous bending fluctuations. As a consequence, the stability of 2D membranes is ensured only by the presence of ripples on the surface of the crystal that shows therefore a natural roughness, with typical height scaling linearly with sample size. Ripples are indeed observed in freestanding graphene, that appears more like a wrinkled membrane with peaks and valleys rather than a completely flat plane, as shown in Figure 10. A clear evidence of the remarkable interest risen about graphene can be enlightened by looking at the number of publications, related to this subject, appeared per year from 2004 up to now: an astonishing exponential growth, never reported before, has been found (Figure 11, for more comprehensive studies on this topic see [44, 165]). The huge variety of applications (already mentioned in the Introduction) in which graphene properties, fully exploited, may guarantee significant improvements of nowadays technologies and the possibility of studying interesting relativistic effects (for example the Klein paradox) directly in a condensed matter system (we will see why in Sec. 1.2 while presenting the band structure of graphene) have been the fundamental reasons at the basis of this result.

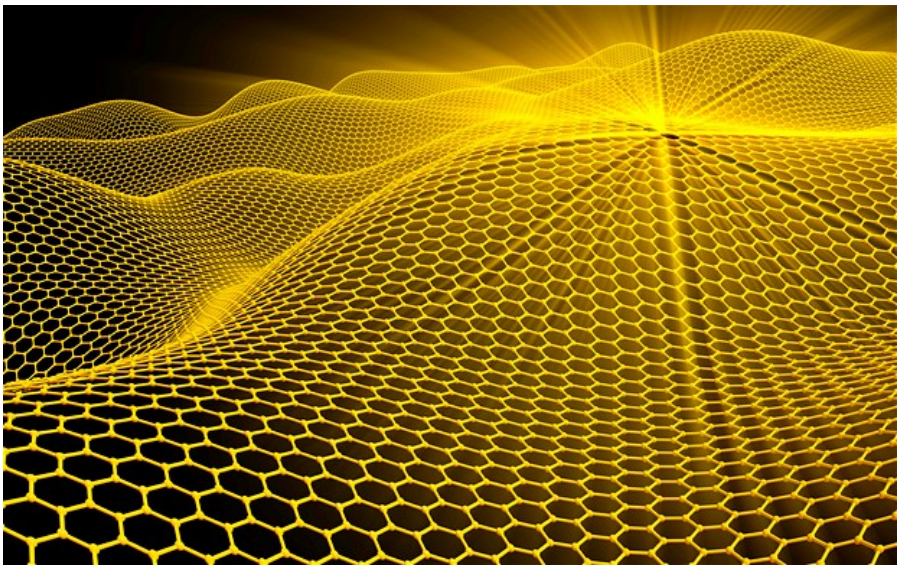

Figure 10: Rippled freestanding graphene membrane. Pictorial view of an ideal freestanding layer of graphene: finite temperature and quantum fluctuations, conspiring to destroy the 2D crystal structure, are suppressed by non-linear couplings responsible for the roughness of the surface, thus not appearing completely flat.

Before introducing the most important and peculiar theoretical properties of MLG, I will shortly examine its crystallographic structure. Graphene, as already mentioned, is a 2D crystal made of carbon atoms arranged in an honeycomb lattice. This lattice can be seen as combination of two interpenetrating triangular lattices, has a unit cell composed by two inequivalent carbon atoms and symmetry space group P6/mmm ([109]); graphene lat-

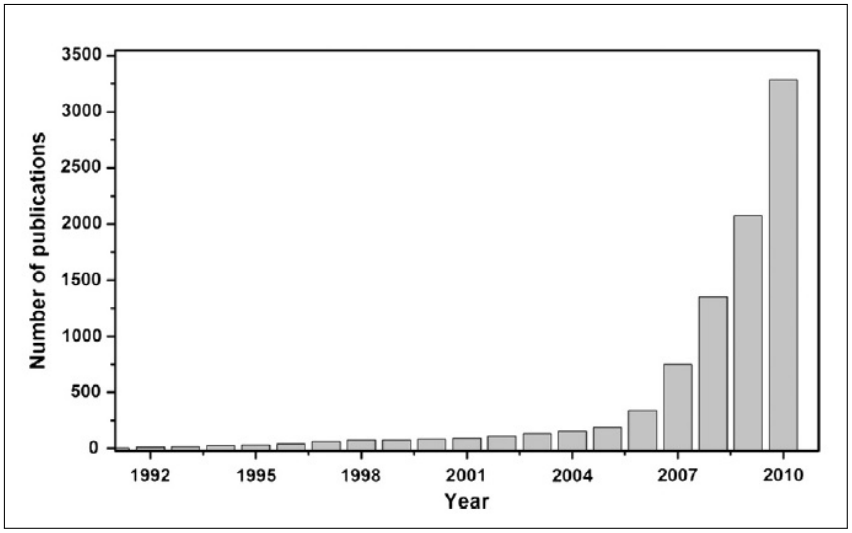

(a)

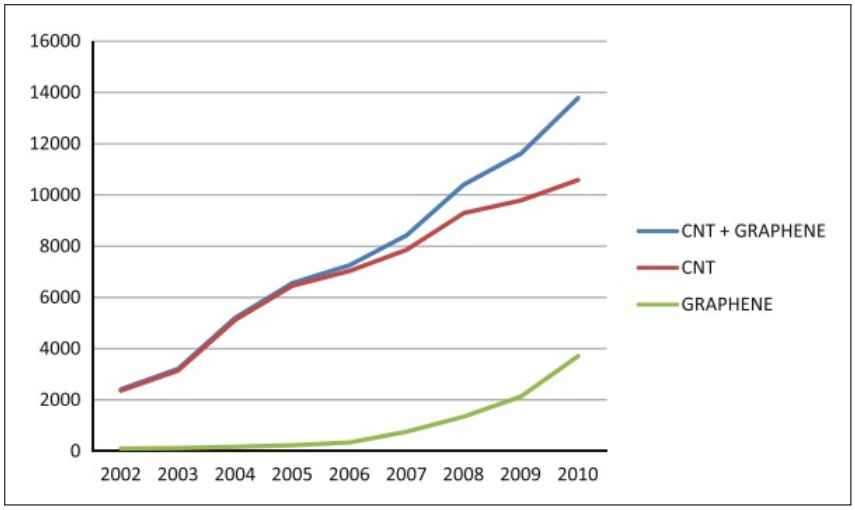

(b)

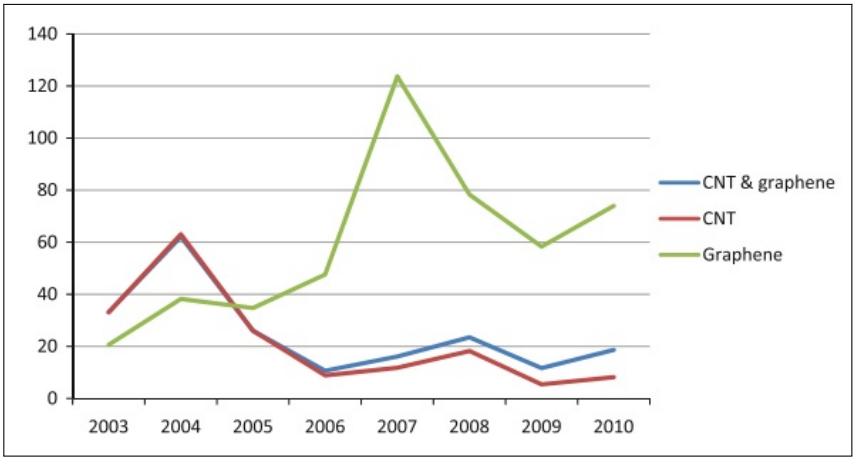

(c)

Figure 11: Scientometric analysis of graphene related literature. (a) Number of articles about graphene published in the past 20 years, according to ISI Web of Knowledge℠. Adapted from [165]; (b) Documents published yearly worldwide, on CNTs and graphene, in the past 8 years and (c) their percentage growth in comparison to the previous year (according to SCOPUS database). Adapted from [44].

tice is therefore a bipartite lattice. Referring to Figure 12, the lattice unit (primitive) vectors can be written as

$$\mathbf{a}_1 = \frac{a}{2}\left(\sqrt{3}, 1\right), \quad \mathbf{a}_2 = \frac{a}{2}\left(\sqrt{3}, -1\right) \tag{3}$$

where $a = \|\mathbf{a}_i\| \approx 2.46\,\text{Å}$ $(i = 1, 2)$ is the lattice constant of graphene. The nearest-neighbour vectors in real space are given by

$$\boldsymbol{\delta}_1 = \frac{\delta}{2}\left(1, \sqrt{3}\right), \quad \boldsymbol{\delta}_2 = \frac{\delta}{2}\left(1, -\sqrt{3}\right), \quad \boldsymbol{\delta}_3 = -\delta\,(1, 0) \tag{4}$$

and $\delta = \|\boldsymbol{\delta}_i\| = a/\sqrt{3} \approx 1.42\,\text{Å}$ $(i = 1, \ldots, 3)$ is the carbon-carbon distance. The reciprocal lattice, also represented by an hexagonal lattice, has unit vectors

$$\mathbf{b}_1 = \frac{2\pi}{a}\left(\frac{1}{\sqrt{3}}, 1\right), \quad \mathbf{b}_2 = \frac{2\pi}{a}\left(\frac{1}{\sqrt{3}}, -1\right) \tag{5}$$

and therefore the reciprocal space lattice constant is $b = \|\mathbf{b}_i\| = \frac{4\pi}{\sqrt{3}a} \approx 2.95\,\text{Å}^{-1}$ $(i = 1, 2)$.

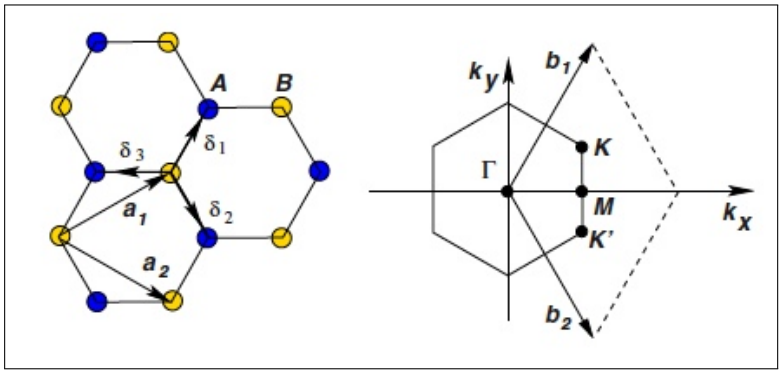

Figure 12: Direct and reciprocal lattice structure of graphene. The honeycomb lattice representing graphene on the left and its 1st Brillouin zone on the right. A and B points in graphene real space lattice are inequivalent carbon atoms representing the basis of graphene unit cell; the corresponding points in the reciprocal lattice are located at K and K'. Adapted from [24].

It is worth mentioning two inequivalent points at the corners of the 1st Brillouin zone, K and K', known as *Dirac points*, because of the important rôle that they play for the physics of graphene: their coordinates in momentum space are represented by the vectors

$$\mathbf{K} = \frac{2\pi}{\sqrt{3}a}\left(1, \frac{1}{\sqrt{3}}\right), \quad \mathbf{K}' = \frac{2\pi}{\sqrt{3}a}\left(1, -\frac{1}{\sqrt{3}}\right). \tag{6}$$

In Sec. 1.2 the reason for the special name assigned to these points will be clarified.

Graphene lattice can be thought of as composed of benzene rings without H atoms, with 3 of the 4 valence electrons of carbon atoms employed for the formation of (strong) trigonal σ bonds between sp^2 hybridized orbitals, usually called conjugated C-C bonds with a length $\delta \approx 1.42\,\text{Å}$ intermediate between a single and a double C-C bond (Figure 13): these bonds, lying in the graphene plane, ensure the mechanical flexibility and the astonishing robustness and strength of the graphene structure, making this material the strongest one known in nature. Moreover, the electrons left-over in

the neighbouring $2p_z$ orbitals of the C atoms form (cyclic) weak covalent π bonds between each other and, being completely delocalized on the lattice, are responsible for the astonishing electronic transport properties of graphene. σ bands are completely filled and very deep in energy, while the π band, also completely filled (for gate voltage $V_g = 0$) and originated by the overlapping of half-filled $2p_z$ orbitals perpendicular to graphene plane, represents the valence band of graphene and has higher energy (the corresponding anti-bonding band π^* is the conduction band and it is completely empty when no gate voltage is applied to the system).

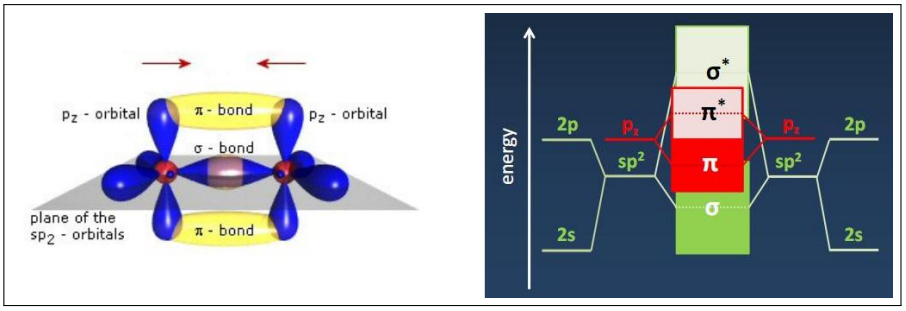

Figure 13: Chemical bonds involved in graphene structure. Schematic view of the chemical bonding between carbon atoms in graphene. The 2s, $2p_x$ and $2p_y$ orbitals of each atom hybridize in three sp^2 orbitals lying in the same plane -the graphene plane- with angles of 120° among them: the bonding between sp^2 orbitals results in strong (deep in energy, as shown on the right) σ bonds tying up nearest-neighbour carbon atoms. The electrons left-over in overlapping $2p_z$ orbitals are weakly bound in covalent π bonds, much higher in energy with respect to the σ bands: the resulting π band is completely filled, while the anti-bonding band π^* is completely empty.

Finally, as already pointed out in Sec. 1.1.1 and graphically shown in Figure 14, graphene can be seen as the "seed", the basic component for the formation of all the other allotropic forms of carbon (except for diamond) in dimension other than 2. Fullerenes can be obtained by introducing pentagons in the graphene lattice and then wrapping-up the resulting structure. Carbon nanotubes are obtained by rolling-up along a given direction a graphene layer and then joining the edges. Graphite is regarded as a stacking of graphene layers weakly coupled by van der Waals forces.

The main crystallographic properties of graphene are listed for completeness in Table 4.

1.2 THEORETICAL OVERVIEW

In this section I will examine in more details the remarkable properties of graphene from a theoretical point of view. These properties are a direct consequence of its lattice structure, presented in Sec. 1.1.2, and show the novel peculiar features owned by this material, completely different with respect to the other common 2D semiconductors: these properties make graphene really attracting and fascinating. I will in particular investigate the electronic band structure of graphene and some of the most important relativistic effects exhibited by its charge carriers, like the Klein paradox,

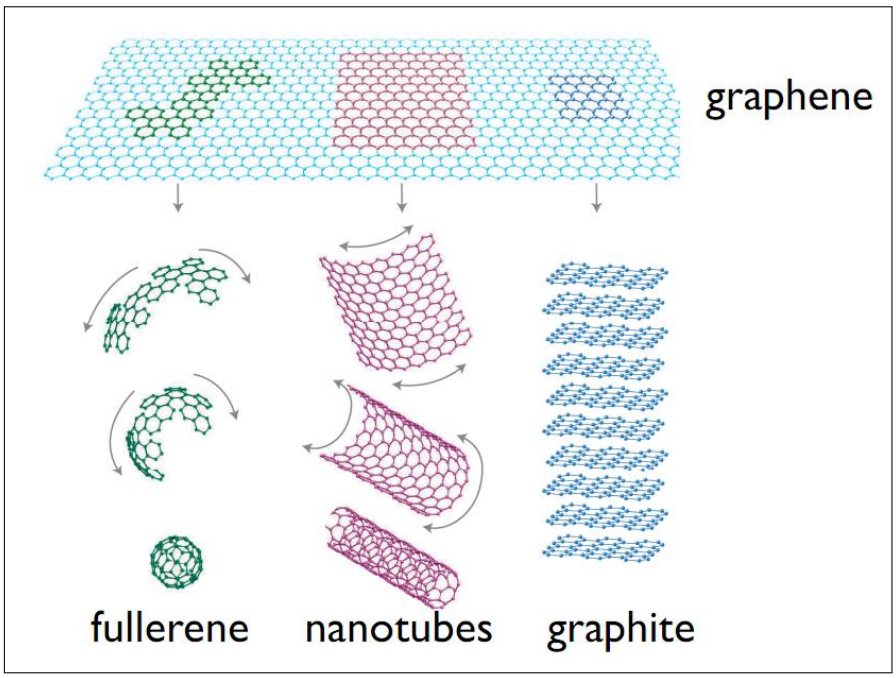

Figure 14: Graphene and the other allotropic form of carbon. Graphene, the 2D allotropic form of carbon, can be regarded as the building block for obtaining all the other most known carbon allotropes -except for diamond- in 0D, 1D and 3D. Adapted from [52].

Graphene crystallographic parameters	
C - C distance	$\delta \approx 1.42\,\text{Å}$
Real space lattice constant	$a = \sqrt{3}\delta \approx 2.46\,\text{Å}$
Real space primitive vectors	$\mathbf{a}_{1/2} = \frac{a}{2}\left(\sqrt{3}, \pm 1\right)$
Reciprocal space lattice constant	$b = \frac{4\pi}{\sqrt{3}a} \approx 2.95\,\text{Å}^{-1}$
Reciprocal space primitive vectors	$\mathbf{b}_{1/2} = \frac{2\pi}{a}\left(\frac{1}{\sqrt{3}}, \pm 1\right)$
Basis - real space unit cell	Two C atoms: **A** and **B**
Basis - reciprocal space unit cell	Dirac Points: **K** and **K′**

Table 4: Graphene crystallographic properties. Main crystallographic parameters of graphene with reference to Figure 12.

an anomalous QHE and a non-zero minimum conductivity present also for vanishing density of states (DOS).

1.2.1 Tight-binding model and graphene band structure

Let's start by determining the electronic band structure of graphene, i.e. the energy dispersion of graphene electrons. I will concentrate only on the derivation of the energy dispersion of π electrons, since only these electrons are responsible for the electronic transport properties and since only π bands show the most peculiar feature of the electronic configuration of graphene, i.e. a linear dispersion relation at low energy near the Dirac points K and K', whose positions are given in 6 (or, equivalently, a conical crossing of the π and π^* bands at the Dirac points). The dispersion relation was first derived by P. R. Wallace in 1947 ([192]) and has been reviewed in many recent publications ([1, 9, 10, 24, 78, 157]). The starting point for making calculations is to write down the Hamiltonian that describes the hopping of electrons between nearest-neighbour carbon atoms in the framework of tight-binding approximation.

Before writing the Hamiltonian, I give a very brief remind about the tight-binding approach to the evaluation of electronic energy bands in crystals: further details can be found in the original paper by J. C. Slater and G. F. Koster ([166]) and in various books and reviews (I recommend in particular [2, 10, 36, 146], the latter being devoted explicitly to tight-binding calculations applied to graphene). According to this approximation, appropriate for the description of electrons in semiconductors and insulators (where electrons move "slowly" or not at all in the crystal and they belong therefore to an atom in the lattice for an appreciable time before they move on; they are in a sense *tightly bound* to each atom of the crystal structure and they only "hop" between atoms to minimize the total energy), the electron wavefunctions $\psi_{\mathbf{k}}(\mathbf{r})$ in the crystal are built as linear combinations of atomic orbitals wavefunctions $\phi_n(\mathbf{r}-\mathbf{R})$, where $\mathbf{r}$, $\mathbf{R}$ represent the real space positions of the electron and nucleus respectively ($\mathbf{R}$ is therefore a generic lattice vector) and $n \in \mathbb{N}$ is the discrete index characterizing different quantized energy levels of a single atom of the lattice (I am assuming here, for simplicity, the case of a crystal with only one atom per unit cell; the generalization to the case of compounds of various atoms per unit cell is straightforward). Each atomic orbital ϕ_n satisfies by definition the equation

$$H_{\text{at}}\phi_n(\mathbf{r}-\mathbf{R}) = \epsilon_n\phi_n(\mathbf{r}-\mathbf{R}) \tag{7}$$

where $H_{\text{at}} = -\frac{\hbar^2}{2m_e}\boldsymbol{\nabla}_{\mathbf{r}}^2 + V_{\text{at}}(\mathbf{r}-\mathbf{R})$ (with m_e electron mass) is the Hamiltonian of a single atom of the crystal, whose nucleus is sat in $\mathbf{R}$ and produces a potential $V_{\text{at}}(\mathbf{r}-\mathbf{R})$. $\phi_n(\mathbf{r}-\mathbf{R})$ is therefore an eigenfunction of the single-atom Hamiltonian relative to the energy eigenvalue ϵ_n. In order to find the eigenfunctions $\psi_{\mathbf{k}}(\mathbf{r})$ of the total Hamiltonian of the crystal $H = -\frac{\hbar^2}{2m_e}\boldsymbol{\nabla}_{\mathbf{r}}^2 + V(\mathbf{r})$ describing one electron in the lattice ($V(\mathbf{r}) = V(\mathbf{r}+\mathbf{R})$ $\forall\mathbf{R}$ is the periodic potential of the system; moreover I am assuming that the Born approximation holds for the crystal, meaning that nuclei's and electrons' motions can be treated separately and I am looking only at the electrons' dynamics in a configuration in which nuclei are fixed at lattice sites $\mathbf{R}$), the idea is to try with an *ansatz* about its form given by

$$\psi_{\mathbf{k}}(\mathbf{r}) = \sum_n b_n(\mathbf{k})B_{n,\mathbf{k}}(\mathbf{r}) \tag{8}$$

with

$$B_{n,\mathbf{k}}(\mathbf{r}) = N^{-1/2} \sum_{\mathbf{R}} e^{i\mathbf{k}\cdot\mathbf{R}} \phi_n(\mathbf{r} - \mathbf{R}). \tag{9}$$

In relation 9 N is the number of unit cells in the crystal, the sum is extended to all the lattice vectors $\mathbf{R}$ representing the positions of the atoms' nuclei in the crystal, $B_{n,\mathbf{k}}(\mathbf{r})$ are Bloch sums of atomic orbitals (meaning that $B_{n,\mathbf{k}}(\mathbf{r} + \mathbf{R_0}) = e^{i\mathbf{k}\cdot\mathbf{R}_0} B_{n,\mathbf{k}}(\mathbf{r})$ for every lattice vector $\mathbf{R}_0$, or, equivalently, meaning that $B_{n,\mathbf{k}}(\mathbf{r})$ can be written as a Bloch function in the form $B_{n,\mathbf{k}}(\mathbf{r}) = e^{i\mathbf{k}\cdot\mathbf{r}} u_{\mathbf{k}}(\mathbf{r})$ with $u_{\mathbf{k}}(\mathbf{r} + \mathbf{R}_0) = u_{\mathbf{k}}(\mathbf{r}) = e^{-i\mathbf{k}\cdot\mathbf{r}} B_{n,\mathbf{k}}(\mathbf{r})$ $\forall \mathbf{R}_0$) and $b_n(\mathbf{k})$ are coefficients to be determined by means of a self-consistent argument, requiring $\psi_{\mathbf{k}}(\mathbf{r})$ to be an eigenfunction of H. Roughly speaking, the coefficients $b_n(\mathbf{k})$ represent the amount of Bloch sum $B_{n,\mathbf{k}}$ present in the crystal wavefunction $\psi_{\mathbf{k}}$.
In order to find explicitly the wavefunctions $\psi_{\mathbf{k}}(\mathbf{r})$ (therefore the unknown coefficients $b_n(\mathbf{k})$ and the energy bands $\epsilon_{\mathbf{k}}$ of the crystal), the equation 8 is inserted in the time independent Schrödinger equation

$$H\psi_{\mathbf{k}} = \epsilon_{\mathbf{k}} \psi_{\mathbf{k}} \tag{10}$$

supposing it is a solution of the eigenvalue problem. Both sides of equation 10 are multiplied by $B^*_{m,\mathbf{k}}(\mathbf{r})$ and then integrated over all the volume A (in real space) occupied by the crystal. The eigenvalue problem 10 simplifies therefore to an algebraic problem consisting in finding the solution of the following homogeneous system of m linear equations:

$$\sum_n \left[H_{mn}(\mathbf{k}) - \epsilon_{\mathbf{k}} S_{mn}(\mathbf{k}) \right] b_n(\mathbf{k}) = 0 \tag{11}$$

in which the unknown variables to be determined are the $b_n(\mathbf{k})$s (the energy bands $\epsilon_{\mathbf{k}}$ are found requiring that $\det\left[H_{mn}(\mathbf{k}) - \epsilon_{\mathbf{k}} S_{mn}(\mathbf{k})\right] = 0$). H_{mn} and S_{mn} are matrices called *Hamiltonian* and *overlapping* matrices respectively; $m, n \in \mathbb{N}$ are matrix indices. The expressions for these matrices, in momentum (12) and real (13) space respectively, are:

$$H_{mn}(\mathbf{k}) = \int_A \mathrm{d}\mathbf{r} B^*_{m,\mathbf{k}}(\mathbf{r}) H B_{n,\mathbf{k}}(\mathbf{r}), \quad S_{mn}(\mathbf{k}) = \int_A \mathrm{d}\mathbf{r} B^*_{m,\mathbf{k}}(\mathbf{r}) B_{n,\mathbf{k}}(\mathbf{r}); \tag{12}$$

$$H_{mn}(\mathbf{R}) = \int_A \mathrm{d}\mathbf{r} \phi^*_m(\mathbf{r}) H \phi_n(\mathbf{r} - \mathbf{R}), \quad S_{mn}(\mathbf{R}) = \int_A \mathrm{d}\mathbf{r} \phi^*_m(\mathbf{r}) \phi_n(\mathbf{r} - \mathbf{R}). \tag{13}$$

Let's point out two important features about the meaning of these relations:

- 12 and 13 are clearly *lattice Fourier transforms* of each other, i.e. $H_{mn}(\mathbf{k}) = \sum_{\mathbf{R}} e^{i\mathbf{k}\cdot\mathbf{R}} H_{mn}(\mathbf{R})$ and similarly $S_{mn}(\mathbf{k}) = \sum_{\mathbf{R}} e^{i\mathbf{k}\cdot\mathbf{R}} S_{mn}(\mathbf{R})$;
- it is clear from 13 that $H_{mn}(\mathbf{R})$ is the probability amplitude that an electron in the atomic orbital ϕ_n at the generic lattice site $\mathbf{R}$ will hop to the atomic orbital ϕ_m placed at $\mathbf{R} = 0$ (the origin of the system) under the action of the Hamiltonian H, while $S_{mn}(\mathbf{R})$ is just the probability amplitude that the two atomic orbitals ϕ_n and ϕ_m overlap each other (therefore the name "overlapping matrix" assigned to S_{mn}).

Once the matrices H_{mn}, S_{mn} have been evaluated and are known, the eigenvalue problem 11 is in principle solvable and the eigenvalues $\epsilon_{\mathbf{k}}$ with the corresponding eigenvectors $b(\mathbf{k})$ (I have written the vector b_n implicitly, without displaying the index n) can be determined. Through 8 it is finally possible to write down explicitly also the approximated electron wavefunction $\psi_{\mathbf{k}}(\mathbf{r})$ we were looking for at the beginning and the problem is completely solved.

Let's go back now to the case of graphene. We have seen in Sec. 1.1.2 that graphene's unit cell is composed by two inequivalent carbon atoms (Figure 12) located at positions $\mathbf{R}_j^A = n\mathbf{a}_1 + m\mathbf{a}_2$, $\mathbf{R}_j^B = \mathbf{R}_j^A + \boldsymbol{\delta}_3$ (with $\mathbf{a}_1 = a\sqrt{3}\hat{\mathbf{x}}/2 + a\hat{\mathbf{y}}/2$ and $\mathbf{a}_2 = a\sqrt{3}\hat{\mathbf{x}}/2 - a\hat{\mathbf{y}}/2$ primitive vectors of the crystal lattice), where the superscripts A, B are used to identify the kind of triangular sublattice (of the hexagonal graphene lattice) the carbon atoms belong to; $j = (n, m) \in \mathbb{N}^2$ is therefore a couple of integer indices specifying in an unique way the positions $\mathbf{R}^A$ of A carbon atoms in the graphene structure, while the positions of B carbon atoms are obtained from any A positions simply through a translation of vector $\boldsymbol{\delta}_3$ (the vector connecting nearest-neighbours carbon atoms). Because of this one-to-one correspondence between the "vector" index $j \in \mathbb{N}^2$ and the A (and consequently also the B) sublattice vectors $\mathbf{R}^A$, we are allowed to add the subscript j to the $\mathbf{R}^A$ (and consequently the $\mathbf{R}^B$). I finally recall that n, m are always integers since $\mathbf{a}_1, \mathbf{a}_2$ are primitive lattice vectors and $\mathbf{R}^A$ are generic *lattice* vectors localizing the positions of all the points in the sublattice A forming the graphene crystal structure: hence, by definition, $\mathbf{R}^A$ are *integer linear combinations* of the primitive lattice vectors ([84]).
In order to apply the tight-binding model to graphene, I will assume the positions of graphene unit cells to be given by the positions $\mathbf{R}_j^A$ of A carbon atoms. The model, as described above, requires to represent the π electrons (the electrons in the p_z orbitals of the carbon atoms, delocalized on the lattice and not involved in the σ bonds constituting the core of the crystal structure) wavefunction $\psi_{\mathbf{k}}(\mathbf{r})$ as a linear combination of the p_z atomic orbital wavefunctions of a single carbon atom. Following P. R. Wallace ([192]), a possible representation of $\psi_{\mathbf{k}}$ is given by:

$$\psi_{\mathbf{k}}(\mathbf{r}) = N^{-1/2} \sum_{j \in \mathbb{N}^2} \left[e^{i\mathbf{k}\cdot\mathbf{R}_j^A} c^A(\mathbf{k}) \phi(\mathbf{r} - \mathbf{R}_j^A) + e^{i\mathbf{k}\cdot\mathbf{R}_j^B} c^B(\mathbf{k}) \phi(\mathbf{r} - \mathbf{R}_j^B) \right] \quad (14)$$

where $\phi(\mathbf{r})$ are the wavefunctions of the p_z orbitals of a single carbon atom and N is the number of unit cells of the crystal. The unknown coefficients $c^A(\mathbf{k}), c^B(\mathbf{k})$ are determined, as already explained, by requiring 14 to be eigenstates of the Hamiltonian H_{graph} describing graphene. The latter must allow π electrons hopping between nearest-neighbour atoms (this is the simpler and most fundamental approximation; it is possible of course to extend the Hamiltonian to higher order, by including next-to-nearest-neighbours hopping and so on), so that hopping of electrons among atoms belonging to the same sublattice A or B is forbidden and only "inter-sublattice" hopping is allowed: hence it can be written, in first quantization formalism, as

$$H_{\text{graph}} = -t \sum_{\langle i,j \rangle} \left(| \phi_j^A \rangle \langle \phi_i^B | + \text{h.c.} \right). \quad (15)$$

The parameter t in 15 is called hopping parameter and it is supposed to be equal for all the three possible nearest-neighbours atoms in which an electron standing on an A/B carbon atom can hop to (its value is $\approx 2.8\,\text{eV}$, as reported in [24]), $\langle i, j \rangle$ denotes nearest-neighbours positions $\mathbf{R}_i, \mathbf{R}_j$ and $| \phi_j^{A/B} \rangle$ is the standard Dirac notation for the wavefunctions $\left\langle \mathbf{r} | \phi_j^{A/B} \right\rangle = \phi(\mathbf{r} - \mathbf{R}_j^{A/B})$. The Hamiltonian 15 allows, as expected, an electron on a carbon atom of kind A (B) at position $\mathbf{R}_j^A$ ($\mathbf{R}_i^B$ respectively) to hop on one of the three nearest-neighbours carbon atoms of opposite kind B (A) at position $\mathbf{R}_i^B$ ($\mathbf{R}_j^A$ respectively) with probability $|t|^2$.

Once the Hamiltonian H_{graph} has been written, the eigenequations for the coefficients $c^A(\mathbf{k}), c^B(\mathbf{k})$ are straightforwardly obtained by evaluating $\left\langle \phi_j^{A/B} \middle| H_{\text{graph}} \middle| \psi_{\mathbf{k}} \right\rangle$, where $| \psi_{\mathbf{k}} \rangle$ is again the standard Dirac notation for the wavefunction $\langle \mathbf{r} | \psi_{\mathbf{k}} \rangle = \psi_{\mathbf{k}}(\mathbf{r})$ given by 14, and requiring that $H_{\text{graph}} \psi_{\mathbf{k}} = \epsilon_{\mathbf{k}} \psi_{\mathbf{k}}$. Making some calculations we end up with the following equations:

$$\begin{aligned} \epsilon(\mathbf{k}) c^A(\mathbf{k}) &= -t c^B(\mathbf{k}) \sum_{m=1}^{3} e^{-i\mathbf{k}\cdot\delta_m} \\ \epsilon(\mathbf{k}) c^B(\mathbf{k}) &= -t c^A(\mathbf{k}) \sum_{m=1}^{3} e^{i\mathbf{k}\cdot\delta_m}. \end{aligned} \tag{16}$$

By defining $S(\mathbf{k}) = -t \sum_{m=1}^{3} e^{-i\mathbf{k}\cdot\delta_m}$, the Hamiltonian 15 can be rewritten as

$$H_{\text{graph}} = \begin{pmatrix} 0 & S(\mathbf{k}) \\ S^*(\mathbf{k}) & 0 \end{pmatrix} \tag{17}$$

and has eigenvalues

$$\epsilon(\mathbf{k}) = \pm |S(\mathbf{k})| = \pm t \sqrt{3 + f(\mathbf{k})} \tag{18}$$

with

$$\begin{aligned} f(\mathbf{k}) &= 2\cos\left(a k_y\right) + 4\cos\left(\frac{a k_y}{2}\right)\cos\left(\frac{\sqrt{3} a k_x}{2}\right) \\ &= 2\cos\left(\sqrt{3} k_y \delta\right) + 4\cos\left(\frac{\sqrt{3}}{2} k_y \delta\right)\cos\left(\frac{3}{2} k_x \delta\right) \end{aligned} \tag{19}$$

(the values of the parameters a and δ are reported in Table 4). The eigenvalues 18 are those we were looking for and represent the π electrons energy bands of graphene: the "+" sign applies to the (empty in the intrinsic undoped case) π^* band, having higher energy, while the "-" sign applies to the (fully occupied in the intrinsic undoped case) π band of lower energy. The energy spectrum of graphene, showing the dispersion relation for the π bands (the behaviour of the functions 18) is reported in Figure 15.

Given that $S(\mathbf{k}) = |S(\mathbf{k})| e^{-i\theta(\mathbf{k})} = |\epsilon(\mathbf{k})| e^{-i\theta(\mathbf{k})}$ (with $\theta(\mathbf{k}) = -\arg[S(\mathbf{k})]$), I can rewrite the eigenequations 16 and the Hamiltonian 17 in the more convenient form:

$$\begin{aligned} c^A(\mathbf{k}) &= \frac{S(\mathbf{k})}{\epsilon(\mathbf{k})} c^B(\mathbf{k}) = \frac{|\epsilon(\mathbf{k})|}{\epsilon(\mathbf{k})} e^{-i\theta(\mathbf{k})} c^B(\mathbf{k}) = \pm e^{-i\theta(\mathbf{k})} c^B(\mathbf{k}) \\ c^B(\mathbf{k}) &= \frac{S^*(\mathbf{k})}{\epsilon(\mathbf{k})} c^A(\mathbf{k}) = \frac{|\epsilon(\mathbf{k})|}{\epsilon(\mathbf{k})} e^{i\theta(\mathbf{k})} c^A(\mathbf{k}) = \pm e^{i\theta(\mathbf{k})} c^A(\mathbf{k}) \end{aligned} \tag{20}$$

and

$$H_{\text{graph}} = |\epsilon(\mathbf{k})| \begin{pmatrix} 0 & e^{-i\theta(\mathbf{k})} \\ e^{i\theta(\mathbf{k})} & 0 \end{pmatrix}. \tag{21}$$

By means of 20 I can write down also the eigenfunction 14 in an explicit way as

$$\psi_{\mathbf{k}}(\mathbf{r}) = (2N)^{-1/2} \sum_{j \in \mathbb{N}^2} \left[e^{i\mathbf{k}\cdot\mathbf{R}_j^A} \phi(\mathbf{r} - \mathbf{R}_j^A) \pm e^{-i\theta(\mathbf{k})} e^{i\mathbf{k}\cdot\mathbf{R}_j^B} \phi(\mathbf{r} - \mathbf{R}_j^B) \right]. \tag{22}$$

The $\mathbf{k}$ dependence of the phase $\theta(\mathbf{k})$ is reported in Figure 16: although in the representation 14 of $\psi_{\mathbf{k}}(\mathbf{r})$ I have chosen the six corners of the reciprocal

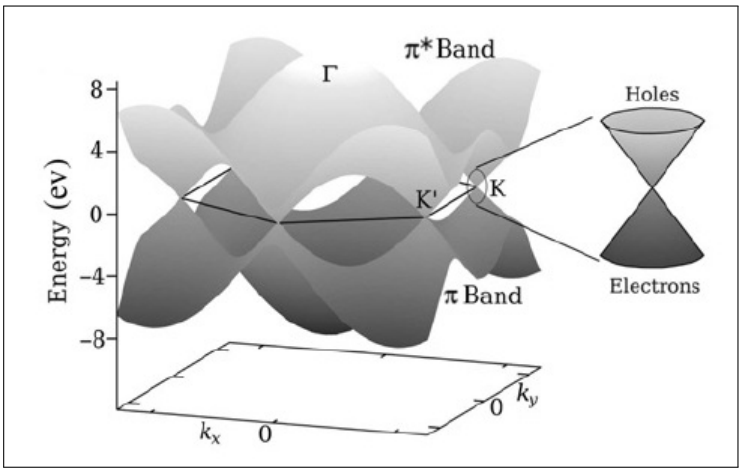

(a)

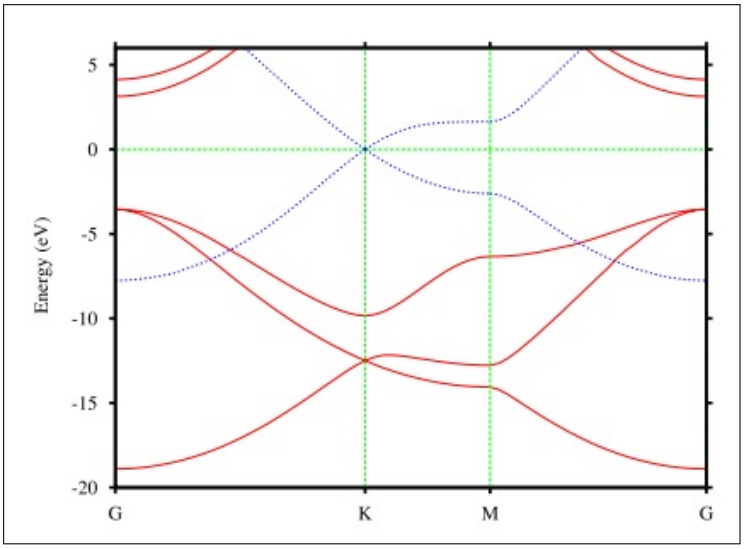

(b)

Figure 15: Graphene band structure. Energy spectrum of single layer undoped graphene considering only nearest-neighbours coupling between electrons in $2p_z$ orbitals: (a) 3D view of the π and π^* bands drawn in the 1^{st} Brillouin zone, with the conical crossing at the Dirac points K and K' enlightened. Adapted from [1]; (b) 2D view of the dispersion relation of the electronic energy bands along the $G = \Gamma \rightarrow K \rightarrow M \rightarrow G$ path in the 1^{st} Brillouin zone (these points are shown in Figure 12): solid red lines are the fully occupied σ bands, while dotted blue lines are π (fully occupied) and π^* (empty) bands. Adapted from [15].

space unit cell (the 1st Brillouin zone) appear to be all inequivalent, it is possible to choose other more useful representations (look for example [10]) according to which only two of the six corners of the unit cell (namely the Dirac points K and K') are inequivalent, while all the points of the reciprocal lattice that can be obtained by translation with various combinations of the primitive reciprocal lattice vectors $\mathbf{b}_1$ and $\mathbf{2}$ (defined in 5) are equivalent to either K or K'. Therefore, it is possible to conclude that as the basis of the real space graphene crystal is made of two inequivalent carbon atoms A and B, also the basis of its reciprocal space crystal contains two inequivalent points K and K' (although in some representation, as the one I have chosen, this is not immediately clear).

1.2.2 Low energy expansions

By inserting the expressions 6 giving the coordinates (in reciprocal space) of the graphene Dirac points K and K' into the energy eigenvalues 18, it easy to check that $\epsilon(K) = \epsilon(K') = 0$. More in general, the energy vanishes at all the points of the reciprocal lattice having coordinates

$$\mathbf{k}^{\xi}_{m,n} = \xi \frac{\mathbf{b}_1 - \mathbf{b}_2}{1} + m\mathbf{b}_1 + n\mathbf{b}_2 \tag{23}$$

where $\xi = \pm$ is the valley index (distinguishing the inequivalent Dirac points K and K'), $\mathbf{b}_1, \mathbf{b}_2$ are the reciprocal lattice primitive vectors defined in 5 and $m, n \in \mathbb{N}$ is a couple of integers. Each point $\mathbf{k}^{\xi}_{m,n}$ is equivalent to all the points having different m, n but same ξ: equivalent points are obtained one from the other by translations with reciprocal lattice vectors. The $\xi = \pm$ pair that is more often chosen contains two corners of the 1st Brillouin zone of the reciprocal space (the points $\mathbf{K}^{\pm}_{0,0}$) that are exactly obtained from the K, K' Dirac points by translation with reciprocal lattice primitive vector $\mathbf{b}_1$ and $\mathbf{b}_2$ (see Figure 12): these corners correspond to the choice $m = n = 0$ in 23. So, more precisely:

$$\begin{aligned} \mathbf{K}^{+}_{0,0} &= \mathbf{K}' - \mathbf{b}_2 \\ \mathbf{K}^{-}_{0,0} &= \mathbf{K} - \mathbf{b}_1 \end{aligned}$$

where the vectors $\mathbf{K}, \mathbf{K}'$ and $-\mathbf{b}_1, -\mathbf{b}_2$ are defined in 6 and 5 respectively.
I can now expand the Hamiltonian 17 around the $\mathbf{K}^{+}_{0,0}, \mathbf{K}^{-}_{0,0}$ points in the 4×4 space defined by $(KA, KB, K'A, K'B)$, in which electron wavefunctions are distinguished according to both the real space sublattice indices A, B (distinguishing the A and B inequivalent points in the real space graphene lattice) and the valley indices K, K' (distinguishing the K and K' inequivalent points in the reciprocal space graphene lattice). Defining $\mathbf{q} = \mathbf{k} - \mathbf{K}^{\xi}_{0,0}$ (with $q = \|\mathbf{q}\| \ll \left\|\mathbf{K}^{\xi}_{0,0}\right\|$ for both $\xi = \pm$), the 4×4 Hamiltonian matrix around the Dirac points K, K' (i.e. the low energy expansion of 17) takes the simple form:

$$H_{\text{graph}}(q) = v_{\text{F}} \times \begin{pmatrix} 0 & z_{m,n}\left(q_x - iq_y\right) & 0 & 0 \\ z^*_{m,n}\left(q_x + iq_y\right) & 0 & 0 & 0 \\ 0 & 0 & 0 & z^*_{m,n}\left(q_x - iq_y\right) \\ 0 & 0 & z_{m,n}\left(q_x + iq_y\right) & 0 \end{pmatrix} \tag{24}$$

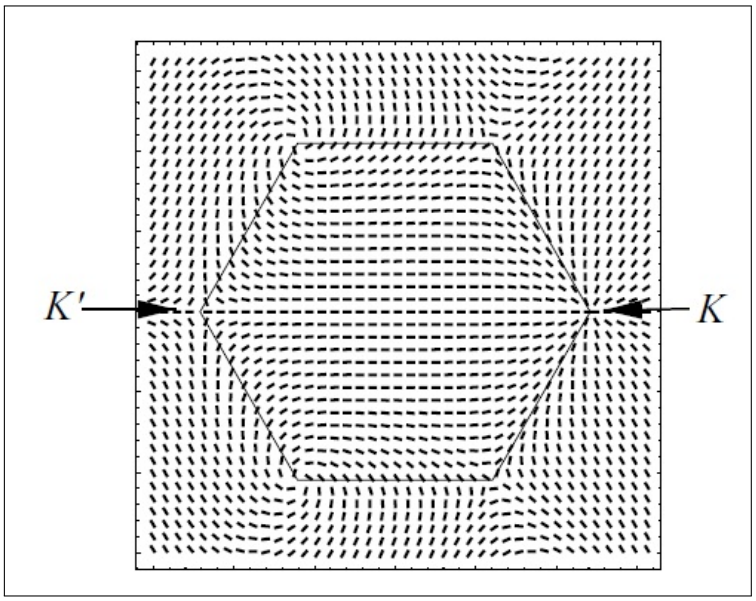

(a)

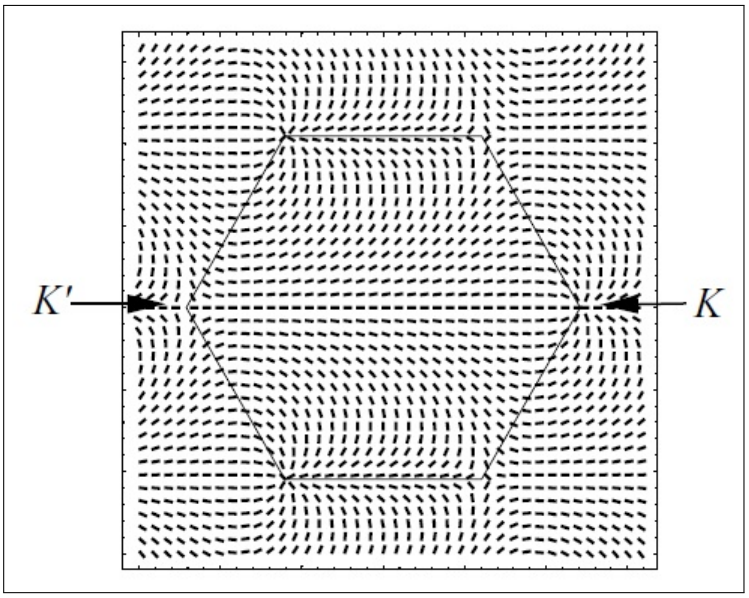

(b)

Figure 16: Dependence of the phase θ on $\mathbf{k}$. The $\mathbf{k}$ dependence of the phase θ is represented by small segments in the two-dimensional reciprocal space of graphene: (a) in the case of the $\psi_{\mathbf{k}}(\mathbf{r})$ representation given by 14. The six corners of the 1st Brillouin zone appear all inequivalent; (b) In the case of a more convenient representation in which there is a common phase factor $\exp\left(i\mathbf{k}\cdot\mathbf{R_j}\right)$ attached to both the atomic orbitals $\mid \phi_j^{A/B} \rangle$ of the A and B carbon atoms. In this case it is clear that there are only two inequivalent point in the 1st Brillouin zone, namely K and K'. Both adapted from [10].

where $v_F = 3\delta|t|/2 = c/300 \simeq 10^{-6}\,m\,s^{-1}$ is the Fermi velocity and $z_{m,n} = e^{2i\pi(m+n)/3}$ is a phase factor depending on the choice of the m, n indices (so, depending on the choice of the vectors $\mathbf{K}^{\xi}_{m,n}$ in the reciprocal space lattice; the presence of this phase factor is related to the fact that, as displayed in Figure 16, in the representation of $\psi_{\mathbf{k}}(\mathbf{r})$ I have chosen all the six points at the corners of the 1st Brillouin zone appear to be inequivalent). However, by choosing $m, n = 0$ or by applying a unitary transformation to the basis functions, the phase factor can be always excluded. As a consequence, the Hamiltonian is rewritten as:

$$H_{graph}(\mathbf{q}) = v_F \begin{pmatrix} 0 & (q_x - iq_y) & 0 & 0 \\ (q_x + iq_y) & 0 & 0 & 0 \\ 0 & 0 & 0 & -(q_x - iq_y) \\ 0 & 0 & -(q_x + iq_y) & 0 \end{pmatrix}. \tag{25}$$

Moreover, the low energy Hamiltonian 25 can be written as a couple of Hamiltonian matrices $H_K(\mathbf{q})$, $H_{K'}(\mathbf{q})$, obtained by projecting it into the 2×2 spaces identified by (KA, KB) and $(K'A, K'B)$ respectively:

$$H_{K,K'}(\mathbf{q}) = v_F \begin{pmatrix} 0 & q_x \mp iq_y \\ q_x \pm iq_y & 0 \end{pmatrix}. \tag{26}$$

Equivalently, the matrix 25 can be written as a 2×2 block supermatrix:

$$H_{graph}(\mathbf{q}) = \begin{pmatrix} H_K(\mathbf{q}) & 0 \\ 0 & H_{K'}(\mathbf{q}) \end{pmatrix} \tag{27}$$

where $H_K, H_{K'}$ are 2×2 matrices defined in 26. By evaluating now the eigenvalues of the matrix 25 (or, equivalently, of the matrices 26), that corresponds to take the low energy expansion of expression 18 around the Dirac points K, K' (in other words it corresponds to expand 18 by choosing $\mathbf{k} = \mathbf{K} + \mathbf{q}$ or $\mathbf{k} = \mathbf{K}' + \mathbf{q}$, with $q \ll \|\mathbf{K}\|$ and $q \ll \|\mathbf{K}'\|$), we obtain the celebrated and famous linear (or, more precisely, conical since it lives in a 3D space and not only in a fixed ϕ plane, where ϕ is the azimuthal angle in spherical coordinates) dispersion relation describing charge carriers (electrons and holes), at low energy (i.e. around the Dirac points), in graphene:

$$\epsilon(q) = \pm q v_F. \tag{28}$$

Undoped graphene has a Fermi energy E_F coinciding exactly with the energy at the conical points (the Dirac points), corresponding to the choice $q = 0$: so, $E_F = \epsilon(0) = 0$. As a consequence, undoped graphene has a completely filled valence band and a completely empty conduction band, with no band gap in between: undoped graphene is therefore an example of a gapless semiconductor. This is a first peculiarity shown by this material, although not the most astonishing one. However, there are many ways to engineer a gap opening in graphene: from a theoretical point of view, spin-orbit coupling leads to the gap opening ([76]), while from an experimental point of view, the gap can be opened for example by shaping graphene sheets as nanoribbons ([128]).

It is worth noting that, if I take now into account also the next-to-nearest neighbour terms in the tight-binding Hamiltonian 15, described by an hopping parameter t', the electronic band structure, instead of being expressed by 18, is given by:

$$\epsilon(\mathbf{k}) = \pm |S(\mathbf{k})| + t' f(\mathbf{k}) = \pm t\sqrt{3 + f(\mathbf{k})} + t' f(\mathbf{k}) \tag{29}$$

where $f(\mathbf{k})$ is defined in 19. In particular, while the π, π^* bands describing the graphene electronic structure (defined by expression 18) are symmetric with respect to the plane $E = 0$ passing through the Dirac points in the 1st Brillouin zone of the reciprocal space (meaning that there is an electron-hole symmetry), the second term in 29 breaks this symmetry, shifting the conical Dirac point from $E_F = 0$ to $E_F = -3t'$, but it does not change the behaviour of the Hamiltonian near the Dirac points. Actually, this linear behaviour is symmetry- and topologically- protected by the time reversal and inversion symmetries invariance characterizing graphene because of the equivalence of the two A and B sublattices constituting the real space lattice and of the equivalence of the two valleys K and K' sublattices constituting the reciprocal space lattice. The graphene band structure, taking into account also the next-to-nearest neighbour hopping, is shown in Figure 17.

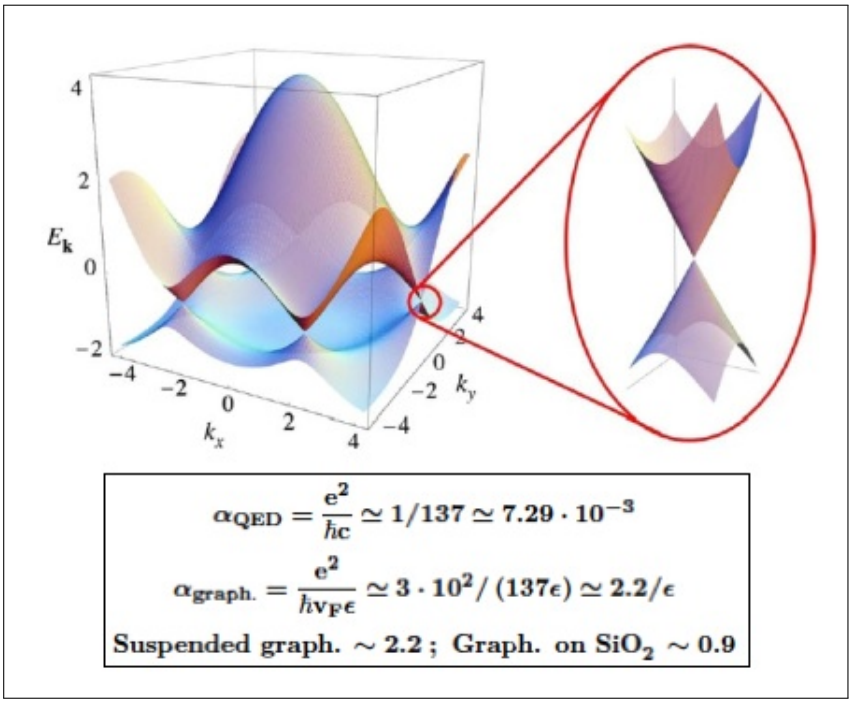

Figure 17: Graphene band structure including next-to-nearest neighbour hopping. Electronic dispersion relation for monolayer graphene, in units of t, assuming finite values of the parameters t and t' ($t = 2.7$ eV and $t' = -0.2t$). It is clear, with respect to the electronic band structure illustrated in Figure 15, that the inclusion of the next-to-nearest neighbour hopping t' in the tight-binding Hamiltonian describing graphene breaks the electron-hole symmetry (indeed π and π^* bands are not anymore symmetric with respect to the $E = 0$ plane). On the right, a zoomed view of the electronic bands around the Dirac points, highlighting their peculiar conical behaviour. As shown in the inset, this behaviour corresponds to consider electrons (and holes) in graphene as particles described in Quantum Electrodynamics (QED), by means of the relativistic Dirac equation, with the only difference that the fine structure constant in graphene is much higher than in QED. Adapted from [24].

1.2.3 Massless relativistic Dirac fermions and graphene

It is clear that the energy dispersion relation 28 resembles the one for ultra relativistic particles ($E = c\,\|p\| = c\,\|k\|$ assuming that $\hbar = 1$), described properly by the Dirac equation for massless particles: this is a first clear indication that charge carriers in graphene do not behave as in usual semiconductors.

A first consequence of this fact is that the cyclotron mass m^* of electrons and holes in graphene depends on electronic density as its square root:

$$m^* = \frac{1}{2\pi}\left[\frac{\partial A(E)}{\partial E}\right]\Bigg|_{E=E_F} = \frac{E_F}{v_F^2} = \frac{q_F}{v_F} = \frac{\sqrt{\pi}}{v_F}\sqrt{n} \tag{30}$$

where $A(E) = \pi q(E)^2 = \pi E^2/v_F^2$ is the area in reciprocal space enclosed by the orbit of the charge carriers, $E_F = q_F v_F$ is the Fermi energy and $n = q_F^2/\pi$ is the charge carriers density. As shown in Figure 18, the fit between the theoretically expected behaviour described by 30 and the experimental data is very accurate, providing a clear evidence for the existence of massless quasiparticles in graphene. Moreover, by fitting the experimental data with the calculated curve is possible to extrapolate an estimation for the value of the Fermi velocity v_F and therefore of the hopping parameter $|t| = 2v_F/3\delta$.

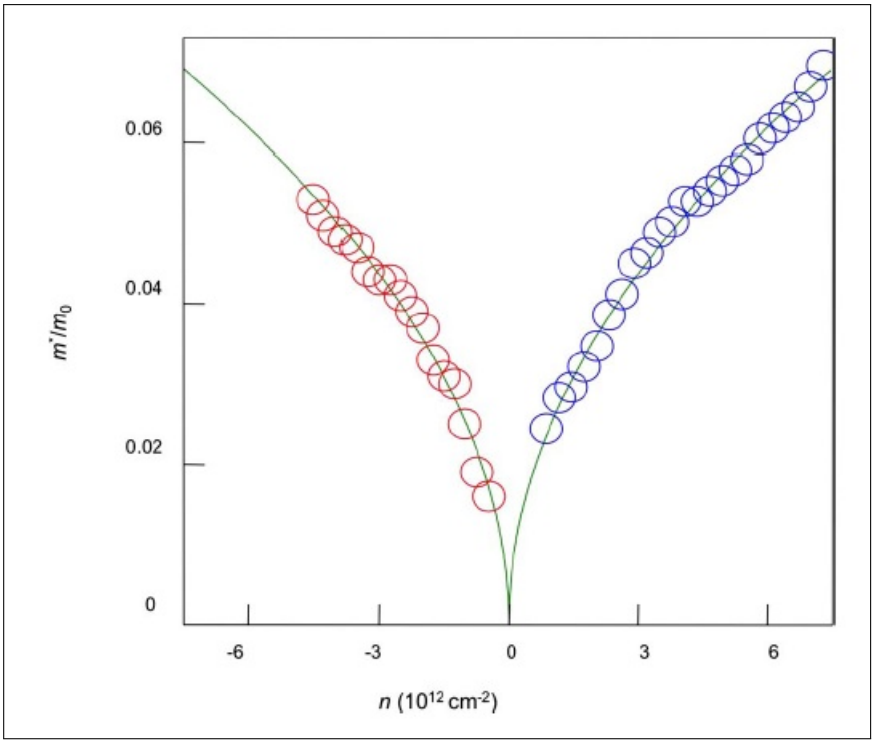

Figure 18: Cyclotron mass dependence on charge carriers density in graphene. Image showing the cyclotron mass dependence of charge carriers in graphene on their concentration n. Positive and negative values of n correspond to electrons and holes respectively. Solid lines are the best fit of 30, while circles are the experimental data: the latter reproduce the expected behaviour with an high level of accuracy. m_0 is the free electron mass. Adapted from [24].

Another consequence of the relativistic-like form of the graphene electronic band structure at low energy is the linear behaviour of the density of

states $\rho(E)$ per unit cell as a function of $|E|$ near the Dirac point (a behaviour proper of semimetallic materials). For $t' = 0$, the density of states close to the Dirac points takes the form (with a degeneracy of 4 included):

$$\rho(E) = \frac{2A_c}{\pi}\frac{|E|}{v_F^2} \tag{31}$$

where $A_c = 3\sqrt{3}\delta^2/2$ is the unit cell area. The full analytical for of $\rho(E)$ in graphene, for the case $t' = 0$, can be found in [24] and it is shown in Figure 19 for both $t' = 0$ and $t' \neq 0$.

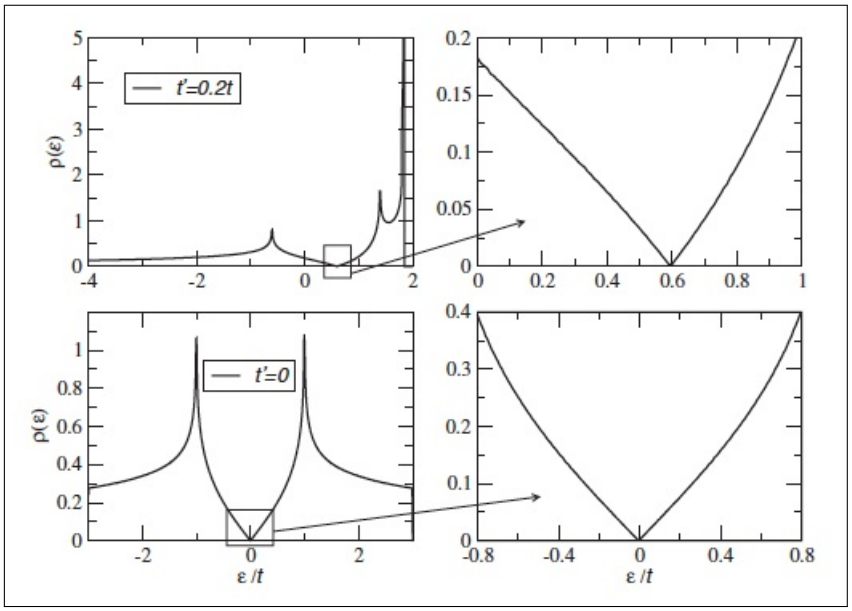

Figure 19: Density of states per unit cell in monolayer graphene. Dependence of the density of states per unit cell $\rho(\epsilon)$ on energy ϵ (in units of t) in monolayer graphene. Density of states has been evaluated from the energy dispersion 29, by choosing $t' = 0.2t$ (*top*) and $t' = 0$ (*bottom*). On the right is shown a magnified view of the density of state close to the Dirac neutrality point of one electron per site. For the case $t' = 0$ (nearest neighbour hopping), the electron-hole nature of the spectrum is evident and the density of states near the Dirac point can be approximated as $\rho(\epsilon) \propto |\epsilon|$. Adapted from [24].

We have seen that undoped graphene has the Fermi energy pinned at the Dirac points, exactly where the density of states of the material vanishes, according to 31. This fact could suggest that the conductivity of undoped monolayer graphene should also vanish at the Fermi energy: experimental results ([125, 134]) and theoretical predictions ([141]) show instead that this is not the case. Indeed, according to [141], because of the unavoidable presence of disorder and impurities, modeled from theoretical point of view by adding delta-like potentials in the Hamiltonian describing charge transport in graphene, this material, even undoped, has a minimum conductivity at the charge neutrality point given by:

$$\sigma(E_F) = \frac{4e^2}{\pi h} \tag{32}$$

independent on impurity concentrations. This is a quite unique feature of graphene and it has been experimentally observed by gating mechanically

exfoliated graphene shaped in Hall bar devices (as those shown in Figure 3) and by varying the gate voltage V_g applied to the material without applying an external magnetic field: the measured longitudinal resistivity ρ, as a function of V_g, presents a sharp peak exactly in correspondence of the charge neutrality point (the Dirac point at $V_g = 0$), as shown in Figure 20a. For $V_g \neq 0$ the resistivity decreases (equivalently, the conductivity $\sigma = 1/\rho$ increases), as expected, meaning that charge carriers have been injected into graphene and the Fermi level has been shifted. Indeed, values of $V_g > 0$ correspond to shift upward the Fermi level with respect to the Dirac point, thus doping graphene with electrons, while values of $V_g < 0$ correspond to shift downward the Fermi level with respect to the Dirac point, thus doping graphene with holes: the situation is chemically represented in Figure 20b. The peculiarity in the resistivity vs. gate voltage behaviour here described is often used to identify monolayer graphene among other carbon structures, being uniquely related to the former.

A more striking evidence of the massless nature of fermions in graphene is obtained by rewriting the tight-binding Hamiltonian 15 in second quantization formalism, by means of creation/annihilation operators:

$$H = -t \sum_{\langle i,j \rangle, \sigma} \left(a^\dagger_{i,\sigma} b_{j,\sigma} + b^\dagger_{j,\sigma} a_{i,\sigma} \right) \tag{33}$$

where $\sigma = \uparrow, \downarrow$ is the electron spin in a fixed arbitrary direction, $\langle i, j \rangle$ identifies nearest neighbour carbon atoms, $a_{i,\sigma}, a^\dagger_{i,\sigma}$ is a couple of annihilation and creation operators, respectively, of an electron of spin σ on site $\mathbf{R}^A_i$ of graphene sublattice A (where $i = (n, m) \in \mathbb{N}^2$ identifies a couple of integer indices specifying in an unique way the positions of A carbon atoms in the graphene structure with respect to the primitive vectors $\mathbf{a}_1, \mathbf{a}_2$ defined in 3) and $b_{j,\sigma}, b^\dagger_{j,\sigma}$ is a couple of annihilation and creation operators of an electron of spin σ on site $\mathbf{R}^B_j$ of graphene sublattice B (I remind that $\mathbf{R}^B_j = \mathbf{R}^A_j + \boldsymbol{\delta}_3$, where $\boldsymbol{\delta}_3$, defined in 4, is a vector connecting nearest neighbour carbon atoms) and t is the already defined hopping parameter. The creation/annihilation operators $a_{i,\sigma}, a^\dagger_{i,\sigma}$ and $b_{j,\sigma}, b^\dagger_{j,\sigma}$ satisfy the usual anti-commutation relations:

$$\left\{ a_{i,\sigma}, a^\dagger_{i',\sigma'} \right\}_+ = \delta_{i,i'} \delta_{\sigma,\sigma'} \mathbb{I}\,, \quad \left\{ b_{j,\sigma}, b^\dagger_{j',\sigma'} \right\}_+ = \delta_{j,j'} \delta_{\sigma,\sigma'} \mathbb{I};$$
$$\left\{ a_{i,\sigma}, a_{i',\sigma'} \right\}_+ = \left\{ b_{j,\sigma}, b_{j',\sigma'} \right\}_+ = \left\{ a_{i,\sigma}, b_{j',\sigma'} \right\}_+ = \left\{ a_{i,\sigma}, b^\dagger_{j',\sigma'} \right\}_+ = 0$$

where $\mathbb{I}$ is the identity operator.

Now, by considering the Fourier transform of the operators $a_{i,\sigma}, b_{j,\sigma}$ (and, similarly, of their hermitian conjugate)

$$a_n = \frac{1}{\sqrt{N}} \sum_{\mathbf{k}} e^{-i\mathbf{k}\cdot\mathbf{R}_n} a(\mathbf{k})$$
$$b_n = \frac{1}{\sqrt{N}} \sum_{\mathbf{k}} e^{-i\mathbf{k}\cdot\mathbf{R}_n} b(\mathbf{k}) \tag{34}$$

where N is the number of unit cells and $\mathbf{R}_n$ the vectors specifying the positions of carbon atoms in real space, and by expanding $a(\mathbf{k}), b(\mathbf{k})$ around the Dirac points $\mathbf{K}$ and $\mathbf{K}'$ (defined in 6), it is possible to show ([24] for more details), with some straightforward algebra, that the Hamiltonian 33 can be written as

$$H = -i v_F \int \mathrm{d}x\, \mathrm{d}y \left[\hat{\Psi}^\dagger_1(\mathbf{r}) \boldsymbol{\sigma} \cdot \boldsymbol{\nabla} \hat{\Psi}_1(\mathbf{r}) + \hat{\Psi}^\dagger_2(\mathbf{r}) \sigma^* \cdot \boldsymbol{\nabla} \hat{\Psi}_2(\mathbf{r}) \right]. \tag{35}$$

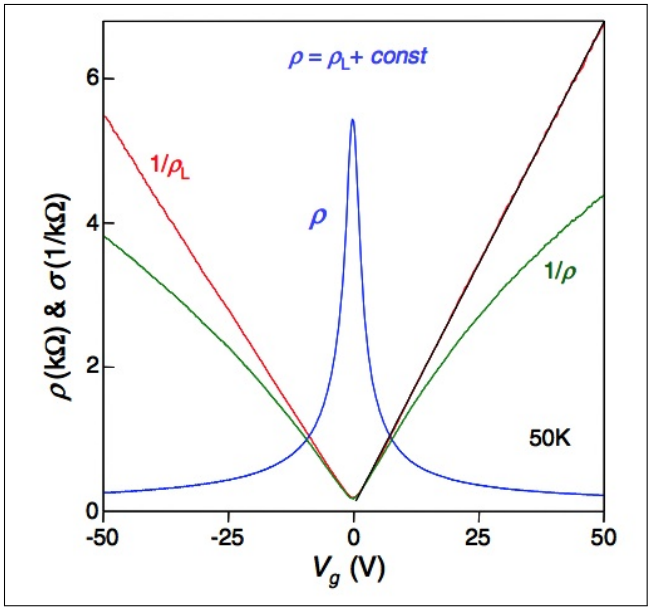

(a)

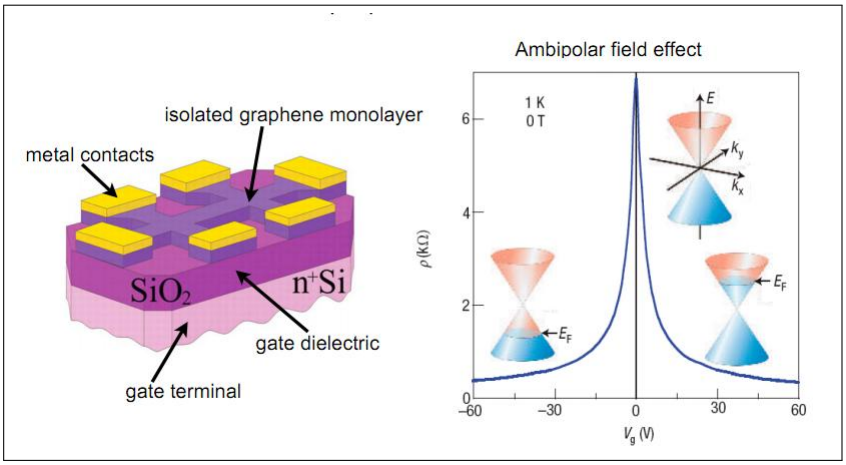

(b)

Figure 20: Minimal conductivity in graphene monolayer and graphene doping. (a) Resistivity ρ (blue curve) and conductivity $\sigma = 1/\rho$ (green curve) of mechanically exfoliated monolayer graphene as a function of the gate voltage V_g. ρ_L (obtained by ρ simply subtracting a constant of $\approx 100\,\Omega$) is inversely proportional to V_g (red curve), thus showing a characteristic peak at $V_g = 0$ (equivalently, a finite minimum conductivity also at vanishing density of states). The thin black line on top of the red curve for $V_g > 0$ is to emphasize the linearity. Measurements have been performed at temperature $T = 50\,K$ to suppress universal conductance fluctuations and magnetic field $B = 0$. Adapted from [125]. (b) Schematic representation of the Ambipolar Field Effect and of the doping mechanism in monolayer graphene. By properly gating graphene deposited onto a SiO_2/Si substrate (left part of the image, adapted from Figure 3a), it is possible to inject charge carriers (electrons or holes), thus changing the intrinsic carriers density, into graphene: in particular, as shown on the right of the image, for $V_g > 0$ electrons are injected into the material and the Fermi level is shifted upward with respect to the Dirac point (at which crossing of the linear bands occurs), while for $V_g < 0$ holes are injected into the material and the Fermi level is shifted downward with respect to the Dirac point. So, doping of graphene is obtained simply by gating the material and external chemical species are not needed, as in usual semiconductors. Adapted from [52].

In 35 $\mathbf{r} = (x, y)$, $\Psi_i^\dagger = \left(a_i^\dagger, b_i^\dagger\right)$ (with the indices $i = 1, 2$ referring to the K and K' Dirac points respectively), $\boldsymbol{\sigma} = (\sigma_x, \sigma_y)$, $\boldsymbol{\sigma}^* = (\sigma_x, -\sigma_y)$ and σ_x, σ_y are the x and y components of the Pauli matrices

$$\sigma_0 = \mathbb{I} = \begin{pmatrix} 1 & 0 \\ 0 & 1 \end{pmatrix}, \ \sigma_x = \begin{pmatrix} 0 & 1 \\ 1 & 0 \end{pmatrix}, \ \sigma_y = \begin{pmatrix} 0 & -i \\ i & 0 \end{pmatrix}, \ \sigma_z = \begin{pmatrix} 1 & 0 \\ 0 & -1 \end{pmatrix}.$$

It is clear that the Hamiltonian 35 is the sum of two copies of the massless Dirac-like Hamiltonian in 2D, $H_{\text{Dirac}} = v_{\text{F}} \boldsymbol{\sigma} \cdot \hat{\mathbf{p}}$ ($\hat{\mathbf{p}} = (-i\partial/\partial x, -i\partial/\partial y)$, $\hbar = 1$ and the parameter v_{F} instead of the speed of light c)[2], one holding for $\mathbf{k}$ around $\mathbf{K}$ and the other one for $\mathbf{k}$ around $\mathbf{K}'$.

This result could be obtained also in first quantization formalism, simply substituting in the matrices 26 the real variables (q_x, q_y) with the corresponding operators $(-i\partial/\partial x, -i\partial/\partial y)$, this way obtaining the couple of Hamiltonians:

$$\begin{aligned} H_K &= -i v_{\text{F}} \boldsymbol{\sigma} \cdot \boldsymbol{\nabla} \\ H_{K'} &= H_K^{\text{T}} \end{aligned} \tag{36}$$

where again $\boldsymbol{\sigma} = (\sigma_x, \sigma_y)$ and "T" denotes the transpose.

It is very important to point out that, in relations 35 and 36, the Pauli matrices do not identify (electron) *spin* degrees of freedom, as for usual Dirac fermions, but rather a new degree of freedom called *pseudo-spin*: pseudo-spin distinguishes between components of the wavefunction ψ describing electrons in graphene corresponding to sublattice A or B in real space. So, pseudo-spin "up" means sublattice A and pseudo-spin "down" means sublattice B. In other words, pseudo-spin provides the description of the distribution of electrons in sublattices A and B.

If working in a four dimensional space with basis $(KA, KB, K'A, K'B)$, instead of employing two copies of two dimensional spaces with bases (KA, KB) and $(K'A, K'B)$ respectively (with the bases taking into account the distinction of the electrons according to the valley -K or K'- they belong to), it is possible to write the Hamiltonian 36 as a 4×4 matrix in compact form, simply by introducing another couple $\boldsymbol{\tau_0} = \left(\tau_{0,x}, \tau_{0,y}\right)$ of Pauli matrices:

$$H = -i v_{\text{F}} \boldsymbol{\tau_0} \otimes (\boldsymbol{\sigma} \cdot \boldsymbol{\nabla}). \tag{37}$$

2 For a relativistic ($E = \sqrt{\|\mathbf{p}\|^2 + m^2}$) spin 1/2 particle of mass m and momentum $\mathbf{p}$ in $(3+1)$D Minkowski (i.e. flat) space-time the Dirac Hamiltonian reads ([22])

$$H_{\text{Dirac}} = \boldsymbol{\alpha} \cdot \mathbf{p} + \beta m = -i \sum_{i=1}^{3} \alpha_i \partial/\partial x_i + \beta m,$$

where $(\boldsymbol{\alpha}, \beta)$ is a set of 4 matrices (they cannot be numbers) such that:

$$\begin{gathered} \alpha_i^\dagger = \alpha_i, \ \beta^\dagger = \beta \ (\forall i = 1, \cdots, 3) \\ \alpha_i^\dagger \alpha_i = \alpha_i \alpha_i^\dagger = \mathbb{I}, \ \beta\beta^\dagger = \beta^\dagger \beta = \mathbb{I} \ (\forall i = 1, \cdots, 3) \\ \{\alpha_i, \beta\}_+ = 0, \beta^2 = \mathbb{I}, \{\alpha_i, \alpha_j\}_+ = 2\delta_{ij} \ (\forall i, j = 1, \cdots, 3). \end{gathered}$$

It follows from the above conditions that the α_i, β matrices must be traceless and with eigenvalues $\pm 1 \Rightarrow \alpha_i, \beta \in M_n(\mathbb{C})$ with $n \in \mathbb{N}$ and n *even*. In $(3+1)$D space-time n must be at least 4 and a possible representation of such matrices is given by the Dirac matrices γ^μ. Nonetheless, for massless particles ($m = 0$) only 3 matrices are needed and so the algebra can be realized by using $n = 2$, hence by choosing $\alpha_i = \sigma_i$, $i = 1, \cdots, 3$ (σ_i are the Pauli matrices). Finally, if the space-time dimension is D$= (2+1)$ (as for graphene) and $m = 0$, we need only 2 matrices that we can choose out of the 3 Pauli matrices σ_i. The Hamiltonian reads therefore as $H_{\text{Dirac}} = \boldsymbol{\sigma} \cdot \mathbf{p}$. In graphene, the only difference with respect to usual massless Dirac fermions is that the speed of light c (set to 1 here) is substituted by the parameter v_{F}. More details about the Dirac equation in $(2+1)$ space-time dimensions can be found in [87].

Therefore, an electron (hole) in graphene is fully described by an 8-components spinor, having 8 degrees of freedom: 2 for the pseudo-spin indices distinguishing between sublattices A and B in real space, 2 for the indices distinguishing between K and K' valleys in reciprocal space and, finally, 2 for the spin ($\uparrow$ or $\downarrow$) of the particle along a certain fixed direction.

For what concerns the eigenfunctions of 36, they are written in momentum space as:

$$\psi_{\pm}^{(K)}(\mathbf{k}) = \frac{1}{\sqrt{2}} \begin{pmatrix} e^{-i\theta_{\mathbf{k}}/2} \\ \pm e^{i\theta_{\mathbf{k}}/2} \end{pmatrix} \tag{38}$$

$$\psi_{\pm}^{(K')}(\mathbf{k}) = \frac{1}{\sqrt{2}} \begin{pmatrix} e^{i\theta_{\mathbf{k}}/2} \\ \pm e^{-i\theta_{\mathbf{k}}/2} \end{pmatrix}. \tag{39}$$

where $\theta_{\mathbf{k}} = \arctan\left(k_x/k_y\right)$.
Spinors 38 represent the eigenfunctions of the Hamiltonian $H_K = v_{\mathrm{F}}\boldsymbol{\sigma}\cdot\hat{\mathbf{k}}$, for momentum $\mathbf{k}$ around the Dirac point K, corresponding to the eigenvalues $E = \pm v_{\mathrm{F}}\|\mathbf{k}\|$ (the "+" sign identifies an electron state, while the "-" sign an hole state), that is, corresponding to the π^* and π bands respectively. Spinors 39 represent instead the eigenfunctions of the Hamiltonian $H_{K'} = v_{\mathrm{F}}\boldsymbol{\sigma}^*\cdot\hat{\mathbf{k}}$, for momentum $\mathbf{k}$ around the Dirac point K', corresponding to the eigenvalues $E = \pm v_{\mathrm{F}}\|\mathbf{k}\|$ (the "+" sign identifies also in this case an electron state, while the "-" sign an hole state), that is, corresponding to the π^* and π bands respectively. It is worth noting that $\psi_{\pm}^{(K)}(\mathbf{k})$ and $\psi_{\pm}^{(K')}(\mathbf{k})$ are related by time-reversal symmetry.

An important feature related to the eigenfunctions 38, 39 is that, by definition,

$$\frac{\boldsymbol{\sigma}\cdot\hat{\mathbf{k}}}{\|\mathbf{k}\|}\psi_{\pm}^{(K)} = \pm\psi_{\pm}^{(K)}, \quad \frac{\boldsymbol{\sigma}\cdot\hat{\mathbf{k}}}{\|\mathbf{k}\|}\psi_{\pm}^{(K')} = \mp\psi_{\pm}^{(K')} \tag{40}$$

Since $\frac{\boldsymbol{\sigma}\cdot\hat{\mathbf{k}}}{\|\mathbf{k}\|}$ is the helicity operator (defined as the projection of momentum operator along the (pseudo)-spin directions), 40 means that electrons and holes in graphene have defined helicity (or, equivalently, chirality), always positive for electrons and always negative for holes. Indeed, equation 40 implies that the pseudo-spin $\boldsymbol{\sigma}$ has its two eigenvalues either in the direction ($\uparrow$) or against ($\downarrow$) the momentum $\mathbf{p}$. Since electrons and holes have a definite pseudo-spin direction (as it should be the case for massless Dirac fermions, [13]), they are said to be *chiral*. Let's note that the chirality of real spin Dirac electrons and holes is not in general definite: indeed, usual Dirac fermions in $(3+1)$D are described by 4 components spinors, due to two projections of spins and two values of electric charge degree of freedom (corresponding to particle-antiparticle or, equivalently, electron-hole states). For fermions in graphene, the latter degree of freedom is not independent of the former, otherwise 16-components instead of 8-components spinors would have been necessary to fully describe them. Chirality is a crucial property of fermions in graphene, explaining many relativistic effects detected in this material, as for example the Klein paradox.

To conclude this brief overview about the most peculiar features concerning electronic transport in monolayer graphene, I want to explicitly summarize the qualitative differences between 2D graphene and 2D usual semiconductor systems ([30]):

1. usual 2D semiconductors typically have very large band gaps (> 1 eV), so that electrons and holes must be studied using completely different

electron-doped and hole-doped structures. On the contrary, graphene is a gapless semiconductor, as we have seen, with the nature of the charge carriers changing at the Dirac point from electrons to holes (or vice versa) in a single structure. As a direct consequence, while graphene has always a semimetallic nature with the Fermi level (i.e. the chemical potential) in the conduction or the valence band, in 2D semiconductors the Fermi level enters the band gap;

2. electrons and holes in graphene are chiral, whereas this is not the case in usual 2D semiconductors;

3. monolayer graphene energy dispersion relation is linear (at low energy) close to the Dirac points, whereas in 2D semiconductors the dispersion is quadratic. This leads to substantial quantitative differences in the transport properties of the two systems;

4. finally, carrier confinement in monolayer graphene is ideally two dimensional, since graphene layer has exactly one atom thickness. 2D semiconductor systems are instead only quasi-2D structures (with an average thickness, in the third dimension, $z \approx 5\,\text{nm}$ to $50\,\text{nm}$, fulfilling the condition $z < \lambda_F$ defining a 2D electron system -λ_F here is the 2D Fermi wavelength), since quantum dynamics of electrons and holes is two dimensional by virtue of confinement effects induced by an external electric field

1.2.4 Quantum Hall Effect in graphene

The physics of Quantum Hall Effect (QHE) concerns the study of two-dimensional gas of electrons subjected to strong perpendicular magnetic fields (usually at low temperatures) and it is the quantum counterpart of the *classical* Hall effect, known already in 1879. QHE (or, more precisely, the Integer QHE) has been discovered in 1980 by K. von Klitzing, who was working on samples prepared by M. Pepper and G. Dorda ([191]): K. von Klitzing has been later awarded (in 1985) with the Nobel Prize in Physics for his important discovery.

The QHE, in summary, states that a 2D electron gas in a strong perpendicular magnetic field has a quantized Hall conductivity G_H (or, equivalently, a quantized Hall resistance $R_H = G^{-1}$):

$$G_H = n\frac{e^2}{h}$$

where e is the elementary charge of the electron, h is the Planck constant and n is either an integer ($n = 1, 2, \ldots$, in which case the effect is known as Integer QHE) or a fractional ($n = 1/3, 2/5, 3/7, \ldots$, in which case the effect is known as Fractional QHE) number. The quantization, as I will now explain, deeply relies on the quantization of the energy levels available for a free electron in a magnetic field $\mathbf{B}$.

The interest for QHE stems from its position at the borderline between low-dimensional quantum systems and systems with strong electronic correlations. In particular, QHE in graphene is of great interest because of the exactly 2D nature of electrons and holes in this system (as I have underlined at the end of Sec. 1.2.1): indeed, QHE in graphene is regarded as one of the most promising physical effects for a new and more robust definition of the quantum resistance standard in Metrology (I have discussed this topic in the Introduction).

For what concerns QHE measurements, the effect is usually detected in devices such as the one depicted in Figure 21, in which a current I is driven in a quasi-2D sample (in practice, a very thin sample in which one dimension is negligible with respect to the other two), perpendicularly to an applied magnetic field $\mathbf{B}$: the quantity measured are the *longitudinal* (parallel to the direction in which I flows through the system, from A to B points) and the *transverse Hall* (perpendicular and in the same plane in which I flows through the system, from P to Q points) resistances.

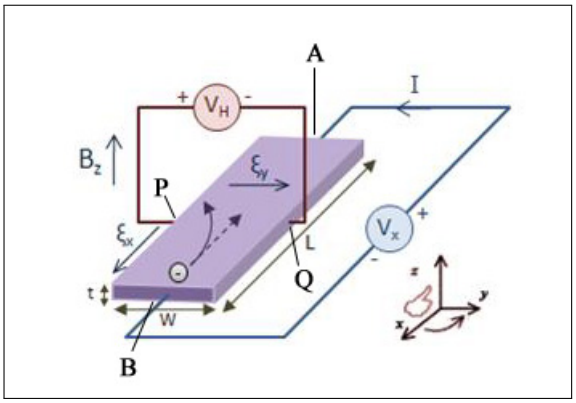

Figure 21: 2D device geometry for Quantum Hall measurements. Image showing the typical sample geometry employed to perform Quantum Hall measurements. The system, lying in the xy-plane, is subjected to a strong perpendicular magnetic field $\mathbf{B} = (0, 0, \|\mathbf{B}\|)$ directed along the z direction: moreover, a current I flows through the sample from A to B. The energy levels allowed to electrons get quantized and a potential drop arises both along the longitudinal (from A to B) and the transverse (from P to Q) directions: the resistances associated to the potential drops are the longitudinal and the Hall resistances, respectively. Because of the quantization of the energy levels, also the Hall resistance R_H is quantized in units of the von Klitzing constant $R_K = h/e^2$. By varying the magnetic field strength $B = \|\mathbf{B}\|$ will show characteristic plateaus. The sample is assumed to be as much as possible two-dimensional, $t \ll w$ and $t \ll L$.

From a classical point of view, the study of the dynamics of charge carriers in a geometry as in Figure 21 dates back to 1879, when Hall showed that the transverse resistance R_H of a thin metallic (conducting) plate varies linearly with the strength $B = \|\mathbf{B}\|$ of the perpendicular magnetic field:

$$R_H = \frac{B}{qn} \tag{41}$$

where q is the carrier charge and n the 2D charge density. The result is obtained by starting from the Drude model describing diffusive transport in a metal. According to this model, the equation of motion describing independent charge carriers (with charge q) of momentum $\mathbf{p}$ in presence of both an electric field $\mathbf{E}$ and a magnetic field $\mathbf{B}$ is given by:

$$\frac{d\mathbf{p}}{dt} = q\left(E + \frac{\mathbf{p}}{m} \times \mathbf{B}\right) - \frac{\mathbf{p}}{\tau} \tag{42}$$

where m is the mass of the charge carriers and τ is a characteristic relaxation time taking into account relaxation processes due to diffusion of carriers by generic impurities. The first term in 42 is nothing but the usual Lorentz force.

The resistivity of the system is obtained by searching for the static solutions (i.e. $\mathrm{d}\mathbf{p}/\,\mathrm{d}t = 0$) of the equation of motion 42. For 2D electrons with $\mathbf{p} = (p_x, p_y)$ (meaning that the z direction is chosen parallel to the magnetic field $\mathbf{B}$) and charge $q = -e$, the static solutions may be written in a very compact form as

$$\mathbf{E} = \rho\mathbf{j} \tag{43}$$

where $\mathbf{j} = -en_e\frac{\mathbf{p}}{m_e}$ is the current density and

$$\rho = \sigma^{-1} = \frac{1}{\sigma_0}\begin{pmatrix} 1 & \omega_c\tau \\ -\omega_c\tau & 1 \end{pmatrix} \tag{44}$$

is the resistivity tensor (while σ is obviously the conductivity tensor). In 44 I have defined the Drude conductivity $\sigma_0 = \frac{n_e e^2\tau}{m_e}$ and the cyclotron characteristic frequency (characterizing the motion of a charge particle in a magnetic field) $\omega_c = \frac{eB}{m_e}$. The off-diagonal elements of the tensor 44 represent exactly the transverse Hall resistivity:

$$\rho_H = \frac{\omega_c\tau}{\sigma_0} = \frac{B}{en_e}. \tag{45}$$

It is worth nothing that, in the case of vanishing impurities (i.e $\omega_c\tau \to \infty$, meaning that we are dealing with a clean sample characterized by very long scattering times), 44 reduces to

$$\rho = \begin{pmatrix} 0 & \frac{B}{en_e} \\ -\frac{B}{en_e} & 0 \end{pmatrix} \tag{46}$$

so that the transport properties of charge carriers under a magnetic field are entirely governed by the transverse Hall components of the resistivity tensor: we are therefore in a full Hall regime.

From a quantum mechanical point of view, the problem of a 2D (*non-relativistic*) electron gas (in which I neglect the interaction among electrons) in a perpendicular magnetic field $\mathbf{B} = \boldsymbol{\nabla} \times \mathbf{A}$ (where $\mathbf{A} = \mathbf{A}(\mathbf{x})$ -with $\mathbf{x} = (x, y, z)$- it the vector potential giving rise to the magnetic field) is instead solved starting from the Hamiltonian describing a free electron ($H = \hat{\mathbf{p}}^2/2m_e$, where $\hat{\mathbf{p}} = (\hat{p}_x, \hat{p}_y) = -i(\partial/\partial x, \partial/\partial y)$ is the momentum operator in two dimensions) with the substitution $\hat{\mathbf{p}} \to \hat{\mathbf{\Pi}} = \hat{\mathbf{p}} + \frac{e}{\hat{\mathbf{A}}}$. This substitution is correct to describe electrons dynamics in a lattice under a magnetic field as long as the lattice spacing a is much smaller than the *magnetic length* $l_B = \sqrt{\frac{\hbar}{eB}}$. Thanks to this substitution, with some quite simple and standard operator algebra and by fixing a proper gauge, it is possible to show that the Hamiltonian describing the electron takes the form of an harmonic oscillator Hamiltonian, i.e.

$$H = \hbar\omega_c\left(\hat{n} + \frac{1}{2}\right) = \hbar\omega_c\left(a^\dagger a + \frac{1}{2}\right) \tag{47}$$

where $\hat{n} = a^d aga$ is the number operator (having integer eigenvalues $n = 0, 1, 2, \ldots$), $\omega_c = \frac{eB}{m_e} = \frac{\hbar}{ml_B^2}$ is the cyclotron frequency and $a, a^\dagger$ are a pair of creation/annihilation operator satisfying the commutation relation $\left[a, a^\dagger\right] = \mathbb{I}$ and defined in terms of $\hat{\Pi}_x, \hat{\Pi}_y$ operators as

$$\begin{aligned} a &= \frac{l_B}{\sqrt{2}\hbar}\left(\hat{\Pi}_x - i\hat{\Pi}_y\right) \\ a^\dagger &= \frac{l_B}{\sqrt{2}\hbar}\left(\hat{\Pi}_x + i\hat{\Pi}_y\right). \end{aligned} \tag{48}$$

The eigenvalues of 47 are simply given by

$$\epsilon_n = \hbar\omega_c \left(n + \frac{1}{2}\right) = \hbar \frac{eB}{m_e} \left(n + \frac{1}{2}\right) \tag{49}$$

with $n \geq 0$ integer. It is therefore clear that the energies characterizing a 2D electron in a perpendicular magnetic field get quantized: this is the most important property in order to explain the QHE, i.e. the quantization of Hall resistance. The quantized energy levels are labeled by the integer n and are called *Landau levels*. In particular, in the non-relativistic case, it is clear from 49 that Landau levels have a linear dependence, for each fixed n, on the magnetic field strength B (Figure 22a).

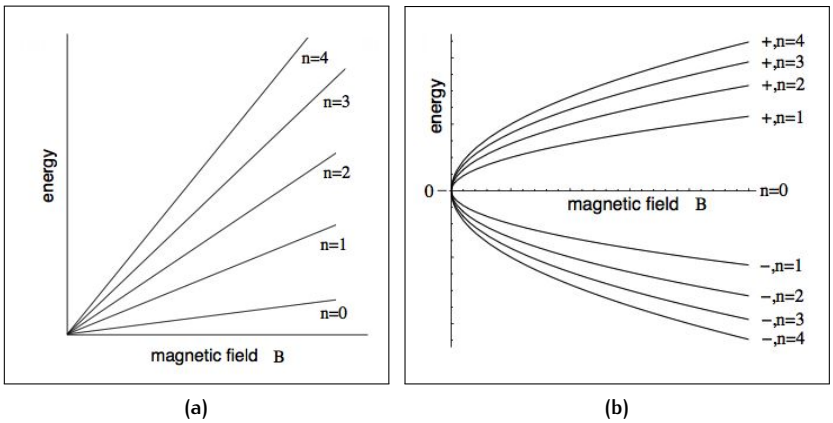

Figure 22: **Dependence of Landau levels energy on magnetic field strenght B.** Plot of Landau levels energy of a 2D electron gas as a function of the magnetic field strength: (a) for the non-relativistic case, in which the energy ϵ_n has a linear dependence on B for every fixed integer n, as inferred from 49. In particular, for each fixed value B, the Landau levels are equally spaced ($\epsilon_{n+1} - \epsilon_n = \hbar\omega_t extupc$) independently of the quantum number n; (b) for the relativistic case, in which the energy $\epsilon_{n,\lambda}$ depends on $\sqrt{Bn}$ for every fixed n, as inferred from 57. In this case the energy levels, for fixed B, are not anymore equally spaced ($\epsilon_{n+1} - \epsilon_n \propto \sqrt{n+1} - \sqrt{n}$). Adapted from [58].

An important feature of Landau levels is their degeneracy. Indeed, in order to find the eigenstates of 47 it is necessary to introduce a new pair of pseudo-momentum operators (not representing really a physical quantity, since they are gauge dependent) $\hat{\boldsymbol{\Pi}} = \left(\hat{\Pi}_x, \hat{\Pi}_y\right) = \hat{\mathbf{p}} - e\hat{\mathbf{A}}$ and an associated new pair of creation/annihilation operators $b, b^\dagger$ defined as

$$\begin{aligned} b &= \frac{l_B}{\sqrt{2}\hbar} \left(\hat{\Pi}_x + i\hat{\Pi}_y\right) \\ b^\dagger &= \frac{l_B}{\sqrt{2}\hbar} \left(\hat{\Pi}_x - i\hat{\Pi}_y\right). \end{aligned} \tag{50}$$

The operators b and $b^\dagger$ satisfy the common commutation relation $\left[b, b^\dagger\right] = \mathbb{I}$ and commute with $a, a^\dagger$ (meaning that $[a, b] = \left[a, b^\dagger\right] = 0$); moreover, it is possible to associate a number operator $\hat{m} = b^\dagger b$ to them. In this way we have obtained a second quantum integer number $m \geq 0$, which is necessary to fully describe, together with the Landau levels integer quantum number $n \geq 0$, the eigenstates of 47. In abstract way, the eigenstates of 47 in the

non-relativistic case are written as $|n,m\rangle = |n\rangle \otimes |m\rangle$; however, the explicit form of the wavefunctions $\phi_{n,m}(x,y) = \langle x,y\ |n,m\rangle$ depends upon the choice of the gauge in which one decides to work.
From a semi-classical point of view, it is possible to relate the pseudo-momentum operators $\hat{\tilde{\mathbf{\Pi}}} = \left(\hat{\tilde{\Pi}}_x, \hat{\tilde{\Pi}}_y\right)$ introduced in order to write the eigenstates of 47 to the classical constant of motion $\mathbf{R} = (X,Y)$, describing the position of the centre of the electronic cyclotron motion in a magnetic field. More precisely, we have

$$X = -\frac{\tilde{\Pi}_y}{eB} \quad Y = \frac{\tilde{\Pi}_x}{eB}. \tag{51}$$

The quantum mechanical treatment discussed up to now concerns only one electron in a magnetic field: however, the generalization to N *independent* electrons is straightforward and similar to what happens when dealing with electrons in a metal, at zero temperature, in absence of a magnetic field. As in in the case of a metal without external magnetic field the electrons fill in all the energy levels starting from the lowest one up to the Fermi level obeying the Pauli Exclusion Principle (forbidding a doubly occupancy of the same quantum state), in the case of a non-relativistic 2D electron gas in presence of a perpendicular magnetic field the electrons fill in all the lowest energy Landau levels. Once one Landau level is filled, the remaining electrons are forced to populate higher Landau levels. In order to describe the Landau levels filling, an important parameter, called *filling factor* is introduced: it is defined as

$$\nu = \frac{hn_e}{eB}. \tag{52}$$

The integer part $[\nu]$ of the filling factor describes exactly the number of completely filled Landau levels; it is interesting to point out that ν can be varied either by changing the electron density n_e (i.e. by changing the charge carriers number) or by changing the magnetic field B.

The quantization of the conductance G of a 2D device, with the geometry shown in Figure 21, follows now simply by evaluating the conductance of a completely filled Landau level. By calculating first of all the quantum mechanical expression for the current I_n^x flowing in the x direction (from A -the left- to B -the right- contact, referring to Figure 21) in the n-th Landau level and by assuming that $\nu = n$, i.e. assuming that all the first n Landau levels (characterized by energy level quantum numbers $0, 1, \ldots, n-1$) are completely filled, it is possible to show ([58]) that the conductance through the device, contributing to the electronic transport, is

$$G = n\frac{e^2}{h} \tag{53}$$

or, equivalently, the Hall resistance (between the upper and the lower edges, referring to the geometry in Figure 21) is quantized as

$$R_H = G^{-1} = \frac{h}{e^2}\frac{1}{n} = \frac{h}{e^2}\frac{1}{\nu}. \tag{54}$$

Relation 54 summarizes the (Integer) QHE and it is the relation I have shown at the beginning of this section: it expresses the fact that the Hall resistance is quantized in units of the von Klitzing constant $R_K = h/e^2 = 25\,812.81\,\Omega$. Moreover, 54 refers to the Integer QHE (IQHE) since the parameter n appearing in the formula is an integer. If Landau levels are assumed to be

spin-degenerate, the filling factor ν corresponding to n landau levels completely filled changes from n to $2n$ and therefore a factor 2 appears in 53 and (at the denominator) in 54.

Before generalizing 54 to the case of Fractional QHE (FQHE) I briefly discuss what happens to the Hall resistance R_H when the filling factor is varied around $\nu = n$ (meaning that we start with n completely filled Landau levels and we increase the levels occupancy). The variation of ν can be achieved, as already pointed out, by varying the magnetic field B: in particular, by decreasing B the filling factor ν is increased. So, let's suppose that at the beginning n Landau levels (from energy quantum number 0 up to energy quantum number $n-1$) are completely filled: the Hall resistance is in this case exactly given by 54. By decreasing B, the $n+1$-th Landau level characterized by energy quantum number n will start to be moderately filled by electrons. However, these electrons will result to be strongly confined, and therefore (classically) localized somewhere in the bulk of the sample, because of confinement potential arising in the system: as a consequence, they will not affect the global electronic transport characteristics, measured by the Hall resistance 54 (measured between the P -upper- and Q -lower- edges, referring to Figure 21) and by the longitudinal resistance (measured between the A and B contacts again referring to the geometry shown in Figure 21), because they will not be probed by the QHE device contacts. The Hall resistance remains unaltered and the longitudinal resistance remains zero, despite the change in Landau levels occupancy. This situation is kept until the magnetic field is decreased enough to allow the (many) electrons injected from the left contact of the device (filling the $n+1$-th Landau level) to be not anymore localized in the bulk of the sample, but to jump from the upper to the lower edge of the device and then to be backscattered to the left contact of the device itself. When this fact happens, a non-zero longitudinal resistance is measured in the device because of the potential drop caused by the electron jumping from the upper to the lower edge of the system. In the meanwhile, the Hall resistance is no longer quantized and it jumps to the value $R_H = \frac{h}{e^2}\frac{1}{n+1}$ associated to the filling factor $\nu = n+1$. This situation explains why the Hall resistance is constant over a rather large interval of magnetic field values B around $\nu = n$ (or, equivalently, for B fixed, it is constant over a large interval of charge carriers densities n_e changing around $\nu = n$) and why the Hall resistance R_H as a function of n_e (or as a function of B) shows characteristic *plateaus* (moreover, in correspondence of each R_H-plateau the longitudinal resistance is zero and only in correspondence of a plateau transition the latter is not anymore zero).

For what concerns the FQHE, the explanation is much more complex and I will not enter into details. The explanation of FQHE deeply relies on the Coulomb interaction between electrons, so on strong correlation effects, up to now neglected: a full description of the new physics underlying the collective behaviour of all the electrons and an exhaustive explanation of the FQHE have been provided by R. B. Laughlin ([92]), who worked on the results previously discovered by D. C. Tsui, H. L. Stormer and A. C. Gossard ([182]). For their fundamental discoveries R C. Laughlin, H. L. Stormer and D. C. Tsui have been awarded in 1998 with the Nobel Prize in Physics. As a consequence of these strong correlation, new plateaus appear in the Hall resistance, corresponding to fractional value of the filling factor ν. Relation 54 is therefore generalized to:

$$R_H = \frac{2ps+1}{p}\frac{h}{e^2} \tag{55}$$

where now the filling factor is given by $\nu = \frac{2ps+1}{p}$, with $p > 0$ integer and $s \geq 0$ integer. It is clear that ν can acquire both integer and fractional values depending on the choice of p and s: moreover, for $p = 1$, the filling factor is again integer and 55 describes the IQHE (the factor 2 accounting for spin degeneracy of Landau levels has been already taken into account in the relation).

I remind the interested reader to some great reviews ([56, 58, 108, 126]), giving comprehensive treatments of the physics of the IQHE and FQHE, far beyond the scopes of this thesis.

For what concerns QHE in graphene, the quantum mechanical treatment of the physics underlying the effect is somewhat similar to the one described above in the case of a non-relativistic 2D electron gas, with the only (important) difference that we have now to deal with *relativistic massless electrons*. The starting point in this case is the Hamiltonian describing electron in graphene near a Dirac point (let's suppose the K Dirac point, but the treatment is identical by considering the K' point), given by 36 ($H_{\text{graph}} = v_{\text{F}}\boldsymbol{\sigma} \cdot \hat{\mathbf{p}}$), or equivalently, in matrix form, by 26. Again, to describe graphene electrons in a strong magnetic field it is necessary to perform the substitution $\hat{\mathbf{p}} \rightarrow \hat{\mathbf{\Pi}} = \hat{\mathbf{p}} + \frac{e}{\hat{\mathbf{A}}}$, obtaining the Hamiltonian

$$H^{B}_{\text{graph}} = v_{\text{F}} \begin{pmatrix} 0 & \hat{\Pi}_x - i\hat{\Pi}_y \\ \hat{\Pi}_x + i\hat{\Pi}_y & 0 \end{pmatrix} = \sqrt{2}\frac{\hbar v_{\text{F}}}{l_B} \begin{pmatrix} 0 & a \\ a^{\dagger} & 0 \end{pmatrix} \tag{56}$$

where the pair of creation/annihilation operators $a, a^{\dagger}$ has been defined in 48. By performing the diagonalization of 56 ([58]), it is possible to find that for the relativistic case the energy of the Landau levels is not anymore given by 49, but by the relation

$$\epsilon_{n,\lambda} = \lambda \frac{\hbar v_{\text{F}}}{l_B}\sqrt{2n} \tag{57}$$

where $\lambda = \pm$ is an extra-index for labeling the Landau levels, characteristic of the relativistic nature of the problem, playing the same rôle that the $\pm$ sign was playing in 28 (so, "+" sign refers to the conduction band, while "-" sign to the valence band). it is worth nothing that, unlike the non-relativistic case, the Landau levels energies have not anymore a linear dependence, for each fixed n and λ, on the magnetic field strength B, but rather a $\sqrt{B}$ dependence, expressed through the $1/l_B$ factor present in 57 (in Figure 22b the dependence of the Landau levels energies on B is illustrated for each n and λ). The corresponding eigenstates of 56 are in this case given by the spinors:

$$\psi_{n=0,m} = \begin{pmatrix} 0 \\ |n=0,m\rangle \end{pmatrix}; \quad \psi_{n\neq 0,\lambda,m} = \frac{1}{\sqrt{2}} \begin{pmatrix} |n-1,m\rangle \\ \lambda\,|n,m\rangle \end{pmatrix} \tag{58}$$

where the spinor $\psi_{n=0,m}$ refers to the zero energy Landau level eigenstate that must be distinguished from the $n \neq 0$ energy Landau level eigenstates given by $\psi_{n\neq 0,\lambda,m}$; $|n,m\rangle$ are the eigenstates of 47 in the non-relativistic case.

Because of the quantization of the energy levels, the Hall and longitudinal resistances measured at the edges of a graphene-based QHE device (similar to the one shown in Figure 21, with the sample now being graphene), will behave in a similar fashion with respect to the non-relativistic case: the Hall resistance R_{H} will get quantized in units of h/e^2 and will show characteristic plateaus as a function of B or, equivalently, as a function of the charge

carrier density n_e (since in graphene charge carriers density and type, i.e. the doping level of the system, is easily changed from electrons to holes simply by varying an external gate voltage V_g, as we have seen in the Introduction, QHE measurements on graphene are usually performed keeping fixed the magnetic field strength B and changing V_g, that is equivalent to change $n_{carriers}$). Nonetheless, there are two important features distinguishing QHE in graphene with respect to QHE in non-relativistic 2D gas, both concerning the filling factor ν:

1. the Landau level degeneracy (in addition to the m degeneracy) for graphene is not anymore 2, as it was for non-relativistic electrons, but 4: indeed, besides the spin degree of freedom (taking two values, $\uparrow$ or $\downarrow$), charge carriers in graphene has an extra degree of freedom that is pseudo-spin (taking also two values, corresponding to sublattices A and B in real space, or to valleys K and K' in reciprocal space);

2. because of the particular form exhibited by the confinement potential giving rise to localization of electrons/holes in graphene ([58]), the $n = 0$ Landau level is split in two branches near the sample edges and it is shifted towards positive energies around the K valley, while towards negative energies around the K' valley. This phenomenon is know as *parity anomaly*. This fact means that the states corresponding to the $n = 0$ Landau level allowed for electrons occupancy are exactly halved at the neutrality Dirac point: in other words, since in undoped graphene the Fermi level is pinned at the Dirac point, there must be a perfect electron-hole symmetry characterizing the material under a strong magnetic field and therefore the $n = 0$ Landau level, split in two halves exactly by the Fermi level, must be half-filled. The situation is illustrated in Figure 23 for convenience.

The above considerations are summarized by introducing a filling factor ν, for describing the IQHE in graphene, given by $\nu = \pm 2(2n+1) = \pm 4\left(n + \frac{1}{2}\right)$ (a negative filling factor means that negative energy Landau levels are occupied up to a certain level, but all the positive energy Landau levels are empty). As a consequence, the Hall resistance in graphene is given by

$$R_H = \frac{h}{e^2}\frac{1}{\nu} = \pm\frac{h}{e^2}\frac{1}{4\left(n+\frac{1}{2}\right)}. \tag{59}$$

Because of the anomalous value of the filling factor ν, the QHE (both Integer and Fractional) in graphene is usually denoted *Anomalous* QHE.

An anomalous FQHE is expected also in graphene systems and it is summarized in the following relation:

$$R_H = \pm\frac{2m(2n+1)+1}{2n+1}\frac{h}{2e^2} \tag{60}$$

that is the relativistic analogous of relation 55. In 60 both $m, n \geq 0$ are integer numbers: again, for $m = 0$ we come back to the IQHE expressed by 59.

Further insights about the Anomalous IQHE and FQHE can be found in [57, 58, 116, 136, 156].

QHE, both Integer and Fractional, has been indeed experimentally measured in graphene samples ([14, 40, 133]) shaped in six-terminal geometries

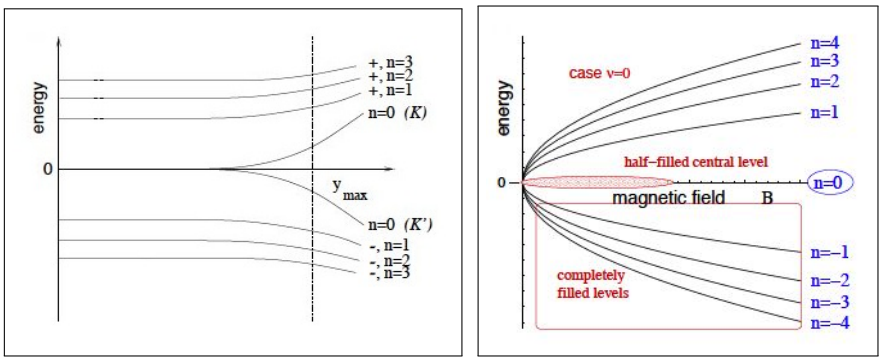

Figure 23: Relativistic Landau levels bending in graphene. Schematic view of the Landau levels bending and occupancy in the case of graphene: (a) bending of the Landau levels, due to potential confinement, near the graphene sample edges. While $\lambda = +$ levels are bent upwards, the $\lambda = -$ levels are bent downwards. The fate of the $n = 0$ level depends instead upon the valley in the reciprocal lattice space: around the K conical Dirac point the level is bent upwards, while around the K' conical Dirac point it is bent downwards. As a consequence, the $n = 0$ level is split in two halves; (b) filling of Landau levels in graphene, at $\nu = 0$. Because of the $n = 0$ level splitting and of the electron-hole symmetry (in undoped graphene), the $\lambda = -$ levels (hole-like levels) are completely filled, whereas the $\lambda = +$ levels (electron-like levels) are completely empty: the $n = 0$ level is exactly half-filled. Adapted from [58].

as illustrated in Figure 3: the effect, as expected, is so robust that Hall resistance plateaus have been detected even at room temperature ([135]). In Figure 24 and Figure 25 some results of QHE experiments performed at different temperatures on various graphene samples are reported, to show the appearance of the Hall resistance plateaus.

The QHE detected in graphene has been one of the most striking proof of the massless relativistic nature of its charge carriers. Moreover, as I have already mentioned in the Introduction, QHE in graphene is nowadays regarded as one of the most promising tools for Metrology, in order to redefine the international quantum resistance standard: due to its inherent 2D nature, Landau levels in graphene are widely spaced and this makes it an ideal material to exploit the physics of QHE. Indeed, thanks to the robustness of the effect, A. Tzalenchuk and co-workers ([184]), by working on monolayer epitaxial graphene at temperature $T = 300\,\mathrm{mK}$, succeeded quite recently in determining the resistance quantum (i.e. the von Klitzing constant) R_K with an accuracy of three parts per thousand million, four order of magnitude better than previously reported in other measurements of QHE on graphene ([55]): this important result really seems to allow achieving the level of precision required in Metrology and opening the doors to a new definition of the quantum resistance standard based on graphene.

1.2.5 Klein Paradox in graphene

The Klein paradox (named after O. Klein who first studied the effect, [85]) is a counterintuitive relativistic process in which an incoming electron of energy $E = \sqrt{\|\mathbf{p}\|^2 c^2 + m_e^2 c^4}$ (where m_e is the mass of the electron, $\mathbf{p}$ its

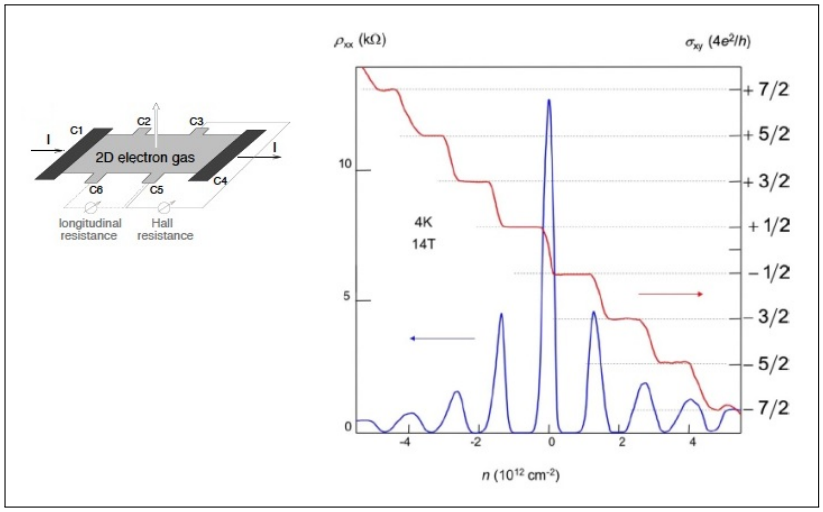

(a)

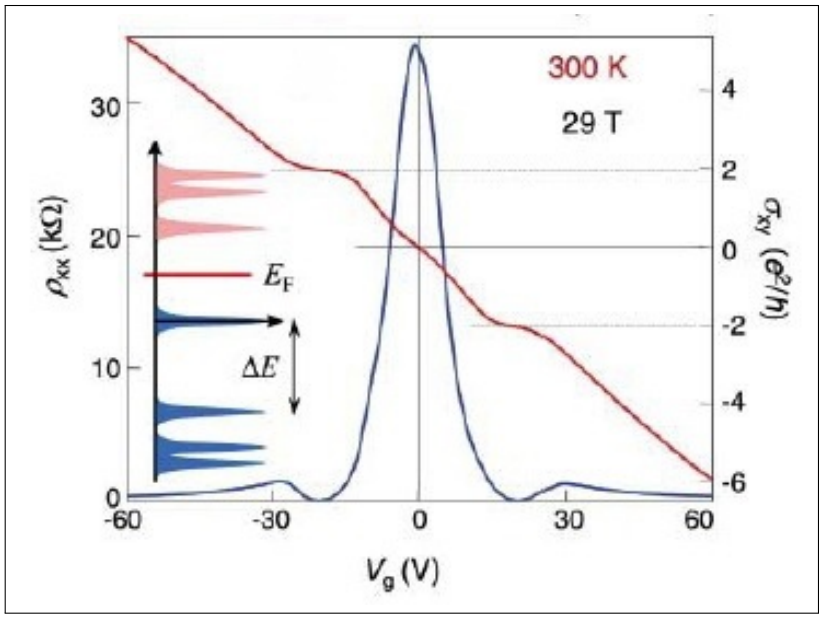

(b)

Figure 24: Experimental evidence of IQHE in graphene. (a) Hall conductivity σ_{xy} (red) and longitudinal resistivity ρ_{xx} (blue) of monolayer graphene mechanically exfoliated from HOPG (shaped into the multi-terminal device geometry schematically depicted on the left) as a function of carriers concentration n. Measurements have been performed at temperature $T = 4\,\mathrm{K}$ and magnetic field $B = 14\,\mathrm{T}$. Characteristic plateaus in the Hall conductivity are clearly visible: on the right the filling factor corresponding to each plateau is shown. Adapted from [24]. (b) Observation of IQHE in monolayer graphene even at room temperature $T = 300\,\mathrm{K}$. The Hall conductivity σ_{xy} (red) and the longitudinal resistivity ρ_{xx} (blue) are shown as a function of the applied gate voltage V_g: positive values of V_g induce electrons, while negative values of V_g induce holes. Measurements have been performed in a magnetic field $B = 29\,\mathrm{T}$. Adapted from [135].

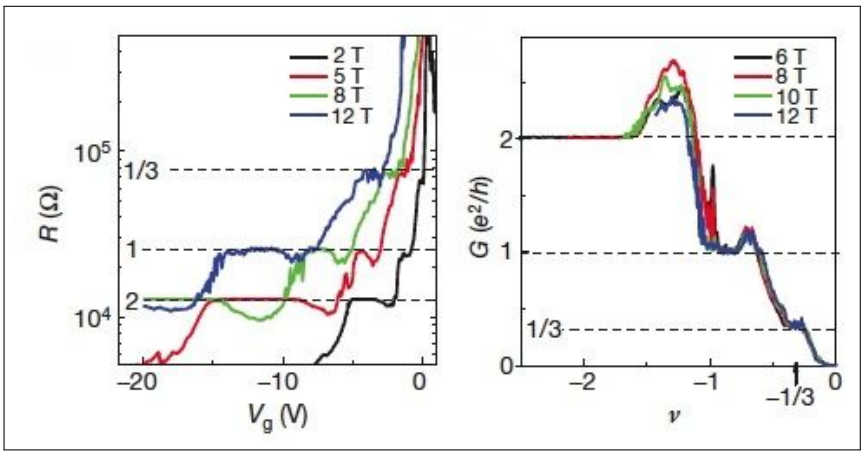

(a)

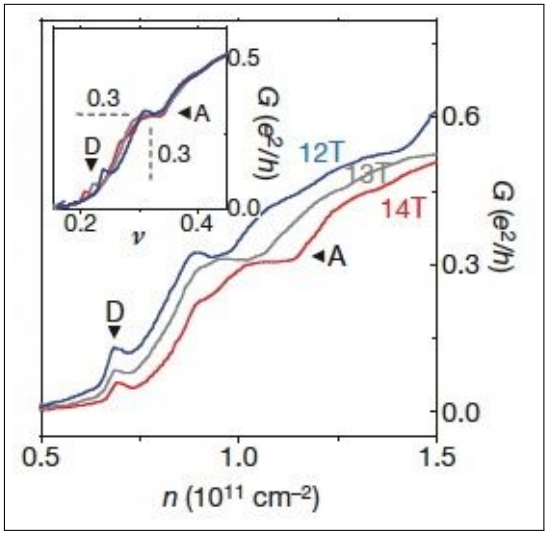

(b)

Figure 25: **Experimental evidence of FQHE in graphene.** (a) FQHE in suspended graphene probed by two-terminal charge transport measurements. On the left the gate voltage dependence of the Hall resistance, at different values of the magnetic fields and fixed temperature $T = 1.2\,\mathrm{K}$, is shown. Quantum Hall plateaus at fractional values of the filling factor clearly appear. On the right, the hole conductance as a function of the filling factor at different values of the magnetic field at the same temperature $T = 1.2\,\mathrm{K}$. The image shows that the data collapse together. Adapted from [40]. (b) Another independent evidence of the appearance of FQHE in graphene, probed again in two-terminal suspended graphene devices. The Hall conductance G, measured at various values of the magnetic field and at fixed temperature $T = 6\,\mathrm{K}$, shows (as clearly appears in the inset showing G as a function of the filling factor ν) the emergence of a plateau at $G \approx 0.3e^2/h$, corresponding to a fractional value of the filling factor $\nu = 1/3$. Adapted from [14].

momentum and c the speed of light) starts to penetrate a rectangular potential barrier of height V_0, when $V_0 > m_e c^2$. The apparently astonishing fact is that for $V_0 > E + m_e c^2$ (the so called *strong regime*), the transmission probability T of the electron through the barrier approaches 1 ([19, 144] for the details of the calculations): therefore, the barrier is transparent to the electron. This result is completely different with respect to the non-relativistic case, for which $T \to 0$ as far as $V_0 \to \infty$ and it has puzzled for many years the physics community: from a theoretical point of view, it is a very interesting problem since it fully relies on relativistic quantum theory.

Indeed, the explanation of the paradox must be searched in the electron-positron (i.e. particle-antiparticle) symmetry inherently associated to a relativistic quantum treatment of fermion dynamics. When the potential barrier is sufficiently high (i.e. $V_0 > E + m_e c^2$), it is strong repulsive for electrons but it becomes attractive for positrons: it is quite straightforward to show ([35, 64, 144, 179]) that, in this regime, positron states arise inside the barrier, aligned in energy with the electron continuum (the states associated to electron energies $E > m_e c^2$) outside (this situation is illustrated in Figure 26 for a step potential, but the behaviour is identical in the case of a potential barrier; indeed, a step potential can be regarded as nothing but a barrier potential with width $D \to 0$). The key point allowing the high-probability tunneling T is the matching between electrons and positrons wavefunctions across the barriers: being electrons (positive energy states) and positrons (negative energy states) intimately related (being one the anti-particle of the other), they are described, according to Dirac theory, by different components of the same spinor wavefunction (equivalently, they are related by charge-conjugation symmetry, [143][3]).

In other words, when an electron traveling forward in time scatters the potential barrier, two events are possible (as schematically shown in Figure 27):

1. the electron is elastically scattered backward in space and forward in time;

2. the electron is scattered forward in space and backward in time (pair annihilation);

Another event is allowed: the pair production, arising from an electron traveling backward in time scattered forward in time across the barrier. The most important observation to relate these events to the explanation of the Klein paradox is that, according to Dirac theory, an electron traveling backward in time is equivalent to a positron traveling forward in time ([143]): as a consequence, the explanation of the paradox relies again on the particle-antiparticle symmetry and on the wavefunction matching occurring at the barrier interface.

Apart from the theoretical perspectives, Klein paradox has never been observed experimentally: in this respect graphene, because of the Dirac-like nature of its charge carriers, offers a completely new and very interesting possibility for testing the paradox.

Let's start by looking at the Hamiltonian 36 describing charge transport in graphene, that I have derived in Sec. 1.2.1: this Hamiltonian, being Dirac-like instead of a Schrödinger-like, forbids to treat separately electrons and holes as described by different dynamical equations, as in usual semiconductors, but forces to treat them on an equal footing, indeed described by a two-

3 It is worth underlying that I am assuming here that no spin-flip processes are occurring across the barrier: this is a good approximation since the probability associated to these events is rather low.

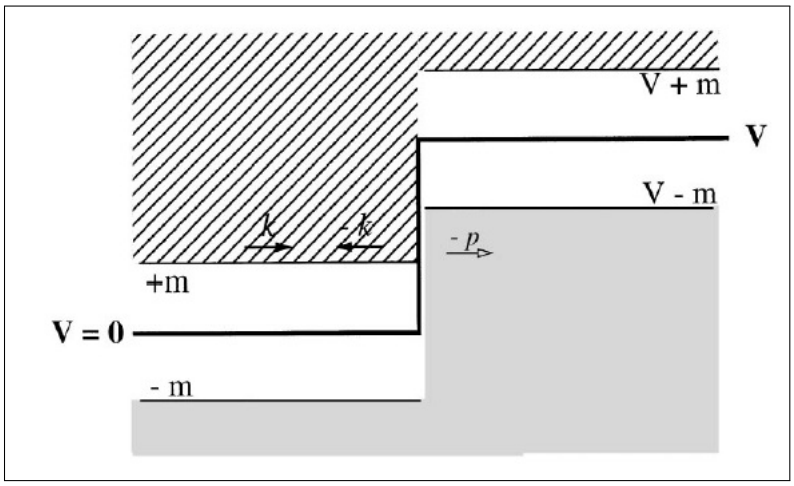

Figure 26: Step potential for Klein paradox. Schematic view of the scattering process of an electron of energy $E > m$ (m is the mass of the electron and $c = 1$ in the figure) across a step barrier of height V. Dashed regions represent the electron continuum ($E > m$ outside the barrier and $E > V + m$ inside), while grey regions represent the positron continuum ($E < -m$ outside the barrier and $E < V - m$ inside). It is clearly visible that the region $m < E < V - m$ (i.e. $V > E + m$) allows for the overlap of electron and positron continuum and for the matching of the wavefunctions at the barrier interface. The explanation of Klein paradox relies on this feature. Adapted from [35].

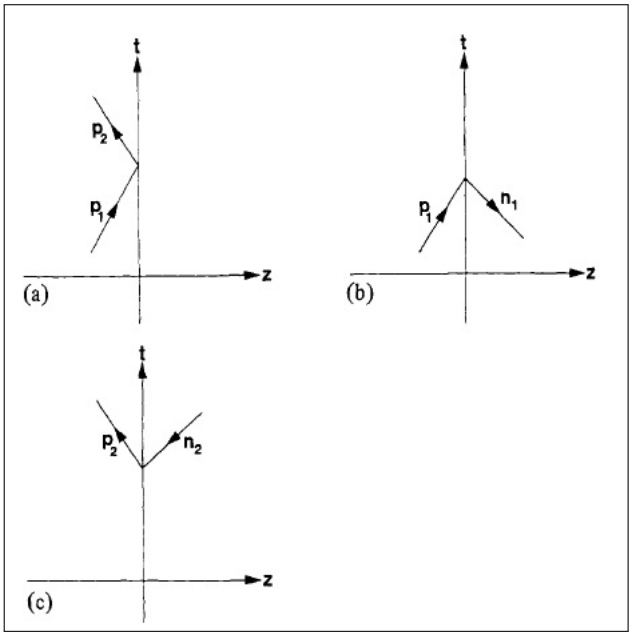

Figure 27: Elementary processes in Klein paradox. Schematic view of the Feynman diagrams representing the possible events occurring to a relativistic electron across a strong potential barrier: (a) the electron is elastically reflected forward in time by the barrier; (b) the electron is reflected backward in time by the barrier and a pair annihilation process occurs; (c) the electron is traveling backward in time is reflected forward in time and a pair production process occurs. Adapted from [64].

component wavefunction (38, 39). Therefore, electrons/holes in graphene are related exactly in the same manner electrons/positrons are connected in QED. The major difference with respect to usual QED, as we have seen in Sec. 1.2.1, is that the spin index associated to electrons and positrons in QED is regarded, for charge carriers in graphene, as a pseudo-spin index distinguishing between sublattices A and B constituting the graphene lattice structure: the charge-conjugation symmetry between particles and antiparticles in QED is a crystal-conjugation symmetry in graphene.

With this observation in mind, it is possible to solve the eigenvalue problem for the Hamiltonian 36 with the potential barrier of width D (xy is the plane in which the graphene layer lies):

$$V(x,y) = \begin{cases} V_0, & 0 < x < D, \forall y \\ 0 & \text{otherwise.} \end{cases} \tag{61}$$

The solution of the problem is quite straightforward and it is possible to show that in the limit $|V_0| \gg |E|$ the transmission probability of graphene electrons through the barrier is given by ([79]):

$$T = \frac{\cos^2\phi}{1 - \cos^2(q_x D)\sin^2\phi} \tag{62}$$

where ϕ is the angle of incidence of the electron on the barrier (i.e. the angle at which the electron propagates with respect to the x axis) and $q_x = \sqrt{(E - V_0)^2/\hbar^2 v_F^2 - k_y^2}$ (E and k_y are the energy and the y component of the wavevector $\mathbf{k}$ of the incident electron).

Equation 62 clearly shows that under some resonance conditions, namely $q_x D = \pi N$, $N = 0, \pm 1, \ldots$, the barrier becomes transparent to electrons (i.e. $T = 1$); moreover, and most important, the barrier is always transparent for incident angles ϕ close to the normal incidence ($\phi = 0$), as shown in Figure 28.

The latter result is the feature unique to the massless Dirac fermions of graphene and it represents the occurrence of Klein paradox in this material. The perfect tunneling, in this case, is understood in terms of the chirality of electrons and holes in graphene and of conservation of pseudo-spin. In absence of pseudo-spin flip processes (equivalent to the approximation of the absence of spin-flip processes done while describing the Klein paradox from a general point of view), an electron moving towards the barrier ($k_x > 0$, $E > E_F$, where E_F is the Fermi energy pinned at the Dirac charge neutrality point), characterized by pseudo-spin $\uparrow$ (referring to Figure 29, $\uparrow$ indicates in this case the right direction), can be scattered only to a left-moving hole state (characterized by $E < E_F$ and, because holes in graphene are particles with fixed chirality -1, $k_x < 0$) inside and to a right-moving electron state outside the barrier, since only these states have pseudo-spin $\uparrow$: the scattering of the electron in a right-moving hole state (characterized by $k_x > 0$), as shown in Figure 29, would result in a pseudo-spin flip process (because holes are chiral particle and therefore, being $k_x > 0$, the pseudo-spin would become $\downarrow$, antiparallel to the hole direction of motion and opposite to the pseudo-spin of the incoming electron). The matching between directions of the pseudo-spin for particles inside and outside the barrier results in a perfect tunneling.

The occurrence of perfect tunneling in graphene systems is quite useful in particular for studying normal metal-insulator-superconductor (N-I-S) hetero-junctions, very useful in Nanoelectronic devices (for example for fabrication of graphene-based Single Electron Transistor): in these structures

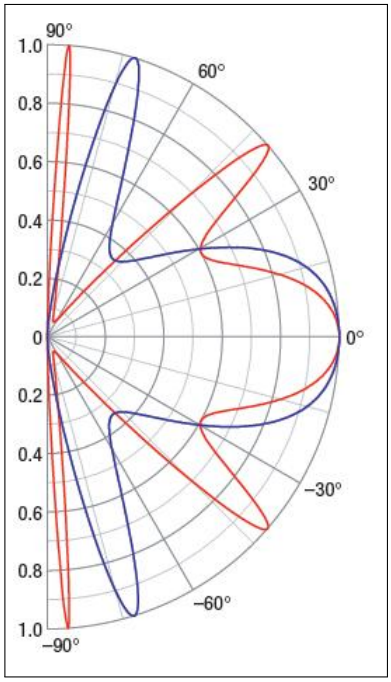

Figure 28: Klein tunneling in monolayer graphene. Transmission probability T through a 100 nm wide barrier as a function of the electron incident angle ϕ in monolayer graphene. Barrier height is $V_0 = 200$ meV (red curve) and 285 meV (blue curve). Electron concentration is $n = 0.5 \times 10^{12}\,\mathrm{cm}^{-2}$, while hole concentrations are $p = 1 \times 10^{12}\,\mathrm{cm}^{-2}$ (red curve) and $3 \times 10^{12}\,\mathrm{cm}^{-2}$ (blue curve). Adapted from [79].

graphene plays the rôle of the normal metal and, by exploiting the feature of the perfect tunneling of its charge carriers across potential barriers (as those arising at the N-I and I-S interfaces), it is possible to enhance the transmission probability of particles across the junction, thus improving the transport properties of the whole device. A study about the tunneling of electrons in such kind of junctions has been reported in [12] and perhaps it may open the route towards the experimental exploitation of the chiral tunneling occurring in graphene in real devices.

To conclude, I have illustrated in this section some of the most striking and intriguing properties of graphene: in particular, I have focused on those peculiarities from which the relativistic behaviour of charge transport in graphene clearly emerges, since this is one of the major differences between this material and the other known and widely exploited semiconductors. I have not sought to present a comprehensive theoretical treatment about graphene, but simply to derive the most important results concerning this material. From these results many other properties of graphene can be derived, as for example its optical, magnetic and thermal response: some of these properties have been summarized in Table 2. For more exhaustive and detailed treatments of the theoretical perspectives concerning graphene I remind to the excellent reviews and books [1, 24, 30, 52, 78, 141, 142].

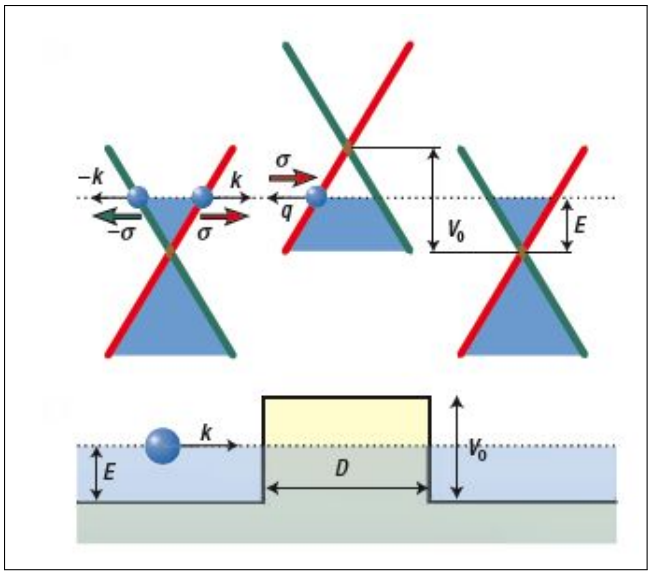

Figure 29: Chiral tunneling in graphene. Schematic diagrams representing the tunneling of graphene electrons through a potential barrier of height V_0 and width D. *Top*: linear behaviour of the band structure in graphene close to the Dirac points. Red and green branches distinguish between a pseudo-spin (σ) vector direction parallel or antiparallel to the direction of motion of the particles (electrons, $E > E_F$ or holes, $E < E_F$), respectively. Dotted line represents the level of the Fermi energy E_F inside and outside the barrier (shown in the bottom): while crossing the barrier, E_F is shifted downward, from the conduction to the valence band, meaning that the incoming electron has been scattered into an hole. The scattering event is allowed because of the overlap between electrons and holes energy continuum. Moreover, in the tunneling pseudo-spin must be conserved: as a consequence, the incoming electron on the red branch cannot be scattered in a state belonging to the green branch. As a consequence, since electrons and holes in graphene are chiral particles, a right-moving electron can be scattered only to another right-moving electron or to a left-moving hole: across the barrier the pseudo-spin is conserved, but the chirality changes since a particle is scattered into its antiparticle. The blue filled areas indicate occupied states into graphene band structure. *Bottom*: schematic view of the potential barrier, showing also the incoming electron characterized by $E > E_F$ and $k_x > 0$. Dotted line and blue filled areas represent the Fermi energy level and the occupied states respectively. Adapted from katsnelson:klein.

1.3 GROWTH TECHNIQUES

In this section I will provide a brief introduction about some of the most important techniques conceived and developed in the last years in order to optimize the growth of graphene layers. I will in particular focus on the mechanical exfoliation of graphene, because of its historical importance in the experimental discovery of graphene, on the reduction of graphene oxides, a chemical route to synthesize graphene layers, on the epitaxial growth of graphene by sublimation of SiC at high temperature and, finally, on the Chemical Vapour Deposition of graphene by decomposition of a carbon precursor in gas phase (usually methane) on a catalytic metallic substrate (the technique employed during my Ph.D. research at I.N.Ri.M., in order to grow graphene).

The introduction does not aim to be fully exhaustive about graphene growth methods, since a full treatment of each technique is obviously too complex and long to be accomplished in this thesis. However, comprehensive and recent reviews on the subject can be found in [59, 165, 169].

1.3.1 Mechanical exfoliation

The mechanical exfoliation of graphene is the method, proposed by A. K. Geim, K. S. Novoselov and co-workers ([134]), that allowed for the first time the deposition of monolayer graphene on an insulating substrate (SiO_2/Si) and the investigation of its properties independently from the substrate itself. The technique simply consists of a peeling process in which commercially available HOPG, dry etched in oxygen plasma, is exfoliated by means of an adhesive (scotch) tape (Figure 30). The method relies on the fact that graphene planes in graphite are bound among each other through weak van der Waals forces: adhesive tape is therefore enough to peel them off from HOPG. Once peeled off from HOPG, graphene flakes are then sticked and therefore transferred on the desired insulating substrate. By characterizing the substrate surface with optical microscopy, it is possible to distinguish among graphene flakes having different number of layers, thanks to the characteristic optical contrast associated to each graphene layer thickness[4]. In this way it is possible to realize that the substrate surface is composed by thin flakes of few-layer and eventually also monolayer graphene.

This technique is high reproducible and, most important, allows to grow graphene flakes characterized by few structural defects and high crystallographic quality: an ideal background in order to detect the numerous exciting mechanical and transport properties of this material. Moreover, monolayer graphene flakes as large as $100\,\mu m^2$ (or even larger in some cases) could be obtained by this method. On the other hand, mechanical exfoliation is not suitable for industrial purposes, since it does not provide upscalability and an eventual pre-deposition patterning of the desired device geometry on graphene.

A slight variant of the mechanical cleavage technique based upon the use of the scotch tape is provided by the exfoliation of HOPG by means of a chemical route. In this case graphite planes are combined in solution

4 It is worth pointing out that in order to determine the right number of graphene layers through optical microscopy characterization, the thickness of the SiO_2 insulating layer plays an important rôle. Indeed, the optical contrast values reported in literature to determine number of graphene layers usually refer to a $\sim 300\,nm$ thick SiO_2 substrate: oxide layers with different thickness do not provide the same optical contrast dependence on number of graphene layers.

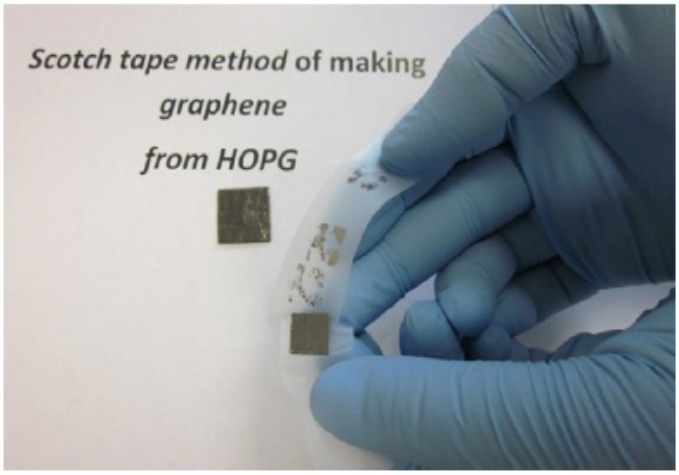

Figure 30: Mechanical exfoliation of graphene. Image showing the mechanical exfoliation procedure employed to deposit monolayer graphene from HOPG by means of a scotch tape. The technique allows to obtain high quality graphene, but it is not scalable. Adapted from [165].

with proper surfactants (in liquid phase) and the subsequent ultrasonication allows few-layer graphene flakes to exfoliate from the sample. This technique provides the possibility of synthesizing graphene sheets in considerable quantities, but the major drawbacks are represented by the small size of the graphene flakes and by the worsening of graphene inherent properties due to the interactions of graphite with the chemical solvents employed during the process.

1.3.2 Reduction of graphene oxides

The chemical conversion of graphite in graphene oxide and the subsequent reduction of the oxide aiming to remove oxygen from graphene has been emerged to be a viable route to grow monolayer graphene. The first step of the process is the synthesis of graphite oxide, obtained by oxidation of graphite using oxidants like sulfuric acid, nitric acid and potassium permanganate. The oxidation process proceeds as in the Hummers method ([68]) and allows to obtain graphite oxide that, compared to pristine graphite, is heavily doped with hydroxyl and epoxy groups functionalizing carbon atoms. Since graphite oxide this way synthesized is highly hydrophilic, it can be easily exfoliated in water: as a consequence, stable dispersions consisting mostly of single-layer graphene oxide can be prepared. It is worth nothing that, although graphite oxide and graphene oxide have similar chemical properties (being both functionalized with the same chemical groups), their structures are different: graphite oxide is a multilayer material, while graphene oxide is a single-layer material. Moreover, because of the presence of oxygen-based functional groups in its structure, graphene oxide is slightly thicker than pristine monolayer graphene.

The major differences between graphene oxide and pristine graphene are represented by the huge number of defects and disorder induced irreversibly in the former by chemical functional groups and by the electrically insulating behaviour observed in graphene oxide in contrast to the semimetallic behaviour of graphene. For this reason, graphene oxide can-

not be employed directly for applications, but a new process, providing the chemical reduction of the material, is needed. Chemical reduction, removing oxygen functional groups from carbon atoms, partially restore the conductivity (i.e. the semimetallic behaviour) in graphene oxide, although at values order of magnitude below those of graphene. The reduction process is performed mainly using several agents including hydrazine and sodium borohydrate: during the process, reduced graphene sheets in solution aggregate and precipitate, because of their less hydrophilic behaviour with respect to graphene oxide. Another approach to achieve the reduction of graphene oxide is the heat treatment of the samples: in this case, graphene oxide is heated at high temperatures (usually $> 1000\,^{\circ}C$), in order to activate the decomposition of epoxy and hydroxyl groups from carbon atoms.

A schematic view of the chemical process employed to synthesize graphene is shown in Figure 31.

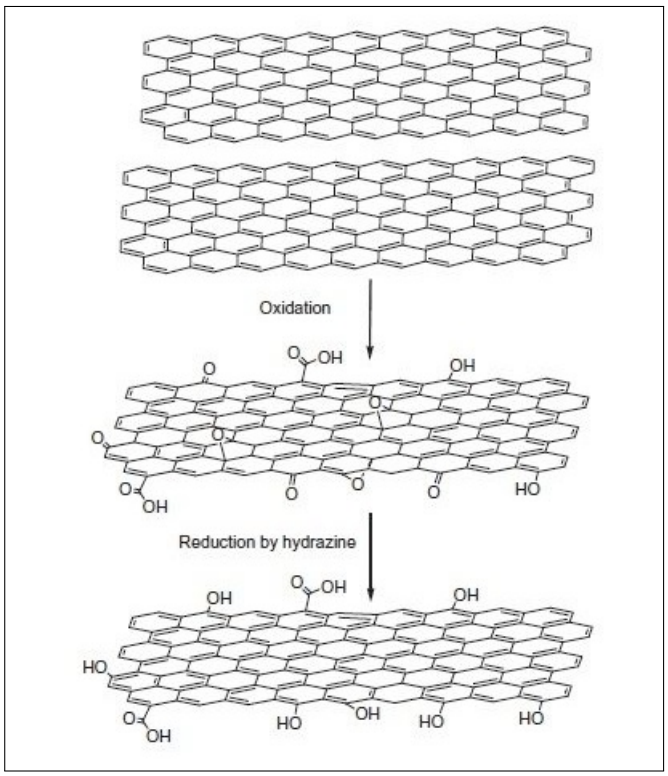

Figure 31: Chemical reduction of graphene oxide for graphene synthesis. Schematic view of the chemical process bringing to synthesis of graphene sheets: graphite is first of all subjected to an oxidation process in order to synthesize graphite oxide. Graphene oxide sheets are then obtained by exfoliation (usually in water) of graphite oxide. The final step concerns the reduction of graphene oxide (performed by means of various reactants, as for example hydrazine) to graphene. Adapted from [165].

The major challenge in the chemical route here described is in the understanding of the molecular structure evolution of graphene oxide during the reduction process: indeed, the final optical and electrical properties of reduced graphene sheets have been demonstrated to depend upon the spatial distribution of functional groups and structural defects (see [165] and references therein to gain further insights).

At present, the chemical reduction of graphene oxide is regarded as a promising method to grow graphene layers because of the considerable

quantity of graphene synthesized during the process; on the other hand, the major drawbacks of the technique are represented by the poor quality usually observed in reduced graphene oxide with respect to pristine graphene (in terms of electric transport properties and of defects induced in the reduced structure during the chemical reduction process) and by the complexity of the whole process.

1.3.3 Epitaxial growth of graphene

The epitaxial growth of graphene, together with the CVD technique that I will describe in Sec. 1.3.4, is one of the most promising method allowing for the deposition of monolayer graphene flakes characterized by large size single crystal domains and for the possible integration in electronic circuitry.

The technique, as reported in many works ([32, 42, 65, 170, 187]), relies on the sublimation of Si atoms from a crystalline SiC (usually 6H-SiC(0001) wafer is employed for the growth, although the use of other carbides have been also reported, see [169] for details) substrate occurring, in vacuum conditions, at temperatures $T \sim 1200$–$1300\,^{\circ}\mathrm{C}$ (in the case the thermal treatment is performed in Ar enriched atmosphere, the temperature is usually increased up to ~ 1500–$1600\,^{\circ}\mathrm{C}$, but the final quality of grown graphene is usually better than in the case of processes carried out in vacuum conditions). The carbon-enriched surface left over by Si sublimation undergoes a subsequent reorganization and graphitization (as shown in Figure 32): a careful control of the sublimation step may lead to the formation of very thin graphene coatings over the entire surface of the SiC wafer, with eventually only a single graphene layer being present.

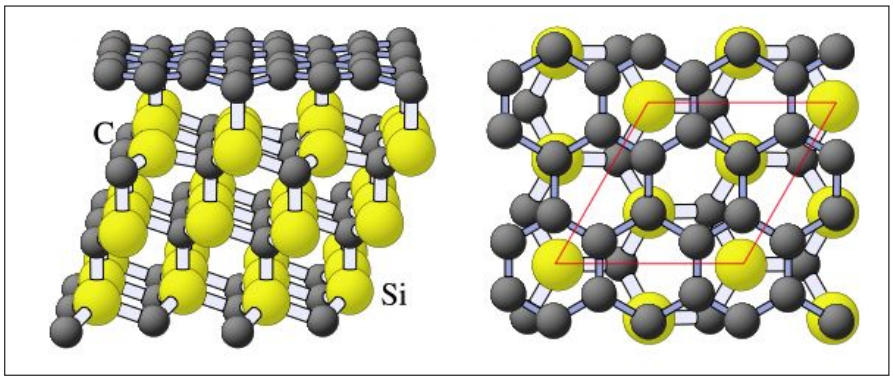

Figure 32: Epitaxial growth of graphene on Si terminated SiC face. Side (*left*) and top (*right*) view of the crystalline structure of a graphene layer grown on SiC(0001) surface, as obtained with *ab initio* simulations: when performed on the Si-face of SiC, the thermal treatment brings to the reorganization of the C-enriched SiC surface resulting in the formation of a first sacrificial buffer layer (with periodicity $6\sqrt{3} \times 6\sqrt{3}\mathrm{R}30°$) covalently bound to the surface. The unit cell of this sacrificial layer is highlighted in red. Graphene layers grow on it by continuing carrying out the process. Adapted from [114].

The sublimation process proceeds in two different ways according to whether the growth is carried out on the Si terminated face of SiC or on the C-face. Thermal treatment performed on the Si-face brings indeed to the formation of a first sacrificial $6\sqrt{3} \times 6\sqrt{3}\mathrm{R}30°$ layer of carbon atoms, covalently bound to the SiC surface ([114]): only after the formation of this layer,

other graphene layers, weakly bound to the substrate, start to grow on the sacrificial layer. It is worth noting that during the growth process no carbon atoms are deposits onto the SiC surface, but the layers are obtained through consumption and sublimation of Si atoms at higher depth inside SiC. So, the growth proceeds from the top of the surface down to the bulk of the material. Graphene layers this way grown are usually characterized by an ordered stacking and by high crystallographic quality. On the contrary, epitaxial growth on C face is characterized by the absence of a sacrificial layer, meaning that graphene layers start to grow directly on the wafer surface, but it does not bring to an ordered stacking of the layers: the latter are organized as in turbostratic graphite, meaning that they have randomly rotated preferential crystallographic orientations among each other. A deep and interesting study of the difference between the epitaxial graphene grown on the Si-face and on the C-face upon sublimation of a 4H-SiC substrate has been reported in [73].

Epitaxial growth of graphene does not necessarily require a post-growth graphene transfer process and allows for the growth of graphene layers resembling the remarkable properties of ideal pristine graphene, thus suitable for integration in Nanoelectronics devices, like Hall bars or FETs (at least when the technique is performed on the Si-face of SiC, [33, 155, 170], although rapid progress has also been made with C-face graphene, as pointed out in [155]); on the other hand, its major disadvantages rely on the quite expensive price of the crystalline SiC substrates needed to start with for graphene growth and on the high temperatures needed for the SiC sublimation process. In order to avoid the latter disadvantage, a slightly different technique, combining the principles underlying both the epitaxial growth and the CVD growth techniques, has been proposed ([75]): instead of using directly SiC as starting material for the sublimation process, a thin (200 nm thick) Ni film is e-beam evaporated onto single-crystalline 6H-SiC(0001) and 3C-SiC substrates. The sample is then processed at temperatures up to $\sim$ 750 °C: during the thermal treatment, Ni and Si at the Ni/SiC interface react forming a NiSi/C mixed phase. As a consequence, C atoms not anymore bound to the SiC sample are left to diffuse inside Ni, as in CVD processes. During the cooling down process C atoms precipitate onto the Ni surface, giving rise to the formation of graphene (as I will explain in Sec. 1.3.4). The formation of high quality graphene deeply relies on the heating rate chosen for the thermal treatment of the sample: indeed a slow heating rate results in the formation of thicker NiSi at the Ni/SiC interface, causing more C atoms to be released in the Ni film during this step. As a consequence, C atoms will exceed their solubility in Ni, precipitating on the surface and forming thicker carbon nanofilms.

1.3.4 The CVD technique

The decompositions of hydrocarbons (like CH_4 and C_2H_2) on metallic catalytic surfaces, the basic principle underlying CVD processes, has been extensively studied from a long time, in particular for the mass production of carbon nanotubes ([169] and references therein).

The technique is performed in proper hot-wall or cold-wall furnaces and it is basically composed by three steps (Figure 33):

1. an heating step, performed in vacuum or under a gas flow (usually H_2 and/or Ar), to anneal the catalyst surface and to remove oxide layers eventually grown on it;

2. a deposition step in which the carbon precursor in gas phase flows into the furnace and its molecules undergo a decomposition process near the catalytic surface, leaving C atoms free to diffuse inside the catalyst or on its surface;

3. a cooling-down step carried out usually in vacuum, in which the temperature is fast decreased down to room temperature, allowing for the nucleation of C atoms on the metallic substrate, later coalescing into larger clusters.

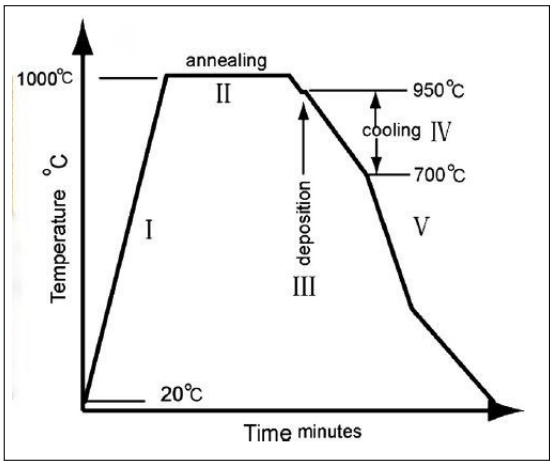

Figure 33: Thermal cycle for CVD growth processes. Typical thermal cycle employed when performing CVD processes. A first step (I), performed in vacuum or under H_2 or Ar flowing, brings the temperature up to the deposition temperature. The second step (II) is performed at the deposition temperature or higher, aiming to anneal the catalytic surface and increase the average size of the grains characterizing its polycrystalline lattice structure. The third step (III) is carried out by flowing the carbon precursor in gas phase inside the furnace, to allow for its decomposition close to the catalytic surface: this is the deposition step. Finally, the fourth step (IV-V) concerns the cooling of the sample down to room temperature and can be divided into more sub-steps: in this step graphene growth on the catalytic substrate occurs. Adapted from [101].

The choice of the metal catalyst for the CVD process plays an important rôle, since the decomposition of hydrocarbons molecules and the subsequent growth of graphene layers proceed in different ways according to the properties of the metallic substrate employed: the growth of higher or lower quality graphene flakes and the average size of graphene crystal domains are strictly related to the underlying lattice structure of the substrate. The choice of a good catalyst, allowing for a monolayer growth of graphene and characterized by a low mismatch between its lattice constant and graphene lattice constant, is therefore of crucial importance in order to optimize and improve the CVD process. Metallic catalysts are usually chosen among the transition metal elements of the Periodic Table, as shown in Figure 34. Indeed, the growth of graphene (not necessarily single layer) on various transition metals has been reported in literature: Ir ([27]), Ru ([112], Pt ([129, 159, 172]), Fe ([86]), Ag ([34]), Co ([185]) Ni ([83, 94, 101, 137, 154]) and Cu ([4, 16, 21, 72, 94–96, 153, 173, 177]).

The catalyst used in CVD processes accomplishes mainly three purposes:

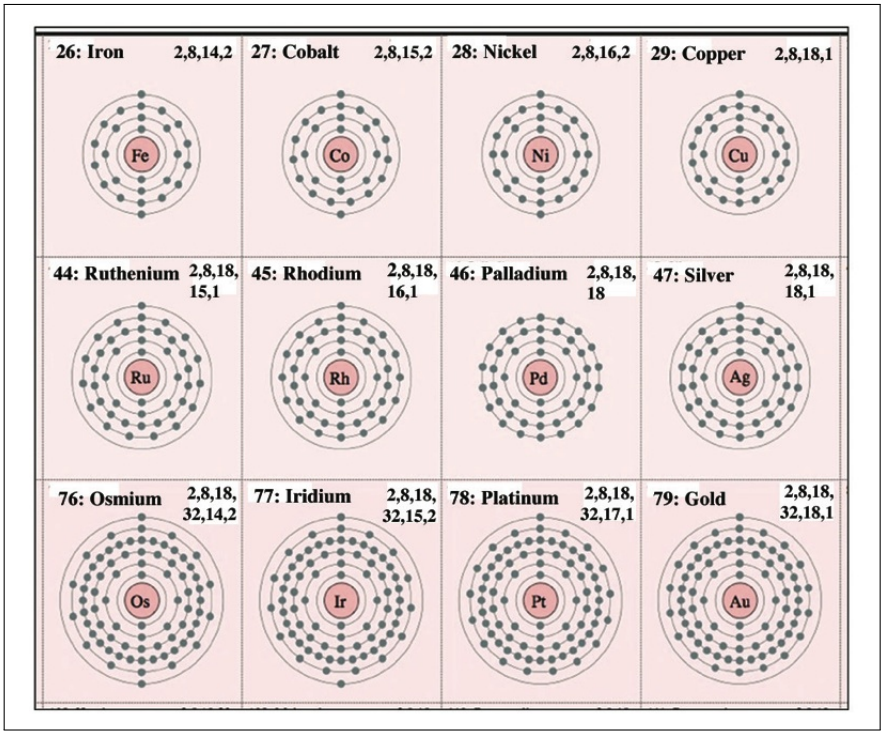

Figure 34: Metal catalysts for CVD processes. Magnified view of the Periodic Table, showing the metallic elements usually employed as catalyst during CVD growth of graphene.

- it reduces the activation energy needed for the decomposition of the carbon precursor molecules, thus decreasing the temperatures employed in CVD processes: for example, while the decomposition temperature of CH_4 molecules is $\gtrsim 1400\,^{\circ}C$ in standard conditions, it is reduced to less than $1000\,^{\circ}C$ in presence of a metallic catalyst. The quite low temperature necessary to carry out CVD processes is one of the most attractive advantages of this technique, making it better than other methods;
- it reduces the energetic barrier needed to start carbon nucleation on the metallic surface and the subsequent growth of graphene layers;
- it enhances the probability that the thermally activated chemical decomposition of carbon precursor molecules occurs only close to to the catalyst surface, and not everywhere in the furnace, hence reducing amorphous carbon precipitation during the growth process. This feature is very important in order to grow crystalline graphene showing few defects in the crystal structure.

For what concerns the process governing graphene growth on the catalyst surface, we can distinguish mainly two kinds of process according to whether carbon atoms diffuse inside the material or they diffuse only on the metallic surface (an experimental study performed on Ni and Cu substrates, based on carbon isotopes labeling and showing the differences among the processes governing graphene nucleation on the two different catalysts, has been reported in [97]):

1. **diffusion/precipitation on surface graphene growth**
   This kind of growth characterizes catalytic substrates, as Ni, having

high carbon solid solubility and diffusion coefficients at high temperatures ($T \sim 800\,^{\circ}\mathrm{C}$) into the metallic substrate itself. This feature allows for the diffusion of C atoms, left unbound from the carbon precursor molecules during the heating process, inside the substrate: because of the high solid solubility of carbon in the substrate (for example, in the case of Ni, ~ 0.6 weight % at $\sim 1326\,^{\circ}\mathrm{C}$), the atoms will occupy interstitial sites into the catalytic crystal structures. Once the temperature is lowered, during the cooling-down process, the solid solubility of carbon decreases and carbon concentration in the substrate will exceed, at a certain temperature (depending on the phase diagram of carbon and the metal catalyst), the maximum value allowed: therefore, carbon atoms will diffuse out of the catalyst bulk, precipitating on the surface. Segregation of C on the surface will then provide the growth of graphene layers. A schematic view of how proceeds graphene growth according to this kind of process is illustrated in Figure 35.

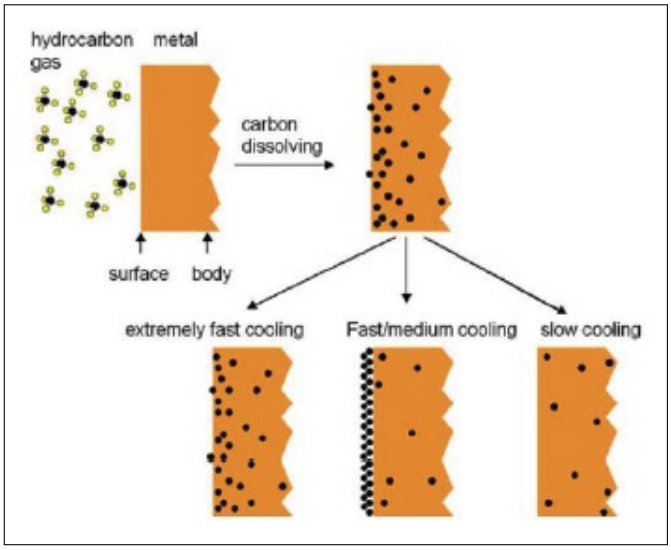

Figure 35: Diffusion/precipitation mechanism governing CVD processes. Schematic view of the steps governing CVD growth of graphene in the case the solid solubility of C atoms inside the catalytic substrate has high values: the first step concerns the decomposition, at high temperature, of the hydrocarbon precursor close to the catalytic surface activating the reaction. Free C atoms are then free to diffuse inside the substrate and thanks to the high solid solubility they will occupy interstitial sites into the catalytic lattice structures. In the subsequent cooling-down step C atoms will diffuse out of the substrate and they will segregate on top of its surface, forming graphene, because the solid solubility of C will be exceeded by lowering the temperature. According to how fast is the cooling-down process, this last step brings to the formation of high quality monolayer graphene, or to the formation of multilayer graphene and amorphous carbon, or finally to the trapping of C atoms inside the material. Adapted from [119].

There are three parameters deeply affecting the quality and the number of graphene layers grown by the CVD process in this case:

- the deposition temperature at which the carbon precursor flows into the reaction chamber;
- the deposition time;

- the cooling-down rate.

In particular, the combination of the first two factors controls the supply rate of C atoms reaching the catalytic surface and diffusing inside it during the deposition step f the CVD process: by increasing one or both these parameters will result in exceeding the carbon solubility into the catalyst already during the heating step, with the consequent formation of amorphous carbon on top of the metallic surface. This fact will unavoidably worsen the quality of grown graphene layers, by inducing a large amount of defects, as clearly demonstrated in [101]. Moreover, in the same work, authors have demonstrated that the last parameter is crucial in controlling the growth of the right number of graphene layers on top of the catalyst surface: indeed, while a too fast cooling rate will result in the trapping of C atoms inside the bulk of the catalyst, a too slow lowering of the temperature will allow the growth of undesired multilayer graphene. Therefore, finding the right cooling-down rate is very important to grow really monolayer graphene during CVD.

Moreover, it is worth mentioning the important rôle played by the substrate grain boundaries during graphene deposition. Indeed, when C atoms will encounter grain boundaries on the catalytic surface, they will preferentially diffuse through them: as a consequence, multilayer graphene and amorphous carbon structures will be usually detected in correspondence of grain boundaries present in the underlying substrate. To reduce this effect, thus to enhance graphene crystal domains size and graphene crystallographic quality, an annealing step at high temperature is always performed before the deposition of graphene, as illustrated in Figure 33, to increase the size of the grains characterizing the unavoidable polycrystalline nature of the catalyst.

2. **decomposition/nucleation on surface graphene growth**
When dealing with transition metals characterized by very low carbon solid solubility, the process governing graphene growth is different: this is the case, for example, of metals like Cu, in which the solubility of C at $T \sim 1084\,^{\circ}\mathrm{C}$ is only 0.001–0.008 weight %.

In the specific case of Cu, the low solubility is due to the low affinity to carbon, arising from its electronic structure showing a completely filled 3d shell. As a consequence, instead of absorbing C atoms, Cu forms only weak bonds with carbon through charge transfer between the π electrons of graphene and its 4s empty states. As a consequence, graphene growth does not occur because of diffusion inside the catalyst and subsequent segregation on the surface, but because of diffusion of C atoms on the surface and subsequent nucleation of small C islands coalescing together to form a full layer completely covering the substrate. As shown in Figure 36, upon breakdown of the hydrocarbon precursor and chemisorption of carbon atoms on Cu surface, the concentration of active carbon species increases until it reaches a critical supersaturation level: at this point nucleation of stable graphene nuclei starts to take place. Since nucleation and growth of nuclei deplete the adsorbed C atoms surrounding them, the concentration of carbon is reduced to a level where nucleation rate is negligible and growth of the nuclei instead continues until the supersaturated amount of surface carbon species above the equilibrium level is consumed. At this point the equilibrium between surface carbon, graphene and carbon

precursor molecules is reached. Depending on the available carbon, graphene nuclei either coalesce to form a continuous film (characterized in any case by a polycrystalline structure) covering the whole Cu substrate or stop growing, reaching a saturated incomplete coverage. The exact nature of the carbon active species chemisorbed on Cu, leading to graphene nucleation, has not been clearly identified yet. A detailed study about the chemical and physical principles governing graphene growth on Cu has been recently published in [82].

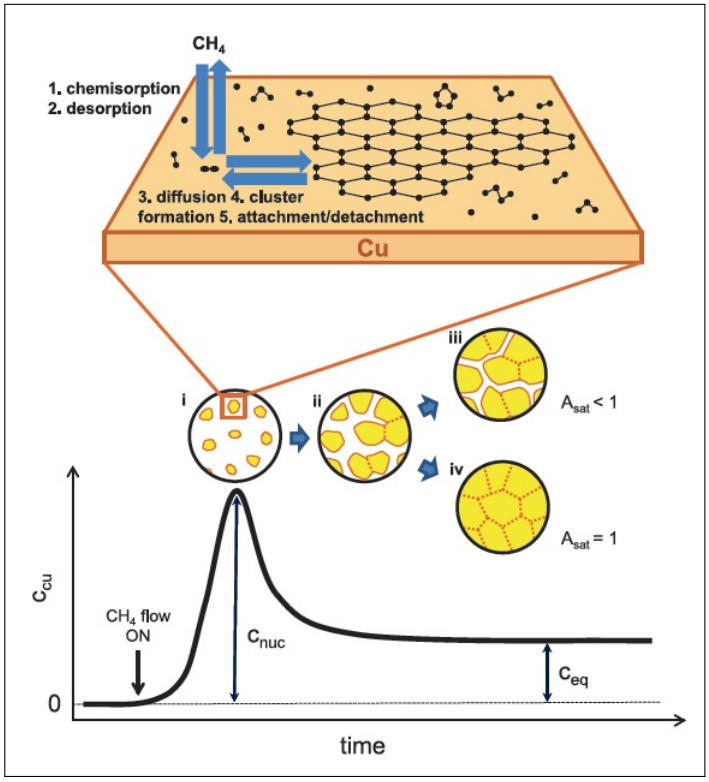

Figure 36: Diffusion/nucleation mechanism governing CVD processes on Cu. Schematic view showing the mechanism governing CVD growth of graphene on Cu. Decomposition of the hydrocarbon precursor leads to supersaturation of carbon atoms adsorbed on Cu surface. When the carbon concentration reaches a critical supersaturation point, nucleation of graphene domains occurs and concentration of active carbon species on the surface is quickly reduced until the equilibrium between carbon species, graphene nuclei and hydrocarbon precursor molecules is reached. Graphene nuclei may then coalesce to form a film covering the whole Cu substrate, or the growth may stop when the amount of supersaturated carbon species is consumed. Adapted from [82].

The two major consequences of this kind of growth are an easiest transfer of graphene from Cu to other insulating substrates and, more important, a self-limited graphene growth, that should stop after one layer of the material has been grown. As a consequence, at least in principle, CVD processes performed on Cu are much easily controlled, since the deposition of multilayers should be avoided by the inherent properties of the catalyst. However, in many experiments multilayer graphene growth has been observed, meaning that some other principles are acting during graphene deposition: also in the CVD processes I have performed on Cu (foils and thin films), as I will report in

Sec. 3.3.2 and Sec. 3.3.3, I have observed this feature. The most important parameter in this kind of graphene growth is therefore the deposition temperature at which chemisorption of C atoms on Cu surface takes place, instead of the cooling-down rate: indeed, this parameter controls the C supply rate on one hand and the diffusivity of C atoms on the Cu surface on the other hand. A low deposition temperature may reduce the concentration and the diffusion ability of carbon on the substrate surface, thus limiting the nucleation and the formation of graphene.

In any case, a major problem arising in CVD processes performed on Cu thin films is the dewetting of the catalytic substrate from the underlying SiO_2/Si wafer: I will devote the whole Chapter 2 to the discussion of this problem and to the development of solutions to avoid (or at least to have a better control) on it. For this reason, the major part of works reported in literature about CVD processes performed on Cu deals with foils ($\sim 25\,\mu m$ thick) instead of thin films ($< 500\,nm$ thick).

Other details about CVD processes on Cu can be found in the nice review [115].

CVD technique is nowadays regarded as one of the most promising method in order to achieve the production of monolayer graphene over large scale areas: indeed, growth of graphene flakes as big as $\sim 100\,\mu m^2$ has been reported in literature ([101]). The major advantages provided by the exploitation of this technique are the low temperatures involved during the process ($T \sim 900$–$950\,^\circ C$), its high accessibility, the fact of being quite inexpensive and the possibility of patterning the desired graphene geometry for device fabrication before performing the CVD process. Nonetheless, it still has some drawbacks: first of all the need of a transfer of graphene grown by CVD from the catalytic substrate to a new insulating substrate, in order to integrate it in devices and to investigate its properties (although some transfer-free CVD methods have been recently proposed, [72, 95]), the polycrystalline structure of graphene layers due to the grain boundaries characterizing the catalyst and the worsening of graphene properties due to interactions with the metallic substrate (for example, charge carrier mobilities in monolayer graphene grown by CVD reach a maximum value of $\sim 7000\,cm^2\,V^{-1}\,s^{-1}$ at low temperatures, as reported in [4], two order of magnitudes lower than in suspended mechanically exfoliated graphene). An optimization of the technique is therefore needed to fully exploit the remarkable properties of graphene in nanoelectronic devices. Other details about the CVD technique can be found in [7, 119, 200].

In particular, the CVD technique is the one I worked on during my research at I.N.Ri.M. laboratories. The catalytic substrates employed during experiments have been Ni and Cu (both foils and thin films). The detailed description of the processes and of the results obtained will be reported in Chapter 2 and Chapter 3.

1.3.5 Other growth techniques

At the end of this chapter I finally mention that other graphene growth techniques have been reported in literature, but their description is far beyond the scope of this thesis. Among them, I remind:

- the unzipping of carbon nanotubes, obtained through chemical treatments in H_2SO_4 and $KMnO_4$ at room temperature, allowing for the production of graphene nanoribbons characterized by a width of $\sim$ 100 nm ([88]);
- the Molecular Beam Epitaxy (MBE) deposition of graphene layers on the $(000\bar{1})$ face of SiC ([124]) and on thin films of Ni ([51]), obtained through evaporation of a carbon solid source, at temperatures ranging between 900 °C and 1100 °C. This kind of techniques allows for a very good control on the crystallographic orientation and on the thickness of grown graphene layers.

2 THIN FILM DEPOSITION AND COPPER DEWETTING

In this chapter I present the main results I have obtained about the deposition of Cu thin films on different substrates (Si, SiO_2/Si and Cr/SiO_2/Si samples). After describing in Sec. 2.1 the experimental apparatus used for the deposition and characterization of the films (mainly an e-beam evaporator, a Scanning Electron Microscope -SEM- system and an X-Ray Diffraction -XRD- system), a detailed presentation of the various procedures used to evaporate Cu films on different substrates and on the final quality of the films will be reported in Sec. 2.2. In Sec. 2.3 I will introduce the main subject of the chapter, namely the *dewetting* effect I have encountered while processing my samples, at high temperatures, in a Rapid Thermal Annealing (RTA) system in order to grow graphene on Cu by CVD. Since dewetting is a major problem limiting the real possibility of synthesizing graphene on Cu thin films, while the employment of thin films would be desirable if a subsequent use of grown graphene for Nanoelectronic applications is requested, a deep study of this phenomenon has been carried out. The very interesting results obtained, summarized in Sec. 2.4, allowed me to propose a new *in situ* technique opening the route towards a real time control of any change in the morphology and in the uniform coverage of the underlying sample occurring at high temperatures on Cu thin films. Hopefully, such a technique, up to now working only in Low Vacuum conditions, is a first step in the direction of a better control of the quality of the catalytic substrate used for graphene growth and on the (many) parameters involved in the CVD process, determining the final uniformity, crystallinity and thickness (number of layers) of graphene.

2.1 THE EXPERIMENTAL APPARATUS

As described in Sec. 1.3.4, a typical CVD process for graphene deposition requires a catalytic substrate to activate the decomposition of the carbon precursor molecules at temperatures lower than 1000 °C: the main rôle of the catalyst is to change the chemical kinetics, by enhancing the rate of the chemical reaction describing the dissociation of the carbon species (equivalently, the catalyst reduces the activation energy necessary to start the reaction, as shown in Figure 37) and, as a consequence, by lowering the temperature at which the reaction occurs. An important feature of chemical reactions involving a catalyst is that while reactants are consumed during the reaction, the catalyst is usually regenerated and its amount remains unchanged. A typical reaction scheme involving two reactants X, Y, a catalyst C and a product of reaction Z proceeds as follows:

1. $X + C \rightarrow XC$;
2. $XC + Y \rightarrow XYC$;
3. $XYC \rightarrow ZC$;
4. $ZC \rightarrow Z + C$

It is clear from the scheme that:

- during the catalytic reaction the catalyst C is consumed in step 1 but it is subsequently produced in step 4 and hence its amount is left almost unchanged;
- during the process the reactants and the product of the reaction are left unchanged by the presence of the catalyst, only the rate of the reaction changes.

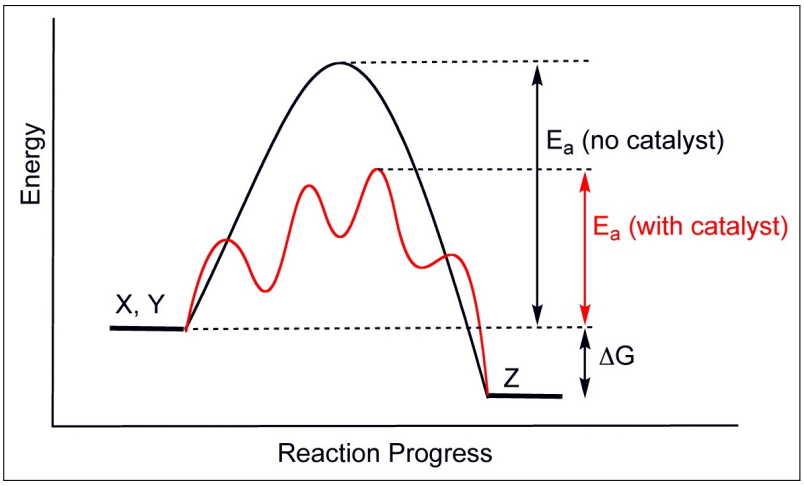

Figure 37: Effect of a catalyst on the activation energy of a chemical reaction. Generic potential energy diagram showing the effect of the presence of a catalyst in a hypothetical exothermic chemical reaction $X + Y \rightarrow Z$. While the overall result of the reaction and the thermodynamics of the process are the same with or without the catalyst, the activation energy in the presence of the catalyst is reduced (because of the presence of a new reaction path) and the reaction is therefore favoured. Courtesy of Wikipedia.

For graphene growth, as already pointed out in Sec. 1.3.4, many catalysts have been proposed during the years and I have discussed why, for many reasons, Cu can be regarded as one of the most promising and useful substrates to synthesize graphene. Nonetheless, a major challenge in the employment of Cu is represented by the use of thin films of this material during the CVD process instead of commercially available foils: while most of the literature describing CVD processes performed on Cu deals with $\approx$ 25–50 µm foils ([4, 16, 17, 21, 28, 96, 97, 153, 171, 177, 199]), not too much has been reported about graphene synthesis on thin films with thickness $\lesssim$ 500 nm ([72, 95, 173, 177] and [94], although in this latter case the thickness was 700 nm). This is mainly due, as I will describe later in this Chapter, to some difficulties arising in working on Cu films at high temperatures, in particular for what concerns the adhesion of Cu to the underlying SiO_2/Si substrate. Nonetheless, thin films are in general necessary for many applications: nano-patterning of electronic structures and integration of graphene in Nanoelectronic devices, for example, require to deal with metallic films instead of foils to be properly implemented. Moreover, employment of thin films, compared to foils, prevents an excessive consumption of Cu, thus making the technique much more cost-effective. Finally, the use of thin films ensures more flexibility for the graphene growth process: indeed, while Cu foils allow only for a large-scale graphene growth (obtained through a CVD

process that brings to graphene deposition everywhere on Cu), eventually followed by a patterning of the desired graphene geometry by means of a lithographic step directly performed on graphene, the employment of Cu thin films allow for a selective graphene growth, obtained by first patterning the device geometry directly on Cu and then by depositing graphene by CVD only on the patterned substrate. The two possibilities offered by the use of Cu films, instead of foils, are schematically depicted in Figure 38. For this reason I have decided to concentrate much of my work on the study and the improvement of CVD growth processes in presence of Cu thin films.

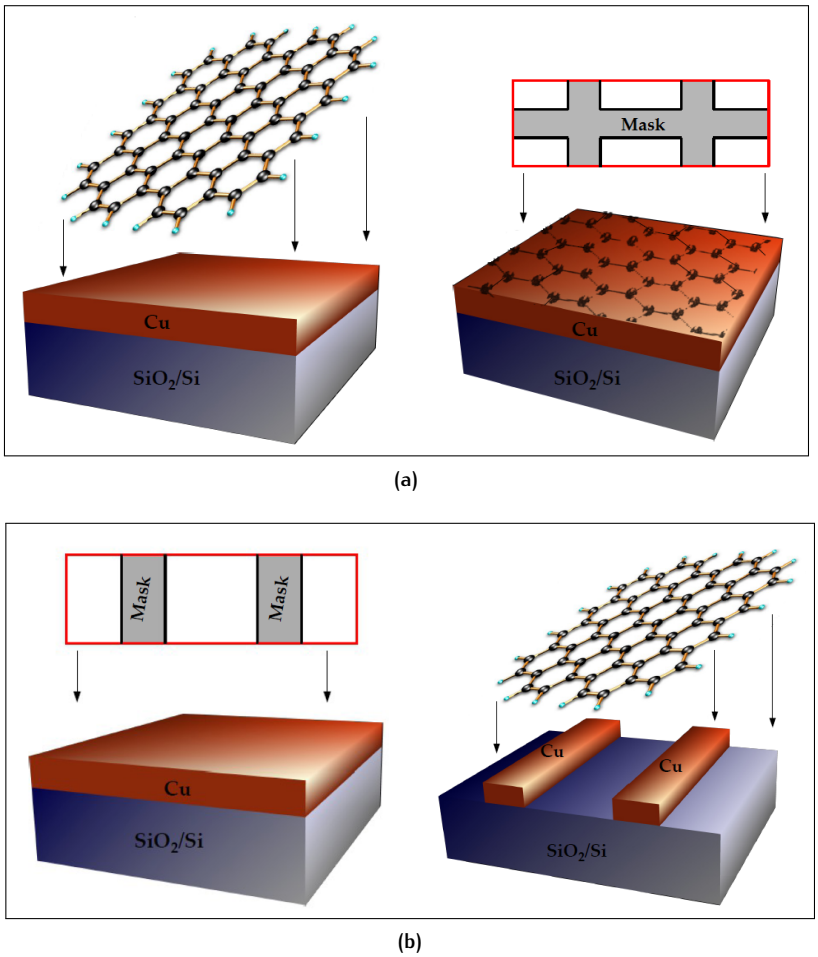

Figure 38: Strategies for graphene growth by CVD on Cu thin films. Schematic view of the different strategies offered by thin films for graphene growth by CVD on Cu: (a) the first strategy consists of a large-scale growth of graphene, deposited by CVD everywhere on the Cu substrate. The patterning of the desired device geometry is obtained only in a subsequent step, through lithography directly performed on graphene (worsening its quality); (b) the second strategy consists instead in a selective growth of graphene: in this case the first step is the patterning of the desired device geometry directly on Cu. Graphene deposition by CVD is performed only after the patterning step: this way graphene will grow only on the geometry pre-patterned on Cu. The second strategy is allowed only when employing Cu thin films and not Cu foils.

The first step in this direction is obviously the deposition of the film, carried out mainly by means of the Electron Beam Physical Vapour Deposition

(EBPVD, often abbreviated as e-beam evaporation) technique. Some preliminary depositions have been performed also by using a thermal evaporator, in order to acquire some experience about the control of the parameters involved in such a technique and to study the kind of film growth occurring during the deposition: thermal deposition has been in any case abandoned soon due to the low deposition rate of the process (and the subsequent huge amount of time needed to deposit few hundreds nanometres), to the high degree of contamination of evaporated films due to the heating of the entire evaporation chamber (in contrast with the case of the e-beam evaporation in which heating is concentrated only on the source target) and to the poorness achieved in the final quality of the films (in terms of uniformity and crystallinity) after the evaporation.
After deposition, the second step involves the characterization of the evaporated films, in order to check their quality, uniformity, the presence of damages, cracks or impurities, the degree of crystallization reached during the process and hence the dimension and orientation of the crystal grains in the case of a polycrystalline growth. The characterization has been performed mainly with a SEM system and an XRD system, both present at I.N.Ri.M. laboratories.

Before showing the main results reached in Cu depositions, I briefly describe the instruments used for the evaporation and the characterization of the films.

2.1.1 Thermal and e-beam evaporators

Thermal and e-beam evaporations of thin films are physical processes consisting in the deposition under Ultra-High Vacuum (UHV) or High Vacuum (HV) conditions of films of various controlled thickness (ranging from few nanometres to millimetres) on a chosen substrate (facing the evaporation source at a proper distance), stroke by a gaseous phase beam of atoms of the desired source material; the beam is obtained by heating above the evaporation/sublimation temperature the source material contained in solid phase in proper crucibles put into an evaporation chamber. The process proceeds atomistically and mostly involves no chemical reactions. The main difference between the thermal and the e-beam evaporation techniques is represented by the physical process governing the heating and therefore the evaporation of the material to be deposited: while in a thermal evaporator the material is contained in a conducting crucible through which a current flows, heating the source simply because of Joule effect (i.e. resistance heat), in an e-beam evaporator the crucible is a target anode bombarded by an electron beam given off by a charged tungsten filament because of thermionic emission. The electrons of the beam are then accelerated to high kinetic energies by an High Voltage difference of $\sim$ 10 kV kept between the filament and the ground and directed towards the target by means of proper magnetic fields. Once the electrons strike the target, their kinetic energy is rapidly converted into thermal energy through different complex interaction processes with the atoms of the material to be evaporated and the thermal energy causes the material to melt and evaporate or to directly sublimate. The evaporated material, in both the techniques, diffuses everywhere into the evaporation chamber and precipitates again in solid phase upon striking the sample surface over which it will be deposited. The concentration of the growth species in gas phase can be controlled by varying the source

temperature and the flux of the carrier gas (for example with a shutter). The evaporation rate Φ_e is dependent on the material to be deposited ([20]):

$$\Phi_e = \alpha_e N_A \frac{P_e - P_h}{(2\pi m R_g T)^{1/2}} \tag{63}$$

where $0 \leqslant \alpha_e \leqslant 1$ is the coefficient of evaporation, $N_A \simeq 6.022 \times 10^{23}$ is the Avogadro's constant, P_e and P_h are respectively the vapor pressure and the hydrostatic pressure acting on the source, m is the molar weight of the source material, $R_g \simeq 8.314\,\mathrm{J\,K^{-1}\,mol^{-1}}$ is the universal gas constant and T is the temperature. Atoms and molecules in gas phase do not collide with each other prior to arrival at the growth substrate surface, because their mean free path is much larger than the source-to-substrate distance. A schematic view of the steps constituting a typical e-beam evaporation process is depicted in Figure 39 to better explain the physical principles underlying the technique.

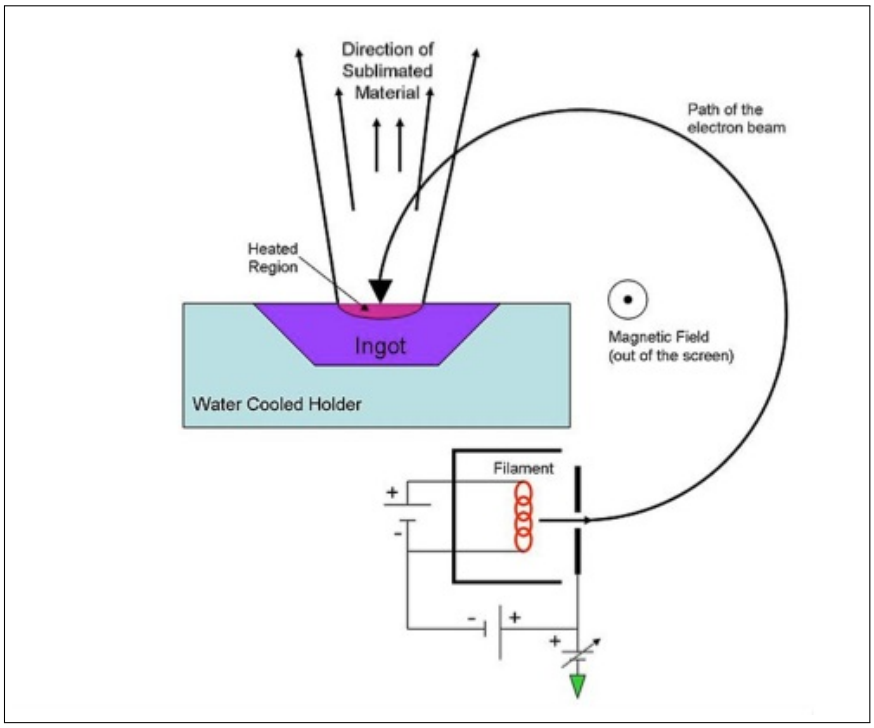

Figure 39: Electron Beam Physical Vapour Deposition process. Schematic view of a typical e-beam evaporation process. Electrons are given off by thermionic effect from a charged tungsten filament (the current flowing in the filament is generated by a Low Voltage difference of few V). They are later accelerated to high kinetic energy by the High Voltage difference kept between the filament and the ground; the beam is directed to the target crucible by a magnetic field usually produced by permanent magnets. Electrons hit the target and their kinetic energy is converted into thermal energy, heating the material to be evaporated up to its melting/sublimation temperature. Atoms from the material to be evaporated are released in gaseous form and diffuse through the chamber. Once the atoms reach the sample surface (usually not heated with external instruments during EBPVD processes) where the deposition will occur, they precipitate into solid phase and film deposition starts. Courtesy of Wikipedia.

The thickness of the growing film and the growth rate during the deposition are controlled in both the evaporators by a thickness monitor connected

to a quartz crystal detector (consisting of a Quartz Crystal Microbalance, QCM) placed in the evaporation chamber, not necessarily at the same distance from the source as the substrate on which film deposition occurs: for this reason a systematic error in the thickness measured by the crystal sensor during the deposition may be sometimes introduced (Figure 40). To account for this error, a calibration of the thickness detector is usually needed in order to determine the corrective factor to be applied to the detected film thickness to obtain a right answer during film growth. This factor is called *geometrical tooling factor* and, assuming the source to be point-like and isotropic, is given by $\eta = \dfrac{d_{\text{meas}}}{d_{\text{detector}}}$, where d_{meas} is the true film thickness as determined in an independent measurement (for example with a profilometre, as the one present at I.N.Ri.M. and shown in Figure 41), while d_{detector} is the film thickness as measured by the crystal detector.

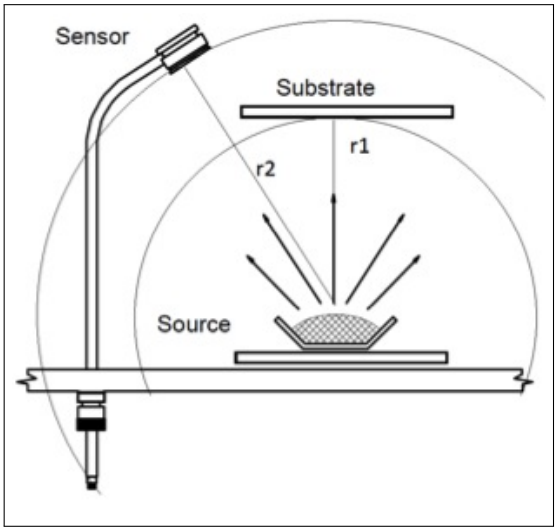

Figure 40: Geometrical tooling factor. Since in many cases the source-to-substrate distance r_1 differs from the source-to-thickness detector distance r_2, a geometrical correction factor to the film thickness as detected by the sensor must be applied to have a correct result: the correction factor is called tooling factor and it is simply given by the ratio between the real thickness of the deposited film and the thickness determined by the detector.

In particular, for the sensor used in the evaporators at I.N.Ri.M. (Figure 42), d_{detector} is given by ([104, 105])

$$d_{\text{detector}} = \frac{N_q \rho_q}{\pi \rho_{ev} Z f_l} \arctan\left\{ Z \tan\left[\frac{\pi (f_u - f_l)}{f_u} \right] \right\} \tag{64}$$

where $N_q = 1.668 \times 10^{13}\,\text{Hz}\,\text{Å}$ is the frequency constant of the QCM, $\rho_q = 2.648\,\text{g}\,\text{cm}^{-3}$ and ρ_{ev} are the quartz mass density and the evaporation material mass density respectively, f_u and f_l are the oscillation frequencies of the sensor before and during the film deposition respectively (these frequencies are of $\sim$ 5–6 MHz) and finally $Z = \sqrt{\dfrac{\rho_q \mu_q}{\rho_f \mu_f}}$ is a constant dimensionless factor (with $\mu_q \simeq 2.947 \times 10^{11}\,\text{g}\,\text{cm}^{-1}\,\text{s}^{-2}$, μ_f shear moduli of the quartz crystal and of the evaporation material respectively). Indeed, a stationary wave arises in a crystal when an AC current produced by two electrodes is flowing through it: the resonance frequency of the crystal is related to its temperature, pressure and thickness. If the latter is varied while keeping fixed all

Figure 41: Profilometre at I.N.Ri.M.. Picture of the profilometre used at I.N.Ri.M. to determine the roughness and the thickness of thin films.

the other parameters, a change in the resonance frequency of the crystal occurs and therefore, every time an amount of a given material is deposited on the QCM during an evaporation process, such a change is detected. From the change in frequency is possible to determine the thickness d_{detector} of the film deposited on the crystal. In general, the change in resonance frequency Δf and the change in mass of the crystal Δm (directly related to d_{detector} if the the mass density of the evaporated material and the cross area of the deposited film -identified with the area of the QCM- are known) are related through the Sauerbrey equation ([160]):

$$\Delta f = -\frac{2\Delta m f_0^2}{A\left(\rho_q \mu_q\right)^{1/2}} \tag{65}$$

where f_0 is the resonance frequency of the fundamental mode of the QCM, Δm is the variation on the crystal mass, A is the crystal area enclosed by the electrodes, ρ_q and μ_q are respectively the mass density and the shear modulus of the quartz crystal (already introduced in equation 64).

The thermal evaporator

The thermal evaporator present at I.N.Ri.M. laboratories is shown in Figure 43 and Figure 44. The evaporation chamber contains two crucibles and is connected through a gate valve to the upper load-lock chamber: in this way the vacuum in the evaporation chamber is maintained also during the substrate loading. A manual micrometre controller allows for tilting the substrates once they are placed into the evaporation chamber.
Primary vacuum, down to $\sim 10^{-2}$–10^{-3} mbar, is ensured by a mechanical vacuum pump (*Alcatel - 2033*), while secondary vacuum (HV conditions) is reached with a turbo-molecular vacuum pump (*Arthur Pfeiffer Vakuumtechnik GMBH - TPH 510 S*); the base pressure of the chamber in HV conditions is $p_{\text{base}} \sim 10^{-6}$–$10^{-7}$ mbar. The pressure is measured by a capacitive vacuum gauge (MKS Baratron, for primary vacuum conditions -i.e. for detecting a minimum pressure of $\sim 10^{-5}$ mbar) and by one cold-cathode Penning

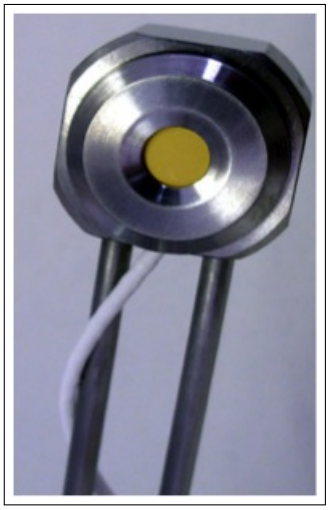

Figure 42: Quartz Crystal Microbalance for thickness detection. Head of the crystal sensor placed inside the thermal and e-beam evaporators at I.N.Ri.M. for real-time detection of the film thickness and growth rate during thin film deposition processes.

ionization vacuum gauge (*Leybold Vakuum GMBH - PR25 Titan 15752*, for detecting HV conditions), both placed close to the substrate surface on which the film is deposited in the evaporation chamber.
The current flowing through the crucibles is varied manually in order to increase or decrease their temperature and hence to change the growth rate during the evaporation process and an independent heater (*Tectra - HC3500*) allows for increasing the temperature also on the deposition substrate. During the evaporation process the pressure in the chamber is $p_{\text{chamber}} \sim 10^{-5}$–$10^{-6}$ mbar (depending on the source material to be evaporated) and the typical growth rate is 1–2 Å s^{-1}. The thickness of the film during the deposition process and the growth rate are controlled by a thickness monitor (*Intellemetrics - IL150*) connected to the QCM placed inside the evaporation chamber.

The e-beam evaporator

The e-beam evaporator system present at I.N.Ri.M. is shown in Figure 45 together with its main components. As for the thermal evaporator, the system is of load-lock type: the evaporation and the substrate loading chambers are therefore connected through a gate valve that can be closed during the loading procedure. The loading process is manually controlled by means of a couple of pliers (catching the sample-holder with the substrate) mounted on two manipulators: one manipulator brings the substrate mounted on a proper sample-holder inside or outside the evaporator chamber, while the second manipulator allows for substrate tilting.

The evaporation chamber contains six crucibles and a shutter to eventually stop the deposition. HV conditions are ensured by a mechanical (*Leybold TRIVAC*) and a turbo-molecular (*Turbotronik NT 151/361*) vacuum pumps bringing the base pressure of the chamber to $p_{\text{base}} \sim 10^{-7}$–$5 \times 10^{-8}$ mbar. During the evaporation processes the typical pressure in the chamber is $p_{\text{chamber}} \lesssim 10^{-6}$ mbar. The pressure in the evaporation chamber is controlled by a hot-cathode Bayard-Alpert ionization gauge (*Granville-Phillips 343 Gauge Controller*). The load-lock chamber is instead kept in Low Vac-

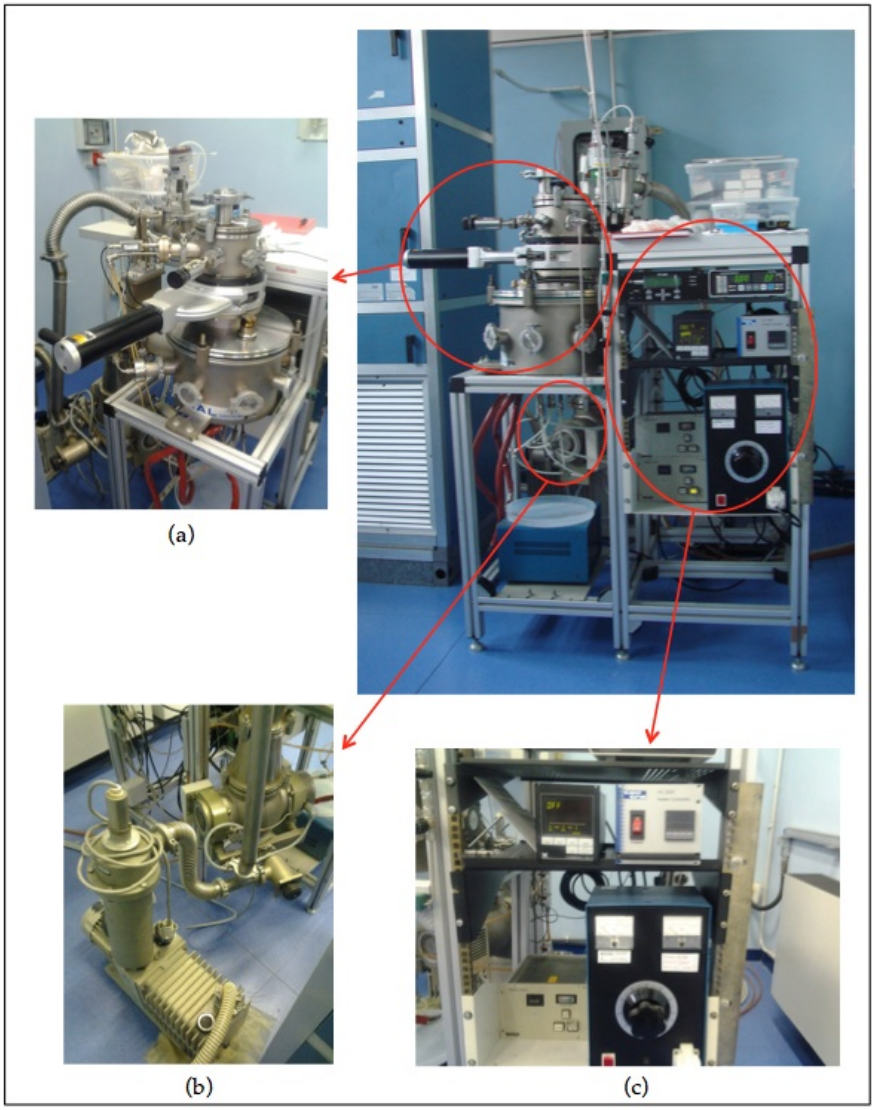

Figure 43: **Thermal evaporator at I.N.Ri.M..** Picture of the thermal evaporator present at I.N.Ri.M. laboratories with its main components enlightened: (a) the evaporation and load-lock chamber; (b) mechanical (on the ground) and turbo-molecular vacuum pumps; (c) pressure, current and thickness controller rack.

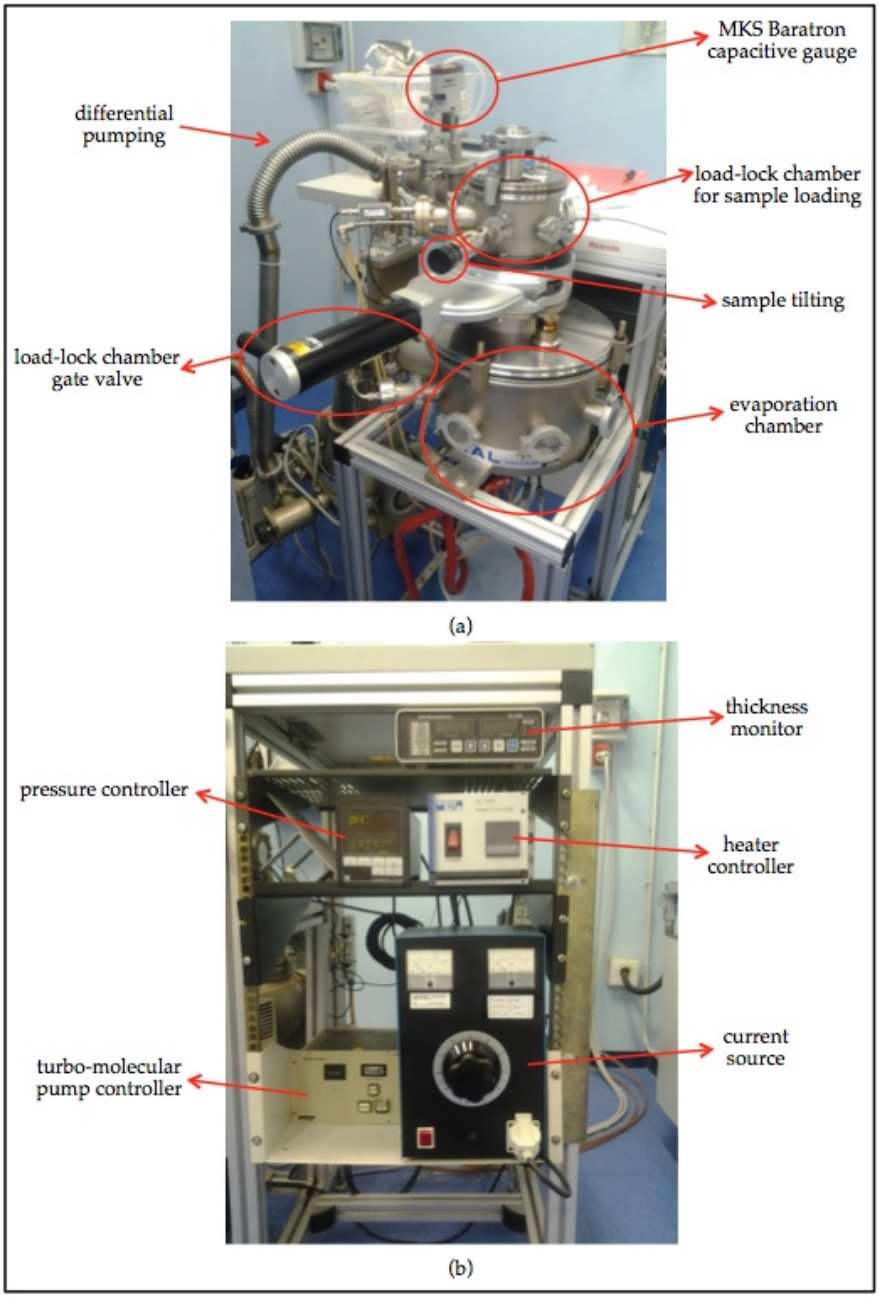

Figure 44: Thermal evaporator components. Detailed view of the thermal evaporator (Figure 43) components: (a) load-lock and evaporator chambers components; (b) controller rack components.

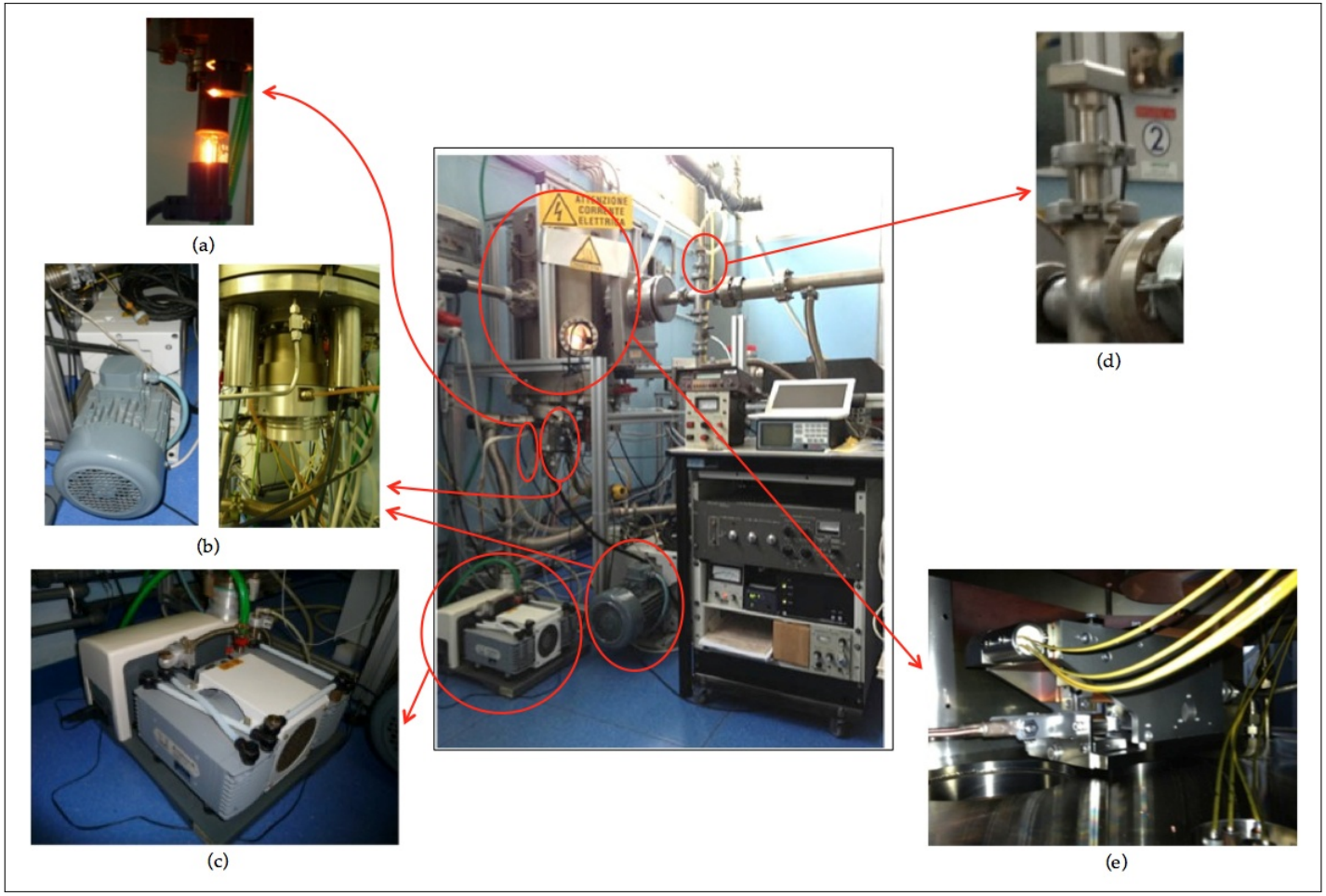

Figure 45: E-beam evaporator at I.N.Ri.M.. Picture of the e-beam evaporator (in the centre) present at I.N.Ri.M. laboratories, with its basic components enlightened: (a) hot-cathode Bayard-Alpert ionization gauge for HV pressure measurement in the evaporation chamber; (b) mechanical (on the ground) and turbo-molecular vacuum pumps for the evaporation chamber; (c) all-in-one mechanical and turbo-molecular vacuum pumping system for the load-lock chamber; (d) Pirani gauge for primary vacuum pressure measurement in the load-lock chamber; (e) e-beam gun placed in the HV evaporation chamber, containing the tungsten filament to produce the electron beam and the magnets to direct the beam on the target crucible.

uum conditions ($p_{\text{load-lock}} \sim 10^{-2}$–$10^{-3}$ mbar) through a mechanical/turbomolecular pumping system and its pressure is measured by a Pirani gauge. The tungsten filament giving off the electron beam is charged by an AC voltage of ~ 12 V (as maximum value), ensuring an AC current flow of $\sim$ 20–40 A. The beam is directed on the target source material through a magnetic field generated by a permanent magnet; once the electrons arrive on the target crucible, a smaller magnetic field produced by two electromagnets provides a finest control of the position of the beam with respect to the crucible and allows also to switch on a sweeping effect on the beam. The acceleration of the electrons is finally provided by an High Voltage generator (*Varian - 10 kV E-Gun™ Control Unit - model 989-1124*, Figure 46) wired to the emission filament chamber: the generator produces an output voltage of 10 kV and it is properly screened from surrounding space to avoid discharges and undesired spurious currents.

Figure 46: High Voltage generator for e-beam deposition. Picture of the High Voltage generator present at I.N.Ri.M.: the generator can receive an input voltage ranging from -9 V and 0 V and provides an output voltage of 10 kV, used to accelerate the electron beam before it reaches the target material to be evaporated.

The current flowing through the tungsten filament, affecting the electrons flux (i.e. the electron beam current) and therefore the growth rate during deposition processes, was at the beginning manually controlled (Figure 47a): this fact resulted however in a very bad control on the current flow, causing a lot of difficulties in keeping the growth rate constant during the evaporations. For this reason, the system that controls current flow, film thickness and growth rate has been very recently automatised (using a *Sycon STC-200* deposition rate controller, Figure 47b), so that it is now possible to set-up the values of the growth parameters simply through an home-made software (developed in LabView environment, Figure 48). A detailed description of this software can be found in [150]. Typical growth rates for Cu range from $\sim 1\,\text{Å}\,\text{s}^{-1}$ to $2\,\text{Å}\,\text{s}^{-1}$ (corresponding to an electron beam current of ~ 150 mA), but higher or lower rates are allowed and are usually needed to evaporate other materials (for example Au or Cr).

Moreover, the evaporator can be properly equipped also with an ion gun: this possibility is meant to exploit the advantages given by the Ion Beam

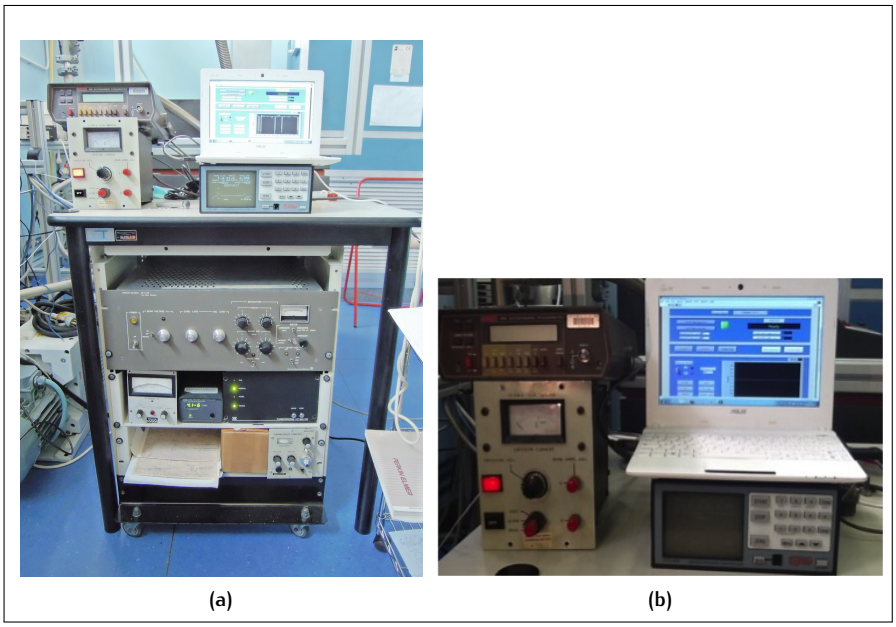

Figure 47: Controller rack for the e-beam evaporator. Picture of the e-beam evaporator controller rack used at I.N.Ri.M. for thin film EBPVD. (a) The full controller rack: at the bottom the pressure detectors' monitors; (b) More detailed view of the system controlling the current flowing through the tungsten filament and the electron beam trajectory (*on the left*) and the film thickness and growth rate (*on the right*).

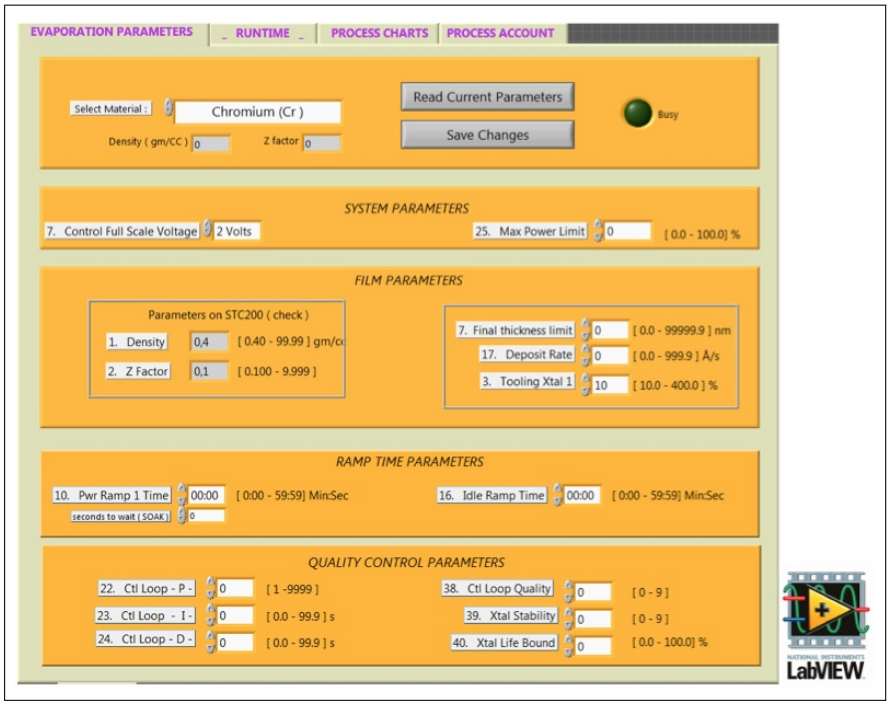

Figure 48: Screenshot for digital control of e-beam evaporations. Picture of the computer screenshot showing the adjustable parameters (mainly the source material to be evaporated, the growth rate and the desired film thickness) for an e-beam evaporation process. The software provides a digital control of the process and has been developed in LabView code.

Assisted Deposition (IBAD) technique (a comprehensive description of the technique can be found in [43]). In this technique ions are given off by an independent gun (atoms' ionization is provided into the gun by interaction with electrons emitted for thermionic effect by a tungsten filament, while ions acceleration is achieved through a voltage difference of few kV, as depicted in Figure 49a), allowing for an independent control of the parameters (energy and current) affecting the ion beam characteristics; the current of the ion beam (ions are charged particles and so there is a current associated to their motion) once it enters the evaporation chamber is controlled through an ammeter (Figure 49b). Usually IBAD technique is employed for etching layers and removing impurities from the substrate surface on which evaporation of thin films will occur. Since I was not interested in this feature, but rather in improving the adhesion between Cu atoms and the substrate, I have employed an inert gas (Ar) in the ion gun (this choice avoids or at least lowers a lot undesired chemical interactions between the ion beam and the evaporated material). This way it is possible to combine the EBPVD with a simultaneous ions emission: Ar ions emitted at high energy from the gun in the e-beam evaporator chamber kick randomly the Cu atoms given off by the e-beam gun, transferring this way the major part of their energy and momentum to Cu. Hence Cu atoms will strike at higher energy the substrate surface, enhancing in principle the sticking coefficient between the deposited film and the substrate.
An Ar^+ gun (*Perkin Elmer* 5 kV *Differential Ion Gun 04-303*, Figure 50) has been recently mounted on the e-beam evaporator: the gun allows to vary both the acceleration voltage (from 0 kV to 5 kV) and the current flowing in the filament giving off the electrons for the ionization process. Ar ion beams are left intentionally unfocused, so they can cover in a raster fashion a larger solid angle in the evaporation chamber, enhancing therefore the cross section of the Cu-Ar collisional events. I have performed some evaporation processes with the IBAD technique, but up to now I have only preliminary results, to be fully analysed and improved in the future.

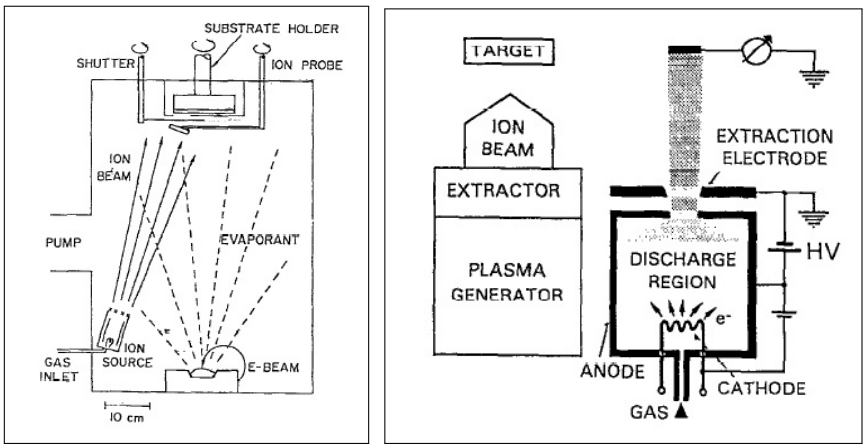

Figure 49: IBAD technique principles. Schematic view of the principles underlying ions' emission during the exploitation of the IBAD technique for thin films deposition: (a) experimental setup for an EBPVD process assisted by Ion Beam emission, as it is for the IBAD processes performed with the e-beam evaporator (Figure 45) employed at I.N.Ri.M. laboratories; (b) schematic cross section of an ion source equipped with an hot filament as electron emitter (electrons are needed for atoms' ionization in the ion gun) and with an ammeter for the measurement of the current associated to the ion beam. Both adapted from [43].

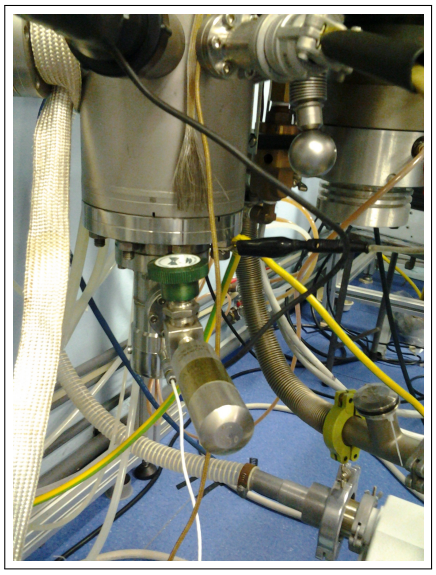

Figure 50: Ar gun for IBAD technique. Picture of the Ar ion gun recently mounted on the e-beam evaporator present at I.N.Ri.M.. The Ar gun is used for IBAD-EBPVD processes.

2.1.2 The SEM technique and instrumentation

The first tool I have widely used to characterize my Cu thin films has been the SEM technique. SEM images provide a quite fast and detailed response about the quality of the films, about their granulometry and uniformity and about the eventual presence of defects. With SEM characterization is also possible to carry out a first investigation searching for the presence of graphene on Cu, although in this case very careful measurements must be performed and it is not an easy task to distinguish between graphene flakes and, for example, Cu preferential exfoliation directions. In any case, many SEM images of Cu thin films both before and after the CVD processes have been acquired during the work in order to investigate the properties of the grown material.
The SEM characterization tool is an imaging technique that falls into the more general category of the Electron Microscopy. As such, SEM produces images of a sample by scanning it with a focused beam of electrons (instead of using visible light photons as in the case of Optical Microscope systems): since electrons have associated wavelengths (through the de Broglie relation $\lambda = h/\sqrt{2m_e E}$, where E is the non-relativistic electron energy and m_e the electron mass) much shorter than visible light photons, the resolution of SEM images is thousands times better than the resolution of optical images, achieving resolutions sometimes higher than 1 nm. The electrons of the incident beam are produced mainly in two ways: they can be emitted by thermionic effect from an electron gun fitted with a tungsten filament cathode or they can be given off by a Field Emission Gun (FEG), which may be of cold-cathode type (using tungsten single crystal emitters) or of thermally assisted Schottky type (using emitters of zirconium oxide). Once produced, the electron beam is accelerated into the so-called electron column (Figure 51) by a voltage difference usually ranging from 0.2 kV to 40 kV and it is focused to spot of $\sim$ 0.4 nm to 5 nm in diameter by means of a system of electromagnetic condensor lens and objective lens. The electron column is always kept in UHV conditions ($p_{\text{column}} \sim 10^{-8}$ mbar).

Samples to be scanned are prepared on proper sample-holders and put into a chamber kept in HV conditions ($p_{\text{chamber}} \sim 10^{-6}$ mbar) during the electron scanning. Primary electron beam arriving on the sample interacts with the electrons of the sample itself loosing its energy in repeated random scattering and absorption processes, occurring in a teardrop-shaped volume known as the interaction volume (Figure 52). This volume extends from less than 100 nm to 5 µm into the sample's surface.

Energy exchange between the primary electron beam and sample's electrons gives rise to the reflection of high-energy electrons by elastic scattering with atoms' nuclei (these electrons are called *back-scattered electrons* and have exactly the same energy of the incoming electrons) and to the emission of low-energy ($\sim$ 10 eV) *secondary electrons* by inelastic scattering processes (these electrons are orbital valence electrons of the specimen's atoms produced everywhere in the sample, but having very low energy, only those produced within few nanometres from the sample surface emerge from the material and can be detected). Back-scattered and secondary electrons are collected by two different detectors and serve two different goals: while secondary electrons allow to extract detailed information about the sample's surface topography (producing a contrast image in grey colors with brighter and darker regions corresponding respectively to flat portions of the sample's surface or to steep surfaces and edges), back-scattered electrons sup-

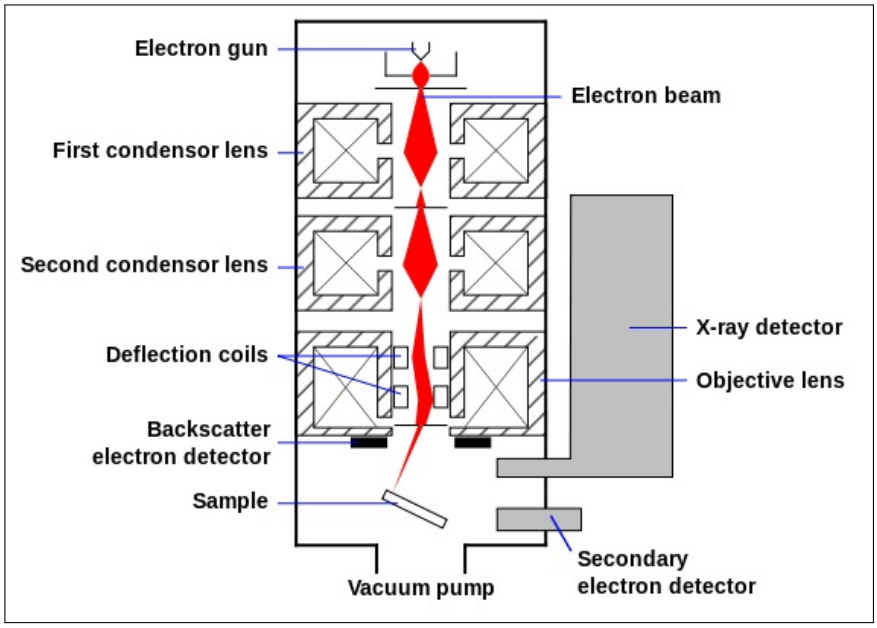

Figure 51: SEM electron column. Schematic view of a typical SEM electron column (equipped also with an X-Ray detector for Energy-dispersive X-Ray Spectroscopy -EDX or EDS- analysis, not necessarily present in SEM instruments): electron beam emitted by the electron gun passes through a focusing system of lenses and arrives on the sample accelerated by the desired voltage difference. All the column is in UHV conditions, while the sample chamber is kept in HV conditions during scanning. Secondary and back-scattered electrons detectors are also shown. Courtesy of Wikipedia.

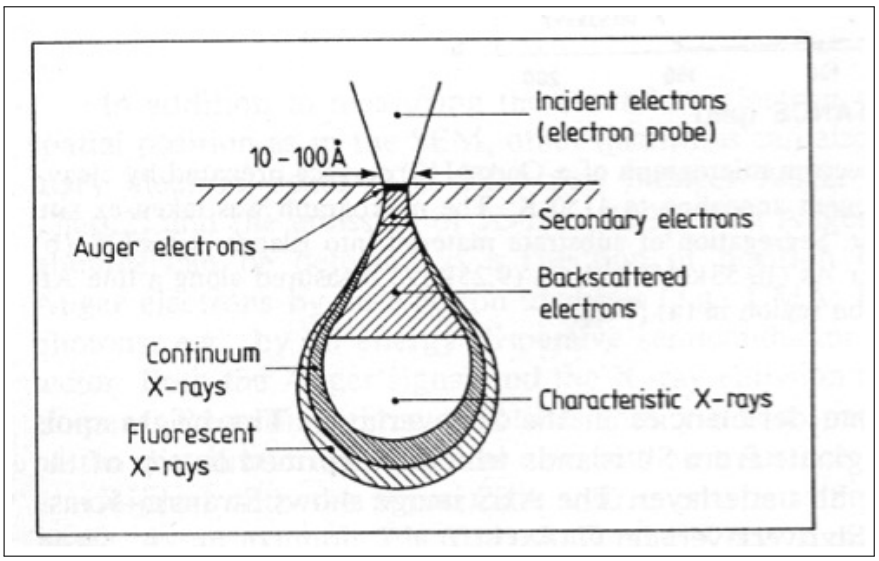

Figure 52: Tear-drop interaction volume for microprobe signals. Schematic overview of the pear-shaped volume of a sample probed by different microprobe signals (electron and X-Ray emission), when a primary electron beam is incident on a solid surface. Back-scattered electrons originate from a deeper region with respect to secondary electrons. Adapted from [25].

ply Z contrast images (where Z is the atomic number of the atomic species present in the sample) useful to acquire informations about the chemical composition or the crystallographic orientations of the sample (since high Z heavy elements emit back-scattered electrons more strongly than low Z light elements, brighter regions in a SEM image produced with back-scattered electrons correspond to the presence of heavier elements).

The SEM microscope (*FEI InspectF*) present at I.N.Ri.M. laboratories is shown in Figure 53. The beam is produced by a Schottky type FEG kept in UHV conditions (10^{-9} mbar) by means of a mechanical/turbo-molecular vacuum pumping system and can be accelerated to energies ranging from 0.5 keV to 30 keV. The electron column is also kept in UHV conditions (10^{-8} mbar) and contains a set of electromagnetic condenser lenses to focus the beam: working carefully beam spots of 1.2 nm are achievable. A final set of lenses allows for the in-plane deflection of the beam along x and y directions. Samples are mounted on a proper sample-holder able to bring up to 8 samples simultaneously; samples' chamber is kept in HV conditions (10^{-6} mbar).
The microscope is equipped with two kind of detectors: a secondary electron detector and a back-scattered electron detector (BSED). The former is an Everhart-Thornley detector (ETD), which is a type of scintillator-photomultiplier system, allowing therefore for a fast detection. Secondary electrons are first collected by an electrically biased grid (usually kept at 200–250 V) and then accelerated to a scintillator. Electrons cause the scintillator to emit flashes light that are conducted to the photomultiplier and at the end converted in a digital image. The luminosity in each point of the image is proportional to the number of secondary electrons arriving to the detector from the corresponding point of the sample. BSED is instead a slow semiconductor detector positioned above the sample, concentric with the primary electron beam: when back-scattered electrons are collected, electron-hole pairs are produced in the detector and are later counted and converted into a digital image. As already mentioned, BSED analysis is useful to acquire informations about the chemical composition and the crystallographic orientations of a sample.

2.1.3 The XRD technique and instrumentation

A second characterization tool I have used to investigate the properties of the e-beam evaporated Cu thin films has been the XRD technique. Although very few measurements have been performed by means of this technique, interesting results about the polycrystalline nature of the films (both before and after graphene growth over them) and the main crystallographic growth orientations of the grains forming the films (changing after the CVD process, as we will see) have been obtained.
XRD technique is a longtime known crystallographic method for determining the atomic structure of a crystal. The technique is based on the diffraction of an incident beam of parallel X-Rays (first observed by M. von Laue, P. Knipping and W. Friedrich in 1912, [50]) caused by regular periodic arrays of atoms (as those present in a crystal), acting as scatterers for the incoming electromagnetic plane waves. Each atom scatters a small portion of the X-Ray radiation primarily through its electrons: these electrons produce spherical waves that are emitted in every direction after the scatter event. The scattered waves have the same wavelength of the incoming beam (there is therefore no change in X-Rays energy) and only different direction:

Figure 53: SEM system at I.N.Ri.M.. Picture of the *Fei InspectF* SEM system present at I.N.Ri.M. laboratories.

hence X-Ray diffraction is a form of elastic scattering. Since spherical waves are diffused by each atom in the crystal, many of them are cancelled out in most directions because of destructive interference: nonetheless, there exist few specific directions for which the waves add constructively, giving rise to diffracted beams. It is possible to show, with a simple geometrical argument proposed by Bragg (see Figure 54 and [2, 84] for reference), that constructive interference can occur only when two conditions are satisfied: the incident wave is specularly reflected from parallel planes of atoms in the crystal and the path-length difference between rays reflected from adjacent planes spaced d apart is an integral number n the wavelength λ of the incident beam. The latter condition is summarized in the Bragg's Law $2d \sin\theta = n\lambda$, where λ is the wavelength of the incident X-Ray beam, $n \in \mathbb{N}$ is an integer, θ is the incident angle of the radiation (evaluated as the angle between the wave vector describing the incoming radiation and the crystal plane of interest) and d is the distance between diffracting parallel crystal planes. In the directions identified by the Bragg's Law, the diffracted beam has higher intensity and appear clearly as spots of a diffraction pattern. By measuring the intensities and the angles of the diffracted beams with an XRD system, it is possible to produce a picture of the density of electrons within the crystal. From the density of electrons, the mean positions of the atoms in the crystal, as well as their chemical bonds and disorder can be determined: the crystal structure can be therefore fully reconstructed with this kind of technique. XRD can be used not only for the investigation of the crystal structure of bulk materials, but also with crystal powders or even thin films: in this cases special configurations of the XRD system must be employed in order to get a correct result about the crystal structure of the material under study.

The XRD system present at I.N.Ri.M., a *PanAnalytical X' Pert Pro MPD*, is shown in Figure 55a. X-Ray waves are produced by the Kα spectral line radiation of Co (corresponding to the transition from the L -$n = 2$- energy

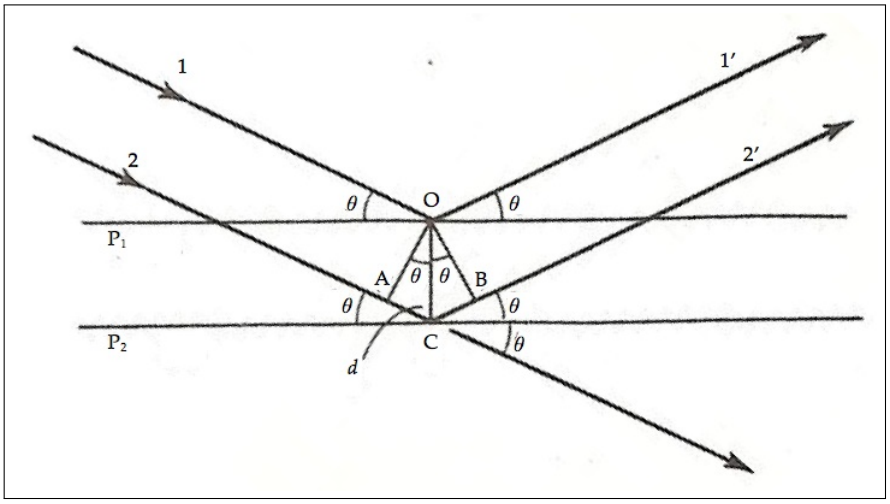

Figure 54: Geometrical derivation of the Bragg's Law. Schematic view of X-Ray diffraction in a crystal. The parallel incoming waves 1 and 2 of the X-Ray beam scatter a periodic arrays of atoms with incident angle θ and are diffused as spherical waves. Assuming the atoms (i.e. the scatterers) are arranged in parallel planes (P_1, P_2) spaced d apart, the diffused rays $1'$, $2'$ are in constructive interference conditions only in those directions for which the path-length difference AC+CB = $2d \sin\theta$ between $1 - 1'$ and $2 - 2'$ waves is equal to $n\lambda$. In that case part of the incoming radiation is deflected by an angle 2θ, being therefore reflected, and a reflection spot appears in the diffraction pattern. The diffraction condition, taking the form of Bragg's Law in real space, can be formulated equivalently also in reciprocal space, as $\Delta\mathbf{k} \cdot \mathbf{R} = 2\pi n$, where $\Delta\mathbf{k}$ is the difference between the incoming and the outgoing wave vectors associated to incident and diffracted X-rays (since the scattering is elastic, the two wave vectors have same aptitude and differ only in direction), $\mathbf{R}$ is a generic lattice vector and $n \in \mathbb{N}$ is an integer: therefore, to have constructive interference $\Delta\mathbf{k}$ must be a reciprocal lattice vector.

level to the atomic ground state) and the system works only in reflection mode. Measurements can be performed in two different optical configurations: when dealing with bulk materials, the crystal is fixed on the sample-holder and both the X-Ray beam and the detector rotate around it in order to get its diffraction pattern. When dealing instead with thin films (as in my case), the X-Ray incident angle is kept fixed and only the detector is free to rotate around the sample (Figure 55b): the system is said to work in pseudo-parallel beam optics. In this configuration the detector rotation's angle θ ranges from 0° to 80° (although, for historical reasons, the directions of diffracted beams are given in terms of the deflection angle 2θ instead of θ). In my measurements the X-Ray incident angle has been set-up to $\Omega = 0.8°$. X-Ray measurements have been performed with the help of Dr. E. Olivetti.

2.2 EVAPORATION OF CU THIN FILMS: PROCESSES AND RESULTS

I can now show the results I have obtained about the thermal and e-beam physical vapour depositions of Cu thin films of different thickness on different substrates, carried out in different experimental configurations.

2.2.1 Cu films by thermal physical vapour deposition

I start by presenting the results obtained with the thermal evaporator. As already pointed out in Sec. 2.1.1, thermal depositions took a lot of time (since the growth rate can never exceed $2\,\text{Å}\,\text{s}^{-1}$, otherwise the pressure in the evaporation chamber becomes too high and too many impurities are deposited on the film) and produced films of very poor quality: they have been therefore soon abandoned in favour of the e-beam evaporations[1]. Nonetheless, exactly because of the very low growth rate, thermal depositions supplied useful insights about the kind of film growth undergone by Cu on Si substrates. These informations may be useful in understanding how to improve the uniformity and reduce the polycrystalline nature of Cu thin films grown by physical vapour techniques. I did not arrive yet to a final conclusion about such an improvement, but I had clear results about which kind of growth is involved during Cu deposition on Si substrates.

It is generally accepted that there are three main modes of crystal growth governing the nucleation of thin films: the island or Volmer-Weber mode, the layer or Frank-van der Merwe mode and the layer plus island or Stranski-Krastanov mode. These growth modes, shown in Figure 56, distinguish among different forms of atomic adsorption occurring on the substrate. In the Volmer-Weber mode small clusters are nucleated directly on the substrate surface and then grow into islands of the condensed phase: this happens because absorbed atoms are more strongly bound to each other than to the substrate. Therefore, from a thermodynamic point of view, in this case the concentration of adsorbed atoms on the deposition surface is often very low, due to fast re-evaporation from the weakly binding substrate, and supersaturation conditions are needed to nucleate the deposit. Therefore, diffusion of the adsorbed atoms on the substrate surface (needed for the

1 I have to point out here that in any case the technical set-up of the e-beam evaporator lasted quite a long time because of some difficulties arisen during the system assembling and during the first trial depositions: in the meanwhile, thermal evaporations continued to be carried out.

(a)

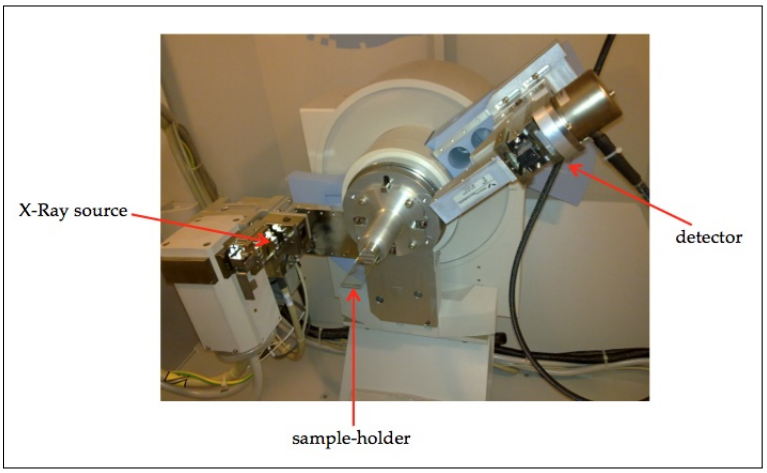

(b)

Figure 55: XRD system at I.N.Ri.M.. Picture of the XRD instrumentation present at I.N.Ri.M.: (a) external view of the whole instrument; (b) detailed view of the inner chamber when working in pseudo-parallel beam optics (the right configuration for studies on thin films), with the description of the components of the system. In this configuration only the detector is rotating around the crystal (fixed on the sample-holder), while the X-Ray source is kept fixed at a certain incident angle (in my case $\Omega = 0.8°$).

growth of a uniform and almost monocrystalline film) is a process highly unfavourable in this case. This mode is displayed by many systems of metals growing on insulators. In the Frank-van der Merwe mode the opposite occurs: since the atoms of the deposit are more strongly bound to the substrate than to each other, first atoms to condense form a complete continuous monolayer completely covering the surface. The first layer is then covered by a somewhat less tightly bound second layer and so on. Providing the decrease in binding is monotonic, toward the value for a bulk crystal of the deposit, the layer growth mode is obtained. In this case the concentration of adsorbed species on the surface is enough to guarantee that first two-dimensional layer growth can exist in undersaturation conditions: layer growth is allowed because in this case the diffusion of the atoms of the deposit on the surface is favoured by the strong adhesive force between film and substrate. This mode is typical of semiconductor growing on semiconductors, in the case of absorbed gases and in some metal-metal systems. The Stranski-Krastanov mode is finally an intermediate case between the other two modes. After forming the first monolayer or few monolayers, subsequent growth is unfavorable and islands are formed on top of this intermediate layer. There are many possible reasons for this mode to occur and almost any factor which disturbs the monotonic decrease in binding energy (characteristic of the layer growth) may be the cause. In this case beyond finite coverage θ island growth is thermodynamically favoured. This mode occurs in metal-metal, metal-semiconductor, gas-metal and gas-layer compound systems.
It is clear, in general, that film growth and nucleation mode depends on two competing effects: the adhesive force (i.e. the binding energy) between the adsorbed atoms and the substrate, favouring atoms diffusion and layer growth, and the cohesive force (i.e. the surface tension energy) between the atoms of the deposited material, favouring instead a re-evaporation of adsorbed species and an island growth. Moreover, a uniform and regular crystalline growth of a film occurs more likely if the adsorption rate of deposited atoms is low enough to allow the atoms already adsorbed on the surface to diffuse and find the minimum energy (hence the most favourable) configuration.

The individual atomic processes responsible for crystal and film growth on surfaces are illustrated in Figure 57. Each of these processes is characterized by a specific activation energy and a frequency factor. From the thermodynamical point of view, film growth is based on a non-equilibrium process. Indeed, in equilibrium conditions all the processes in Figure 57 proceed in opposite direction at equal rates. Hence, for example, in equilibrium adsorption condensation and re-evaporation processes would be in detailed balance, with the result that no net film growth would occur: the macroscopic parameter θ, describing the coverage of the substrate surface by layers of the deposited material, would be constant. In such conditions, the system would be properly described by unchanging macroscopic variables, although at microscopic level it is continuously changing through the various surface processes shown in Figure 57. Therefore, in order to occur, film growth must be a non-equilibrium kinetic process and the final macroscopic state of the system depends on the route taken through the various reaction paths of Figure 57. The state obtained is not necessarily the most stable one, but it is kinetically determined. A more detailed explanation of the physical processes governing crystal growth is beyond the scope of this thesis; a comprehensive treatment of the subject can be found in the great

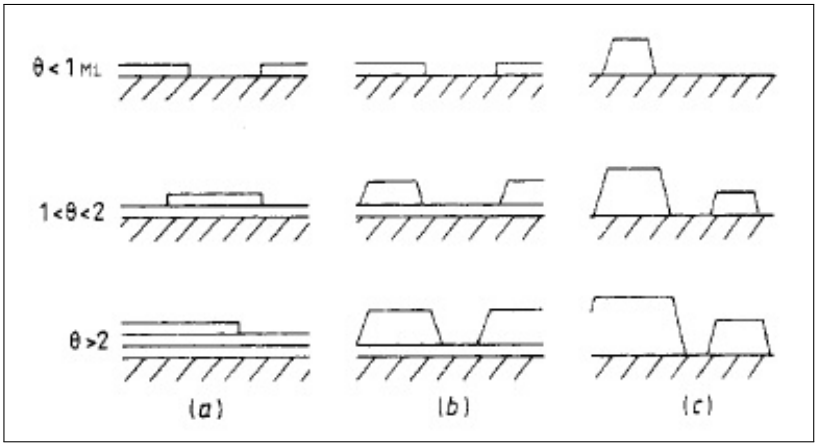

Figure 56: Thin film growth modes. Schematic view of the three generally accepted modes governing adsorption and crystal growth of thin films and bulk materials on a substrate (the parameter θ represents here the coverage of the substrate surface): (a) the layer or Frank-van der Merwe mode, characterized by a uniform coverage of the substrate surface; (b) the island plus layer or Stranski-Krastanov mode, characterized by a mixing of the other two growth modes; (c) the island or Volmer-Weber mode, characterized by nucleation and formation of small clusters coalescing in higher islands, producing a polycrystalline coverage of the substrate surface. Adapted from [188].

reviews [45, 60, 175, 188] and in the references therein. The few notions I have reminded on the subject are enough for a right interpretation of the results I have obtained.

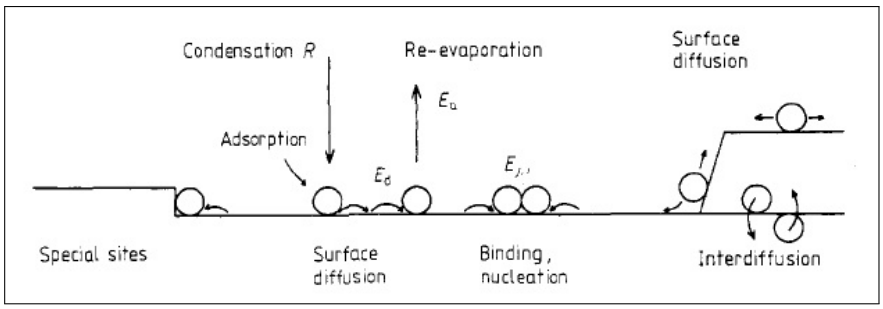

Figure 57: Processes governing thin films growth. Schematic diagram of the processes occurring at atomic scale during nucleation and growth of thin films on a surface. Final formation of the films depends on the activation energies and characteristic times of each process. Adapted from [188].

In order to investigate film growth, Si substrates presenting two different crystallographic orientations, namely $\langle 100 \rangle$ and $\langle 111 \rangle$, have been used. The substrates have been first of all cleaned in HF solution in order to remove the native oxide present on them and then subjected to thermal evaporation processes carried out varying the growth parameters. The main results can be summarized as follows (a more detailed description of the various depositions performed and of the results obtained can be found in [53]):

1. **Cu on Si$\langle 100 \rangle$:** first processes has been performed on Si$\langle 100 \rangle$ substrates and SEM images of the structures obtained are illustrated in Figure 58. Growth parameters, referring to the results of Figure 58,

have been chosen as follows (from here on, d_{Cu} refers to the thickness of deposited Cu, as indicated by the thickness monitor of the thermal evaporator):

- $T_{substrate} = 600\,°C$;
- growth rate = $2\,Å\,s^{-1}$;
- $d_{Cu} = 0.5\,nm$.

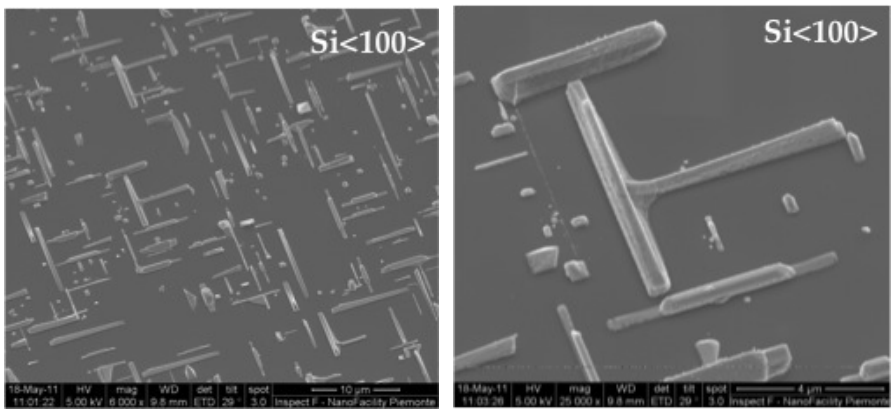

(a) (b)

Figure 58: Thermal evaporation of Cu on Si⟨100⟩. SEM images of Si⟨100⟩ surface after thermal evaporation of 0.5 nm of Cu. Formation of Cu crystal domains (of $\sim$ 5–10 µm in lateral size) along the preferential crystallographic orientation ⟨100⟩ of the underlying Si substrate is clearly visible.

I have performed also other depositions on this kind of substrate, by lowering the growth rate and the final film thickness, obtaining the same results: we can conclude therefore that these parameters do not seemingly influence the growth mode of Cu films;

2. **Cu on Si⟨111⟩:** a second set of evaporations have been performed on Si⟨111⟩ substrates and SEM images of the typical structures obtained are shown in Figure 59. The change of the Si substrate was meant to confirm that Cu films grow following the crystallographic orientation of the underlying crystalline surface. Growth parameters for the process of Figure 59 are as follows (it is worth noting that the growth rate has been in this case appreciably lowered in order to reduce the deposition of undesired impurities on the Cu film):

   - $T_{substrate} = 600\,°C$;
   - growth rate = $0.5\,Å\,s^{-1}$;
   - $d_{Cu} = 20\,nm$.

   Other processes have been performed by varying the Si substrate temperature and the final Cu film thickness, in order to investigate how these parameters influence the kinetics of the film growth process.
   In one process the Si substrate has not been heated at all (so, $T_{substrate} = 27\,°C$, the room temperature) and this choice resulted (as shown in Figure 60) in a reduced mobility and diffusion of Cu atoms on the Si surface: hence, as expected, Cu atoms were able to organize themselves only in very small crystal domains, much smaller than in the previous cases. On the other hand, I must point out that a too high substrate

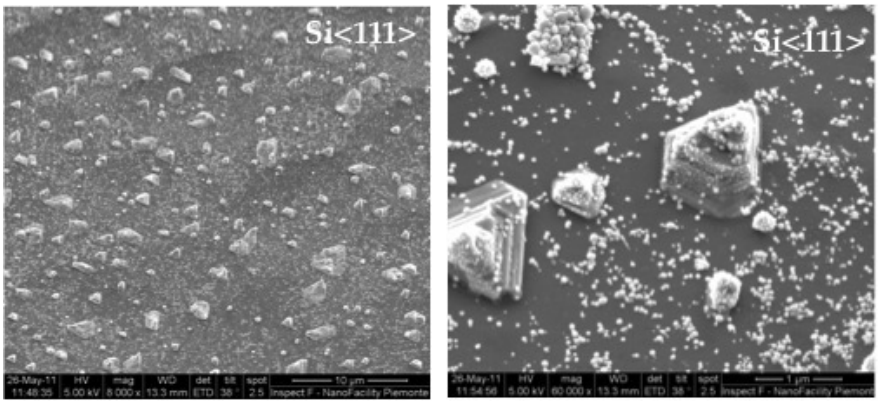

(a) (b)

Figure 59: Thermal evaporation of Cu on Si⟨111⟩. SEM images of Si⟨111⟩ surface after thermal evaporation of 20 nm of Cu. Again, formation of Cu crystal pyramidal domains (of $\sim 1\,\mu$m in lateral size) following the preferential crystallographic orientation ⟨111⟩ of the underlying Si surface is clearly visible.

temperature can result in a higher contamination of the Cu film due to deposition of impurities: therefore, a compromise between a low substrate temperature allowing only for an amorphous, rather than a crystal, film growth and an high substrate temperature, resulting in contamination of the film, must be found.

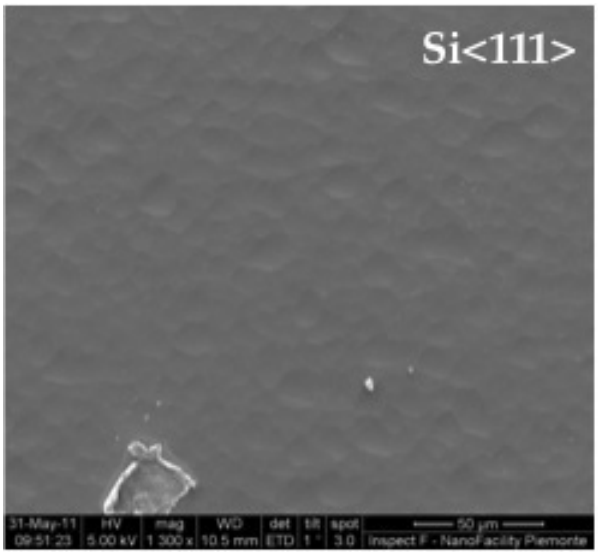

Figure 60: Thermal evaporation of Cu on Si⟨111⟩ at room temperature. SEM image of Si⟨111⟩ surface after thermal evaporation of 30 nm of Cu: deposition has been performed without heating the Si substrate and therefore only initial stage of nucleation of small crystal domains can occur.

Another process has been carried out by increasing the Cu film thickness to $d_{Cu} = 68.4$ nm. As expected, in this case film growth proceeds faster and it is possible to notice, in Figure 61, that pyramidal crystal structures have higher sizes with respect to those illustrated in Fig-

ure 59 and coalescence processes bringing to the formation of small clusters are visible.

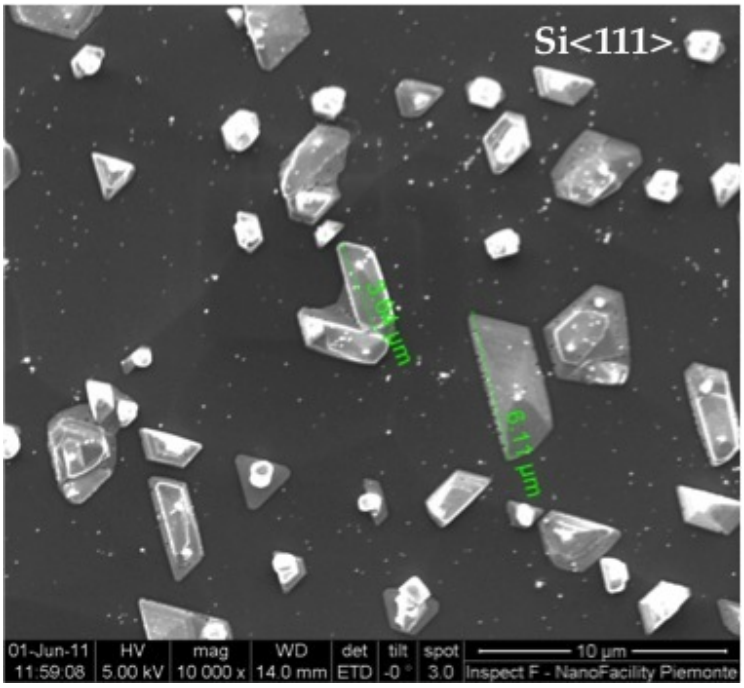

Figure 61: Effect of film thickness on the thermal evaporation of Cu on Si⟨111⟩. SEM image of Si⟨111⟩ surface after thermal evaporation of 68.4 nm of Cu: the mean lateral size of the pyramidal structures is $\sim 6\,\mu m$, much higher than in the case of a thinner film.

We can conclude from the processes on the Si⟨111⟩ substrates that the kinetics of Cu film growth is highly influenced by the initial temperature of the underlying substrate surface (an higher temperature resulting in a more favourable nucleation of deposited Cu atoms in crystal domains) and by the final thickness of the film (an higher thickness allowing for a faster nucleation of islands in clusters).

From the results shown above we can conclude that Cu films grow on Si substrates clearly according to the Volmer-Weber mode: therefore, islands formation occur before a complete layer of Cu, covering the whole Si surface, is grown. As a consequence, the final Cu film will be characterized by an undesired polycrystalline nature caused by islands coalescence: the film surface will show many grains with different crystallographic orientations and many associated grain boundaries. This kind of growth is due to the weak adhesive force between Cu and Si, favouring the nucleation of Cu small clusters positioned randomly on the substrate surface instead of the diffusion of Cu adsorbed atoms on the surface. The weak binding between Cu and Si will be once more confirmed by the dewetting effect, occurring at high temperature on Cu samples deposited onto Si, that I will discuss in Sec. 2.3): the weak adhesive forces between the two materials, together with the polycrystalline nature of the Cu films, are indeed the reasons why this phenomenon occurs.
The presence of grain boundaries on Cu films is highly deprecated because of the bad effect they have on the properties of CVD graphene grown on them, as I will more extensively discuss in Sec. 2.2.3.

A way to grow monocrystalline Cu thin films is therefore needed and in the same section I will present a possible route to achieve this goal, by using a Si⟨110⟩ substrate to start with for the EBPVD process.

In any case, I have to point out that, as I have experienced and I will discuss in detail in Sec. 2.3 and in Sec. 3.3.2, Cu films deposited directly on Si substrates (without SiO_2 insulating layers in between) are unfortunately not suitable to be directly used in CVD processes: indeed, either they dewet from the underlying surface or they melt together with Si substrate (the reason why this latter fact occurs is described in Sec. 2.2.3). In particular, the latter experimental evidence explains why Cu directly deposited onto Si presents major problems when undergoing CVD processes. Therefore, in what follows, Cu films have not been deposited anymore on Si substrates, but rather on insulating SiO_2/Si substrates. However, thermal evaporation processes performed directly on Si surfaces have been interesting because they provided useful insights about the Cu growth mechanism.

2.2.2 Cu films by EBPVD

I report now the results I have obtained about EBPVD of Cu thin films. As already pointed out at the end of the previous section, e-beam evaporations have been carried out using only insulating SiO_2/Si substrates (with oxide thickness of $\sim 300\,nm$ and p-type ⟨100⟩ oriented Si) to avoid problems of Cu-Si melting during the CVD processes. A detailed investigation of film growth mechanism has been avoided, since in this case I aimed to deposit thicker films with respect to the thermal evaporation case. However, the details about the mechanisms governing film growth had already been acquired during thermal evaporation processes.

SiO_2/Si substrates subjected to EBPVD have been first of all carefully cleaned in acetone and isopropanol and then properly cut with a diamond tip and mounted on the e-beam evaporator sample-holder with the configuration shown in Figure 62: in this way it has been possible to deposit thin films on more than one sample within a single evaporation process.

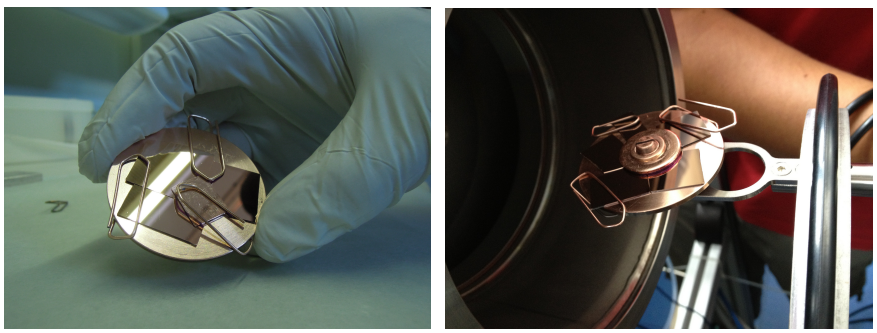

(a) (b)

Figure 62: Sample-holder configuration for EBPVD processes. Picture showing the sample-holder configuration employed for e-beam evaporation processes: (a) detailed view of the configuration used, allowing the deposition of thin films on more samples in a single process; (b) the sample-holder mounted on the e-beam evaporator pliers and ready for loading in the evaporation chamber.

Commercially available pellets-shaped-Cu (*TESTBOURNE LTD.*, diameter 3 mm × length 3 mm, 99.9999% pure), to be used as source material in evaporation processes, have been also cleaned in acetone and isopropanol and then put into a Mo crucible (Figure 63): Mo crucibles, contrary to other kinds of crucibles, allow indeed (as reported in many technical manuals) for a better control of the Cu film growth rate during the deposition, avoiding in particular electrostatic discharges (caused by electric charge accumulation on crucible edges) resulting in undesired spikes during Cu emission.

Figure 63: Mo crucible for EBPVD of Cu thin films. Picture of the crucible used for the deposition of Cu thin films: Cu, shaped in small pellets, is put inside the crucible after a careful cleaning process.

The deposition processes I have performed can be divided into three main categories[2]:

1. **EBPVD of Cu films**
   The greatest number of depositions regarded the evaporation of Cu thin films of various thicknesses (ranging from 200 nm to 500 nm) used mainly to study CVD growth of graphene on Cu catalytic substrates showing different properties, but later employed also for dewetting studies. The electron gun (e-gun) system at work during a typical Cu evaporation process is shown in Figure 64.

   The typical values of the growth parameters I have worked with during Cu EBPVD are the following:

   - $p_{\text{base}} \sim 10^{-7}$–$5 \times 10^{-8}$ mbar;
   - $p_{\text{chamber}} \sim 10^{-5}$–$10^{-6}$ mbar;
   - growth rate $\sim$ 1.4–1.7 Å s^{-1}

   where I remind that p_{base} and p_{chamber} are the values of the pressure in the evaporation chamber as measured by the ionization gauge before and during the deposition respectively. Growth rates have been intentionally kept quite low, in order to increase the final quality of the film. Some SEM images of the deposited films (characterized by

2 It is worth making a comment about the e-beam evaporations I have performed: some problems I initially had with the High Voltage generator, especially with current screening, caused many troubles and resulted in a delay of all the work. However, in the last months I succeeded in optimizing the performances of the instrument, thus solving the initial problems and being able to carry out much more deposition processes than at the beginning.

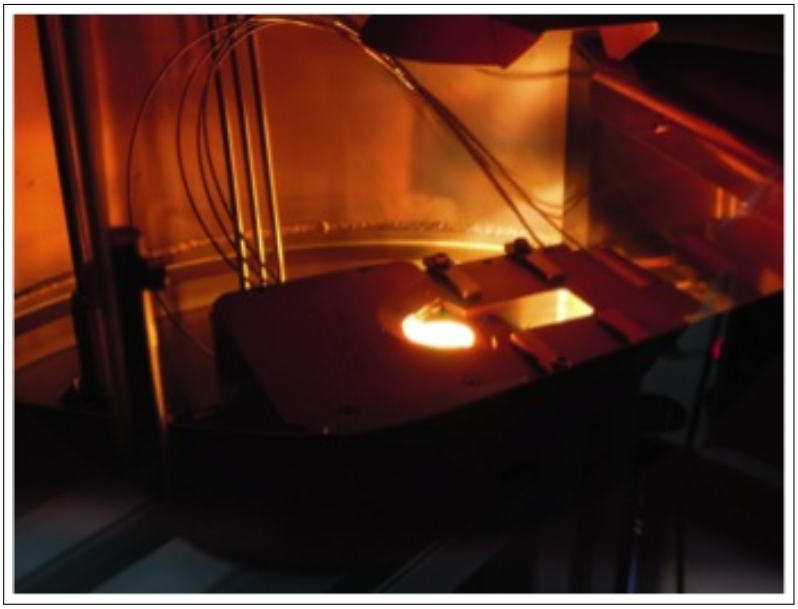

Figure 64: E-gun system during Cu evaporation processes. Picture showing the e-gun (containing the tungsten filament giving off the electron beam) and the crucible containing Cu during a typical EBPVD process.

thicknesses $d_{Cu} = 200\,nm$ and $d_{Cu} = 500\,nm$ -for other thicknesses the images are similar) are shown in Figure 65.

It is clear from Figure 65 that Cu films show again a polycrystalline surface, characterized by grains of sub-micrometre size (typical sizes range from $\sim 70\,nm$ to $\sim 130\,nm$): this fact means that Cu growth proceeds also in this case following the Volmer-Weber mode, as already occured for thermal evaporation depositions. Moreover, the small grains size suggests that, before undergoing a CVD graphene synthesis process, Cu substrates must be subjected to an annealing process in order to increase the mean dimension of the grains. To further investigate the polycrystalline nature of Cu samples, a 500 nm film has been subjected also to XRD analysis (the details about this technique, the intrumentation present at I.N.Ri.M. and its experimental set-up for the case of Cu thin films measurements are found in Sec. 2.1.3), bringing to the spectrum shown in Figure 66.

The spectrum shows that there are two preferential growth directions: $\langle 111 \rangle$ and $\langle 220 \rangle$, with the former having higher intensity than the latter. This is an interesting result because, as already pointed out at the end of Sec. 2.2.1, Cu$\langle 111 \rangle$ substrate should guarantee a good final quality of graphene layers grown by CVD on it. The real problem is that, as I will report in Sec. 3.3.3, the CVD process usually changes the crystallographic orientations of the grains and their relative intensities: such a change would be avoided only by starting with a monocrystalline Cu surface, but my results show that Cu growth on SiO_2/Si substrates is not governed by a Frank-van der Merwe mechanism ensuring a uniform (monocrystalline) layer coverage.

Another proof of the grains structure of the Cu surface is given by the Scanning Tunneling Microscopy (STM) analysis that I could perform very recently on my samples. I analysed also in this case a 500 nm

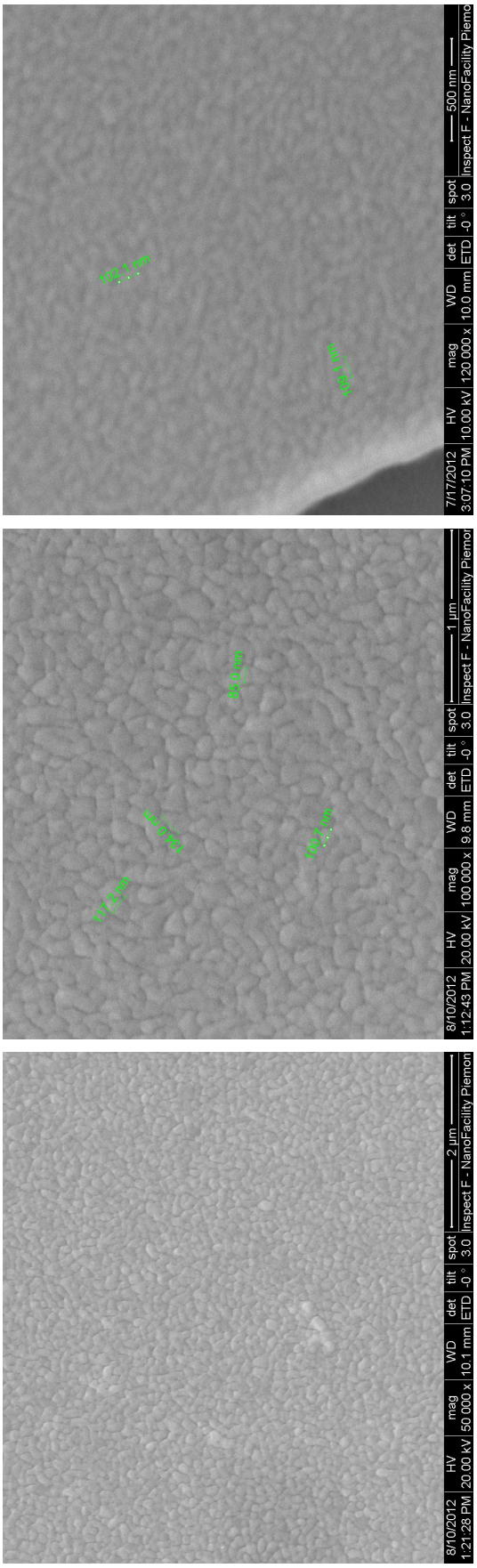

Figure 65: SEM images of pristine Cu films. Various SEM images showing how appears the Cu surface after EBPVD process: (a) for $d_{\mathrm{Cu}} = 500\,\mathrm{nm}$; (b) magnification of image (a), showing details about the typical size of the grains characterizing the surface; (c) for $d_{\mathrm{Cu}} = 200\,\mathrm{nm}$.

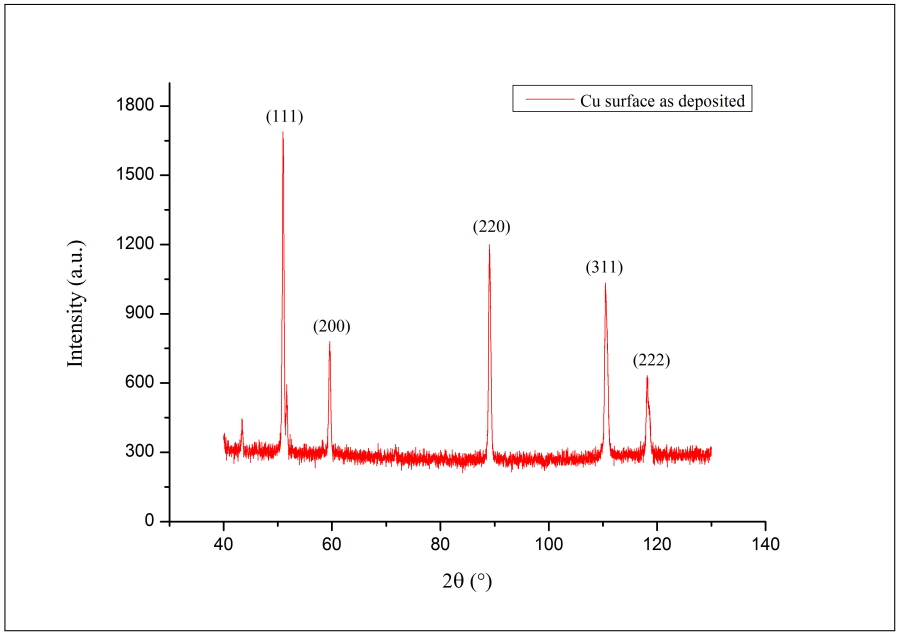

Figure 66: XRD analysis of the as deposited Cu surface. XRD spectrum illustrating the main crystallographic directions characterizing the crystal domains structure of the 500 nm thick Cu film shown in Figure 65a. The spectrum has been acquired with an incident angle $\Omega = 0.8°$.

thick Cu film, scanning a small region ($\sim 10^{-2}\,\mu m^2$) of its surface (the choice about the extension of the scanned surface is imposed by the long time needed for the scanning process) and obtaining the result illustrated in Figure 67.

From STM analysis a clear indication about the roughness of the Cu surface can be extrapolated: analysing the acquired data, a root mean square (RMS) roughness of ~ 2 nm has been obtained, although height variations as small as few angstroms have also been detected (as shown in Figure 67b). These results clearly show that a domed morphology characterizes the Cu films surface: this morphology is probably due to the islands coalescence processes occurring during the film growth and this is another indication that the island mechanism is governing the film deposition.

The main conclusion we can therefore extract from the analyses performed on Cu films after EBPVD processes is that the films fully cover the SiO_2/Si substrates, but they are again characterized by a polycrystalline nature, with grains average sizes of ~ 100 nm.

2. **EBPVD of Cu films on Cr buffer layers**
Other depositions has been performed with the aim of having a greater number of different samples to be employed in dewetting studies, for getting further insights about this phenomenon. For this reason evaporation processes in which very thin Cr buffer layers have been grown onto SiO_2/Si substrates before depositing Cu (250 nm and 500 nm thick) have been carried out. The aim of these depositions was to investigate the rôle played by Cr buffer layers intercalated between Cu and SiO_2 during heating processes at temperatures of $\sim 900\,°C$: in particular I was interested in understanding if Cr could enhance the adhesion

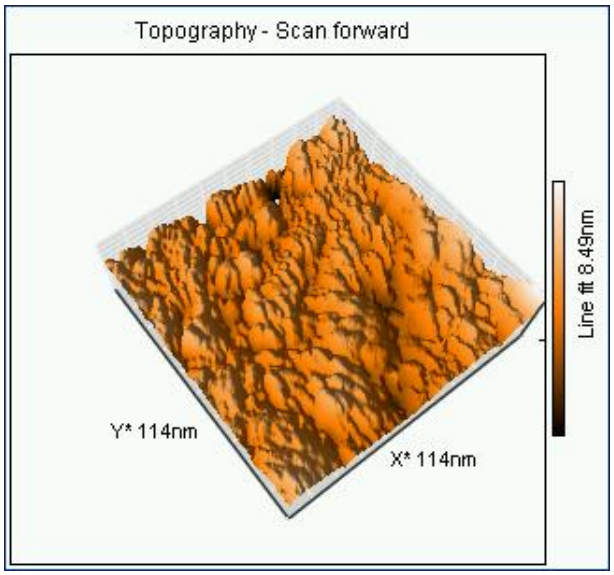

(a)

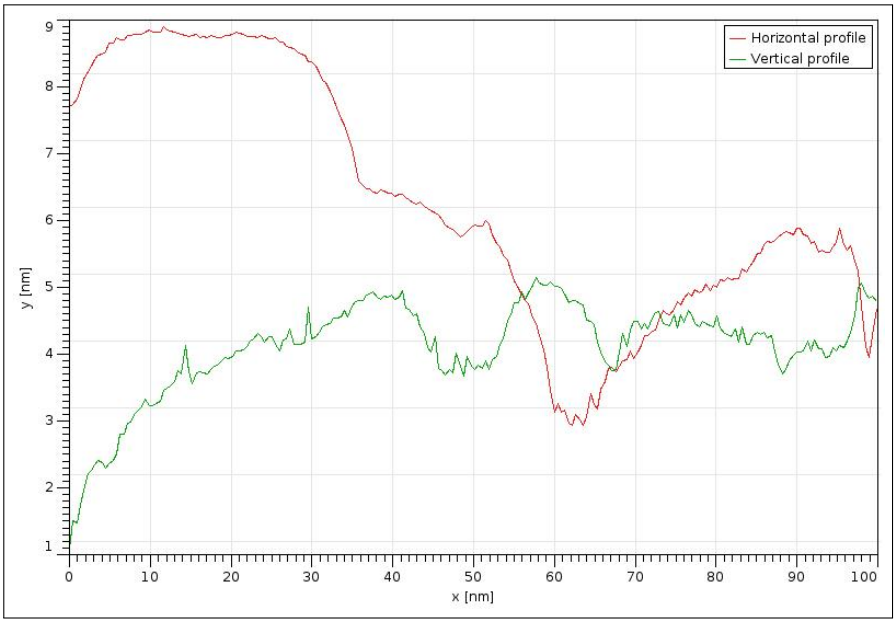

(b)

Figure 67: STM analysis and roughness of pristine Cu films. STM images of a 500 nm thick pristine Cu film: (a) 3D view of a small region ($\sim 10^{-2}\,\mu m^2$) of the sample scanned by the STM; (b) topographic behaviour along two different (randomly chosen) directions of the scanned Cu surface. The roughness of the surface can be clearly infered from the profiles.

of Cu films to the underlying surface, preventing dewetting effects at high temperatures. The Cr-Cu-SiO_2/Si samples have been therefore subjected only to the thermal cycles used for dewetting studies (described in Sec. 2.4) and not to full CVD thermal cycles. The growth parameters during Cu depositions have been set-up as described in the previous item, while for processes with Cr the parameters were as follows:

- $p_{base} \sim 10^{-7}$–5×10^{-8} mbar;
- $p_{chamber} \sim 10^{-6}$ mbar;
- growth rate ~ 0.3 Å s^{-1};
- $d_{Cr} \sim 13$ nm.

I can underline one interesting feature proper of Cr evaporations: the pressure in the evaporation chamber during deposition is in this case lower than in the case of Cu evaporations, because Cr atoms act as impurities getters, reducing therefore the number of free atoms -other than Cr- present in gaseous form in the chamber (however, the pressure is not lowered exactly at the beginning of the deposition, because initially the atoms of the evaporated material diffuse into the chamber in every direction, this way causing an increase of the pressure).

SEM images referring to a Cu-Cr-SiO_2/Si sample (with $d_{Cu} \sim 500$ nm and $d_{Cr} \sim 13$ nm) are shown in Figure 68.

Cu films show again a polycrystalline nature, with grains size similar to that of the Cu films directly deposited onto the SiO_2/Si substrates (i.e. ~ 100 nm). Hence, the presence of the Cr buffer layer, probably because of its extremely thin thickness, is not apparently changing and affecting the island mechanism governing Cu film growth. Moreover, I do not expect a change in the preferential crystallographic orientations of the Cu crystal domains with respect to the previous case (because Cr layer is very thin and probably its body-centered cubic -bcc- crystal structure cannot deeply affect the face-centered cubic -fcc- structure of Cu) but an XRD analysis of the samples would be necessary to investigate this fact.

3. **IBAD-EBPVD of Cu films**
Finally, very recently I have started performing IBAD-EBPVD processes. Up to now I have deposited only few Cu films (with thickness $d_{Cu} \sim 200$ nm) and I am still optimizing the deposition conditions (in particular the Ar gun parameters controlling the ions' acceleration voltage and the ion beam current) in order to get significant changes in Cu film morphology and adhesion to the SiO_2/Si substrate with respect to the standard (i.e. not IBAD) EBPVD. IBAD processes have been carried with the following conditions:

- $p_{base} \sim 10^{-7}$–5×10^{-8} mbar;
- $p_{chamber} \sim 3 \times 10^{-7}$ mbar;
- Cu growth rate ~ 1.4–1.7 Å s^{-1};
- $d_{Cu} \sim 200$ nm;
- $I_{emission} = 25$ mA;
- $V_{gun} = 1$ kV;
- $I_{ion\ beam} \sim 350$–450 µA

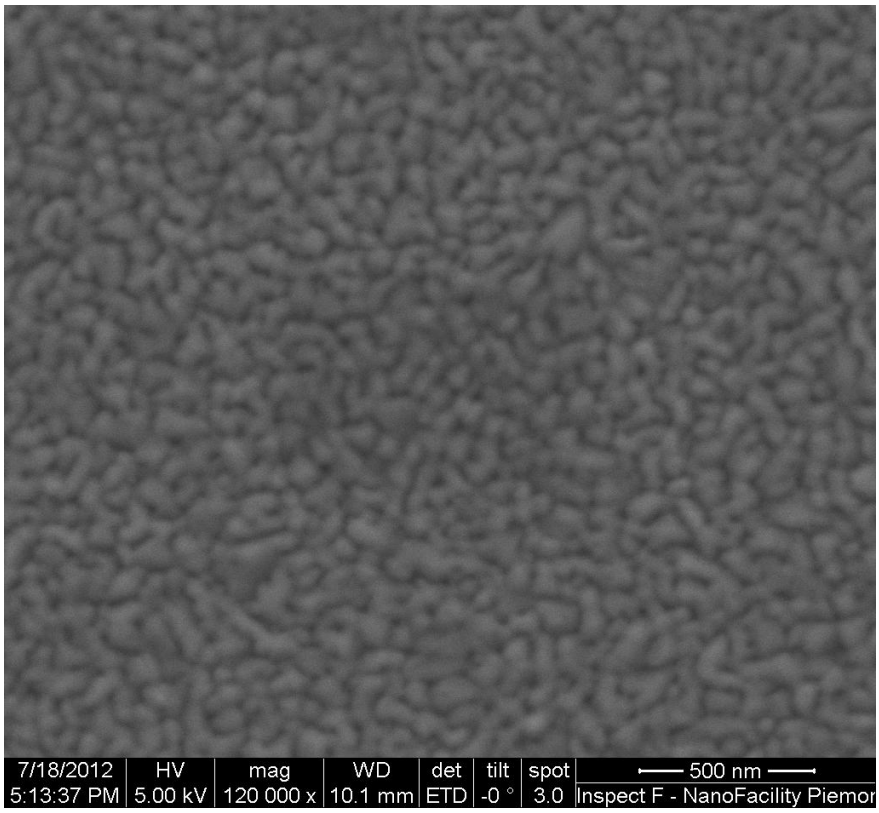

(a)

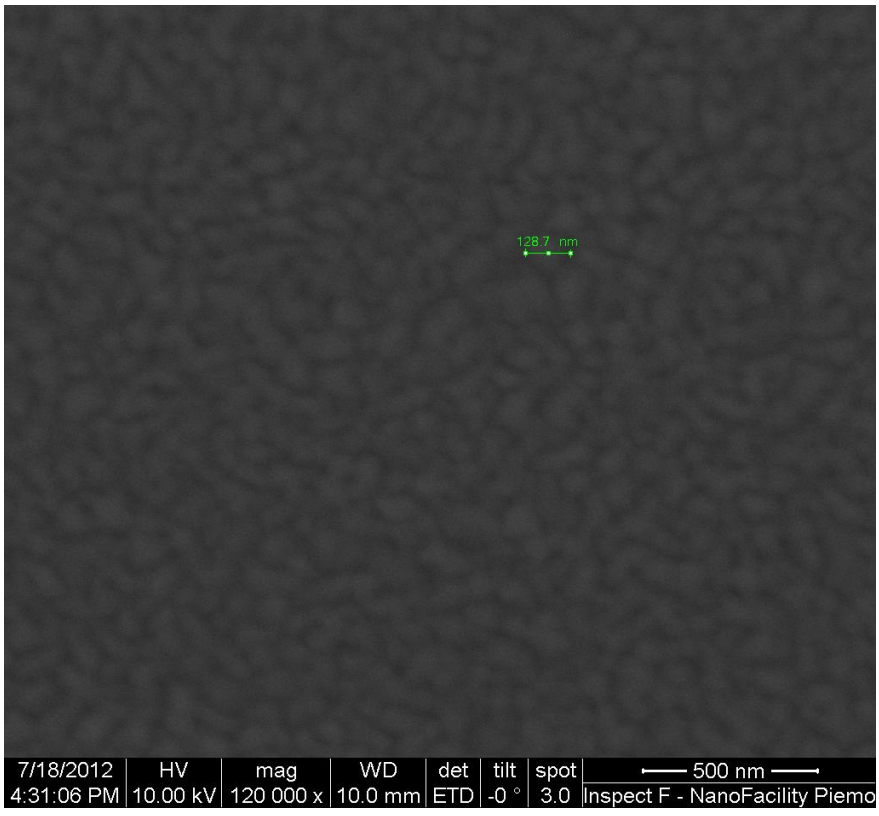

(b)

Figure 68: SEM images of pristine Cu films deposited on Cr buffer layers. SEM images showing a 500 nm thick Cu film deposited onto a $\sim$ 13 nm thick Cr buffer layer: (a) a region of the sample; (b) another region of the sample, showing details about the typical size of the grains characterizing the surface.

where $I_{emission}$ is the current charging the tungsten filament of the Ar^+ gun for thermionic emission of electrons, V_{gun} is the acceleration voltage of the Ar ions produced by ionization of Ar atoms through collisional events occurring with the emitted electrons and $I_{ion\ beam}$ is the current of the ion beam (as already explained in Sec. 2.1.1, ions are charged particles and so there is a current associated to their motion) once it enters the evaporation chamber.

SEM images of a Cu sample as obtained after an IBAD process are shown in Figure 69.

An important feature is evident by looking at Figure 69: the Cu surface is showing again a polycrystalline nature, as in the deposition processes described previously, but this time the grains size is much smaller than in the other cases. While for Cu films deposited with the standard EBPVD process the grains had a typical size of ~ 100 nm, in the case of IBAD processes the size of the domains characterizing the Cu surface is lowered to $\sim$ 40–50 nm. A detailed theoretical analysis of the IBAD process and a quantitative estimation of the effect that Ar-Cu collisional events have on the film growth process is still underway and therefore a clear explanation about the decrease in grains size is still missing.

The main conclusion we can extract from all the EBPVD processes I have here described is therefore about the polycrystalline nature shown by the Cu deposited films, due to a Volmer-Weber growth mechanism implying islands coalescence processes and nanocrystal domains formation: the same growth mode was already observed in thermal evaporation processes, as pointed out in Sec. 2.2.1.

2.2.3 Conclusions

From the results obtained about thermal and EBPVD evaporations of Cu onto SiO_2/Si substrates, we can conclude that the films grow according to the island Volmer-Weber growth mode, implying the formation of many crystal domains ($\sim$ 100nm in size in the case of EBPVD processes) oriented along different crystallographic directions: this fact is due to the amorphous nature of SiO_2, not allowing a monocrystalline crystal growth. The polycrystalline nature this way characterizing Cu films and the presence of grain boundaries is highly deprecated because of the bad effect they have on the properties of CVD graphene eventually grown on them. Intuitively it is clear that graphene will grow on Cu following as much as possible the crystal structure of the underlying surface: the presence of grain boundaries will be therefore reflected on graphene, representing a factor limiting the possibility of synthesize large size graphene flakes (i.e. graphene layers showing only one crystallographic orientation). Moreover, grain boundaries (representing crystal defects) present in graphene structure deeply worsen the great transport properties shown by this material. A detailed study of the worsening effects induced by grain boundaries eventually present on a catalytic substrate on the quality and transport properties of graphene grown by CVD has been reported in [63, 181]: the results clearly show how graphene transport properties are badly affected by a polycrystalline nature of the catalytic substrate, confirming this way the intuition.

Therefore, a monocrystalline growth of Cu films is highly desirable: a possible route towards the achievement of this result is represented by the

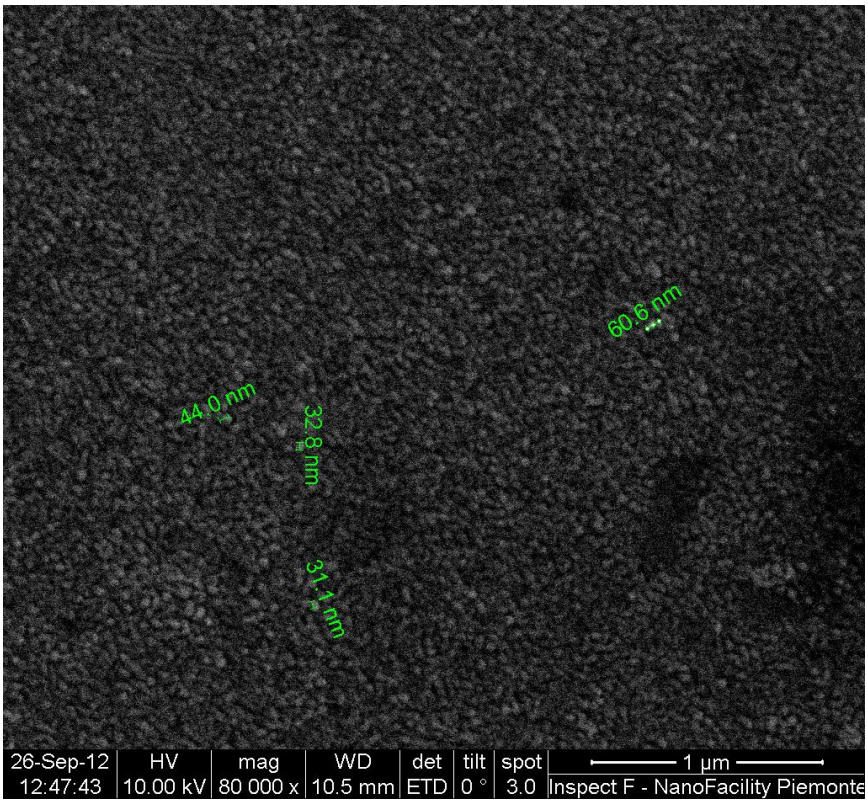

(a)

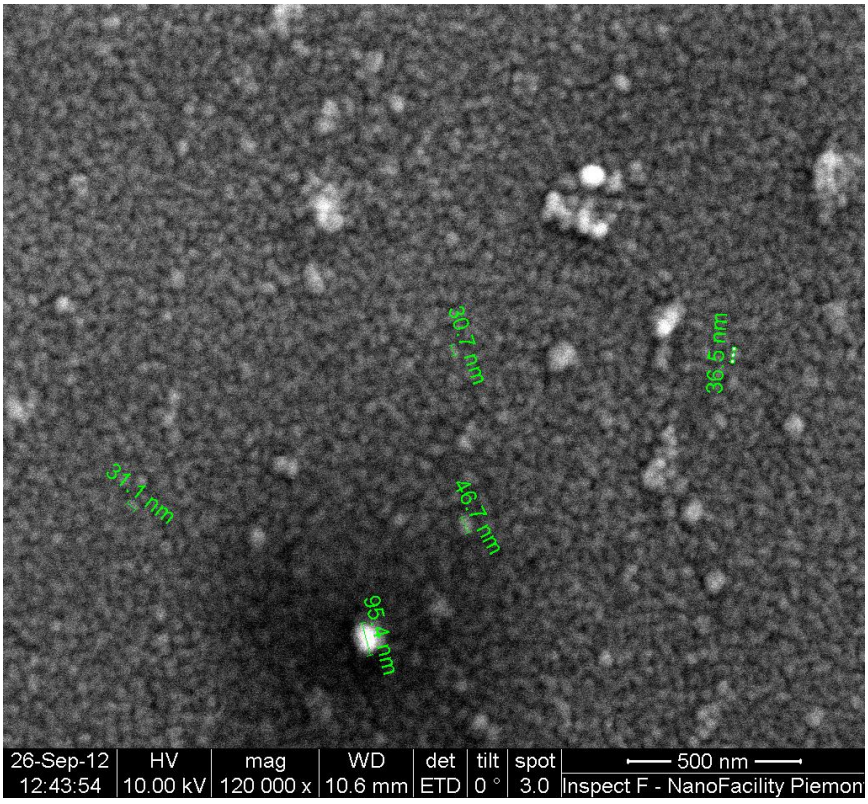

(b)

Figure 69: SEM images of Cu films deposited with IBAD technique. SEM images showing a 200 nm thick Cu film deposited onto a SiO_2/Si substrate with an IBAD-EBPVD process: (a) a region of the sample, showing details about the typical size of the grains characterizing the surface; (b) another region of the sample, showing grains of similar size.

employment of crystalline Si⟨110⟩ substrates. It has been indeed reported ([74]) that a ⟨110⟩ oriented Si surface induces a ⟨111⟩ preferential crystallographic direction for Cu films grown on them, avoiding the formation of undesired Cu grain boundaries, since in this case a layer Frank-van der Merwe growth mode is governing the film deposition process. Besides ensuring a monocrystalline Cu growth, this route is interesting because some studies performed by various research groups ([201, 205]) on graphene samples synthesized by CVD on Cu substrates having different crystallographic orientations have shown that graphene grows primarily in registry with Cu⟨100⟩ and Cu⟨111⟩ underlying lattices and, moreover, graphene properties are poorer on the Cu⟨100⟩ surface than on the Cu⟨111⟩ lattice (since on the latter graphene forms a microscopically uniform sheet, characterize by an hexagonal superstructures and presenting crystal grains as large as few µm, while on the former graphene shows exposed nanoscale edges and does not grow uniformly). Therefore, Cu deposition on Si⟨110⟩ should allow for growing catalytic films of the better crystallographic quality for subsequent graphene synthesis.

Very recently I have tested this route by evaporating a $d_{Cu} = 500\,nm$ thick Cu film onto a Si⟨110⟩ substrate: the results of the XRD analysis performed on the Cu surface after the EBPVD process clearly show, as expected, a completely different spectrum with respect to the one reported in Figure 66 (associated to an e-beam evaporated Cu film onto SiO_2/Si substrate), showing this time only the ⟨111⟩ crystallographic direction (Figure 70). Moreover, it is worth noting that EBPVD process has been performed at room temperature: therefore, a preferentially crystallographic oriented Cu growth can be obtained also without resorting to an independent Si substrate heating.

Nonetheless, a major problem arises at this point because Cu films deposited onto Si substrates without any oxide layer in between are unfortunately not suitable to be directly used in CVD processes. Indeed, either Cu undergoes dewetting if it is an enough thin film (as I will show in Sec. 2.3 this is a common problem of any Cu thin film) or it melts with the underlying Si substrate if it is a foil (meaning that $d_{Cu} \gtrsim 1\,mm$). Indeed, as I will describe in Sec. 3.3.2, the first CVD processes I have performed on Cu foils directly in contact with an underlying Si wafer substrate resulted in the melting of both the elements. This happens because Cu-Si samples subjected to thermal cycles at temperatures higher than $\sim 900\,°C$ form a stable solid mixed phase, melting together: this fact is evident by looking at the Cu-Si binary phase diagram (Figure 71). The diagram stresses that although Cu and Si, as separated species, have melting temperatures (respectively $T_{Cu} = 1085\,°C$ and $T_{Si} = 1414\,°C$ at ambient pressure) much higher than the temperatures reached in a typical CVD process ($T_{CVD} \lesssim 1000\,°C$), when put together they interact (with Cu that dissolves interstitially in Si) forming a stable solid mixed phase characterized by a melting temperature ranging between $\sim 800\,°C$ and $\sim 860\,°C$. More details about the Cu-Si binary system can be found in [139].

So, Si⟨110⟩ allows a monocrystalline Cu deposition, but the obtained samples are not feasible for undergoing CVD processes. A possible way out of this problem is represented by the use of a Si layer epitaxially grown on an underlying porous Si⟨110⟩ substrate, as starting material for Cu evaporation processes. Indeed, it has been reported long ago ([107]) that Molecular Beam Epitaxy (MBE) growth of Si on crystal porous Si should allow to keep the preferential crystallographic orientation of the underlying substrate also on the grown film. Because of the presence at I.N.Ri.M. laboratories of an MBE

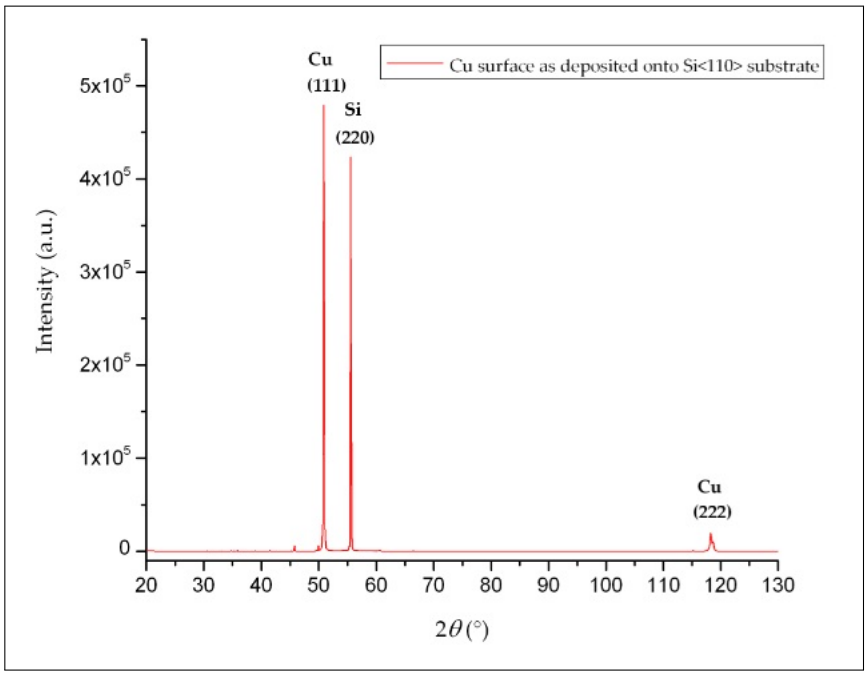

Figure 70: XRD analysis of a pristine Cu film e-beam evaporated onto crystalline Si⟨110⟩. XRD spectrum illustrating the main crystallographic directions characterizing the crystal domains structure of a 500 nm thick Cu film deposited by EBPVD onto a monocrystalline Si⟨110⟩ substrate. As expected, a predominant crystallographic orientation (⟨111⟩) characterizes the Cu surface (I remind that the ⟨222⟩ peak corresponds to a crystal plane identifying the same crystallographic direction of the ⟨111⟩ crystal plane -see for example [84] for details about the meaning of Miller indexes): the result is deeply different from what reported in Figure 66, related to Cu deposition onto an amorphous SiO_2 substrate not allowing a monocrystalline film growth. The ⟨220⟩ peak corresponding to the ⟨110⟩ crystallographic orientation of the Si substrate is also shown. The spectrum has been acquired with an incident angle $\Omega = 0.8°$.

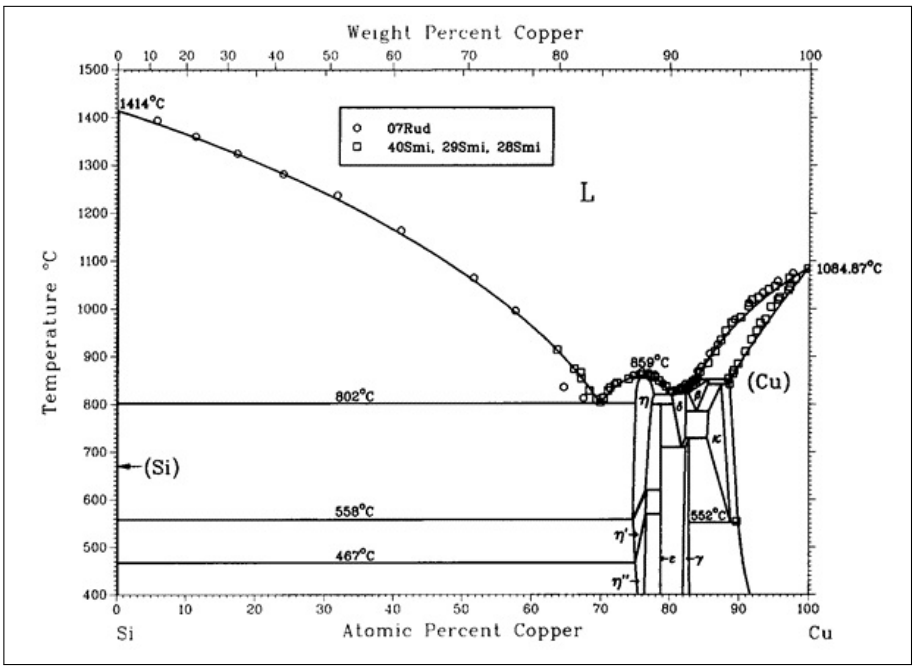

(a)

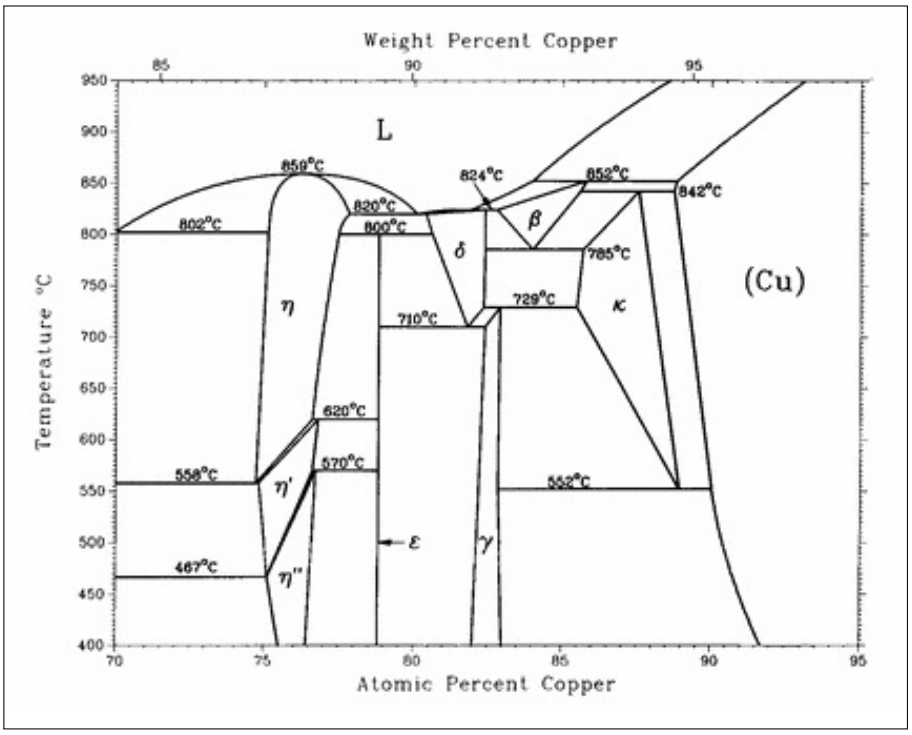

(b)

Figure 71: Cu-Si binary phase diagram. Illustration of the Cu-Si binary phase diagram: (a) when the concentration of Cu in the Cu-Si system is below a certain value ($\sim$ 85% of the total concentration), the two elements form a stable solid mixed phase with melting temperature drastically lowered with respect to the melting temperatures of the separated species; (b) enlarged view of the region of the diagram corresponding to Cu concentration ranging from 65% to 90%. Adapted from [139].

facility, I have planned to grow the needed Si⟨110⟩ surface directly onto a ⟨110⟩ porous Si substrate by homoepitaxy. Once I will obtain the Si layer to start with, I will deposit a Cu thin film on it by performing an usual EBPVD process. After growing the Cu⟨111⟩ desired catalyst for CVD processes, a Si oxidation process will be needed in order to avoid Cu-Si melting. Here comes the second and most important reason why employing porous Si as starting material of all the described process: indeed, porous Si, unlike crystalline standard Si, allows to perform the oxidation process also after Cu evaporation. Oxidation of porous Si is carried out at room temperature or even at lower temperatures by means of chemical or electrochemical techniques (for example by using boiling hydrogen peroxide) and the porosity of the material allows to prevent the Si expansion usually encountered in this process. At the end, I will come out with a Cu⟨111⟩ monocrystalline thin film, ideal for graphene growth by CVD, deposited on an insulating SiO_2 substrate allowing for thermal treatments at high temperatures without melting problems. I have planned to grow the first Si⟨110⟩ samples onto porous Si substrates in the near future, to check the feasibility of the method here described.

2.3 THE DEWETTING EFFECT: EXPERIMENTAL EVIDENCE

Once Cu catalytic thin films have been prepared, they have been subjected to CVD processes in order to (hopefully) grow graphene on them. However, a major problem immediately has arisen and appeared by looking at the SEM images of the samples after CVD processes: in most cases Cu droplets and wrinkles were present on the SiO_2/Si surface and no signature of graphene could be therefore found. Droplets formation, surely occurring during the CVD process, is due to the so called *dewetting* effect: this effect deeply affects the morphology of a deposited film, changing a full coverage of the underlying surface in a random distribution of drops (of the initially deposited material) on the surface (Figure 72). The origin of dewetting of Cu deposited on Si in quite complex and not completely clear yet: however, in general, it is certainly due to the fact that thin films deposition occurs usually under conditions for which atomic motion is highly limited and non equilibrium structures are obtained at the end of the deposition process. As a consequence, at room temperature most films are found in a metastable state: upon heating, since the mobility of the atoms constituting the film will be increased enough, they will spontaneously undergo a dewetting process forming isolated droplets and islands on the underlying substrate. This configuration will indeed correspond to a more favoured thermodynamic state, characterized by a decrease in the total energy of the system. It is worth noting that the dewetting effect proceeds with the material in the solid-state phase and usually no phase transitions occur during the process. Moreover, the analyses I have performed up to now about this phenomenon allowed me to conclude that the effect occurs when at least three conditions are satisfied:

- the adhesive forces between the evaporated material (Cu in my case) and the underlying surface (SiO_2/Si) become, at a certain temperature, weaker than the cohesive forces among the atoms of the evaporated

material itself (thus surface tension energy is higher than adhesion energy);

- the evaporated material is organized in crystal domains, thus having a polycrystalline structure;
- the deposited film is thin enough (let's say $d \lesssim 500\,\text{nm}$, where d is the film thickness).

A more detailed and exhaustive description of the dewetting effect and of the thermodynamic processes governing islands formation can be found in the great review [178].

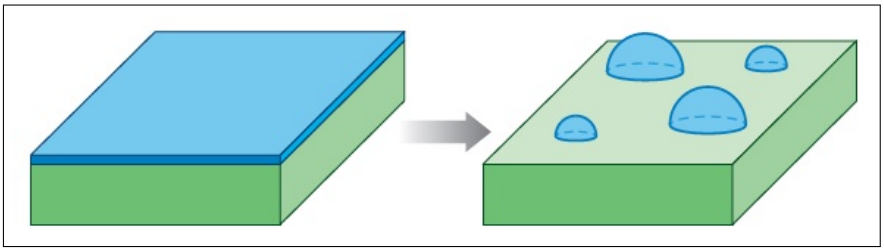

Figure 72: The dewetting effect: a schematic view. Schematic description of the dewetting effect occurring on thin films: the film, initially covering in a continuous way the underlying substrate, starts changing its morphology upon heating, forming isolated islands. The effect occurs with the material in the solid-state phase. Adapted from [178].

When dewetting occurs, no graphene growth can occur: therefore, having a technique allowing for a better control of this effect would be appreciable and would improve our knowledge about graphene synthesis by CVD over catalytic thin films.
Actually, by exploiting the properties of the RTA system present at I.N.Ri.M. and used for CVD processes, I have hopefully started the development of such a technique. Before discussing, in Sec. 2.4, the details about the technique and its underlying principles, a description of the RTA system and a presentation of the processes that provided a clear evidence of the dewetting effect are needed.

2.3.1 The RTA-CVD system

The RTA system present at I.N.Ri.M. laboratories (*Jipelec JetFIRST 100*) used for carrying out CVD processes is shown in Figure 73.
The system is composed by:

- a vacuum pumping system;
- a gas delivery system;
- a reactor chamber with heating halogen lamps.

The vacuum pumping system is formed by a mechanical and a turbomolecular vacuum pumps, allowing to reach HV conditions in the reaction chamber before thermal CVD processes ($p_{\text{react. cham.}} \sim 10^{-6}\,\text{mbar}$). Every CVD process I have performed (that will be described in detail in Chapter 3) has started therefore with a pre-vacuum step carried out at room temperature, aimed to remove as much as possible any impurity eventually

Figure 73: RTA system for CVD processes at I.N.Ri.M.. Picture of the system for graphene synthesis present at I.N.Ri.M. laboratories. The system is equipped with four gas lines and allows for fast cooling, being a cold-wall system: flash graphene growth processes can be therefore tested.

present in the reaction chamber. It is worth mentioning that during heating and during deposition steps (when gas is flowing in the reaction chamber) the turbo-molecular pump is not working (to avoid possible damages to it) and therefore HV conditions are not reached: the system in this case works only in Low Vacuum conditions. Typical pressure values measured in the reaction chamber during a CVD process are as follows:

- $p_{\text{react. cham.}} \sim 1.2 \times 10^{-2}$ mbar when no gas is flowing and the system is heated;
- $p_{\text{react. cham.}} \sim 1.28$–$1.65$ mbar in correspondence of 40 sccm of H_2 (and no CH_4) flowing in the system;
- $p_{\text{react. cham.}} \sim 3.3 \times 10^{-1}$ mbar in correspondence of 10 sccm of CH_4 (and no H_2) flowing in the system.

For what concerns the gas delivery system, the RTA is equipped with four gas lines (during CVD processes I have used three gas: H_2 during the heating and annealing steps in order to flatten the substrate surface, CH_4 as carbon precursor for graphene growth and N_2 for the after cooling purge of the system) controlled through mass flow meters (except for the N_2 gas line). The flow meters already mounted and automatically controlled by the system allow only to deal with gas flows ranging from 0 sccm (Standard Cubic Centimetre per Minute in Standard Ambient Temperature and Pressure Conditions, i.e. $p = 1$ bar $= 100$ kPa and $T = 25\,^{\circ}\text{C} = 298.15$ K) to 2000 sccm. Since during CH_4 delivery a finer control on gas flow is needed, a manually controlled flow meter on the CH_4 line has been added, allowing to change gas flow from 0 sccm to 50 sccm with a sensitivity of ~ 0.1 sccm. For better understanding, the modified gas delivery system now present in the RTA system is schematically illustrated in Figure 74.

Heating in the reaction chamber is provided, through a quartz window, by twelve halogen lamps placed above the sample-holder on which the sub-

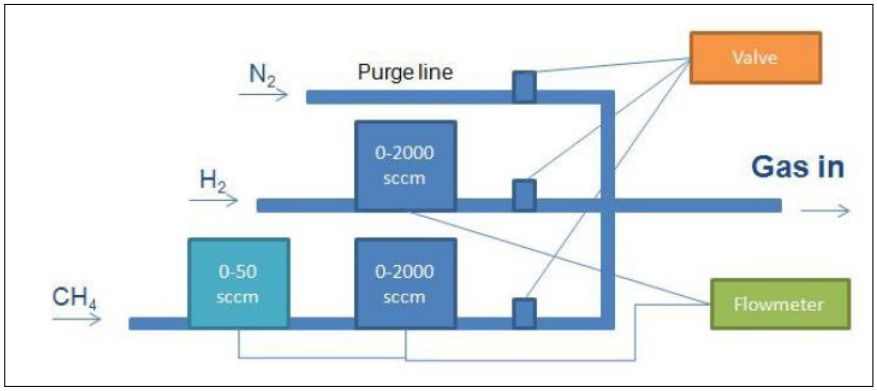

Figure 74: RTA gas delivery system. Schematic view of the gas delivery system present in the RTA: gas flow is controlled by four flow meters, one of them being mounted by us to reduce properly CH_4 flow.

strate subjected to CVD processes is positioned and allowing for a non-uniform heating on three different regions of the sample (center, front-rear and left-right). In any case I have never exploited this feature, always heating uniformly the samples subjected to CVD. Temperatures up to $T_{max} \sim 1300\,^{\circ}C$ are allowed. Moreover, being a cold-wall system characterized by a small heat capacity (because only the sample is heated during the process and not the all wall), fast cooling-down processes, up to $\sim 300\,^{\circ}C\,min^{-1}$, are also allowed (although I have never reached such an high value in my experiments). The power of the lamps is automatically changed by the system in order to allow a real-time matching between the desired temperature, set-up by the user, and the real temperature measured in the reaction chamber.
The most important technical feature of the system, for the purpose of dewetting studies, is exactly represented by the way the temperature of the sample is read by the instrument during a thermal process. The system is equipped with three thermocouples (allowing to check an eventual temperature gradient present across the sample-holder) and one pyrometer, all placed *on the back* of the sample-holder (I remind that the sample-holder is instead heated from above by the halogen lamps), as shown in Figure 75. While the thermocouples are directly in contact with the back of the sample-holder, the pyrometer detects the radiation coming from the sample through a small window ($\sim 25\,mm^2$) put in correspondence of the centre of the sample-holder. During my experiments I have always used only one thermocouple[3] and a 4" Si wafer as sample holder.

The pyrometer mounted in the RTA system (*IMPAC Infratherm IN 5/5*) at I.N.Ri.M. is an optical instrument (as every pyrometer) sensitive to the thermal radiation emitted at a certain absolute temperature T by a body having a certain emissivity ϵ_{system}. The emissivity ϵ_{system} is the ratio between the energy radiated by the particular material under investigation (in my case the surface of the sample subjected to the CVD process) and the energy radiated by a black body at the same temperature. As known, for a black body

3 I must point out that unfortunately I have experienced many troubles with the thermocouple initially mounted in the RTA system and after many tests I have been able to establish that it was underestimating the real temperature of the system of $\sim 150\,^{\circ}C$: therefore, some CVD processes have been carried with a nominal temperature, read by the thermocouple, much lower than the correct one. Recently I have changed the old thermocouple with a new one, giving correct values of the temperature. For each CVD process I will point out if the temperature reported is correct or not. However, dewetting studies have been performed with the new thermocouple, thus the reported temperature are correct.

$\epsilon_{bb} = 1$ for every wavelength λ of the electromagnetic spectrum, at any temperature T and in any directions (angle of view), while for a real object $0 < \epsilon_{system} < 1$ and, in general, $\epsilon_{system} = \epsilon_{system}(\lambda, T)$ (so that a real object usually emits different amounts of energy by electromagnetic radiation, at the same temperature, depending on the radiation wavelength). Moreover, the emissivity of a real object could also depend on its thickness and on the angle of view. In the case the emissivity of a real object, ϵ_{system}, is less than 1 but constant over all the electromagnetic spectrum and not depending on the angle of view, the object is called *grey body*.

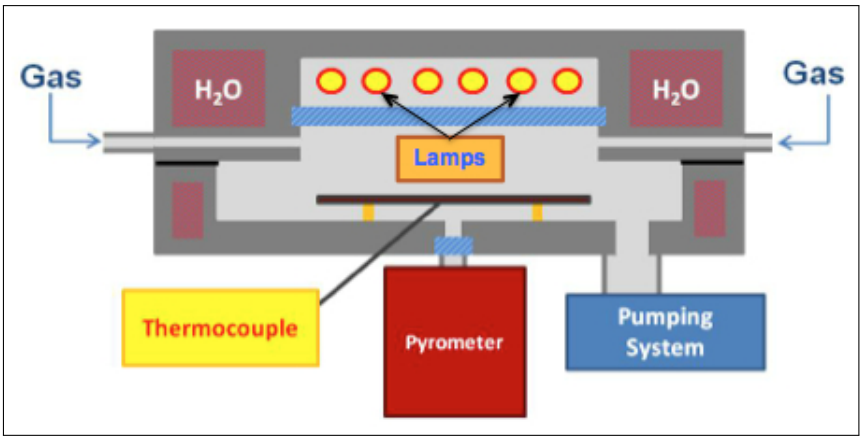

Figure 75: RTA working principles. Schematic view of the RTA system, showing its working principles: the sample-holder, a 4" Si wafer, is the grey plate directly in contact with the thermocouple. It is heated by the halogen lamps from above, but its temperature is detected on its back by a thermocouple and a pyrometer.

A pyrometer receives the heat radiation emitted by the measured object and focused by optical lens and it converts the radiation into an electrical signal proportional to the radiation power; the electrical signal is than digitally linearized and converted into a standard analog output signal, in the specific case of the pyrometer of the RTA system a voltage signal V_{pyro}. Usually, the emitted radiation is not detected by the pyrometer at any wavelength but only at a specific value often ranging in the infrared region of the electromagnetic spectrum. In particular the pyrometer into the RTA system receives radiation in the middle infrared region, specifically at $\lambda = 5.14\,\mu m$: it is therefore sensitive to the value of emissivity that a material has at the same wavelength.

So, the response given by the pyrometer at every absolute temperature T (and shown by the RTA system) is a voltage V_{pyro} satisfying[4]

$$V_{\text{pyro}} = f(B_{\bar{\lambda}}) = f(B_{\bar{\lambda}}(T, \epsilon_{\text{system}}[\bar{\lambda}])) = f\left(\epsilon_{\text{system}}[\bar{\lambda}]\frac{2hc^2}{\bar{\lambda}^5}\frac{1}{e^{\frac{hc}{\bar{\lambda}k_B T}} - 1}\right) \quad (66)$$

where $\bar{\lambda} = 5.14\,\mu\text{m}$, h is the Planck constant, k_B is the Boltzmann constant, c is the speed of light, $B_{\bar{\lambda}}$ is the spectral radiance (according to the Planck's Law, [71, 80, 148]) of the electromagnetic radiation emitted at a certain absolute temperature T and fixed wavelength $\bar{\lambda}$ (the wavelength to which the pyrometer is sensitive) by a body having an emissivity $\epsilon_{\text{system}}[\bar{\lambda}]$ at $\bar{\lambda}^5$. As

4 The exact analytical form of the function $f(B_{\bar{\lambda}})$ relating the voltage signal V_{pyro} provided by the pyrometer and the spectral radiance $B_{\bar{\lambda}}$ -or, equivalently, V_{pyro} with the temperature T and the emissivity of the system $\epsilon_{\text{system}}[\bar{\lambda}]$ at $\bar{\lambda} = 5.14\,\mu\text{m}$- is not known because it is an internal function of the RTA system, not reported in the technical manual. A possible easy way to evaluate f could be the following: take a black body like object as sample and perform a whatever wanted thermal process, with temperatures ranging between 300 °C at 1000 °C, in Low Vacuum conditions. At the end plot the values V_{pyro} measured by the pyrometer as a function of $B_{\bar{\lambda}} = \frac{2hc^2}{\bar{\lambda}^5}\frac{1}{e^{\frac{hc}{\bar{\lambda}k_B T_{\text{system}}}} - 1}$, where T_{system} is the real temperature of the system, for example the temperature read independently by a thermocouple. In any case, being the pyrometer *a priori* calibrated with the emissivity of a black body, $T_{\text{system}} = T_{\text{pyro}}$ as explained later in the text. Finally, fit the points with a curve $f(B_{\bar{\lambda}})$: the function providing the best fit of the experimental data is the desired function f. However, no matter how $f(B_{\bar{\lambda}}(T, \epsilon_{\text{system}}[\bar{\lambda}]))$ is done, its most important feature, as revealed by a detailed study of the calibration curves evaluated for different samples, is that it is a monotonic increasing function, and therefore an injective function, in both the variables T and $\epsilon_{\text{system}}[\bar{\lambda}]$. This means that $\forall \epsilon_{\text{system}}[\bar{\lambda}]$ (fixed), $f(B_{\bar{\lambda}}(T_1, \epsilon_{\text{system}}[\bar{\lambda}])) > f(B_{\bar{\lambda}}(T_2, \epsilon_{\text{system}}[\bar{\lambda}]))$ iff $T_1 > T_2$; in a similar way, and more important for my studies, $\forall T$ (fixed) $f(B_{\bar{\lambda}}(T, \epsilon^1_{\text{system}}[\bar{\lambda}])) > f(B_{\bar{\lambda}}(T, \epsilon^2_{\text{system}}[\bar{\lambda}]))$ iff $\epsilon^1_{\text{system}}[\bar{\lambda}] > \epsilon^2_{\text{system}}[\bar{\lambda}]$. The latter inequality implies in particular that, $\forall T \neq 0$ it can never happen that $\exists \tilde{T}$ such that $f(B_{\bar{\lambda}}(\tilde{T}, \epsilon^1_{\text{system}}[\bar{\lambda}])) = f(B_{\bar{\lambda}}(\tilde{T}, \epsilon^2_{\text{system}}[\bar{\lambda}]))$ whenever $\epsilon^1_{\text{system}}[\bar{\lambda}] \neq \epsilon^2_{\text{system}}[\bar{\lambda}]$: indeed, since $f(B_{\bar{\lambda}}(T, \epsilon_{\text{system}}[\bar{\lambda}]))$ is injective, for this $\tilde{T}$ the equality $\epsilon^1_{\text{system}}[\bar{\lambda}] = \epsilon^2_{\text{system}}[\bar{\lambda}]$ should hold, but this is impossible for hypothesis. So, functional curves showing V_{pyro} as a function of T_{system} for different materials characterized by constant emissivities $\epsilon^1_{\text{system}}[\bar{\lambda}]$ and $\epsilon^2_{\text{system}}[\bar{\lambda}]$ (evaluated at $\bar{\lambda} = 5.14\,\mu\text{m}$) for all the temperatures explored by the RTA thermal process can never intersect, but they must proceed apart one another. If an intersection between two curves occurs, a change in the emissivity of one of the two systems is underway: if the emissivity does not depend on the temperature (and since the emissivity is always detected at the same wavelength and at the same angle of view by the pyrometer), only a change of the constitutive material of the system can explain the change. This is the basic observation for performing dewetting studies, as we will see in Sec. 2.4.

5 Actually it would be in principle possible to relate the voltage signal V_{pyro} to the total radiation power $P = \epsilon_{\text{system}}[\bar{\lambda}]\sigma T^4$ emitted, according to Stefan-Boltzmann Law, by a grey body having an emissivity $\epsilon_{\text{system}}[\bar{\lambda}]$ equal to the emissivity at $\bar{\lambda}$ of the sample undergoing the CVD process; $\sigma = \frac{2\pi^5 k_B^4}{15c^2h^3} = 5.67 \times 10^{-8}\,\text{W}\,\text{m}^{-2}\,\text{K}^{-4}$ is the Stefan-Boltzmann constant. Said in other words, it would be possible to assume that the pyrometer is treating the sample in the reaction chamber as a grey body, although in general this approximation does not hold: if this is the case, the pyrometer receives a radiation power $B_{\bar{\lambda}}$ at wavelength $\bar{\lambda}$ and temperature T, it searches for the Planck curve (with $\bar{\lambda}$ and $\epsilon_{\text{system}}[\bar{\lambda}]$ fixed) best fitting the value $B_{\bar{\lambda}}$ it has received and it integrates the Planck function over all the electromagnetic spectrum, thus assuming the sample to be a grey body. I am not sure about the procedure used by the pyrometer to give out V_{pyro}: if it simply employes the value $B_{\bar{\lambda}}$ it receives or if it converts this value in a total radiation power P. In any case I will try to show here that this fact does not affect qualitatively, but only quantitatively, the results obtained in dewetting studies about the emissivity of a system. Indeed, the only difference between a grey body and an usual object is that while for the former Stefan-Boltzmann Law holds exactly, for the latter this is not the case: this law, providing the total power P irradiated by a grey body of constant emissivity ϵ_{system} in thermal equilibrium at temperature T, is obtained indeed by integration of the Planck's Law over all the wavelengths λ and over all the solid angle Ω describing an half-sphere in 3D. As written in 66, Planck's Law for the radiation emitted at wavelength λ by a black body at thermal equilibrium at temperature T can be written as $B_\lambda(T) = \frac{2hc^2}{\lambda^5}\frac{1}{e^{\frac{hc}{\lambda k_B T}} - 1}$.

a consequence, in a thermal process the temperature T_{pyro} provided by a pyrometer is given by

$$T_{\text{pyro}} = \frac{hc}{\bar{\lambda} k_{\text{B}}} \left[\ln \left(1 + \frac{2hc^2 \epsilon_{\text{system}}[\bar{\lambda}]}{\bar{\lambda}^5} \frac{1}{f^{-1}\left(V_{\text{pyro}}\right)} \right) \right]^{-1}. \tag{67}$$

The "problem" is that a pyrometer does not know *a priori* the emissivity ϵ_{system} of the irradiating material, thus considering it always as a black body and setting $\epsilon_{\text{system}}[\bar{\lambda}] = \epsilon_{\text{bb}} = 1$. Therefore, the pyrometer response will be wrong every time an object different from a black body is subjected to a thermal process: if T is the right temperature of the system that the pyrometer should give out according to 67, and $\epsilon_{\text{system}}[\bar{\lambda}]$ is the emissivity of the sample at $\bar{\lambda}$, the (wrong) temperature provided by the pyrometer will satisfy

$$B_{\bar{\lambda}}(T, \epsilon_{\text{system}}[\bar{\lambda}]) = B_{\bar{\lambda}}(T_{\text{pyro}}, \epsilon_{\text{bb}}[\bar{\lambda}] = 1) \tag{68}$$

or, more explicitly,

$$\frac{e^{\frac{hc}{\bar{\lambda} k_{\text{B}} T_{\text{pyro}}}} - 1}{e^{\frac{hc}{\bar{\lambda} k_{\text{B}} T}} - 1} = \frac{1}{\epsilon_{\text{system}}[\bar{\lambda}]}. \tag{69}$$

When dealing with a grey body of emissivity ϵ_{system}, the only difference in the Planck's Law is that $B_\lambda(T) \to \epsilon_{\text{system}} B_\lambda(T)$. The Stefan-Boltzmann Law is than simply obtained by integration of Planck's Law: $P = \int_0^\infty \mathrm{d}\lambda \int_0^{2\pi} \mathrm{d}\phi \int_0^{\pi/2} \mathrm{d}\theta \cos\theta \sin\theta \epsilon_{\text{system}} B_\lambda(T) = \epsilon_{system} \sigma T^4$. The problem is that every time ϵ_{system} depends on the wavelength λ, the integration cannot be anymore performed analytically and therefore Stefan-Boltzmann Law does not hold. The point is that I do not know if either the pyrometer is converting directly the spectral radiance $B_{\bar{\lambda}}(T)$ into the signal V_{pyro} according to 66 or, assuming the sample to be a grey body with emissivity $\epsilon_{\text{system}} = \epsilon_{\text{system}}[\bar{\lambda}]$, it is replacing the spectral radiance with the total power $P = \epsilon_{\text{system}} \sigma T^4$ and then it is converting P into V_{pyro}. In the first case the only relations to hold exactly and to use for quantitative analyses are 66 and 67, while in the second case the -perhaps wrong- assumption of treating the sample as a grey body holds and it is allowed to replace $B_{\bar{\lambda}}(T)$ with the simpler formula for P into 66 and 67. In the latter case it must be only remembered that $\epsilon_{\text{system}}[\bar{\lambda}]$ appearing in P does not really refer to a wavelength-independent emissivity, but its value holds only at $\bar{\lambda} = 5.14\,\mu\text{m}$. From a qualitatively point of view, since both $B_{\bar{\lambda}}(T, \epsilon_{\text{system}})$ and $P(T, \epsilon_{\text{system}})$ are monotonic increasing function of the variables T and ϵ_{system}, and also the unknown function f used by the pyrometer to convert the radiation signal into a voltage signal is a monotonic increasing function of these variables (as explained in the previous footnote), all the observations done in the text based on the monotonic behaviour of f and $B_{\bar{\lambda}}(T, \epsilon_{\text{system}})$ continue to hold also in the case $B_{\bar{\lambda}}(T, \epsilon_{\text{system}})$ is replaced with $P(T, \epsilon_{\text{system}})$. Form a quantitative point of view things are not so simple: Planck's Law, being local in the wavelength, holds always and it is therefore the right relation to employ in order to obtain the temperature T_{pyro} of the system in 67 or in order to obtain the emissivity $\epsilon_{\text{system}}[\bar{\lambda}]$ at $\bar{\lambda}$ of a body emitting radiation at absolute temperature T. Such an emissivity is evaluated correctly by matching $B_{\bar{\lambda}}(T, \epsilon_{\text{system}}[\bar{\lambda}])$ with the spectral radiance $B_{\bar{\lambda}}(T_{\text{pyro}}, \epsilon_{\text{bb}} = 1)$ "seen" by the pyrometer - that always assumes the sample to be a black body with $\epsilon_{\text{system}}[\bar{\lambda}] = \epsilon_{\text{bb}} = 1$, if it has not been calibrated before. The same quantities T_{pyro} and $\epsilon_{\text{system}}[\bar{\lambda}]$ could be evaluated also by means of the global Stefan-Boltzmann Law (hence by replacing $B_{\bar{\lambda}}(T, \epsilon_{\text{system}})$ with $P(T, \epsilon_{\text{system}})$), but if the assumption of treating the sample as grey body is wrong, a quantitatively wrong response would be obtained. For example, if the (always true) equality $B_{\bar{\lambda}}(T, \epsilon_{\text{system}}[\bar{\lambda}]) = B_{\bar{\lambda}}(T_{\text{pyro}}, \epsilon_{\text{bb}} = 1)$ is replaced with the equality $P(T, \epsilon_{\text{system}}[\bar{\lambda}]) = P(T_{\text{pyro}}, \epsilon_{\text{bb}} = 1)$ (holding instead only when the sample under study is a grey body), the relation $T_{\text{pyro}} = \epsilon_{\text{system}}[\bar{\lambda}]^{1/4} T$ between T_{pyro} and T would be obtained: the problem is that this relation does not hold anytime the assumption of treating the sample as grey body is wrong. Assuming *a priori* the sample to be a grey body would bring to think that the relation $T_{\text{pyro}} = \epsilon_{\text{system}}[\bar{\lambda}]^{1/4} T$ holds correctly and therefore to evaluate, using it, a wrong value of emissivity $\epsilon_{\text{system}}[\bar{\lambda}]$. However, if the user is interested only in qualitative studies, then he/she can freely choose how to express V_{pyro}, as a function of P or as a function of B_λ. The only important thing to remember in order to make correct quantitative analyses is that while the local Planck's Law holds always, the global Stefan-Boltzmann Law could have been used wrongly. In my case I have decided to express T_{pyro} as a function of $B_{\bar{\lambda}}$ since this way I am sure to evaluate always correct quantities. I will show in Sec. 2.4 how it is possible to understand in which cases the replacement $B_{\bar{\lambda}} \to P$ can be performed without getting wrong results.

The pyrometer will therefore indicate the temperature T_{pyro} that a black body should have to emit at wavelength $\bar{\lambda}$ the spectral radiance $B_{\bar{\lambda}} = \epsilon_{\text{system}}[\bar{\lambda}] \frac{2hc^2}{\bar{\lambda}^5} \frac{1}{e^{\frac{hc}{\bar{\lambda} k_B T}} - 1}$ emitted instead at the same wavelength by the sample subjected to the thermal process in the RTA system kept at temperature T ($\neq T_{\text{pyro}}$) and having an emissivity $\epsilon_{\text{system}}[\bar{\lambda}]$ (at $\bar{\lambda} = 5.14\,\mu\text{m}$). As a consequence, a pyrometer calibration process must be performed for any material put into the RTA system before running any CVD process. During the calibration process the pyrometer receives the heat radiation, it converts the signal into a voltage value V_{pyro} and a temperature value T_{pyro} according to 66 and 67 (with $\epsilon_{\text{system}}[\bar{\lambda}] = \epsilon_{\text{bb}} = 1$) and it compares T_{pyro} with the temperature T_{real} of the system measured by another independent thermal instrument present in the reaction chamber (in the case of the RTA system this instrument is the thermocouple) and *assumed to be the right real temperature of the sample* (so that $T_{\text{real}} = T_{\text{thermoc}}$). If $T_{\text{pyro}} \neq T_{\text{thermoc}}$, the calibration process forces the pyrometer to associate the measured V_{pyro} with the true temperature T_{thermoc} and not with the temperature T_{pyro} of a black body (in other words the system changes the function $f(B_{\bar{\lambda}})$): in this way all is going as the value of the emissivity considered by the pyrometer would have been changed from $\epsilon_{\text{bb}} = 1$ to the real value $\epsilon_{\text{system}}[\bar{\lambda}]$, in order to make the two temperatures T_{real} and T_{thermoc} coincident. The calibration procedure is repeated until the mismatch between the two temperatures is below a certain accepted value.

Practically, the pyrometer calibration procedure of the RTA system present at I.N.Ri.M. proceeds as follows:

1. first of all an autotuning of the regulation temperature mode under thermocouple control must be performed. This step is quite technical and long and it is not useful to describe it in detail. It is based on a calibration of the temperature read by the thermocouple in eight zones of the sample at eight different values of temperature ranging from 300 °C to 1000 °C in step of 100 °C and involves the use of Proportional/Integral/Derivative (PID) parameters already provided by the system or manually inserted by the user;

2. after thermocouple calibration it comes the most important step of the pyrometer calibration procedure, useful for my studies on the dewetting effect. The calibration is performed by running *in Low Vacuum conditions* (so without gas flowing in the reaction chamber) a thermal cycle raising the temperature from room temperature to 1000 °C in step of 50 °C (each constant temperature step lasting 30 s), with the power of the lamps controlled through the temperature T_{thermoc} read by the thermocouple (a typical thermal cycle is shown in Figure 76 for explanation). Once the cycle is finished, a table reporting the voltage values V_{pyro} (in mV) read by the pyrometer and provided by the system corresponding to each constant temperature value T_{thermoc} read by the thermocouple must be compiled. Since the thermal cycle is stopped at $T_{\text{max}} = 1000\,°\text{C}$ (at higher temperatures the thermocouple may be damaged) pyrometer voltage values corresponding to temperatures up to 1300 °C must be extrapolated. The extrapolation is performed assuming a linear behaviour between V_{pyro} and T_{thermoc} holds for temperatures higher than 950 °C. When the table has been saved into the system, the thermal cycle is run again and the all described procedure described in this item is repeated as many times as needed in order to make the thermocouple temperature readouts (T_{thermoc}) and

the pyrometer temperature readouts T_{pyro} (obtained from the voltage V_{pyro} through the relation 67) as close as possible. It is worth noting that pyrometer temperature readouts start to be correct only for temperatures higher than 300 °C: below this temperature the pyrometer readout does not provide temperature reading;

3. a final step, similar to the one described in item 1, concerns an autotuning of the regulation temperature mode under pyrometer control. It involves again the use of PID parameters and the set-up of the temperature read by the pyrometer in eight zones of the sample. A detailed description of this step is not needed for my purposes.

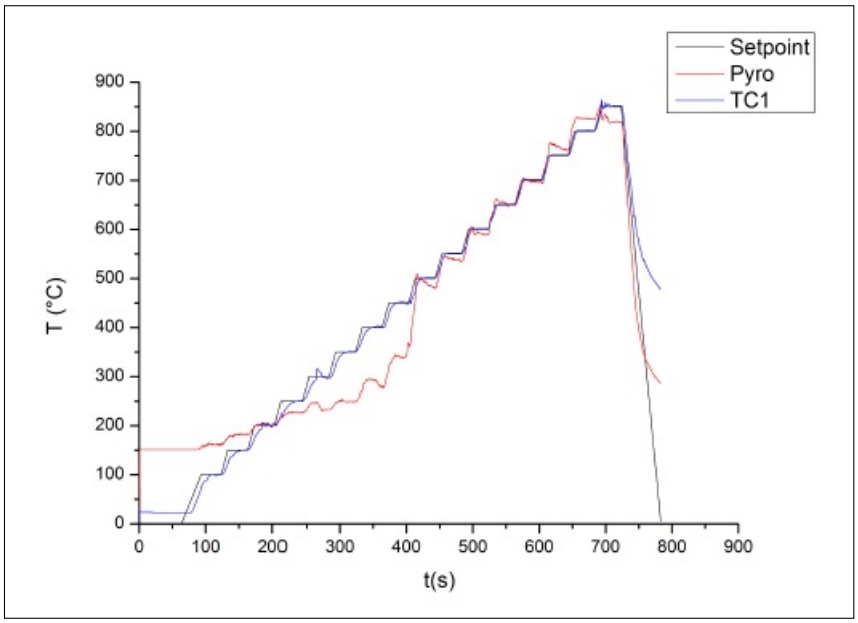

Figure 76: Thermal cycle for pyrometer calibration process. Schematic view of a typical thermal cycle used for pyrometer calibration in presence of an arbitrary material. In the figure three curves are visible: the temperature set-up by the user, the temperature read by the thermocouple "TC1" and the temperature read by the pyrometer "Pyro" as provided directly by the system after a conversion from the voltage signal V_{pyro} to the temperature T_{pyro} through 67. The temperature read by the pyrometer is not matching the other two temperatures in many points: hence the calibration process needs to be repeated.

Once the pyrometer calibration is finished, the value of the emissivity of the material used during the calibration process has been set-up and the temperature (setting the power of the lamps), during any CVD process performed with that kind of material, can be controlled by means of the pyrometer. Any time the material is changed, a new calibration process must be performed. During a CVD process the temperature is preferentially controlled through the pyrometer to avoid thermocouple damages caused by a temperature higher than 900 °C and to avoid also a wrong thermocouple readout of the temperature itself due to the presence of gas flowing in the reaction chamber (I remind that the thermocouple detects a precise temperature only in Low Vacuum conditions).
The calibration thermal cycle here described represents one of the most important feature used in my dewetting studies, as it will be clear in Sec. 2.4.

Moreover, in order to expose the Cu surface undergoing dewetting directly to the pyrometer, a way to put Cu samples not on the top but on the back of the sample-holder of the RTA system has been engineered, thus employing the sample/sample-holder configuration shown in Figure 77b: in this way any change in emissivity of the sample (due to Cu dewetting) can be directly detected by the pyrometer (for reasons that I will explain in Sec. 2.4) because it is receiving the radiation emitted directly from the Cu surface rather than from the Si wafer sample-holder surface (as it would be in the standard configuration shown in Figure 77a).

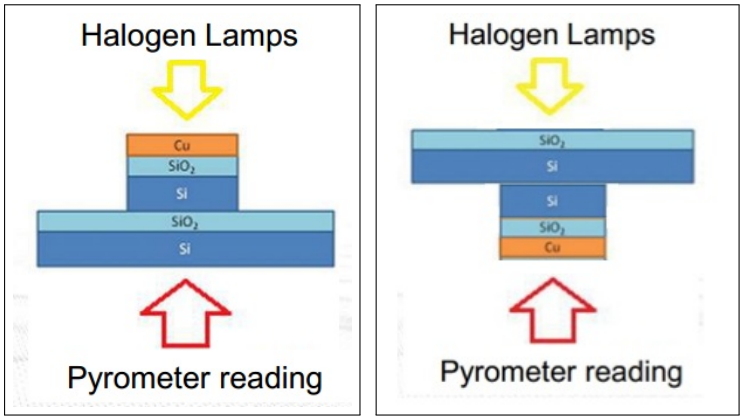

Figure 77: Sample-holder configuration for dewetting studies. Schematic view of the sample-holder configuration used during thermal processes performed in the RTA system: (a) standard configuration with the Cu sample, deposited onto a SiO_2/Si substrate, placed on top of the oxidized Si wafer representing the sample-holder and directly heated by the halogen lamps; (b) alternative configuration used for dewetting studies, in which the Cu sample deposited onto the SiO_2/Si substrate is placed on the back of the Si wafer, allowing for a direct exposition of the Cu surface to the pyrometer.

The desired configuration has been practically obtained by keeping Cu samples fixed on the back of the Si wafer (representing the sample-holder of the RTA system) through properly shaped Mo "pliers", as shown in Figure 78.

CVD processes with the RTA system are finally very easily performed by a digital set-up of the different parameters (value of gas flow, temperature set points, duration of each step of the CVD thermal cycle) involved in the steps composing the desired thermal cycle. In practice setting-up a thermal cycle consists in writing down a recipe (with the number of steps constituting the thermal cycle and the values of the parameters involved in each step) and in running it through the system.

2.3.2 Experimental evidence of Cu dewetting in CVD processes

After the description of the RTA working principles I can now report the results of the first CVD processes I have performed on Cu thin films evaporated onto SiO_2/Si substrates with the EBPVD technique described in Sec. 2.2.2: these results clearly evidence that Cu dewetting has occurred

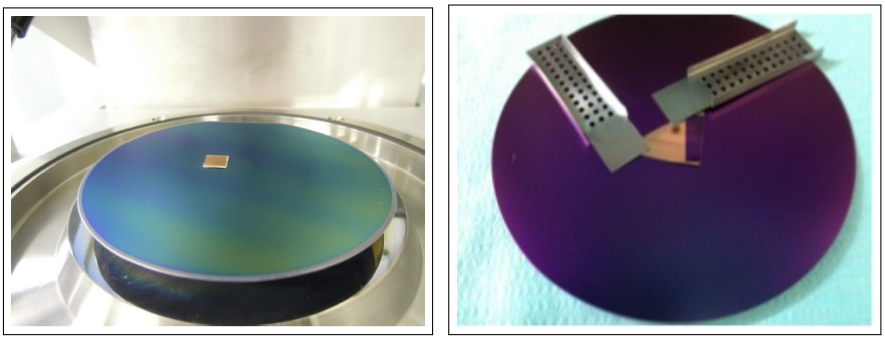

(a) (b)

Figure 78: Practical realization of the sample-hodler configuration for dewetting studies. Picture showing the sample-holder of the RTA system: (a) in the standard configuration, with the sample on top; (b) in the alternative configuration with the sample on the back, kept fixed by Mo "pliers".

in any tested CVD process on all but one the samples I have employed in each process.

The successfully e-beam evaporated Cu thin films subjected to CVD process were characterized by two different thicknesses: $d_{Cu} = 260\,nm$ and $d_{Cu} = 500\,nm$. For both the thicknesses I have performed two kinds of CVD thermal cycles, that I will denote as cycle *A* and cycle *B*, whose parameters have been chosen as described in Table 5.

During the processes the typical pressures measured in the RTA reaction chamber during gas flow are the following:

- $p_{H_2=40\ sccm} \simeq 1.65\,mbar$;
- $p_{H_2=40\ sccm\ +\ CH_4=5\ sccm} \simeq 1.65\,mbar$;
- $p_{CH_4=10\ sccm} \simeq 3.3 \times 10^{-1}\,mbar$.

The reported cycles have been chosen according to some criteria: cycle *A* has been inspired (but it is not identical) by a CVD process (described in Sec. 3.3.2) that I have performed previously on Cu foils and that provided a successful growth of few-layer graphene (in some regions also monolayer graphene) on the catalytic substrate, while cycle *B* has been inspired (but again it is not identical) by an interesting result reported in literature by L. Tao and co-workers ([177]), describing a successful CVD growth of graphene on top of Cu thin films. Both cycles have some features common to every CVD process usually performed in order to synthesize graphene:

1. a first heating step carried out with a gas flowing in the system, aimed at annealing the catalytic surface. This annealing step is meant to increase the grain sizes characterizing the metallic surface undergoing the CVD process (we have seen in Sec. 2.2 that both thermal and EBPVD Cu thin films show a polycrystalline nature with grain sizes of the order of $\sim 100\,nm$ or even less in the case of Cu films deposited with the IBAD technique) and to remove oxide layers eventually grown on top of Cu upon exposition of Cu samples to the external atmosphere. The increase in size of the crystal domains characterizing the film surface occurs mainly because of the increase in temperature occurring during the annealing step, inducing an increase in the thermal energy (i.e. kinetic energy) owned by the Cu atoms: as a

Cycle A	Cycle B
• pre-vacuum step; • room temperature to $T = 300\,^{\circ}\mathrm{C}$, $\Delta t = 60\,\mathrm{s}$, NO GAS FLOWING; • $300\,^{\circ}\mathrm{C}$–$850\,^{\circ}\mathrm{C}$, $\Delta t = 300\,\mathrm{s}$, 40 sccm H_2; • $850\,^{\circ}\mathrm{C}$, $\Delta t = 60\,\mathrm{s}$, 40 sccm H_2; • $T^A_{\mathrm{dep}} = 850\,^{\circ}\mathrm{C}$, $\Delta t = 120\,\mathrm{s}$, 40 sccm H_2 + 5 sccm CH_4; • $850\,^{\circ}\mathrm{C}$ down to room temperature, $\Delta t = 300\,\mathrm{s}$, 40 sccm H_2; • final system purge with N_2	• pre-vacuum step; • room temperature to $T = 600\,^{\circ}\mathrm{C}$, $\Delta t = 180\,\mathrm{s}$, NO GAS FLOWING; • $600\,^{\circ}\mathrm{C}$–$875\,^{\circ}\mathrm{C}$, $\Delta t = 330\,\mathrm{s}$, 40 sccm H_2; • $875\,^{\circ}\mathrm{C}$, $\Delta t = 300\,\mathrm{s}$, 40 sccm H_2; • $T^B_{\mathrm{dep}} = 875\,^{\circ}\mathrm{C}$, $\Delta t = 300\,\mathrm{s}$, 10 sccm CH_4; • $875\,^{\circ}\mathrm{C}$–$550\,^{\circ}\mathrm{C}$, $\Delta t = 390\,\mathrm{s}$; • $550\,^{\circ}\mathrm{C}$ down to room temperature, $\Delta t = 120\,\mathrm{s}$; • final system purge with N_2

Table 5: CVD processes highlighting Cu thin films dewetting. Detailed description of the two thermal cycles employed in the CVD processes that brought to Cu dewetting.

consequence, atoms with increased mobilities are allowed to better diffuse onto the underlying substrate, reorganizing themselves in more favourable regular lattice structures that lower the total internal energy of the system. Gas usually employed in the annealing step are H_2 and Ar, because of their low chemical reactivity: moreover, H_2 plays a rôle in keeping the Cu surface as flat as possible during annealing. Since RTA system was already equipped with an H_2 gas line and since Ar does not seem to play a major rôle, I have decided to use only H_2 during the annealing step;

2. a constant temperature step aimed at depositing graphene on the catalytic substrate. This step is obviously performed at the temperature for which the dissociation of carbon precursor molecules can be activated, with the carbon precursor in gas phase flowing into the system: in my experiments CH_4 has been chosen as precursor. During this step also H_2 can in principle flow in the reaction chamber together with the carbon precursor: the problem is to determine if the presence of H_2 may be detrimental or not for the final quality of graphene grown by CVD. This problem has been long debated and contrasting conclusions can be found in literature: while in [177] it has been reported that H_2 has a bad effect on CH_4 decomposition and therefore on the whole process of graphene synthesis, in [190] it has been shown how the presence of an H_2 enriched atmosphere during the deposition step seems to favour the activation of CH_4 chemical dissociation and, at the same time, to improve the final quality of graphene layers (in terms of crystallographic morphology, flakes size and number of lay-

ers)[6]. It is therefore clear that a final answer is still far from being established. In my cycles I have decided to try both the possibilities, in order to compare the results. Indeed, in CVD processes successfully performed on Cu foils with a thermal cycle similar to cycle *A*, I could establish that H_2 presence was not in that case detrimental for graphene growth. Nonetheless, very recently I have performed CVD processes on Cu thin films using a thermal cycle similar to the one that I will describe in Sec. 3.3.3 (see Figure 125) -for which Cu dewetting is surely prevented- but with H_2 flowing in the chamber together with CH_4 also during the deposition step, and I have discovered by characterizing the samples with Raman spectroscopy that no signature of graphene could be found on them. Therefore, for the CVD processes I will perform in the future, I have decided to avoid H_2 flowing in the chamber together with CH_4 during the deposition step;

3. a cooling-down step, bringing the temperature down to room temperature, that can be again performed with or without gas flowing in the chamber. Usually employment of a gas in this step is not really necessary, but not even damaging for graphene crystal quality. I have pointed out in Chapter 1 the great importance of this step for CVD growth of graphene on catalytic substrates (such as, for example, Ni) having high carbon solid solubility. On the contrary, this step is in principle less fundamental for decomposition and nucleation-on-surface mediated CVD processes (so, those performed on metallic catalyst, as for example Cu, characterized by very low carbon solid solubility), since graphene growth in this case occurs usually directly during the deposition step. After reaching room temperature, the system is purged by flowing N_2 in the reaction chamber.

Apart from the common steps highlighted above, cycle *A* and cycle *B* show some fundamental different features, that it is worth mentioning explicitly:

- deposition temperatures for the two cycles are slightly different: $T^A_{dep} = 850\,°C$ and $T^B_{dep} = 875\,°C$;
- in cycle *A* the heating step bringing the temperature up to the deposition temperature has been much faster than in cycle *B*: 6 min for the former against 8.5 min of the latter;
- in cycle *A* the time I have kept the sample at the maximum temperature of all the process, i.e. T^A_{dep}, is much shorter than in cycle *B*

6 As a third possibility, it has been also reported in [173] that the presence of H_2 in the reaction chamber together with CH_4 during the deposition step could have a beneficial and convenient effect in preventing Cu dewetting: indeed, the remarkable increase in the partial pressure inside the reaction chamber due to the presence of H_2 should prevent a fast evaporation of Cu at the deposition temperatures usually employed in CVD processes performed on this metal, i.e. $T_{dep} \sim 900$–$950\,°C$. This fact seems to agree with my results, since Cu dewetting is not occurred, as explained later in the text, while performing thermal cycle *A* on the 500 nm thick Cu film (so, when H_2 was flowing with CH_4 during the deposition step). At the same time, the presence of H_2 together with CH_4 during the deposition step of the same CVD process has appeared to be detrimental, bringing to no signature of graphene growth on top of the surface at the end of the thermal process. This point, together with some other CVD processes I have performed very recently on Cu films of the same thickness (500 nm), with H_2 flowing together with CH_4 during the deposition step, not bringing again to a successful graphene growth, convinced me to avoid the use of H_2 during the deposition step in the CVD processes to carry out in the future.

(for which the maximum temperature is T^{B}_{dep}): 3 min in the first case against 10 min in the second case;

- in cycle *A*, H_2 was flowing with CH_4 during the deposition step and then (alone) also during the cooling-down step, while in cycle *B* I have used H_2 only during the annealing step;
- in cycle *A* CH_4 flowed in the system for the deposition step for a shorter time than in cycle *B* (2 min vs. 5 min respectively). Moreover, CH_4 flow in the reaction chamber is higher for cycle *B* than for cycle *A*: 10 sccm against 5 sccm;
- the cooling-down step is also different for the two cycles, being faster for cycle *A* (for which it lasted 5 min) than for cycle *B* (8.5 min, as it was for the heating step). Moreover, in cycle *B* this step has been divided in two sub-steps: the first one, performed slowly, bringing the temperature down to 550 °C and the second one, much faster, bringing the temperature down to room temperature.

For better convenience, I have summarized in Table 6 the two CVD processes (described by the thermal cycles *A* and *B*) that I have performed on two Cu thin films of different thickness ($d_{Cu} = 260$ nm and $d_{Cu} = 500$ nm), trying to highlight only those steps of the two processes that show the most important and fundamental differences for graphene growth.

		T_{dep} (°C)	
		850 (cycle *A*)	875 (cycle *B*)
d_{Cu} (nm)	260	60 s: 40 sccm H_2 120 s: 5 sccm CH_4 + 40 sccm H_2	300 s: 40 sccm H_2 300 s: 10 sccm CH_4 (**no H_2**)
	500	60 s: 40 sccm H_2 120 s: 5 sccm CH_4 + 40 sccm H_2	300 s: 40 sccm H_2 300 s: 10 sccm CH_4 (**no H_2**)

Table 6: Differences in deposition step of CVD processes highlighting Cu dewetting. Summary of the peculiar features distinguishing the CVD processes described in Table 5 and performed on two Cu thin films of different thickness. The most important differences concern the deposition step, whose parameters are reported in this table: while for cycle *A* this step is fast and characterized by H_2 flowing together with CH_4, in cycle *B* the same step lasts a longer time and is characterized by no H_2 flowing together with the carbon precursor.

Problems have arisen when I have analysed the SEM images acquired on the samples subjected to the CVD processes (Figure 79, Figure 80, Figure 81): indeed, the $d_{Cu} = 260$ nm thick Cu samples that had undergone both thermal cycles *A* and *B*, and the $d_{Cu} = 500$ nm thick Cu sample that had undergone thermal cycle *B*, showed clear features of Cu dewetting occurred on the surface during the processes[7]. Instead of uniformly covering the

7 While on the thinner Cu films ($d_{Cu} = 260$ nm) dewetting is so pronounced that any characterization of the sample searching for graphene is quite useless, on the $d_{Cu} = 500$ nm film subjected to thermal cycle *B* dewetting is less pronounced and quite large areas still covered by Cu are clearly visible on the SiO_2/Si substrate: therefore, in this case, I cannot exclude *a priori* that few-layer graphene is grown on these areas, but unfortunately I have not characterized

SiO_2/Si substrates (as it was before running the processes), we have clearly seen that Cu reorganized in droplets and wrinkles of different sizes, randomly spread on the underlying surface, deeply changing its morphology. Although dewetting of Cu thin films with thicknesses lower than $\sim 500\,\text{nm}$, subjected to temperatures higher than $\sim$ 950–1000 °C, is a known problem ([115]), the result I have obtained was quite unexpected for me (at least for the thicker Cu film) because of the relatively low temperatures $T^A_{\text{dep}}, T^B_{\text{dep}}$ employed in my processes and for the not so long deposition time (at least no longer than standard deposition times reported in literature) I have used for both thermal cycles A and B. I have understood only later, by performing other experiments, that the problem essentially relied on a malfunction of the thermocouple present in the RTA system[8], resulting in an underestimation of the real temperature of the system of $\sim 150\,^\circ\text{C}$ (I have already mentioned the troubles I had with the RTA system thermocouple while describing the system in Sec. 2.3.1): therefore, the deposition temperatures $T^A_{\text{dep}}, T^B_{\text{dep}}$ reported in Table 5 and Table 6 are only nominal temperatures and the real deposition temperatures felt by the samples have been (at least) $T^A_{\text{dep}} \sim 1000\,^\circ\text{C}$ and $T^B_{\text{dep}} \sim 1025\,^\circ\text{C}$. At these temperatures it is clear that Cu films as thin as the ones I have employed could dewet from the underlying surface, since the activation energy for adhesion processes (involving atoms of the same chemical species) bringing to dewetting has been already reached (indeed, as underlined above, evidence of Cu dewetting occurring on $d_{\text{Cu}} = 500\,\text{nm}$ -or lower- thick films has been already reported in literature for temperatures lower than 1000 °C, so lower than the one used in my processes).

By the way, apart from the exact knowledge of the temperature at which the processes have been carried out, the results I have obtained are interesting because they have given me the first clear and unambiguous evidence of Cu thin film dewetting occurring during CVD processes: since dewetting is a problem limiting the possibility of growing graphene onto Cu thin films, I have decided to go deeper inside this problem, in order to check if there were possible routes enabling a better control on dewetting phenomena (at least allowing for understanding and estimating the temperature at which dewetting occurs on Cu films characterized by different thickness). I have this way developed a technique that I will describe in Sec. 2.4.

It is worth pointing out that in one of the four cases shown in Table 6, namely the case concerning thermal cycle A carried out on the $d_{\text{Cu}} = 500\,\text{nm}$ thick sample, dewetting of the Cu film has not occurred, as shown in Figure 82a (for reasons that are not quite clear yet). Nonetheless, Raman analysis (I will describe this characterization technique in Sec. 3.1.1, but it is necessary to anticipate one result here) performed directly on the Cu sample after the process, without transfer of graphene to a new insulating substrate, has not shown any fingerprint related to the presence of mono- or few-layer graphene on top of the surface: indeed, in the acquired spectrum (reported in Figure 82b), no 2D peak at $\sim 2700\,\text{cm}^{-1}$ is visible (a sharp and intense 2D peak at $\sim 2700\,\text{cm}^{-1}$ in the Raman spectrum is the striking signal of

this kind of samples with Raman analysis, and hence I do not have a final answer about this point. However, it is worth mentioning that a recent work ([77]) indeed reported the presence of graphene grown by CVD on Cu surfaces showing geometrical shapes similar to those I have obtained because of dewetting of 500 nm thick Cu samples (Figure 81).

8 I have later changed the old thermocouple used for these CVD processes with a new one giving a right estimation of the temperature of the system; for examples, all the qualitatively results about Cu calibration curves and dewetting reported in Sec. 2.4 have been performed with the new thermocouple.

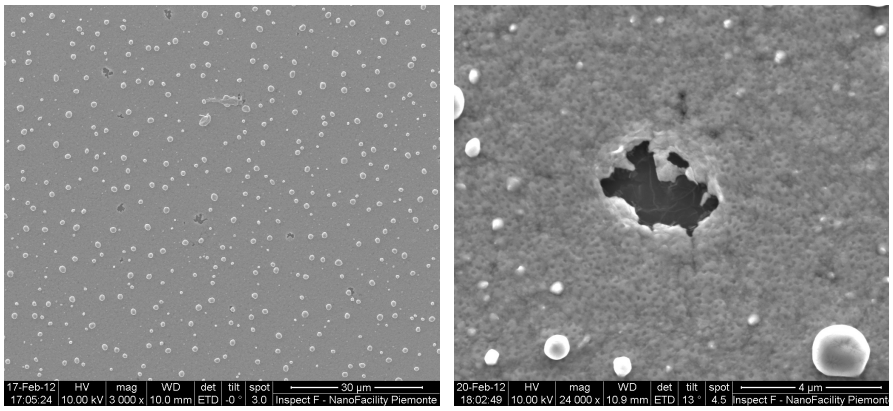

(a) (b)

Figure 79: Evidence of Cu dewetting on $d_{\mathbf{Cu}} = 260\,\mathrm{nm}$ thick film processed at $T_{\mathbf{dep}} = 850\,^{\circ}\mathrm{C}$. SEM images of 260 nm thick Cu samples at the end of the CVD process performed using thermal cycle A, characterized by deposition temperature $T^{A}_{\mathrm{dep}} = 850\,^{\circ}\mathrm{C}$: (a) Cu droplets are present on the surface, a clear signal that Cu dewetting has occurred during the process; (b) magnified view of another region of the same sample, showing a big crack on the surface.

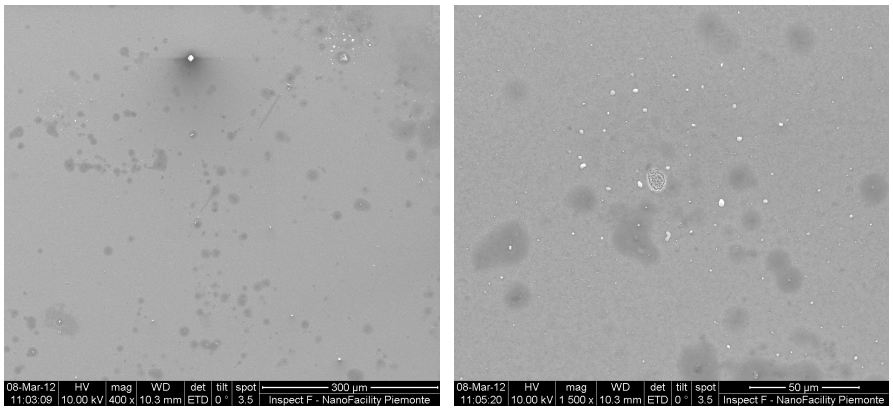

(a) (b)

Figure 80: Evidence of Cu dewetting on $d_{\mathbf{Cu}} = 260\,\mathrm{nm}$ thick film processed at $T_{\mathbf{dep}} = 875\,^{\circ}\mathrm{C}$. SEM images of 260 nm thick Cu samples at the end of the CVD process performed using thermal cycle B, characterized by deposition temperature $T^{B}_{\mathrm{dep}} = 875\,^{\circ}\mathrm{C}$: (a) Cu droplets much smaller than those reported in Figure 79 are again visible on the surface: a signal that Cu dewetting effects are more pronounced at higher temperature, as expected; (b) magnified view of another region of the same sample, showing almost no evidence of Cu presence on the surface.

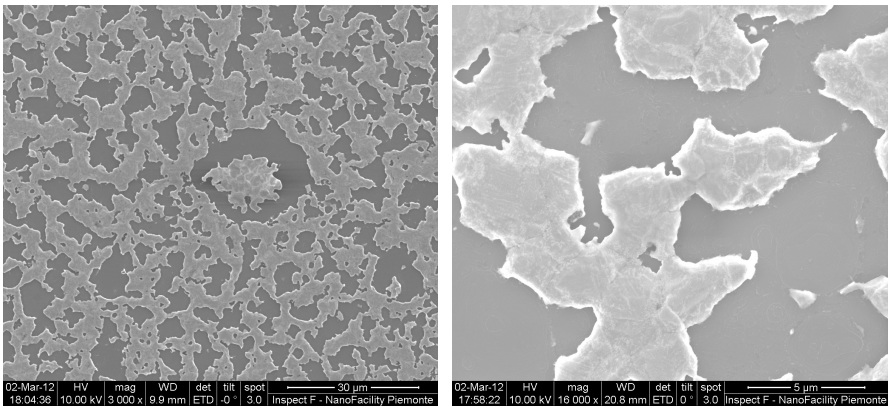

(a) (b)

Figure 81: Evidence of Cu dewetting on $d_{Cu} = 500\,nm$ thick film processed at $T_{dep} = 875\,°C$. SEM images of 500 nm thick Cu samples at the end of the CVD process performed using thermal cycle *B*, characterized by deposition temperature $T^{B}_{dep} = 875\,°C$: (a) also in this case, as it was for thinner samples (Figure 79 and Figure 80), changes in Cu morphology due to dewetting occurred during the CVD process are clearly visible, although atoms reorganize themselves in more complex geometrical shapes than simply droplets; (b) magnified view of another region of the same sample, showing a detailed view of Cu surface geometry after dewetting.

the presence of graphene on a substrate), while a G peak at $\sim 1600\,cm^{-1}$, related to the presence of mainly amorphous carbon or graphite, and a D peak at $\sim 1350\,cm^{-1}$, related to the presence of defects in the carbon lattice structure, are clearly visible. The fact that no graphene growth has occurred during the CVD process can be probably attributed to two features characterizing thermal cycle *A*: the quite short deposition time (only 2 min) and the low quantity of CH_4 flowing into the reaction chamber during the deposition step (5 sccm).

At the end of this section, for completeness, I mention the fact that the situation, when dealing with thermally evaporated Cu films, is similar or even worse than the one described up to now for EBPVD films: this fact is not surprising, since the thickness of thermally evaporated Cu films is much lower than the thickness of EBPVD films (as reported in Sec. 2.2.1). An annealing process performed at $T_{annealing} = 900\,°C$ on a 50 nm thick thermally evaporated Cu film has indeed provided another clear evidence that dewetting and formation of Cu droplets on the underlying Si surface was underway during the thermal cycle, as evidenced by SEM analysis carried out on the sample after the process (Figure 83).

2.4 AN *in situ* TECHNIQUE FOR DEWETTING CONTROL

After the detailed illustration of the working principles of the RTA system used at I.N.Ri.M. for CVD processes (Sec. 2.3.1) and after the presentation of examples of dewetting phenomena occurred on top of Cu thin films during CVD processes (Sec. 2.3.2), I can finally come to the main result of this chapter: the development of an *in situ* technique allowing for a real time qualita-

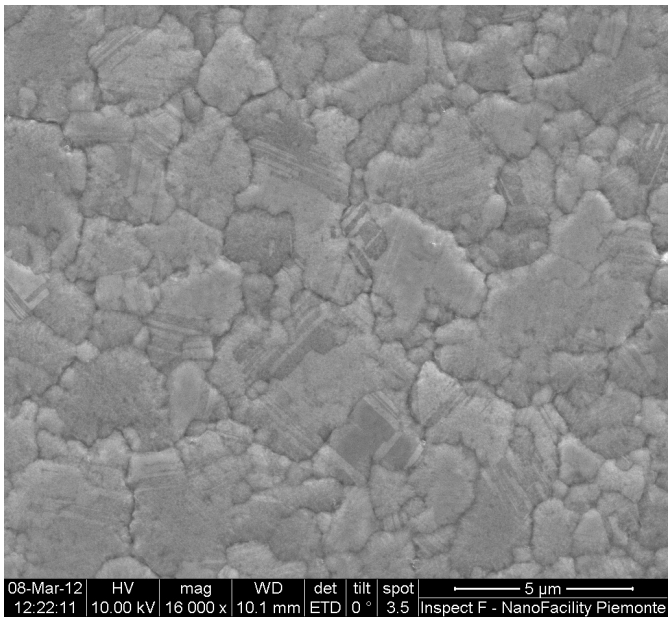

(a)

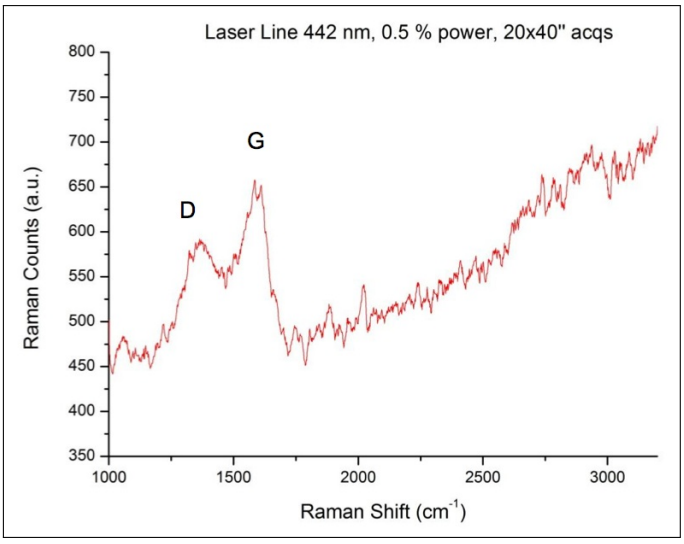

(b)

Figure 82: CVD process at $T^{A}_{\mathbf{dep}} = 850\,^{\circ}\mathrm{C}$ on $d_{\mathbf{Cu}} = 500\,\mathrm{nm}$ thick Cu film. SEM images of a 500 nm thick Cu sample at the end of the CVD process performed using thermal cycle A, characterized by deposition temperature $T^{A}_{\mathrm{dep}} = 850\,^{\circ}\mathrm{C}$: (a) in this case dewetting is not occurred and Cu covers the whole SiO_2/Si substrates. The metallic surface is still characterized by a polycrystalline structure, but the average size of the grains ($\sim 5\,\mu\mathrm{m}$) is increased with respect to the grains size evaluated on pristine films of same thickness just after the deposition (Figure 65b). The increase in size is due to the annealing step performed under H_2 flow during the CVD process; (b) Raman spectrum acquired directly on the Cu sample with $\lambda = 442\,\mathrm{nm}$ laser light. The spectrum is the result of 20 acquisitions, each one lasting 40 s. Pronounced D and G peaks, at $\sim 1350\,\mathrm{cm}^{-1}$ and $\sim 1600\,\mathrm{cm}^{-1}$ respectively, are clearly visible: these peaks are associated to the presence of graphitic-like structures on the Cu surface (mainly amorphous carbon or graphite) and to defects present in the lattice crystal. The 2D peak at $\sim 2700\,\mathrm{cm}^{-1}$, the most important feature bringing evidence of the presence of mono- or few-layer graphene on the surface, is instead not visible: a clear and unambiguous signal that graphene growth has not occurred during the CVD process.

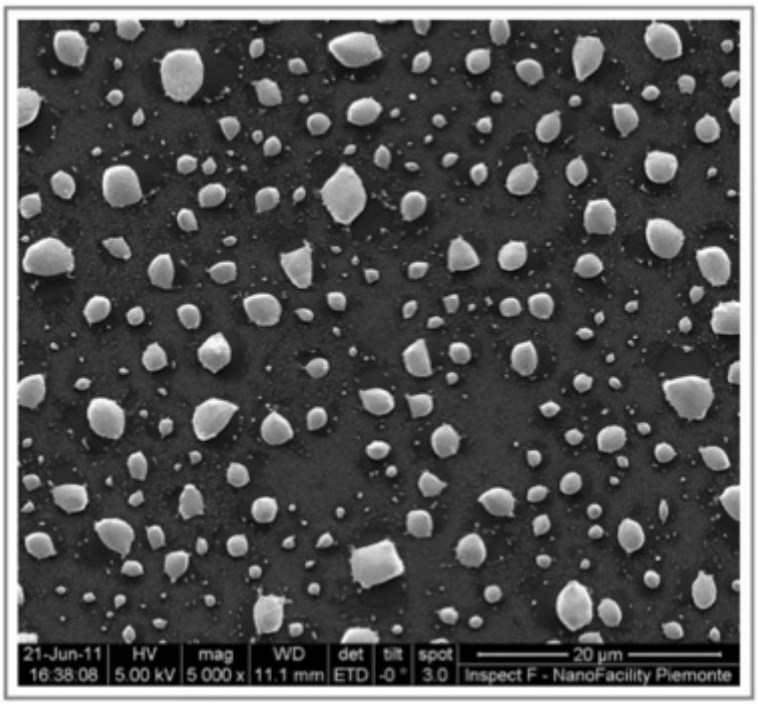

Figure 83: Evidence of Cu dewetting on $d_{Cu} = 50\,nm$ thick (thermally evaporated) film annealed at $T_{dep} = 900\,°C$. SEM images of a 50 nm thick thermally evaporated Cu sample at the end of an annealing process performed at $T_{annealing} = 900\,°C$. Droplets on the surface are clearly visible, meaning that also in this case, as in the case of EBPVD films, Cu dewetting has occurred during the thermal process.

tive detection of any dewetting effect and change in morphology occurring on Cu samples undergoing a thermal process in Low Vacuum conditions in the RTA system.
The key question, in order to understand the technique, is: is there any physical quantity related to a sample subjected to a thermal process in the RTA system that changes its value if dewetting of the material constituting the sample is occurring during the process itself? Is there a way to detect such a change in real-time through the RTA system response? The answer is yes: such a quantity is the emissivity of the system $\epsilon_{system}[\bar{\lambda}]$ at $\bar{\lambda} = 5.14\,\mu m$ and the way to detect an eventual change in its value is by looking to a change in the V_{pyro} vs. $T_{thermoc}$ behaviour (or equivalently in the T_{pyro} vs. $T_{thermoc}$ curve), occurring during a calibration-like thermal process, with respect to an expected behaviour. The expected behaviour of the V_{pyro} vs. $T_{thermoc}$ curve is obtained by looking at already acquired calibration curves, showing the relation V_{pyro} vs. $T_{thermoc}$ for certain materials for which the emissivity is known to be surely constant at any temperature of the calibration process (or, at least, only weakly dependent on temperature). I remind that, as explained in Sec. 2.3.1, $T_{thermoc}$ is the temperature read by the thermocouple present in the RTA system and considered to be the real temperature of the system, while V_{pyro} is the voltage signal provided by the pyrometer at any temperature through the relation 66, holding for a material of known emissivity $\epsilon_{system}[\bar{\lambda}]$ at $\bar{\lambda} = 5.14\,\mu m$ (i.e. the wavelength at which the spectral radiance of the heat radiation emitted by the material during the thermal process is detected by the pyrometer of the RTA system). I remind moreover that, as explained in detail in Sec. 2.3.1, calibration curves (i.e. V_{pyro} vs. $T_{thermoc}$ curves corresponding to calibration thermal processes as those shown in Figure 76) obtained through pyrometer calibration processes of different materials having emissivities, at $\bar{\lambda}$, constant over all the temperatures explored during the processes (or weakly dependent on these temperatures) can never intersect each other unless a change in emissivity occurs on a certain sample. The only reason why such a change in emissivity is occurring, if $\epsilon_{system}[\bar{\lambda}]$ is constant or weakly varying as a function of temperature, as supposed, is that a change in the constitutive material of the sample is also underway: indeed, a change in the constitutive material implies a change in emissivity and the latter implies a change in the behaviour of the calibration curve of the starting material.

Indeed, let's suppose to deal with a material of emissivity ϵ_{system} (independent of temperature for simplicity) and let's suppose that the pyrometer has been calibrated with such a material: this means that the temperature T_{pyro} provided by the pyrometer through 67 must be equal to the real temperature $T_{thermoc}$. As a consequence, a T_{pyro} vs. $T_{thermoc}$ curve will be represented by a straight line bisecting the first quadrant of the $(T_{pyro}, T_{thermoc})$ plane. Let's suppose now that at a certain temperature $\tilde{T}_{thermoc}$ the emissivity of the material changes from $\epsilon_{system}[\bar{\lambda}]$ to $\epsilon'_{system}[\bar{\lambda}]$ (independent of temperature too). Since a real-time change in the system set-up of the value of emissivity "seen" by the pyrometer is not allowed (otherwise the calibration procedure would not be necessary), the pyrometer will continue to give a response, in terms of temperature T_{pyro}, as the emissivity of the system would still be $\epsilon_{system}[\bar{\lambda}]$. So, since at $\tilde{T}_{thermoc}$ the spectral radiance received by the pyrometer is (according to Planck's Law) $B_{\bar{\lambda}} \propto \epsilon'_{system}[\bar{\lambda}]\left(e^{\frac{hc}{\bar{\lambda}k_B\tilde{T}_{thermoc}}} - 1\right)^{-1}$

but the pyrometer itself is still calibrated with the emissivity $\epsilon_{system}[\bar{\lambda}]$, the temperature given by the pyrometer will satisfy a relation analogous to 69:

$$\frac{e^{\frac{hc}{\bar{\lambda}k_B T_{pyro}}}-1}{e^{\frac{hc}{\bar{\lambda}k_B \tilde{T}_{thermoc}}}-1}=\frac{\epsilon_{system}[\bar{\lambda}]}{\epsilon'_{system}[\bar{\lambda}]} \tag{70}$$

From relation 70 it is possible (but not useful for my purposes) to express directly T_{pyro} as a function of $\tilde{T}_{thermoc}$. Moreover, if $\forall T_{thermoc} > \tilde{T}_{thermoc}$ the emissivity of the material will not change anymore, thus remaining fixed at $\epsilon'_{system}[\bar{\lambda}]$, the temperature T_{pyro} indicated by the pyrometer will continue to be wrong and to differ from the real temperature $T_{thermoc}$: as a consequence, $\forall T_{thermoc} > \tilde{T}_{thermoc}$, the T_{pyro} vs. $T_{thermoc}$ will not show anymore a straight line behaviour bisecting the first quadrant of the $(T_{pyro}, T_{thermoc})$ plane and meaning that $T_{pyro} = T_{thermoc}$, but rather the behaviour associated to the relation 70. In particular, if $\epsilon'_{system}[\bar{\lambda}] > \epsilon_{system}[\bar{\lambda}]$, T_{pyro} will be greater than $T_{thermoc}$ $\forall T_{thermoc} > \tilde{T}_{thermoc}$; otherwise, if $\epsilon'_{system}[\bar{\lambda}] < \epsilon_{system}[\bar{\lambda}]$ the opposite will be true[9].

Similarly, the change in emissivity occurring at $\tilde{T}_{thermoc}$ will be reflected in the behaviour of the V_{pyro} vs. $T_{thermoc}$ curve: indeed, at $\tilde{T}_{thermoc}$, the spectral radiance received by the pyrometer will be $B_{\bar{\lambda},\tilde{T}_{thermoc}}(\epsilon'_{system}[\bar{\lambda}]) \propto \epsilon'_{system}[\bar{\lambda}] \neq B_{\bar{\lambda},\tilde{T}_{thermoc}}(\epsilon_{system}[\bar{\lambda}])$. Therefore, the voltage signal $V_{pyro}(\tilde{T}_{thermoc})$ produced by the pyrometer at temperature $\tilde{T}_{thermoc}$ (through 66) will lie, at the same temperature, on the calibration curve corresponding to a material having emissivity $\epsilon'_{system}[\bar{\lambda}]$. The V_{pyro} vs. $T_{thermoc}$ curve will show therefore a discontinuity (in reality a sudden very sharp change in slope) exactly at $\tilde{T}_{thermoc}$, where an intersection between two calibration curves (those related to emissivities $\epsilon_{system}[\bar{\lambda}]$ and $\epsilon'_{system}[\bar{\lambda}]$) is occurring. Moreover, $\forall T_{thermoc} > \tilde{T}_{thermoc}$ the calibration curve corresponding to a material having emissivity $\epsilon_{system}[\bar{\lambda}]$ will be exactly superimposed to the calibration curve associated to a material having emissivity $\epsilon'_{system}[\bar{\lambda}]$. Therefore -supposing the calibration curve of the material having emissivity $\epsilon'_{system}[\bar{\lambda}]$ is known- at the temperature at which an intersection between the calibration curve related to a material having emissivity $\epsilon_{system}[\bar{\lambda}]$ and the (known) calibration curve related to $\epsilon'_{system}[\bar{\lambda}]$ will be eventually detected, there will be a clear evidence that the emissivity of the sample undergoing the thermal process is changed: moreover, as already pointed out in Sec. 2.3.1, the possibility that the function f relating the spectral radiance detected by the

9 Now I can suggest how it is possible to understand if the pyrometer is directly converting the spectral radiance $B_{\bar{\lambda}}$ into the voltage signal V_{pyro} or if it converts the local spectral radiance into a global radiation power P (given by the Stefan-Boltzmann Law), treating the sample as a grey body. Let's suppose to plot the T_{pyro} temperatures evaluated by the pyrometer as a function of the real temperatures of the system $T_{thermoc}$ read by the thermocouple. Up to $\tilde{T}_{thermoc}$ the two temperatures will be equal and the plot will be a straight line showing slope 1. For $T_{thermoc} > \tilde{T}_{thermoc}$, because of the change of emissivity, the behaviour of the T_{pyro} vs. $\tilde{T}_{thermoc}$ curve will deviate from slope 1 in a way providing that the relation 70 is satisfied. Now, if the Stefan-Boltzmann Law is also satisfied (i.e. the assumption of dealing with a grey body is not wrong), we know that besides 70 also the relation $T_{pyro} = \left(\epsilon'_{system}[\bar{\lambda}]/\epsilon_{system}[\bar{\lambda}]\right)^{1/4} T_{thermoc}$ must be satisfied. So, the relation between T_{pyro} and $T_{thermoc}$ should be still linear, with a slope $\epsilon'_{system}[\bar{\lambda}]/\epsilon_{system}[\bar{\lambda}] \neq 1$. Hence, a possibility to check if the grey body assumption holds it to plot first of all $e^{\frac{hc}{\bar{\lambda}k_B T_{pyro}}} - 1$ vs. $e^{\frac{hc}{\bar{\lambda}k_B \tilde{T}_{thermoc}}} - 1$, to fit the result with a straight line and to check that the slope of the line is exactly $\alpha = \epsilon_{system}[\bar{\lambda}]/\epsilon'_{system}[\bar{\lambda}]$, as it should be according to 70. Then it is possible to plot T_{pyro} vs. $T_{thermoc}$ and to fit the curve with a straight line having slope $\alpha^{-1/4}$: if the fit gives a statistically acceptable result, the grey body assumption is correct, otherwise the assumption is wrong.

pyrometer to the voltage V_{pyro} may be responsible for such an intersection must be discharged (because f is constructed in a way ensuring that calibration curves related to different -constant in temperature- emissivities proceed apart one another; in other words, if a discontinuity is detected in one calibration curve at a certain temperature $\tilde{T}_{thermoc}$, the same discontinuity should appear also in all the other calibration curves, but experimental evidence shows that this is not the case).

It should be clear now why and how a change in the emissivity of a material can be detected, during a thermal process run in the RTA system, by analysing the V_{pyro} vs. $T_{thermoc}$ curves or the T_{pyro} vs. $T_{thermoc}$ curves. The only thing that remains to understand is the cause of the change in emissivity of the material subjected to the thermal process. The answer in this case is based purely on physical reasoning: assuming that the emissivities $\epsilon_{system}[\bar{\lambda}]$ (at $\bar{\lambda} = 5.14\,\mu m$) of the materials undergoing calibration-like thermal processes *are constant or weakly varying as a function of temperature*, at least in the temperature range explored during the calibration process (this is the really important hypothesis in order to make all the reasoning correct and meaningful -in any case, for the materials object of my studies, i.e. Cu and SiO_2/Si, this assumption is safely acceptable), the only reason why a change in emissivity of a material can occur during the thermal process is that the chemical composition of the material is changing. In my case, since chemical reactions between Cu and SiO_2 must be excluded, the only explanation for a change of the chemical composition of the material subjected to the thermal process is dewetting. Since Cu dewetting occurs at high temperatures during the calibration thermal process, there will be a temperature $\tilde{T}_{thermoc}$ above which the sample surface emitting radiation will not be anymore primarily Cu (since Cu has formed many droplets on the surface, reducing its emitting power), but SiO_2. Since SiO_2 layers, when very thin as in my case ($\sim 300\,nm$), can be considered as white body (having zero emissivity) transparent to the radiation, the real emitting medium is Si. Moreover, since the pyrometer is directly exposed to the sample surface emitting radiation (the configuration of the reaction chamber of the RTA system during calibration processes used for dewetting studies is shown in Figure 77b), it can detect any change in emissivity occurring on the material: being in particular $\epsilon_{Si}[\bar{\lambda}] \gg \epsilon_{Cu}[\bar{\lambda}]$, the change in the pyrometer response is particularly evident. In order to better understand the reasoning here explained, a schematic view of what is happening to the Cu surface and therefore to the emissivity of the system under investigation during the calibration-like thermal cycle shown in Figure 76, has been depicted in Figure 84.

It is worth mentioning, before showing the results obtained, that the technique described is both an *in situ* and a *real-time* technique allowing for detection of dewetting effects (and, in general, changes in morphology) occurring on Cu surface during thermal processes:

- *in situ* because the sample subjected to dewetting study does not need to be kept out from the RTA system in which CVD processes are performed;
- *real-time* because any change in surface emissivity can be detected by looking at the V_{pyro} vs. $T_{thermoc}$ curve shown on the monitor of the RTA system at the same time the thermal process is being performed.

After having explained in great details the physical principles underlying the technique I have developed to study dewetting effects occurring on Cu,

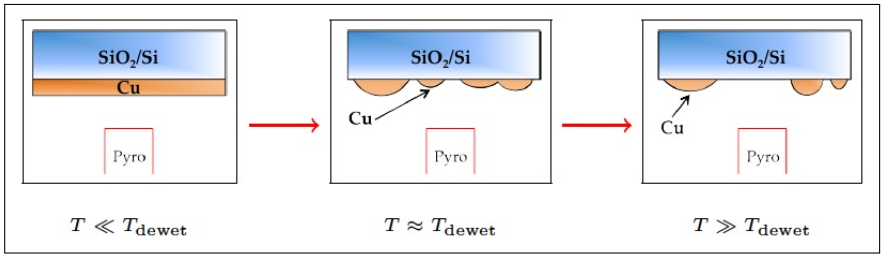

Figure 84: Dewetting and pyrometer detection of changes in emissivity. Schematic view of the dewetting effect occurring on Cu thin films (at temperature T_{dewet}) and of the related change in spectral radiance detected by the pyrometer (due to the change in the emissivity of the system). Upon heating of the system, through the thermal cycle shown in Figure 76, Cu will dewet from the underlying SiO_2/Si surface: therefore, the emissivity of the system $\epsilon_{system}[\bar{\lambda}]$ will change, according to the relation 71. As a consequence, also the spectral radiance $B_{\bar{\lambda}}(T, \epsilon_{system}[\bar{\lambda}])$, emitted at wavelength $\bar{\lambda}$ by the sample, will change and the pyrometer, being directly exposed to the Cu surface, will detect such a change. For temperatures $T \ll T_{dewet}$ no dewetting has occurred yet on the Cu surface and $\epsilon_{system}[\bar{\lambda}] = \epsilon_{Cu}[\bar{\lambda}]$; instead, when approaching T_{dewet}, the pyrometer will start to detect the presence of the underlying SiO_2/Si substrate, with the emissivity assuming the form 71. Finally, for $T \gg T_{dewet}$, the pyrometer will be eventually exposed only to the SiO_2/Si surface and therefore $\epsilon_{system}[\bar{\lambda}] = \epsilon_{Si}[\bar{\lambda}]$. See text for further details.

I can finally discuss the results I have obtained.
All the samples subjected to dewetting investigation have undergone the calibration-like thermal process illustrated in Figure 85 (so a thermal process similar to those used for the calibration of the pyrometer, in which the temperature is increased from room temperature to 1000 °C in steps of 50 °C; however in my processes I have decided to arrive at a maximum temperature 900 °C to avoid thermocouple damages)[10]. All the processes have been performed in Low Vacuum conditions ($p_{chamber} \sim 10^{-2}$ mbar), without gas flowing in the reaction chamber.

The first samples undergoing the calibration process (described in Sec. 2.3.1) of Figure 85 have been p-type SiO_2/Si substrates identical to those used for Cu thin films deposition. In this way the pyrometer has been calibrated according to the emissivity $\epsilon_{Si}[\bar{\lambda}]$ of Si at wavelength $\bar{\lambda} = 5.14\,\mu m$ (in principle the emissivity of the oxide SiO_2 should be also considered, but at this wavelength and because of its thin thickness -$\sim$ 300 nm- it is a good approximation to treat SiO_2 as a transparent object not emitting radiation): for my SiO_2/Si samples I have $\epsilon_{Si}[\bar{\lambda}] \sim 0.7$–$0.8$ almost independent of temperature (I have chosen this value according to [98]). The calibration curves obtained at the end of the calibration process, showing V_{pyro} (in mV) as a function of $T_{thermoc}$ (in °C) for the SiO_2/Si substrates are reported in Figure 86 and there will be considered as the *reference curves for dewetting studies* (meaning that, in absence of dewetting effects, I expect to obtain a behaviour of the Cu calibration curves similar to that of these curves).

Once the reference calibration curves have been obtained, the same thermal cycle performed with the SiO_2/Si substrates and shown in Figure 85 has been carried out on different Cu thin films deposited in different ways

10 For Cu samples evaporated with IBAD technique I applied the same thermal cycle shown in Figure 85 but with a maximum temperature T_{max} 800 °C, because over that temperature I have experienced some problems with the response of the thermocouple.

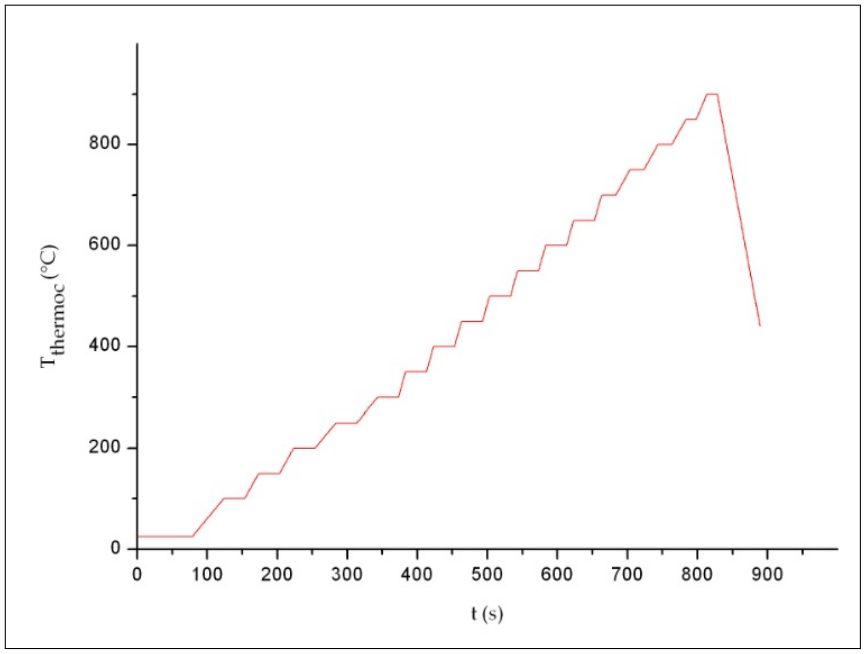

Figure 85: Thermal cycle for dewetting studies. Schematic view of the thermal cycle set-up to carry out dewetting studies. Temperature is increased up to 900 °C in steps of 50 °C. During the thermal cycle the power of the lamps of the RTA system is controlled through the temperature read by the thermocouple, in such a way to provide at any time a matching between the desired set-up temperature represented in the picture and the temperature read by the thermocouple. All the process is performed in Low Vacuum conditions.

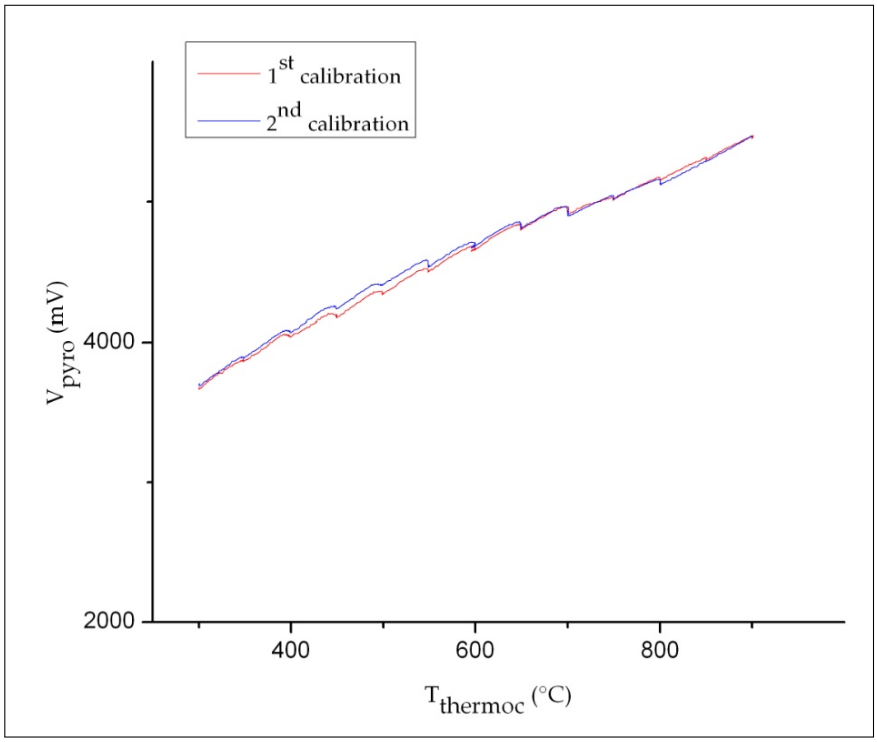

Figure 86: Calibration curves for SiO_2/Si substrates. Plot of the voltage signal V_{pyro} provided by the pyrometer as a function of the temperature $T_{thermoc}$ read by the thermocouple (this temperature is identical, at any time, with the temperature set-up in the system and shown in Figure 85) at the end of the calibration process performed on a couple of SiO_2/Si substrates through the thermal cycle of Figure 85: the curves are identical, meaning that the calibration procedure has been performed in a right way. After calbration process the pyrometer is calibrated on the emissivity of Si. Curves are shown starting from 300 °C because for lower temperatures the pyrometer does not work correctly.

on SiO_2/Si samples (the Cu film deposition process has been described in Sec. 2.2.2). The emissivity of Cu at wavelength $\bar{\lambda}$ is $\epsilon_{Cu}[\bar{\lambda}] \sim 0.02$–$0.04$, much lower than the emissivity of Si at the same wavelength and again almost independent of temperature in the range explored by the calibration process. Since the thermal cycle has been performed with the pyrometer calibrated on the emissivity of Si and since $\epsilon_{Cu}[\bar{\lambda}] < \epsilon_{Si}[\bar{\lambda}]$, for the comprehensive reasoning described above I expect that, by performing the thermal process, if dewetting is not occurring the calibration curves (V_{pyro} vs. $T_{thermoc}$) associated to Cu samples will have a behaviour similar to those of the references curves, but lower in V_{pyro} (indeed, the radiance at $\bar{\lambda}$ and temperature $T_{thermoc}$ of a Cu surface is lower than the one at same wavelength and temperature of a Si surface, because $\epsilon_{Cu}[\bar{\lambda}] < \epsilon_{Si}[\bar{\lambda}]$; since V_{pyro} is a function of the spectral radiance monotonic increasing in the emissivity, as explained in Sec. 2.3.1, the calibration curve related to a Cu sample will have lower values of V_{pyro} than the calibration curve related to a Si sample). However, if at a certain temperature T_{dewet} Cu will start to dewet from the underlying Si surface (because cohesion forces become stronger than adhesion forces), the pyrometer directly exposed to the sample surface will not detect anymore the Cu radiance, but the radiance emitted by Si. Therefore, at T_{dewet} the spectral radiance received by the pyrometer will suddenly increase and this fact will be reflected in an increase (i.e. a change in slope) of the Cu calibration curve, that will intersect the reference curves at $T_{dewet} + \delta T$ and will proceed superimposed to them $\forall T > T_{dewet} + \delta T$ (theoretically $\delta T = 0$, but in reality the change in slope is smooth and not discontinuous; δT is in some sense a "measure" of the time needed by Cu to dewet completely from the portion of Si surface exposed to the pyrometer). Viceversa, if an increase in the slope of the Cu calibration curves is detected at a certain temperature T_{dewet} and at temperature $T_{dewet} + \delta T$ the Cu curve intersects the reference curves, proceeding superimposed to them $\forall T > T_{dewet} + \delta T$, then a Cu dewetting phenomenon is certainly occurred at temperature T_{dewet}. In practice all is going as described in the reasoning above with the only difference that while in the reasoning I was assuming to use the pyrometer calibrated on an emissivity $\epsilon_{system}[\bar{\lambda}]$ (for us now $\epsilon_{Si}[\bar{\lambda}]$) and to start the calibration thermal cycle with a material having the same emissivity $\epsilon_{system}[\bar{\lambda}]$, changing at T_{dewet} (above called $\tilde{T}_{thermoc}$) into the emissivity $\epsilon'_{system}[\bar{\lambda}]$, now I am starting the thermal cycle with a material of emissivity $\epsilon'_{system}[\bar{\lambda}]$ (for us $\epsilon_{Cu}[\bar{\lambda}]$) changing at T_{dewet} into $\epsilon_{system}[\bar{\lambda}]$: so now all is going as in the previous reasoning thought as going backwards instead of forwards in temperature. Moreover, for all the above reasons, I can model the change in emissivity $\epsilon_{system}[\bar{\lambda}]$ undergone by my Cu samples through the following compact form:

$$\epsilon_{system}[\bar{\lambda}] = f\left(A^{unc}_{SiO_2}\right)\epsilon_{Si}[\bar{\lambda}] + g\left(A^{unc}_{SiO_2}\right)\epsilon_{Cu}[\bar{\lambda}] \tag{71}$$

where $A^{unc}_{SiO_2}$ is the portion of surface area of the SiO_2 substrate exposed to the pyrometer that has been uncovered during the thermal process because of Cu dewetting. The functions f, g fulfill:

$$\forall T \ll T_{dewet} \text{ (no Cu dewetting)} : \begin{cases} f\left(A^{unc}_{SiO_2}\right) = 0 \\ g\left(A^{unc}_{SiO_2}\right) = 1 \end{cases}$$

and

$$\forall T \geq T_{\text{dewet}} + \delta T \text{ (full Cu dewetting)} : \begin{cases} f\left(A_{SiO_2}^{\text{unc}}\right) = 1 \\ g\left(A_{SiO_2}^{\text{unc}}\right) = 0. \end{cases}$$

The samples I have subjected to the thermal cycle have been chosen as follows:

1. Cu films of different thickness ($d_{Cu} = 200\,\text{nm}$, $d_{Cu} = 250\,\text{nm}$ and $d_{Cu} = 500\,\text{nm}$) deposited by EBPVD directly onto SiO_2/Si substrates;

2. Cu films of different thickness ($d_{Cu} = 250\,\text{nm}$ and $d_{Cu} = 500\,\text{nm}$) deposited by EBPVD onto a Cr buffer layer ($d_{Cr} \sim 13\,\text{nm}$), evaporated onto SiO_2/Si substrates;

3. one Cu film with thickness $d_{Cu} = 200\,\text{nm}$ deposited by IBAD-EBPVD directly onto SiO_2/Si substrates.

I have used various Cu films having different properties because I was interested in understanding which conditions (if there exist) prevent in the better way the dewetting effect (preventing dewetting effect is useful for graphene deposition purposes): for example, if a Cr layer is enhancing the adhesion forces between Cu and the underlying substrate, thus causing dewetting to occur at higher temperature or to not occur at all. Similarly, I was interested in understanding if Cu films deposited with IBAD technique are better stuck to the SiO_2/Si substrate or not.
All the interesting calibration curves (V_{pyro}, T_{thermoc}) I have obtained for the different samples are reported in Figure 87, together with the reference curves of the SiO_2/Si substrates.

A careful qualitative analysis of the curves obtained allows to highlight many interesting features regarding the Cu samples employed:

- all the calibration curves show, at different temperatures, a change (more or less pronounced depending on the thickness of the related Cu film) in their behaviour with respect to the reference curves: therefore, we can conclude that all the samples I have employed have undergone a dewetting process (with the process occurring at different temperatures according to the properties of the specific sample);

- comparison of calibration curves related to Cu samples of different thickness clearly shows that, as expected, T_{dewet} depends on the thickness of the film: indeed, while for films having $d_{Cu} = 200\,\text{nm}$ and $d_{Cu} = 250\,\text{nm}$ dewetting is very pronounced and begins at $T_{\text{dewet}} \sim$ 580–600 °C, for what concerns the $d_{Cu} = 500\,\text{nm}$ thin films, a much less pronounced dewetting effect occurs only at a much higher temperature $T_{\text{dewet}} \sim 800\,°\text{C}$. Moreover, calibration curves associated to thinner films intersect reference curves in a very low interval δT, while the change in slope of the Cu 500 nm calibration curve is much lower (indeed up to SI900°C no intersection of this curve with the reference curves occurs). This result allows me to conclude that, since in CVD processes on Cu temperatures higher than 900 °C are usually reached, the minimum thickness of a Cu thin film employed as catalytic substrate for graphene deposition should be at least $\sim d_{Cu} = 500\,\text{nm}$: thinner films will certainly dewet from the surface, hence not allowing for graphene deposition;

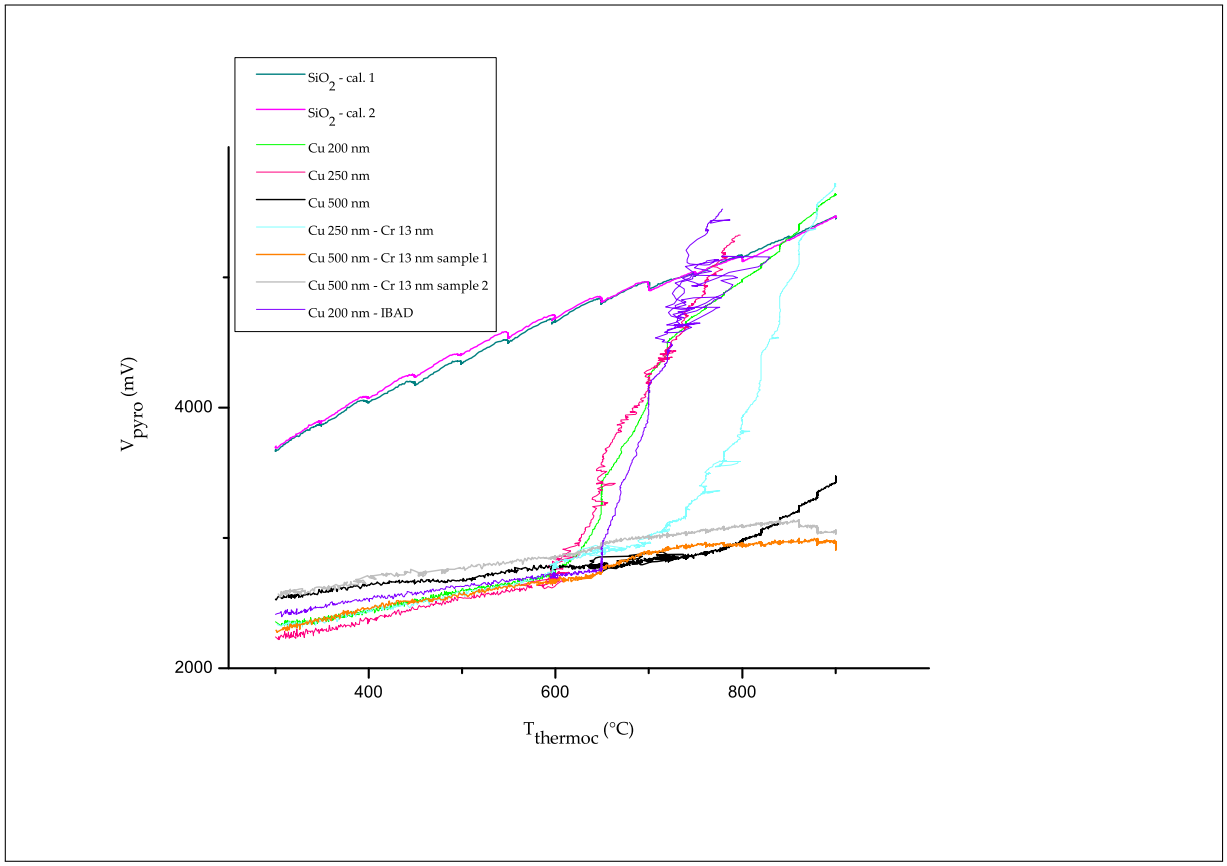

Figure 87: Cu calibration curves for dewetting studies. Graph showing the main results of my studies on dewetting effects occurring on various Cu thin films deposited in different ways on SiO_2/Si substrates or on Cr buffer layers: the calibration curves V_{pyro} vs. $T_{thermoc}$ for all the samples subjected to the thermal cycle shown in Figure 85. The curves at higher voltage are the reference calibration curves evaluated for SiO_2/Si substrates already illustrated in Figure 86. The Cu calibration curves start at lower voltage, as expected, since $\epsilon_{Cu}[\bar{\lambda}] \ll \epsilon_{Si}[\bar{\lambda}]$. At different temperatures all the curves start to increase their slope: a clear signal of dewetting phenomena starting to occur on the samples. The temperatures at which the slope changes is identified with T_{dewet}. After intersection with the reference curves, Cu calibration curves should superimpose to them: it is still unclear the reason why this fact does not happen.

- comparison of calibration curves related to Cu samples and Cu-Cr samples having the same Cu film thickness ($d_{Cu} = 250\,nm$ or $d_{Cu} = 500\,nm$) shows that T_{dewet} and dewetting processes are quite similar with or without the presence of the Cr buffer layer, although $T_{dewet}^{Cu\text{-}Cr}$ in the case of Cu-Cr samples is always a bit greater than the corresponding T_{dewet}^{Cu} of Cu samples deposited directly onto SiO_2/Si substrates: this means that probably Cr (at least with the thickness $d_{Cr} \sim 13\,nm$ I have evaporated) is only slightly and not significantly chancing the adhesion between Cu and SiO_2/Si substrate. Further investigations with thicker Cr layers have been planned to understand if this conclusion depends or not on the Cr thickness;

- comparison between Cu films having $d_{Cu} = 200\,nm$ deposited with or without IBAD technique shows that T_{dewet} and dewetting processes are similar independently of the fact that deposition has been performed with or without Ion Beam Assistance; this means that probably, at least with the values of the Ar gun voltage and ion beam current I have chosen, the increase in energy of the Cu deposited atoms due to the collisions with Ar ions is not enhancing too much the adhesion between Cu and SiO_2/Si substrate. Further investigation with thicker Cu films and with different values of ion beam current have been planned in order to understand if this conclusion depends or not on the free parameters to set-up for the deposition process.

This analysis is quite satisfactory, but the curves show also some important features not completely clear and understood yet:

- first of all, according to my reasoning all the calibration curves associated to the same material constituting the starting emitting surface exposed to the pyrometer (so, all the curves related to Cu films and, on the other hand, all the curves related to Cu-Cr films) should be quite well superimposed $\forall T < T_{dewet}$. Instead, by looking at the calibration curves related to Cu samples with thickness $d_{Cu} = 200\,nm$, $d_{Cu} = 250\,nm$ and $d_{Cu} = 500\,nm$ in the temperature range $300\,°C \leq T_{thermoc} \leq\sim 550\,°C$, or by looking at the two Cu 500 nm-Cr calibration curves in the same temperatures interval, it is clear that experimentally this is not true. Up to now I have not understood yet the reasons explaining such a behaviour. There are some possible explanations: the emissivity of Cu $\epsilon_{Cu}[\bar{\lambda}]$ at $\bar{\lambda} = 5.14\,\mu m$ greatly depends on Cu thickness, or maybe there are some missing points in my reasoning, or there are some experimental unknown problems occurring during the calibration-like processes. Another reason may be represented by the presence of impurities or by the formation of oxide layers on top of the surface, changing the emissivity of some samples subjected to the thermal processes, although this possibility is quite unlikely because I have prepared and cleaned the specimens in a very careful way;

- much more unclear is the behaviour of the calibration curves after the dewetting temperatures (so, after the changes in their slope) and, in particular, after they intersect the SiO_2/Si reference curves. According to my reasoning the Cu calibration curves should proceed superimposed to the reference curves after the intersections, but (at least up to the temperatures of my thermal process) they seem to continue increasing. This is a really puzzling point and I have no explanations for this unexpected behaviour.

In any case, although other processes are underway to better clarify the unclear features, I can safely say that the technique I have developed provides a qualitatively correct and real-time indication of any change in morphology and of any dewetting effect occurring on the Cu samples undergoing a thermal process in Low Vacuum conditions. To be more sure, I have also analysed at SEM all the samples subjected to the calibration-like thermal process here described, after the thermal process itself was completed. All the images I have acquired, reported in Figure 88, Figure 89 and Figure 90, clearly show the formation of Cu droplets on the sample surface and a not anymore uniform coverage of the underlying SiO_2/Si substrate (comparing these figures with those shown in Sec. 2.2.2 acquired immediately after the Cu film deposition, the difference is really evident).

It is interesting to note that on thicker Cu samples ($d_{Cu} = 500\,nm$) dewetting is occurring in a completely different fashion with respect to thinner Cu films: indeed, for thicker samples dewetting proceeds by removal of full crystal grains of Cu from the surface, while in the case of thinner films the formation of geometrical objects having different random shapes (not necessarily drop-shapes) seems to be the preferential route for dewetting. Also this feature and the reasons for this qualitative difference are not completely clear yet.

The dewetting studies discussed in this section and performed on various Cu samples, deposited with different techniques (EBPVD and IBAD-EBPVD) onto SiO_2/Si substrates or onto Cr intercalated buffer layers), allowed me to conclude that it is possible to find a (quite small) range of Cu film thickness and of temperatures for thermal treatment of Cu thin films that prevents Cu dewetting. This conclusion has been obtained by exploiting the *in situ* technique I have developed to have a real-time qualitative control on any change of morphology occurring on Cu surfaces during thermal cycles: in particular, it explains why a great percentage of works found in literature concerning CVD growth of graphene on Cu deal with foils (usually 25 µm thick) instead of thin films. Moreover, thanks to this result, I have already been able to successfully grow few-layer graphene by a CVD process performed onto a $d_{Cu} = 500\,nm$ thick Cu catalytic substrate, as I will explained in Sec. 3.3.3, and I am confident of exploiting again the result for the thermal processes that I will carry out in the future.

In conclusion, in this chapter I have shown the results I have obtained concerning Cu thin films thermal and e-beam depositions onto SiO_2/Si substrates and then I have presented a new *in situ* technique developed for studying dewetting of the films from the underlying substrate. I have shown first of all that e-beam evaporation processes allows to grow Cu films of better quality and in a faster way with respect to thermal evaporation processes, although a polycrystalline nature of the final deposited film (due to an island or Volmer-Weber crystal growth) is always observed.
Moreover, various CVD processes performed on Cu samples of different thickness have evidenced that Cu thin films are subjected to dewetting effects forbidding graphene deposition: Cu begins to form droplets and wrinkles on the surface during the thermal processes, thus leaving uncovered the underlying SiO_2/Si substrate.
I have finally shown how it is possible in real-time to control if dewetting is occurring on Cu surface directly exploiting the properties of the RTA system used for CVD processes and the physical principles governing heat irradiation and pyrometer working operations. The technique I have described

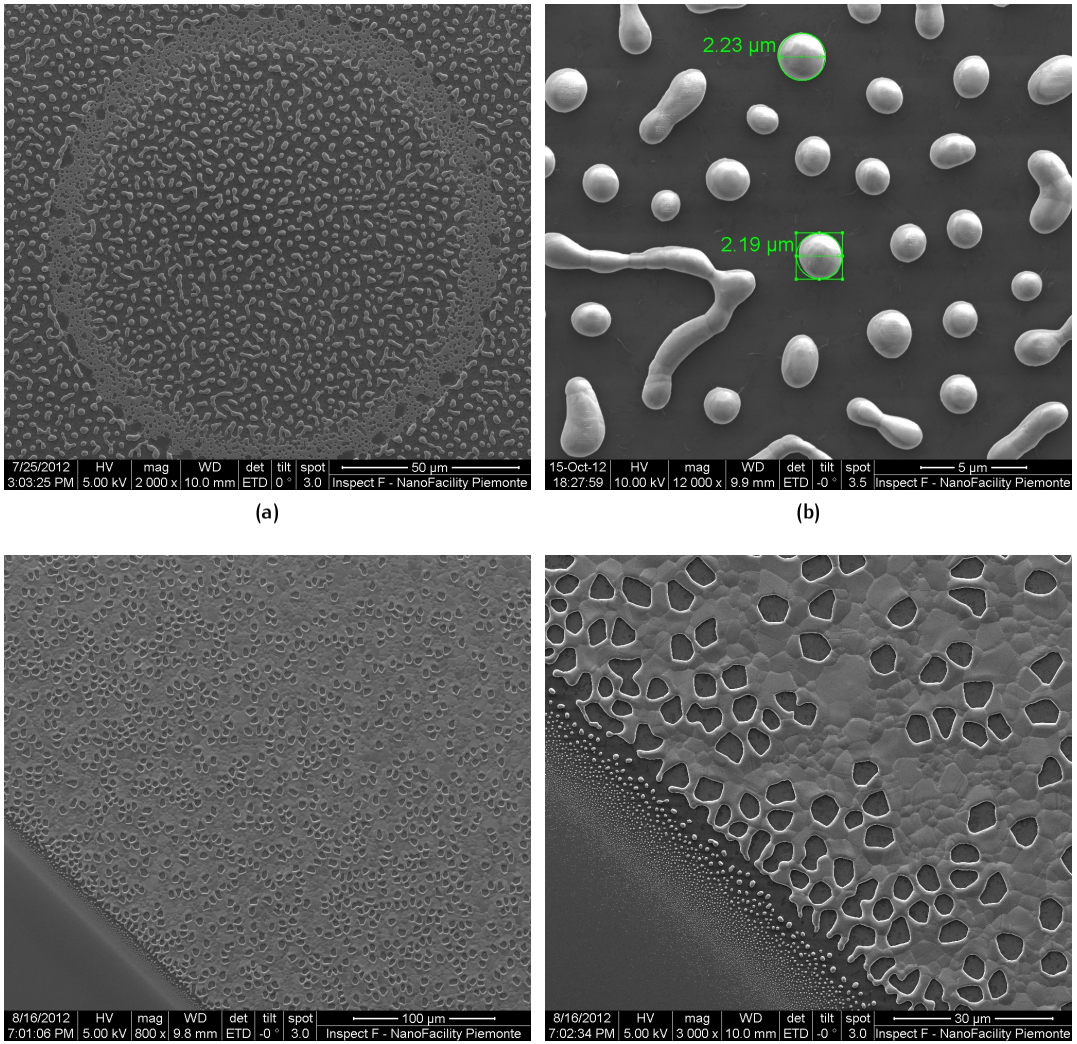

Figure 88: Cu thin films directly deposited onto SiO_2/Si substrates after dewetting. SEM images of Cu thin films of different thickness (directly deposited by EBPVD onto SiO_2/Si substrates) after carrying out the thermal cycle shown in Figure 85: (a) for $d_{Cu} = 200\,nm$ thick samples; (b) for $d_{Cu} = 250\,nm$ thick samples, with typical sizes of Cu droplets clearly illustrated; (c) for $d_{Cu} = 500\,nm$ thick samples; (d) enlarged view of image (c), showing the kind of dewetting occurring on thicker Cu films. In all cases dewetting is clearly occurred during the thermal process.

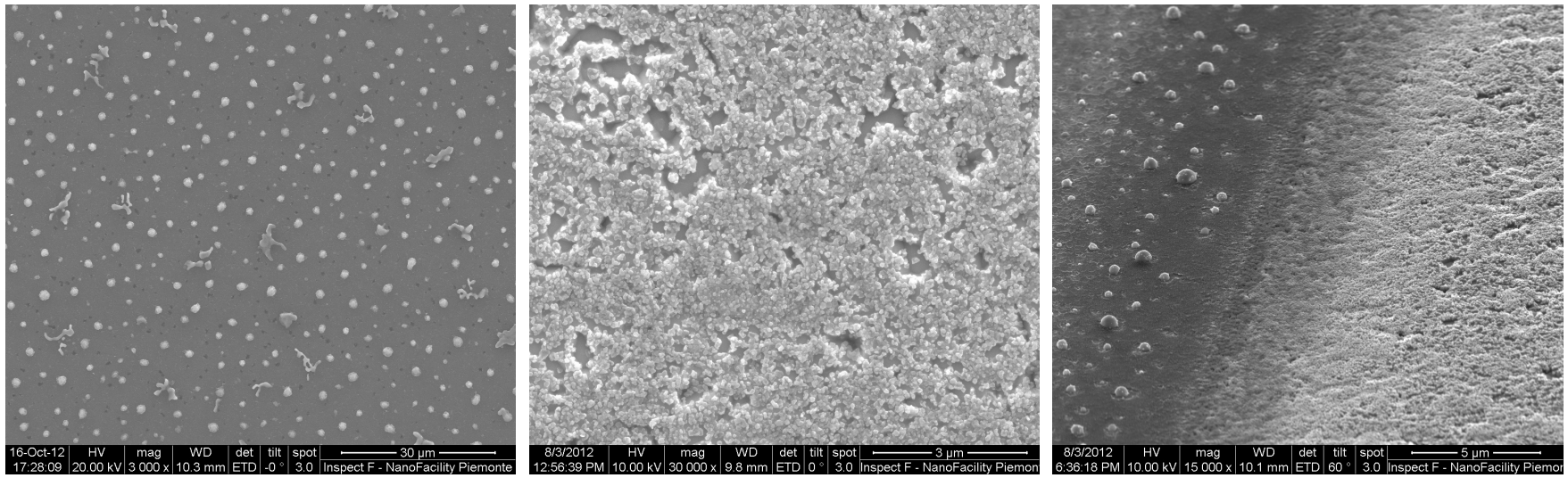

Figure 89: Cu thin films deposited on Cr buffer layers after dewetting. SEM images of Cu thin films of different thickness deposited onto a $\sim$ 13 nm thick Cr buffer layer after carrying out the thermal cycle shown in Figure 85: (a) for $d_{Cu} = 250$ nm thick samples; (b) for a $d_{Cu} = 500$ nm thick sample (called "sample 1" in Figure 87); (c) for another $d_{Cu} = 500$ nm thick sample (called "sample 2" in Figure 87). In all cases dewetting is occurring, although in a different fashion with respect to the samples of the same thickness shown in Figure 88 and directly deposited onto SiO_2/Si substrates.

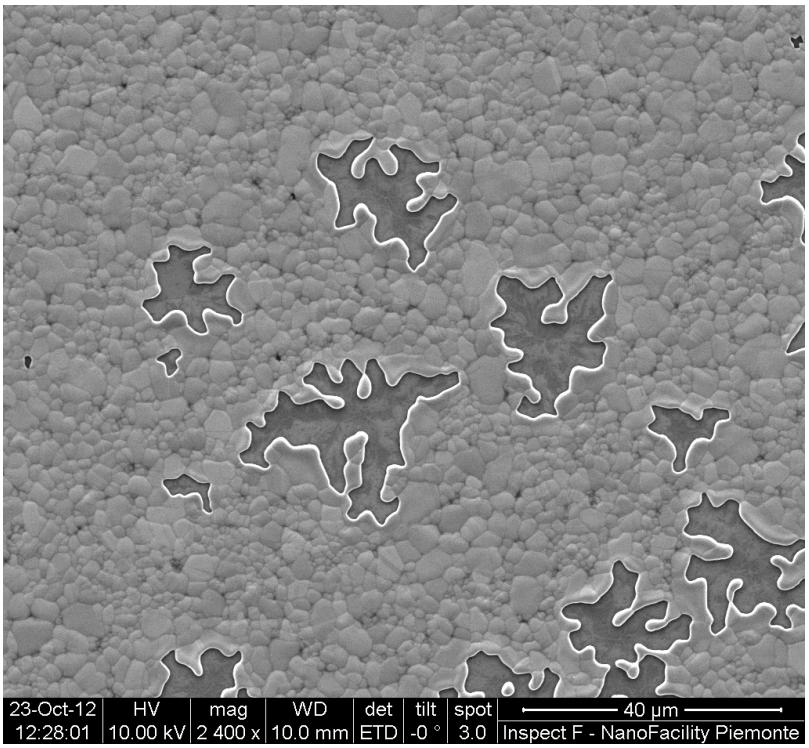

(a)

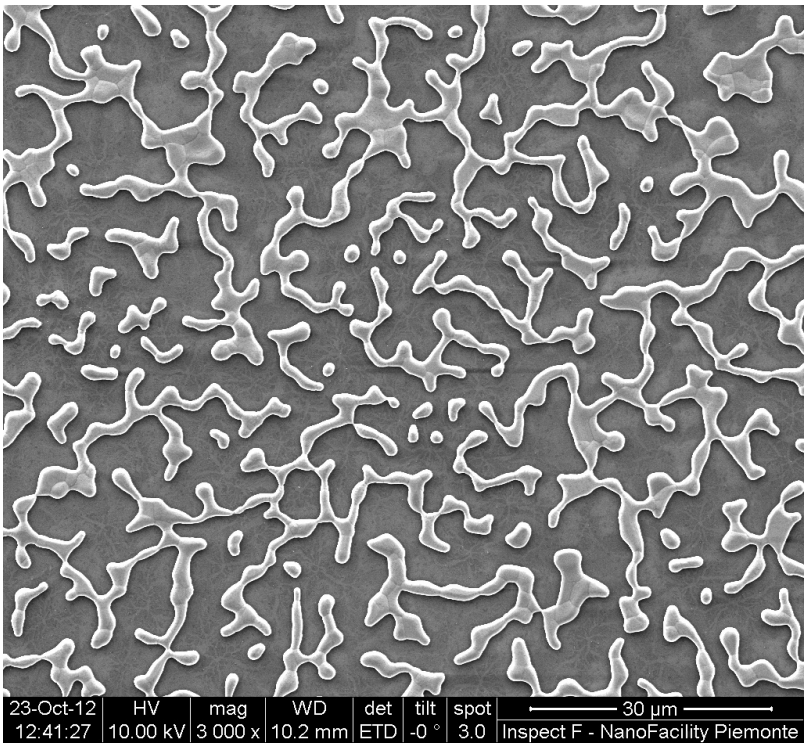

(b)

Figure 90: Cu films deposited onto SiO_2/Si substrates with IBAD technique after dewetting. SEM images of a 200 nm thick Cu film deposited directly onto SiO_2/Si substrates by means of IBAD-EBPVD technique after carrying out the thermal cycle shown in Figure 85: (a) region of the sample on which dewetting is occurring by removal of full Cu domains; (b) another region of the same sample on which dewetting proceeds in a more random fashion.

is in situ and works up to now only in Low Vacuum conditions (although further developments for adapting it to work also when gas is flowing in the RTA reaction chamber are underway: a possibility is to use two pyrometers instead of a pyrometer and a thermocouple to detect the temperature of the system, since pyrometer temperature detection is not affected by the presence of gas flow): the results I have reported for different Cu samples prove that the response given by this technique is quantitatively satisfactory and very useful, since it allows to understand which kind of Cu films (in terms of thickness of the films and of deposition technique) better prevents dewetting phenomena, therefore enabling CVD graphene growth.
However, some features found analyzing the results obtained are still unclear and need further investigations. I have planned to submit for publication, as soon as possible, the reported achievements on dewetting studies.

3 GRAPHENE DEPOSITION AND CHARACTERIZATION

In this last chapter I will finally present the results concerning graphene deposition and characterization. Sec. 3.1 will be devoted to a brief review of the most important techniques employed in graphene characterization. In particular I will focus on one of the most powerful, nondestructive and unambiguous tool nowadays used in order to characterize graphene: Raman spectroscopy. It has been demonstrated that this technique gives a clear fingerprint about the quality of grown graphene (detecting the eventual presence of defects or doping in graphene layers) and the number of graphene layers present on a certain substrate (well discriminating up to 5–6 layers). A brief presentation of the X-Ray Photoelectron Spectroscopy (XPS) technique will be also provided, since it has been used sometimes to characterize some samples. In Sec. 3.2 I will describe the process I have used to transfer graphene from the catalytic substrates employed during CVD processes to SiO_2 insulating substrates: this process is necessary in order to analyse the intrinsic properties of graphene and to integrate graphene in many devices. The process I have used is a standard transfer process reported in literature, based on the chemical etching of the metallic catalyst underlying graphene by means of proper reactants. Finally, in Sec. 3.3 I will report the details about the CVD processes I have performed on various substrates: Ni, Cu foils and Cu thin films. I will show that while on Ni I didn't get particularly interesting results, on both Cu foils and films I have succeeded in synthesizing few-layer graphene. In particular, I will present in details the most interesting and important result that I have obtained while characterizing graphene grown on Cu thin films with Raman analysis: a laser induced etching effect, due to the local thermal heating of graphene layers subjected to Raman spectroscopy, providing a useful tool in order to get (at least locally) monolayer graphene by means of a post-growth process.

3.1 GRAPHENE CHARACTERIZATION TOOLS

Let's start this chapter by describing the main tools I have employed to characterize graphene at the end of CVD growth processes. Being a truly 2D lattice, almost all the standard surface characterization techniques can be in principle employed to extract informations about the eventual presence of graphene layers onto a certain substrate and about their crystallographic quality. Among them, the most commonly used are:

- Scanning Tunneling Microscopy (STM) and Low-Energy Electron Diffraction (LEED), to investigate the periodicity of the crystal lattice, the electric charge distribution and the C atoms positions;

- XPS, Angle Resolved Photoemission Spectroscopy (ARPES) and Auger spectroscopy to investigate the chemical composition of the sample (in particular to check the eventual presence of C atoms on the sample

and the kind of bonds involving them) and (in the case of ARPES technique) its electronic band structure;

- SEM to investigate the sample's surface topography, inferring from the contrast of the images useful informations about the eventual presence of graphene layers onto the underlying substrate;
- optical microscopy to image, from optical contrast analysis, the eventual presence of graphene layers onto the substrate (this technique is particular powerful in the case of graphene grown or transferred onto a $\sim 300\,\text{nm}$ thick SiO_2 substrate, since in this case the optical contrast has characteristic values allowing to clearly distinguish and identify mono-, bi- and few-layer graphene layers present on the insulating surface);
- Raman spectroscopy, based on inelastic light scattering, to identifies in a unambiguous way the number of graphene layers present onto the underlying substrate and to investigate the eventual presence of dopants (electrons or holes shifting the graphene Fermi level, pinned otherwise at the Dirac points) or crystal defects in the graphene lattice structure.

While the first three techniques are electrons and X-Rays based tools, the last two are optical-based techniques involving therefore the employment of light. Moreover, among the listed techniques, the most powerful ones giving clear fingerprints about the presence of graphene onto a certain substrate are ARPES and Raman spectroscopy; the other ones do not provide enough unambiguous informations allowing to claim final answers about graphene characterization.

Since during the research I could access only SEM, XPS and Raman spectroscopy instruments, my discussion will be limited to these techniques. SEM technique and the instrumentation present at I.N.Ri.M. laboratories to exploit its capabilities has been already presented in Sec. 2.1.2; in what follows I will therefore focus on Raman spectroscopy (Sec. 3.1.1) and on XPS technique (Sec. 3.1.2), providing a brief description of both the techniques and of the instrumentation used to exploit them in graphene characterization.

3.1.1 Raman spectroscopy of graphene

Raman spectroscopy is a technique for measuring vibrational modes of molecules and phonon spectrum of lattice structures, based on the Raman phenomenon first detected by the Indian physicists Sir C. V. Raman and Sir K. S. Krishnan in liquids ([152]) and independently by the Russian physicists G. Landsberg and L. Mandelstam in crystals ([91]), but previously already predicted from a theoretical point of view by A. Smekal ([167]). The phenomenon relies on *inelastic* light scattering of photons with phonons (i.e. vibrations of atoms in a crystal). From a classical point of view, when an incident radiation (i.e. incident photons, from a quantum mechanical point of view -from now on I will equivalently use the terms "radiation" and "photons" for ease of readability), representing an oscillating electric field, interacts with an atom (or a molecule) it induces an oscillating dipole moment on the atom itself and, according to the classical theory of electromagnetism, the oscillating dipole moment will re-emit radiation of intensity $I = I_{\text{el}} + I_{\text{Stokes}} + I_{\text{anti-Stokes}}$. The first term I_{el} contributing to the intensity

of re-emitted radiation is the dominant one and it corresponds to elastically scattered photons (the so called *Rayleigh scattering*), re-emitted from the atoms of the lattice with same energy (and therefore same frequency and wavelength) and same phase of the incident photons. The second and third terms, I_{Stokes} and $I_{\text{anti-Stokes}}$, although less dominant, are those contributing to the inelastic Raman scattering of incident light we are interested in: I_{Stokes} is associated to a photon re-emitted from the atom with lower energy (therefore lower frequency) and different phase with respect to the incident photons, while $I_{\text{anti-Stokes}}$ corresponds to a photon re-emitted from the atom with higher energy (therefore higher frequency) and again different phase with respect to the incident radiation. The energy difference $\left|\Delta E_{\text{phot}}\right| = \left|E^{\text{em}}_{\text{phot}} - E^{\text{inc}}_{\text{phot}}\right| = \left|h\left(\nu^{\text{em}}_{\text{phot}} - \nu^{\text{inc}}_{\text{phot}}\right)\right|$ between the absorbed (incident) and emitted photon energies (E^{inc}_{phot} and E^{em}_{phot} respectively, while ν^{inc}_{phot} and ν^{em}_{phot} are the associated photon frequencies) is exactly equal to the energy of the excited (Stokes) or absorbed (anti-Stokes) phonon vibrational mode of the atoms in the lattice and it is independent of the absolute values of the energies of the photons (since $\left|\Delta E_{\text{phot}}\right|$ corresponds to the energy difference between two resonant states characterizing the phonon spectrum of the crystal under investigation):

$$\left|\Delta E_{\text{phot}}\right| = E_{\text{phon}} = \hbar\omega_{\text{phon}} \tag{72}$$

where $\hbar$ is the reduced Planck constant and ω_{phon} is the phonon frequency. The quantum mechanical treatment of the Raman scattering process is a bit more complex since it involves the use of second order perturbation theory to solve the the time-dependent Schrödinger equation describing the system composed by the field (the photons) and the atoms in the lattice. In perturbation theory the Raman effect is associated to the absorption and subsequent re-emission of a photon via an intermediate excited quantum state of the material, corresponding to a vibrational mode of the atoms in the crystal: the intermediate state can be either a "real" stationary state or also a virtual state. By the way, from a qualitative point of view, the classical and quantum mechanical treatments of the Raman phenomenon rely on the same physical principles describing light inelastic scattering. A comprehensive schematic view of the different possible outcomes of a scattering event between incident light and atoms in a crystal is shown in Figure 91.

The spectrum showing the intensities of emitted photons is called *Raman spectrum* and it is displayed in terms of the Raman shift $\pm\left|\Delta k_{\text{phot}}\right| = \pm\left|k^{\text{inc}}_{\text{phot}} - k^{\text{em}}_{\text{phot}}\right| = \pm\left|\frac{1}{\lambda^{\text{inc}}_{\text{phot}}} - \frac{1}{\lambda^{\text{em}}_{\text{phot}}}\right|$ (where the "+" sign is associated to Stokes Raman scattering, the "-" sign to anti-Stokes Raman scattering and $\lambda^{inc}_{\text{phot}}$, $\lambda^{em}_{\text{phot}}$ are the incident and emitted photons wavelengths respectively), so according to the energy difference with respect to absorbed incident photons. The Stokes and anti-Stokes spectra form a symmetric pattern above and below the absorbed energy of the incoming photon, because of the symmetric behaviour of relation 72 with respect to $E^{\text{inc}}_{\text{phot}}$ when dealing with the same upper and lower resonant states involved by the light scattering event (so, with the same value of the phonon energy E_{phon}). However, since the intensities of the pairs of Stokes/anti-Stokes symmetric peaks depend on the population of the initial states of the material, they will be in general different. Indeed, at thermal equilibrium, it is possible to show, by applying the laws of Statistical Mechanics, that the upper state will have a lower

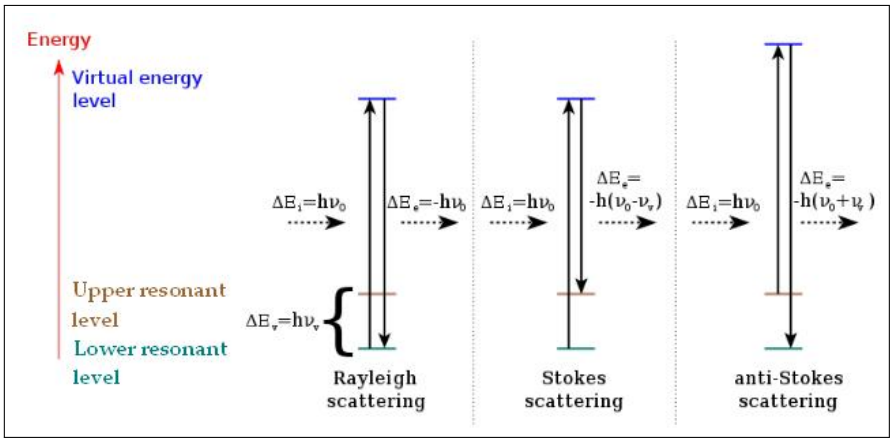

Figure 91: Schematic representation of a light scattering event. Schematic view of the possible outcomes of a scattering event between incident light (photons) and a molecule (an identical representation holds for atoms in a crystal). The incoming photon energy is absorbed by the molecule, that is therefore excited in a virtual state. When the molecule relaxes back, three possibilities may occur: (*left*) it goes back to the vibrational state it started in, emitting a photon having the same energy of the incoming radiation (Rayleigh elastic scattering); (*centre*) it goes back in an excited vibrational state, higher in energy with respect to its initial state, emitting a photon lower in energy with respect to the incoming radiation (Stokes Raman inelastic scattering producing a phonon); (*right*) it goes back in an vibrational state lower in energy with respect to its initial state, emitting a photon higher in energy with respect to the incoming radiation (anti-Stokes Raman inelastic scattering absorbing a phonon). Adapted from Wikipedia.

or equivalent population with respect to the lower state: as a consequence, the anti-Stokes peaks intensity will be always lower than the corresponding Stokes peaks intensity. Moreover, an important outcome of the quantum mechanical model for Raman scattering is the temperature dependence of the ratio between the intensities of symmetric pairs of Stokes and anti-Stokes peaks, given by ([49]):

$$\frac{I_{\text{Stokes}}}{I_{\text{anti-Stokes}}} = \left[\frac{\chi_{\text{Stokes}}\left(E^{\text{inc}}_{\text{phot}}\right)}{\chi_{\text{anti-Stokes}}\left(E^{\text{inc}}_{\text{phot}}\right)}\right]^2 \left(\frac{\nu_{\text{phot}} - \nu_{\text{phon}}}{\nu_{\text{phot}} + \nu_{\text{phon}}}\right)^3 e^{h\nu_{\text{phon}}/k_{\text{B}}T} \tag{73}$$

where ν_{phot} is the frequency of the incoming photon, ν_{phon} the frequency of the excited phonon of the crystal, $\chi_{\text{Stokes}}\left(E^{\text{inc}}_{\text{phot}}\right)$ $\left(\chi_{\text{anti-Stokes}}\left(E^{\text{inc}}_{\text{phot}}\right)\right)$ the Stokes (anti-Stokes respectively) Raman susceptibility[1], $E^{\text{inc}}_{\text{phot}}$ the incoming photon energy, h the Planck constant, k_{B} the Boltzmann constant and T the absolute temperature of the material. Other details about the general theory of the Raman effect can be found in [67, 102], but they are beyond the scopes of this thesis.

The Raman spectrum of exfoliated monolayer graphene deposited onto a 300 nm thick SiO_2 layer exhibits two most prominent features: the *G band* at $\sim 1582\,\text{cm}^{-1}$ and the *G′ band* (also called *2D band* since it has a frequency almost twice the frequency of the D band) at $\sim 2700\,\text{cm}^{-1}$, using laser excitation (providing the incoming photons for the Raman scattering events) at 514 nm. Moreover, in the case of disordered samples (having defects such as vacancies in the crystal structure) or at the edges of a graphene crystal domain another feature appears in the spectrum: the so called disorder-induced *D band* at $\sim 1350\,\text{cm}^{-1}$. A typical spectrum of defected monolayer graphene, acquired at laser wavelength 514 nm onto SiO_2, appears therefore as illustrated in Figure 92.

The three prominent peaks of graphene are all related to the Raman active phonon modes present in the phonon spectrum of this material (Figure 93). Since, as discussed in Chapter 1, monolayer graphene unit cell contains two carbon atoms (A and B), its phonon spectrum show six dispersion bands: three optic (O) branches and other three acoustic (A) branches. Moreover, the phonon branches are divided according to whether the atoms vibrations are perpendicular to the graphene plane, i.e. out-of-plane (o), or they are in-plane (i). Finally, atomic vibrations are classified as longitudinal (L), if atoms vibrate in parallel to the A-B carbon direction, or as transverse (T) if atoms vibrate perpendicularly to it. As a consequence, along the high symmetry directions ΓM and ΓK of graphene 1$^{\text{st}}$ Brillouin zone, we can identify six different phonon bands: iLO, iLA, iTO, iTA, oTO, oTA.

Near the Γ point (at the zone centre where $\|\mathbf{k}\| \sim 0$) the iTO and iLO phonon modes are degenerate and correspond to the vibrations of sublattice A against sublattice B: the degenerate (at zone centre) modes belong to the two-dimensional representation E_{2g} and they are therefore Raman active modes (see [110, 195] for more details). For points inside the 1$^{\text{st}}$ Brillouin zone the iTO and iLO branches are not anymore degenerate and are characterized by different symmetries. The G band of graphene is exactly associated to the doubly degenerate iTO-iLO phonon band at the zone

1 In general the Raman susceptibilities depend on the incoming photon energy: nonetheless, in the specific case of graphene, they are almost equal and slowly varying with $E^{\text{inc}}_{\text{phot}}$, as long as the latter is far enough from the π Plasmon resonance at $\sim 3.5\,\text{eV}$. Therefore, the factor with Raman susceptibilities can be usually neglected in graphene.

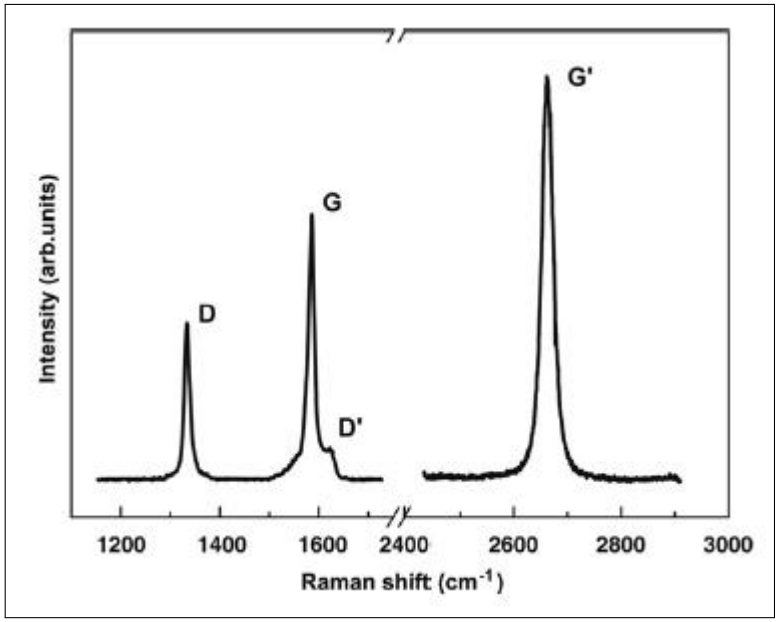

Figure 92: **Raman spectrum for defected exfoliated monolayer graphene onto SiO_2 substrate.** Image showing a typical Raman spectrum acquired at laser wavelength 514 nm, characterizing monolayer graphene on top of an SiO_2 substrate. G and 2D peaks are clearly visible; moreover, disorder-induced D and D′ peaks are also present, meaning that there are defects in the graphene crystal structure or that the spectrum has been acquired on a graphene edge. Adapted from [110].

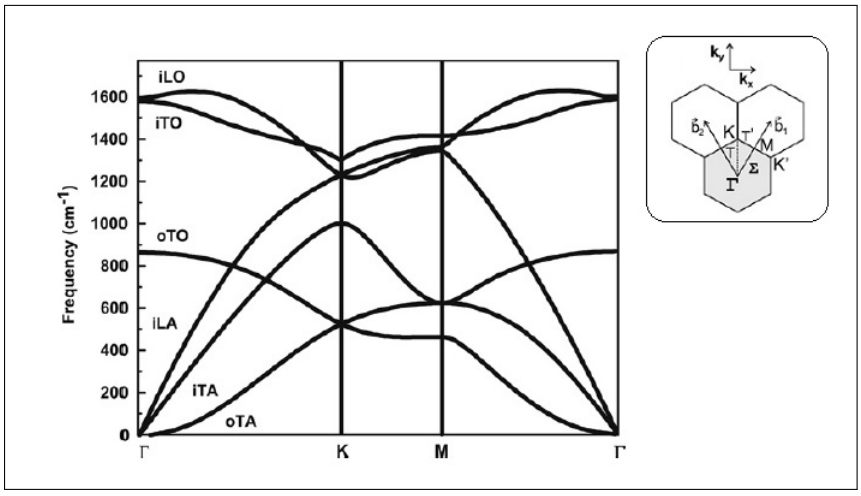

Figure 93: **Phonon dispersion bands in graphene.** Calculated phonon dispersion bands for graphene along the high symmetry direction $\Gamma KM\Gamma$ of the 1st Brillouin zone (shown on the top right), highlighting the six phonon branches: iTO, iTA, oTO, oTA, iLO, iLA. Graphite shows similar phonon dispersion curves. Adapted from [110].

centre: it comes from a first-order one phonon single resonant scattering process involving the absorption of the incoming photon of energy E_{laser}, the subsequent creation of an electron-hole pair (with $E_{\text{electron}} = E_{\text{laser}}/2$), the scattering of the electron with a phonon (characterized by wavevector $\left\|\mathbf{q}_{\text{phon}}\right\| \sim 0$) and the recombination of the electron with the hole, giving rise to the emission of an outgoing photon. The process is called *intra-valley* process since it involves points belonging to the same Dirac cone around only one Dirac point (K or equivalently K').

The first-order Raman scattering processes responsible for the G band in graphene and graphite spectrum is schematically described, in terms of Feynman diagrams, as shown in Figure 94. The individual diagrams are graphical representations of the terms that arise from a time dependent perturbation theory analysis of the probability of a Raman scattering event using Fermi's Golden Rule ([8, 49]). The diagrams describe sequential processes such as:

- the creation of an electron-hole pair (solid arrows) by absorption of an incoming photon (zigzag lines), the scattering by either the electron or the hole with a phonon (dotted arrow) and the emission of the outgoing shifted photon after recombination of the scattered electron-hole pair (Figure 94, diagrams (a) and (b));

- the creation/annihilation of a low-energy electron-hole pair by the incoming and outgoing photons and the subsequent emission of a phonon by the electron-hole pair (Figure 94, diagram (e));

- other terms (Figure 94, diagrams (c) and (d)) including the direct decay of the incident photon into the scattered photon and the emitted phonon (Figure 94, diagram (f)).

All the diagrams contribute (at first-order) to the final amplitude associated to the Raman scattering event giving rise to the G band. Higher order scattering processes involving the emission of more than one phonon are described by introducing additional electron-phonon vertices. Further details about the evaluation of the diagrams can be found in [8, 103].

An important feature of the G band for monolayer graphene samples is its dependence on the eventual presence of dopants in the material. Indeed, as reported in [203], the width and the frequency of the G band is affected by changes in the gate voltage eventually applied to monolayer graphene: since, as we have seen in Chapter 1, by varying the gate voltage V_g the Fermi level of graphene is continuously shifted upwards or downwards with respect to the Dirac point (meaning that a change in V_g is equivalent to doping the material by increasing electrons or holes carrier density), the dependence of G band linewidth and frequency on V_g can be interpreted as a dependence on doping. This dependence is due to the fact that, when the Fermi level is moved away from the Dirac points by applying a $V_g \neq 0$, either the initial states for optical phonon excited electronic transitions are empty or the final states are filled (Figure 95). This means that the phonons at the Γ point of the 1^{st} Brillouin zone can no longer excite electron-hole pairs across the Fermi level and this fact generates both the change in linewidth and the shift in frequency of the G peak. In particular, as shown in Figure 95, a blueshift of the G band is always associated to the presence of doping in graphene (so to the application of an external gate voltage V_g), independently on the type of charge carriers dopants (electrons or holes).

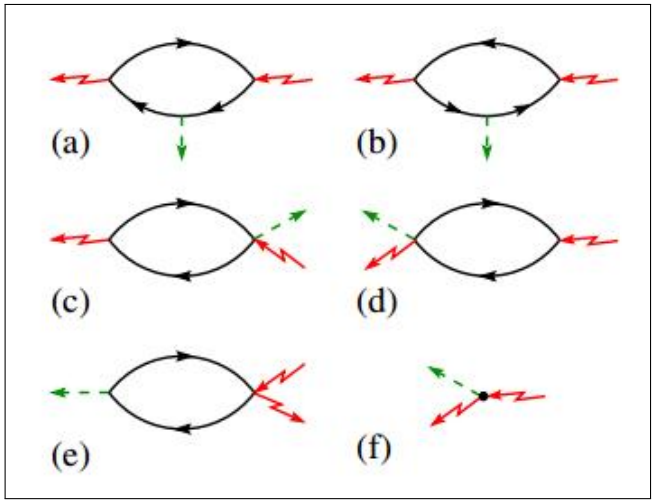

Figure 94: First-order Raman scattering processes contributing to G band. Schematic representation of the Feynman diagrams contributing (at first-order) to the probability amplitude of the Raman scattering events originating the G band. Solid arrows represent electronic excitations, dotted arrows phonons and zigzag lines incident and emitted photons. See text for details. Adapted from [8].

In any case, the G band is not a peculiarity of graphene, since it is found also in graphite and in carbon-related crystal structures. The most peculiar Raman peak for graphene systems is instead associated to the very sharp 2D band found in their spectrum (Figure 92). This band is related to second-order two phonons second and triple resonant scattering processes involving iTO phonons near the K Dirac point at the edge of the 1^{st} Brillouin zone. Exactly at the K point, the phonon mode coming from the iTO branch is non-degenerate and belongs to the A_1' irreducible representation of the point group D_{3h} (in Schoenflies notation). The double resonance process associated to the 2D band involves the excitation of an electron-hole pair by absorption of the incoming photon (with energy E_{laser}). The electron, of wavevector $\mathbf{k}$ around K, is then inelastically scattered by a phonon of wavevector $\mathbf{q}_{\text{phon}}$ to a point belonging to a circle around K', with wavevector $\mathbf{k}' = \mathbf{k}+\mathbf{q}_{\text{phon}}$. The electron is then scattered back to a $\mathbf{k}$ state around K by a second phonon and it recombines with an hole at same $\mathbf{k}$ emitting the outgoing photon detected in Raman analysis.
The process responsible for the disorder-induced D band is quite similar, since it is again a second-order double resonance process, but it involves only one phonon (as in the case of the G band): indeed, for the D band, an electron belonging to a point in a circle around K Dirac cone is *elastically* scattered to a point belonging to the K' cone by a defect in the crystal (a not by a phonon) and it is then inelastically scattered back by a phonon (as for the 2D band). The resonance processes here described responsible for the D and 2D bands are called *intervalley* processes since they involve two points belonging to two different Dirac cones, one around the K Dirac point and one around the K' Dirac point.
In principle many different initial electronic state around the K Dirac point and phonons with different symmetries (with respect to the iTO phonons symmetry) and wavectors may be involved in double resonance processes. However, due to singularities in the density of phonon states satisfying the

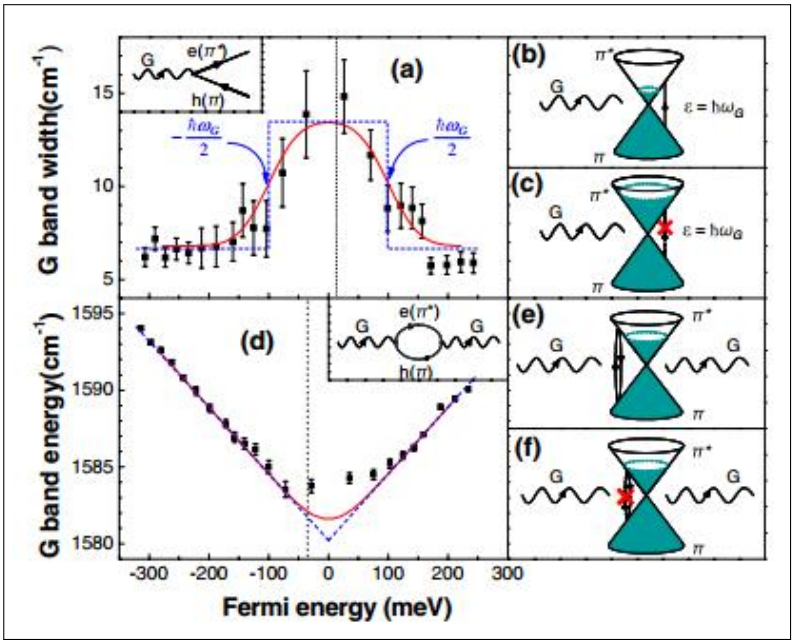

Figure 95: G band dependence on applied external gate voltage V_g. Experimental detection of the G band linewidth and frequency dependence on varying gate voltage V_g in electrostatically-gated monolayer graphene (equivalently, doped graphene): (a) G band width as a function of V_g (V_g moves away from the Dirac point, pinned at $E_F = 0$, the Fermi level); (b) broadening of the G phonon due to phonon decay into electron-hole pairs (allowed because of the low doping level); (c) sharpening of the G band due to the fact that phonon decay is forbidden at high doping (both *p*- or *n*-type) because of Pauli Exclusion Principle; (d) G band frequency blueshift in doped graphene due to reduced phonon energy renormalization at high doping; (e) renormalization of G phonon energy due to interaction with virtual electron-hole pairs; (f) virtual electron-hole pair transitions with energy ranging from 0 to $2|E_F|$ are forbidden at high doping. This fact reduces the renormalization of the G phonon energy. In (a) and (d) dashed blue lines and solid red lines are the fits to experimental data for ideal and nonuniform graphene, respectively. The insets are Feynman diagrams for electron-phonon coupling applicable to the case of the G phonon. In (b), (c), (e) and (f) only the diagrams for *n*-type doped graphene are shown; diagrams for *p*-type graphene are similar. Electron-phonon coupling strength is throughout assumed to be $D = 12.6\,\text{eV}\,\text{Å}^{-1}$. Adapted from [203].

double resonance condition $\left\|\mathbf{q}_{\text{phon}}\right\| \simeq 2\,\|\mathbf{k}\|$, the angular dependence of the electron-phonon scattering matrix elements and the destructive interference effects when the Raman transition probability is evaluated, only few specific double resonance processes contribute strongly to the D and 2D bands ([]): for example, only iTO phonon branches are involved in intervalley double resonance processes, since only these phonons couple to the electrons along directions associated with singularities in the phonon density of states satisfying the double resonance condition.

Moreover, when E_{laser} is increased with respect to the Fermi level of undoped graphene (pinned at the Dirac points) the wavevector $\mathbf{k}$ of the electron involved in the 2D double resonance process moves away from the K Dirac point and therefore the amplitude of the corresponding phonon wavevector $\left\|\mathbf{q}_{\text{phon}}\right\|$ is also increased. As a consequence, by changing laser energy it is possible to observe the behaviour of the phonon energy $\hbar\omega_{\text{phon}}$ along the dispersion band of the phonon involved in the double resonance process. Such an effect has been indeed theoretically calculated and observed experimentally ([47]), as shown in Figure 96a, in the case of exfoliated graphene deposited onto an insulating SiO_2 substrate. However, it is worth nothing that the effect is independent of the substrate, since it has been clearly detected also in Raman spectra acquired directly on a Cu substrate ([28]), as illustrated in Figure 96b.

The triple resonance process also responsible for the 2D band proceeds in the same way of the double resonance once, with the only difference that both the electron and the hole created by the absorption of the incoming photon are scattered from the Dirac cone around K to the Dirac cone around K' and they recombine at the $\mathbf{k}'$ state around K', instead of the electron being scattered back to K Dirac cone for recombination. A comprehensive schematic view of the Raman scattering processes involved in the formation of D, G and 2D peak characterizing monolayer graphene is reported in Figure 97.

In particular, the triple resonance process shown in Figure 97 explains the sharpness and the large intensity of the 2D band, relative to the intensity of the G band, characterizing monolayer graphene Raman spectra: it is worth pointing out that this triple resonance process, in which all the steps are resonant, can occur only because of the peculiar linear electronic dispersion relation of monolayer graphene. Hence, since the graphene electronic band structure is strictly related to the number of graphene layers, it is expected that the Raman shift (i.e. the frequency) and the full width at half maximum (FWHM) of the graphene 2D band will change by changing number of layers. Indeed, this fact has been experimentally observed in the seminal work of A. C. Ferrari and co-workers ([47]): it has been clearly shown that while for monolayer graphene the 2D peak is centred at $\sim 2690\,\text{cm}^{-1}$ (at laser wavelength 514 nm) and it is characterized by a sharp (i.e. with FWHM $\sim 24\,\text{cm}^{-1}$) single Lorentzian shape, for bilayer graphene the same peak is blueshifted and, more important, it is broadened, being fitted in this case with four Lorentzian curves. The broadening is strictly related to the electronic band structure of bilayer graphene, showing completely different features with respect to the band dispersion of monolayer graphene. The same behaviour (frequency blueshift and shape broadening) is observed by increasing the number of graphene layers, as shown in Figure 98a. Moreover, the ratio I_{2D}/I_G between 2D and G intensities is found to decrease while the number of graphene layers is increased (Figure 98b). Therefore, we can conclude that the position, the sharpness and the relative intensity

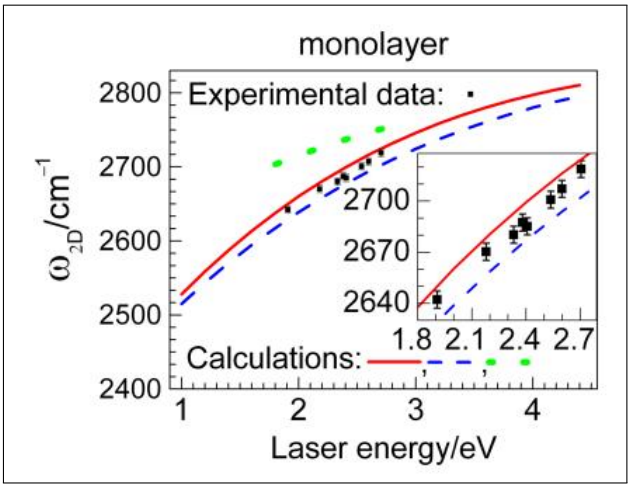

(a)

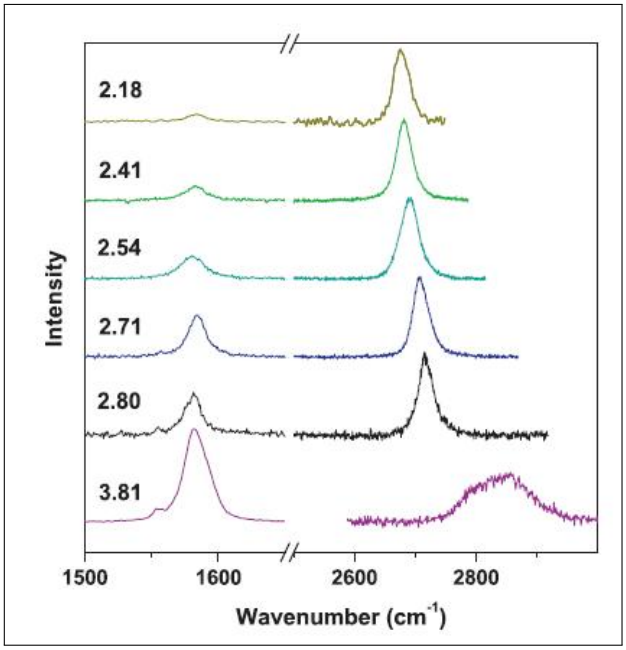

(b)

Figure 96: 2D band Raman shift dispersion as a function of E_{laser}. Images showing theoretically calculated and experimentally observed dispersion of the 2D band frequency as a function of the excitation energy laser E_{laser} for monolayer graphene: (a) in the case of Raman spectra acquired on exfoliated graphene deposited onto SiO_2 (solid squares). Dotted, solid and dashed lines refer to the dispersion of the 2D band of monolayer graphene with laser energy as calculated using different approaches (Density Functional Theory, tight-binding method and Green's function theory. The inset is a magnified view of the dispersion curve in the visible range and show an almost perfect agreement between theory and experiments. Adapted from [194]; (b) in the case of Raman spectra acquired directly on monolayer graphene grown by CVD on a Cu foil, without transfer process. The evolution of the G peak is also reported. Adapted from [28].

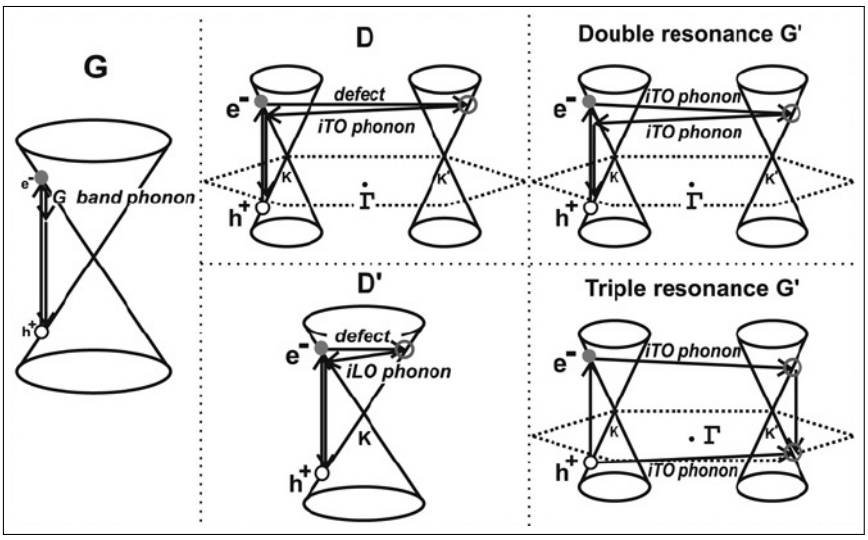

Figure 97: **Raman resonance processes responsible for D, G and 2D bands in monolayer graphene spectra.** Schematic view of the first-order and second-order resonance processes responsible for D, G and 2D bands formation in monolayer graphene spectra: (*left*) first-order one (doubly degenerate) phonon intra-valley process responsible for the G band; (*centre*) on top, second-order one phonon intervalley double resonance process responsible for the D band (involving a crystal defect) and on bottom, same but intra-valley process responsible for the D′ band shown in Figure 92; (*right*) on top, second-order two phonons intervalley double resonance process responsible for the 2D band and on bottom, same second order but triple resonance process. Resonance points are shown as open circles. Adapted from [110].

of the 2D peak relative to the G peak is a clear fingerprint allowing to determine in an unambiguous way the number of graphene layers present on an insulating SiO_2 substrate. In particular, it allows to clearly distinguish up to $\sim$ 5–6 graphene layers. Nonetheless, the described method works well to establish the number of graphene layers only for exfoliated graphene (however, also in this case the number of Lorentzian curves needed to fit the 2D band as number of graphene layers increases and the I_{2D}/I_G intensities ratio are slightly affected also by the laser energy employed to acquire the Raman spectra, as reported in [49, 110]): for few-layer graphene grown on SiC ([49]) and, even more important for my purposes, for few-layer graphene grown by CVD on a catalytic substrate ([110]), the evolution (and, in particular, the broadening and the shape) of the 2D peak with the number of graphene layers is different and does not follow such a clear behaviour (Figure 99).

Apart from the differences due to the graphene growth method, to the kind of substrate used for graphene transfer and to the energy laser, it is usually assumed ([31, 47]) that a Raman spectrum identifying monolayer graphene, in the case of laser wavelength 514 nm and graphene deposited onto a SiO_2/Si substrate after mechanical exfoliation of HOPG, should display at room temperature the following characteristics:

- a G band at $\sim 1580\,cm^{-1}$;
- a 2D band at $\sim 2690\,cm^{-1}$ characterized by FWHM $\sim 24\,cm^{-1}$;
- I_G/I_{2D} ratio $\simeq$ 0.2–0.3.

Besides the 2D band, also the the G peak characterizing graphene Raman spectrum shows interesting features, quite important in order to explain in a proper way the results reported in Sec. 3.3.3, that I can summarize as follows:

1. **G band frequency dependence on number of graphene layers**
   Although the number of graphene layers affects predominantly the frequency, intensity and shape of the 2D band, a slight dependence of the G band frequency on this feature has been reported in literature ([193]). Indeed, a relation connecting the number n of graphene layers present on a certain substrate and the frequency ω_G of the G peak has been extrapolated in the same work and it can be written as[2]

$$\omega_G = 1581.6 + \frac{11}{1 + n^{1.6}}. \tag{74}$$

   It is therefore clear, from 74, that increasing the number of graphene layers the G band is redshifted, as illustrated in Figure 100 (an opposite behaviour with respect to the 2D band, that is blueshifted by increasing number of layers, as shown in Figure 98);

2. **G band intensity dependence on number of graphene layers**
   Number of graphene layers affects not only G band frequency, but also G band intensity ([131, 197]): this is understood as more carbon atoms are detected by laser incident light for multilayer graphene and because of interference effects occurring in multilayer graphene, induced by multiple reflection of the light in the multilayer structure. The G band intensity of graphene layers depends indeed on the electric field distribution inside the material, which is a result of interference effects

2 Other works ([61]) has reported a slightly different relation, but qualitatively the behaviour of the G peak frequency vs. number of graphene layers curves is similar in both cases.

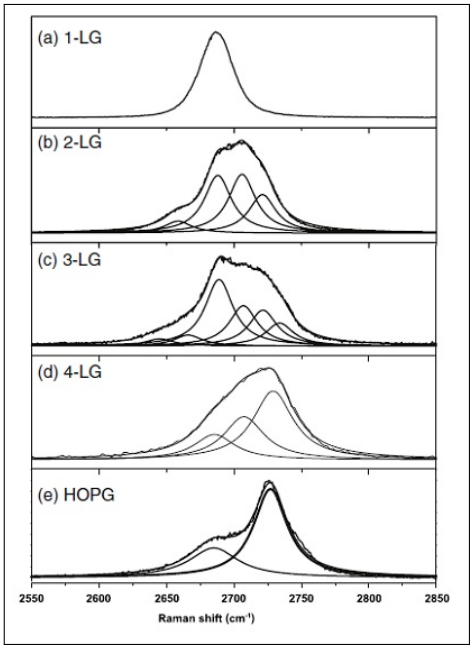

(a)

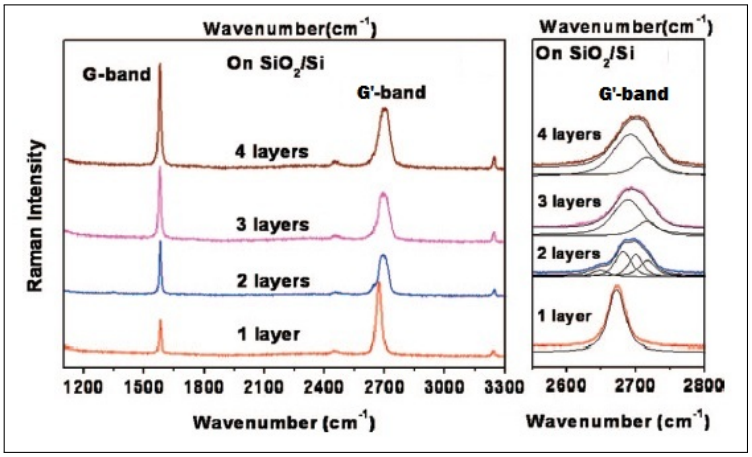

(b)

Figure 98: Evolution of 2D band frequency and shape and of I_{2D}/I_G ratio with number of graphene layers. Images showing the evolution in the shape and position of the 2D band with number of graphene layers: (a) in the case of exfoliated graphene deposited onto SiO_2, with acquisitions carried out with laser wavelength $\lambda = 514\,\text{nm}$, a clear broadening of the peak is visible when passing from 1 graphene layer (for which only 1 Lorentzian is needed to fit the peak) to 3 layers (for which 4 Lorentzian curves are instead necessary, as it is for bilayer graphene). Passing from 4 to HOPG the splitting of the band closes up again (the peak characterizing HOPG is indeed fitted with 2 Lorentzian curves), being in any case more broadened than for monolayer graphene. A blueshift in the frequency of the band is moreover clearly visible. Adapted from [110]; (b) another schematic view of the evolution of G and 2D bands frequencies, intensities and FWHMs with the number of graphene layers for graphene deposited onto a SiO_2/Si substrate. In particular, on the left is clearly visible that I_G increases, while I_{2D} decreases while increasing number of graphene layers: as a consequence, the I_{2D}/I_G ratio is decreasing when the number of graphene layers present on the substrate is increased. The evolution of the G and 2D bands are largely completed at the $\sim$ 5–6 layer level, meaning that Raman spectroscopy allows to distinguish in an unambiguous way up to $\sim$ 6 graphene layers. Adapted from [198].

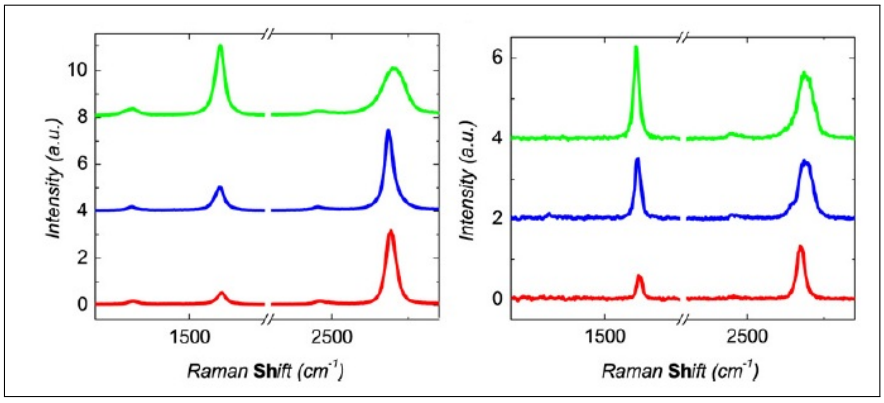

Figure 99: Evolution of G and 2D band frequency, shape and intensities with number of graphene layers for CVD graphene grown on Ni. Raman spectra of mono-, bi- and tri-layer graphene acquired at laser wavelength 532 nm: (*left*) in the case of graphene grown through a CVD process on a Ni⟨111⟩ precursor and then transferred onto an SiO_2/Si substrate; (*right*) in the case of graphene prepared by mechanical exfoliation of HOPG directly onto a SiO_2/Si substrate, shown for comparison. It is clear that the shape of the 2D band evolves in different ways in the two cases. Adapted from [110].

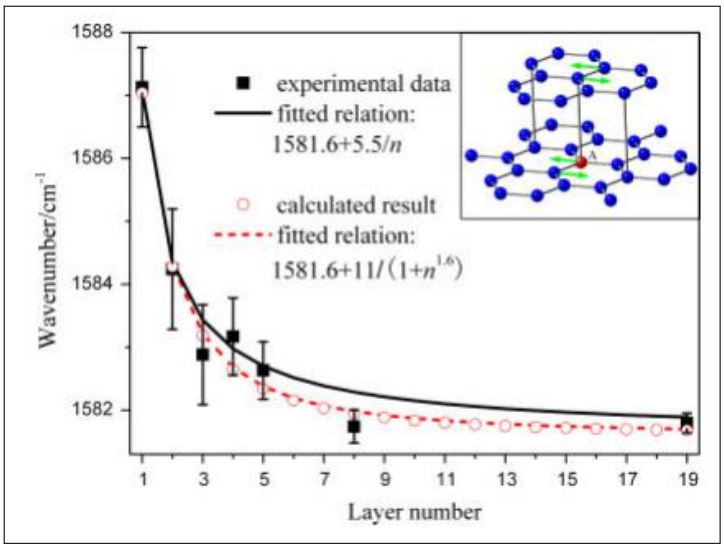

Figure 100: Evolution of G band frequency with number of graphene layers. Theoretical prediction and experimental observation of the G band frequency dependence on number of graphene layers. Squares and solid line refer to experimental data and fitted relation ($\omega_G = 1581.6 + \frac{5.5}{n}$) for the G peak Raman shift vs. number of layers function, as evaluated by [61] for mechanically exfoliated multilayer graphene films supported onto Si⟨100⟩/SiO_2 substrates. Error bars indicate the data range of seven independently repeated experiments. Circles and dashed lines refer instead to G frequency values calculated in [193] and to the least-squares fit of the data, giving as a result the relation 74. It is clear that in both cases the peak is blueshifted while decreasing number of graphene layers. In the upper-right inset the atomic displacements responsible for the G peak in graphite are shown (these displacements correspond to sublattice A against sublattice B vibrations). Adapted from [193].

between all transmitted optical path in graphene/graphite sheets. The total amplitude of the electric field at a certain depth z in the graphene sheets is viewed as an infinite sum of the transmitted laser intensities. Moreover, the electric field amplitude is affected also by the multi-reflection of scattering Raman light in graphene at the graphene/air and graphene/substrate interfaces. Thus, the total Raman signal contributing to the G band is a result of interference of transmitted laser light followed by multiple reflection of Raman scattering light. The dependence of the intensity of the Raman signal on different thickness of graphite ranging from bulk, which is opaque (no light is reflected from the substrate), to monolayer graphene, where only few percent of the incident light is absorbed in the layer for a single pass, and reflected light from the substrate can produce a significant enhancement of the optical fields at the graphene layer, shows a peak (Figure 101) for graphene thicknesses ($\sim$ 9 layers) where comparable fractions of the light are either reflected or transmitted by the graphene layer. For such multilayer graphene thicknesses, there is a substantial interference enhancement of the Raman signal, that is therefore larger than the signal of bulk graphite[3].

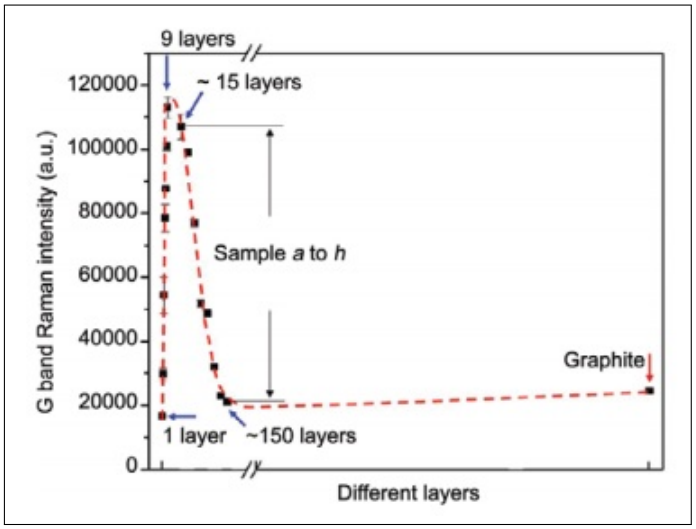

Figure 101: G peak intensity dependence on number of graphene layers. The G band Raman intensity of graphene sheets as a function of the number of layers. The red dashed curve is a guide to the eye. The peak at $\sim$ 9 layers in G peak intensity is due to interference enhancement effects induced by multi-reflection of Raman scattering light. Adapted from [131].

3. **G band frequency dependence on temperature**
An important feature of the G band characterizing graphene Raman spectra is the dependence of its frequency on the temperature of the sample subjected to Raman analysis. Indeed, as reported in [18] and shown in Figure 102a, the G band Raman shift for monolayer graphene obtained by micromechanical cleavage of bulk Kish graphite and deposited onto insulating SiO_2/Si substrates is redshifted by increasing

3 It is worth pointing out that for similar arguments, based on interference effects involving the Raman scattering light, the intensities of G and 2D graphene peaks show also a dependence on the thickness of the SiO_2 insulating layer present in graphene/SiO_2/Si samples, as reported in [49].

temperature, as evinced by characterizing with micro-Raman analysis the samples heated at different temperatures. The change of phonon frequency with temperature is regarded as manifestation of the anharmonic terms in the lattice potential energy and it allows to determine the temperature coefficient χ for the graphene G mode, defined as the slope of the frequency vs. temperature linear dependence. The same change in G band frequency, although much less pronounced, has been detected on monolayer graphene grown by CVD on Cu foils (both on graphene supported on a substrate and on graphene suspended over properly patterned holes), by characterizing with micro-Raman analysis graphene samples annealed at different temperatures (Figure 102b). The latter effect will be of great importance in the discussion of the results that I will report in Sec. 3.3.3, regarding the CVD growth of graphene on Cu thin films.

To conclude this brief review about Raman spectroscopy on graphene it is worth mentioning that the G and 2D band frequencies and intensities characterizing graphene may depend also on many other effects, as for example chemisorption of chemical species like H_2 and O_2 ([106, 174]) and by strain applied to graphene sheets ([46, 121]).

Further details about Raman spectroscopy on graphene and related systems can be found in literature: the number of works on the topic is huge and I remind the reader only to the reviews [37, 49, 110, 157, 158, 183] and references therein.

For what concerns the experimental instrumentation, Raman spectroscopy analyses on graphene samples have been performed with two *Renishaw inVia Raman Microscope* instruments present at the Nanostructured Interfaces and Surfaces (NIS) Centre of Excellence of the University of Turin and with the help of Dr. A. Damin. Both the instruments (shown in Figure 103) are equipped with two laser exciting lines:

- one instrument with a He-Cd laser (Kimmon IK Series) at wavelengths 325 nm and 442 nm;
- the other instrument with an Ar^+ Laser (SpectraPhysics) at wavelength 514 nm and with a diode laser (Renishaw) at wavelength 785 nm.

All the Raman spectra characterizing my samples have been acquired employing only two laser wavelengths, at 442 nm and at 514 nm. The instruments allow to focus the laser incident beam on spots of $\sim 1\,\mu m^2$ and they are equipped also with optical microscopes allowing to search for the regions of the samples to be subjected to the acquisition process.

3.1.2 XPS technique

XPS is a quantitative spectroscopic technique, considered non-destructive, widely used in surface physics, mainly to determine the chemical composition of the surface region ($\sim$ 5–10 nm in depth inside the sample) of a material and the identification of chemical bonds between specific atoms present on the sample surface.
The technique is based on the exploitation of the photoelectric effect ([41]), according to which electrons are emitted from a material upon absorption of photons (in XPS the incident X-Ray radiation) of energy $E_{phot} = h\nu$ (where ν is the frequency of the incoming radiation) greater than the binding energy E_b of the electrons in the material and of the work function Φ of the

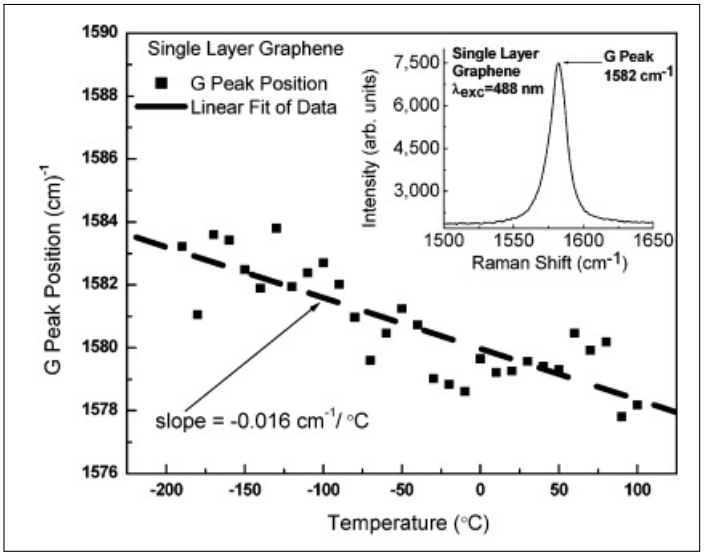

(a)

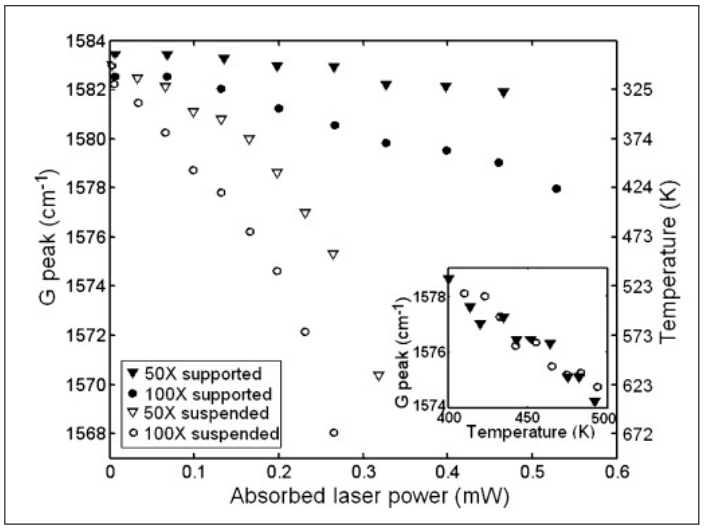

(b)

Figure 102: Temperature dependence of G peak frequency in monolayer graphene. Experimental evaluation of the temperature vs. G peak frequency linear dependence for monolayer graphene: (a) in the case of mechanically exfoliated graphene deposited onto a 300 nm thick SiO_2/Si substrate. Raman spectroscopy has been carried out at laser wavelength 488 nm. The G mode temperature coefficient (i.e. the slope of the straight line fitting the experimental data) is also reported. In the inset, the shape of the G peak is illustrated. Adapted from [18]; (b) in the case of graphene grown by CVD on a 25 µm thick Cu foil. G peak frequency and temperature measured on the supported graphene and at the center of the suspended graphene are shown as a function of absorbed laser power when the stage temperature is kept at room temperature. The inset shows the redshift of the G peak frequency measured with low laser power on both supported and suspended graphene as a function of temperature. Raman spectra have been acquired at laser wavelength 532 nm. It is clear from the experimental data that the presence of the supporting substrate highly reduces the in-plane thermal conductivity of graphene: therefore, in-plane thermal conductivity of monolayer graphene grown by CVD on Cu becomes comparable to the thermal conductivity of the Cu substrate itself. Adapted from [16].

Figure 103: Instrumentation for Raman spectroscopy at NIS Centre - Turin. Image of the Raman spectrometer present at NIS Centre - Turin employed for graphene characterization. The instrument is equipped with four laser exciting lines, but I have always worked at only two wavelengths: 442 nm and 514 nm.

spectrometer. The kinetic energy of the photoemitted electron is therefore determined with an energy conservation argument as

$$E_{kin} = h\nu - E_b - \Phi. \tag{75}$$

The most important observation to take advantage of the photoelectric effect in XPS analysis relies on the fact that the binding energy of core electrons (those not involved in chemical bonds) in atoms is a characteristic of each atom of the Periodic Table and it is slightly affected by chemical bonding and surroundings ([132]): therefore, E_b is a clear signature of the atom to which the photoemitted core electron belongs to (Figure 104). As a consequence, by detecting the kinetic energy distribution of the photoemitted core electrons from a material irradiated with electromagnetic rays of known frequency ν, it is possible, through inversion of 75, to reconstruct the binding energy distribution of the same electrons. Since the binding energy is in one-to-one correspondence with the atoms of the Periodic Table, it is possible from this distribution to get an unambiguous information about the chemical species and elements constituting the material and also about their chemical states.

In XPS, soft X-Rays (with $E_{phot} \sim 1.5\,keV$) illuminate a region of the sample to be analysed and the kinetic energy of the photoemitted electrons is detected (Figure 105a): however, a typical XPS spectrum does not show the nummber of detected electrons as a function of kinetic energy, but rather the counts as a function of binding energy (univocally determined as $E_b = h\nu - E_{kin} - \Phi$, where ν and Φ are known, while E_{kin} is experimentally detected), as shown in Figure 105b.

Typical XPS experiments are carried out in Ultra High Vacuum (UHV) conditions in order to avoid contaminations of samples under study and, above all, an eventual change in kinetic energy of photoemitted electrons due to collisional events occurring before detection.
Usually, a commercially available XPS system is composed by the following elements (Figure 106):

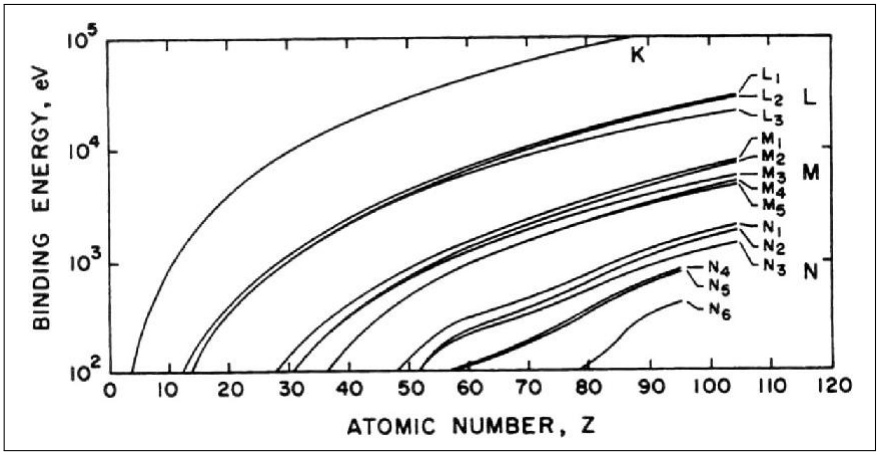

Figure 104: Core level electrons binding energy for several elements. Images showing the dependence of the electrons binding energy on the atomic number Z. The relation allows to determine in a unique way the atomic number once the binding energy is known. Adapted from [26].

- an X-Ray source, producing soft X-Rays by bremsstrahlung (continuous emission) or discrete emission caused by interaction between the electrons emitted by thermionic effect from a cathode and the atoms present in an anode (usually an Al slab);
- a collimator focusing the X-Ray beam and a filter providing a first selection of the desired X-Ray frequencies;
- a monochromator, diffracting the X-Ray beam on a thin disc of natural, crystalline quartz with $\langle 1010 \rangle$ orientation and generating the final X-Ray beam, at fixed energy $\sim 1.5\,\text{keV}$, sent on the sample under study;
- an electron collection lens and an electron energy analyzer, usually a concentric hemispherical analyzer, discriminating electrons kinetic energies by exploitation of spherical capacitance arguments.

The highest spatial resolution achievable in XPS analysis is $\sim 10\,\mu\text{m}$; moreover, electrons detected are those originating from within the top 5–10 nm of the analysed material, since photoelectrons produced deeper into the sample are either recaptured or trapped in various excited states inside it and cannot therefore escape from its surface.

XPS analyses carried out to characterize the graphene samples I have prepared by CVD processes have been alway performed with a commercially available XPS instrument present at the Department of Physics of the University of Turin, with the help of Dr. A. Battiato.

3.2 GRAPHENE TRANSFER PROCESS

Once graphene has been grown by CVD on a catalytic substrate, a transfer process is usually performed in order to put graphene on an insulating substrate (usually a SiO_2/Si wafer). This step is needed in order to fully investigate and exploit intrinsic graphene properties in applications: indeed, the presence of a metal catalyst underlying graphene unavoidably

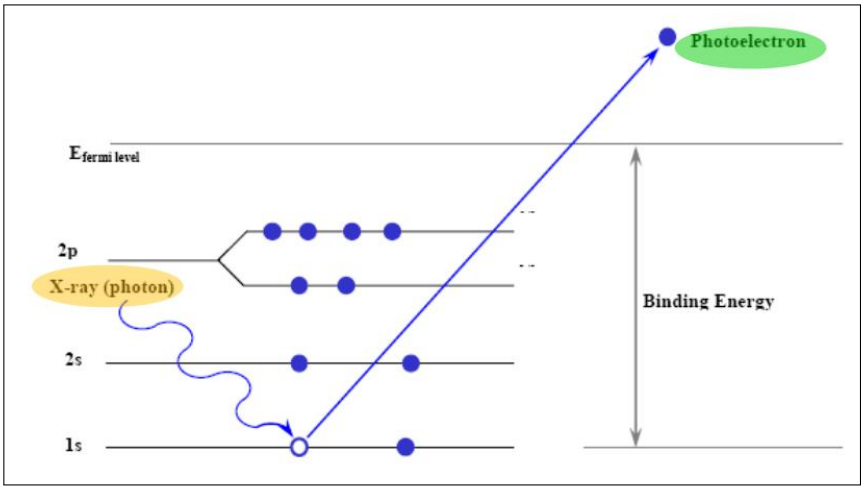

(a)

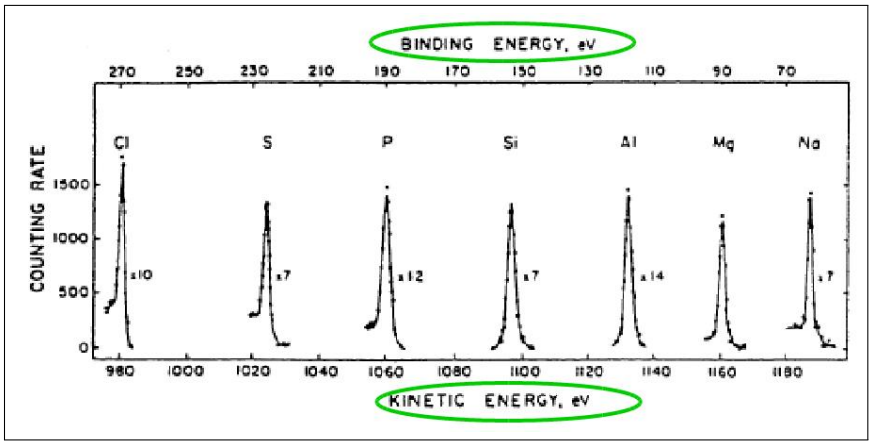

(b)

Figure 105: **Photoelectric effect and typical spectrum for XPS analysis.** (a) Schematic view of photoelectric effect exploited in XPS analysis: the incoming X-Ray is absorbed by the material and its energy excites a core electron, that is emitted and detected; (b) typical spectrum obtained after XPS analysis: the number of electrons detected can be shown as a function either of the experimentally determined kinetic energy or of the binding energy (evaluated through inversion of relation 75). The evaluated E_b is an unambiguous fingerprint of the atom to which the detected electron belongs to. Adapted from [26].

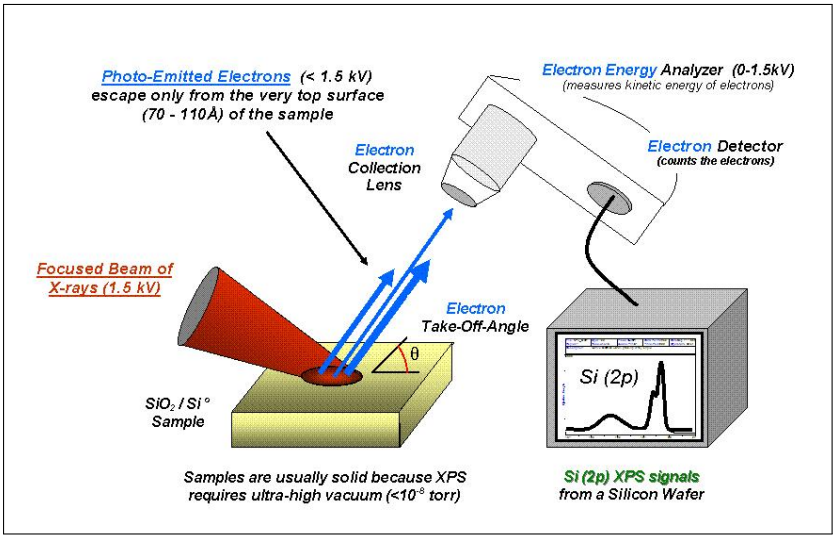

Figure 106: Typical instrumentation for XPS analysis. Schematic view of a typical commercially available system for XPS analysis: soft X-Rays ($E_{\text{phot}} = 1.5\,\text{keV}$), generated by an X-Ray source and properly focused, illuminate a region of the sample to be analysed. Photoemitted electrons escaping the sample surface at a fixed angle are collected in an electron energy analyzer, counting them and measuring their kinetic energies. The XPS signal (spectrum) is then produced on a monitor and it allows to determine the chemical species present on the sample surface. Courtesy of Wikipedia.

worsens the remarkable properties of this material (because of the interactions between graphene and the substrate), in particular the charge carriers mobilities. Moreover, full integration of graphene into conventional device circuitry requires graphene transfer on insulating substrates in order to be compatible with nowadays thin film technology. Although some transfer-free graphene deposition methods have been proposed in the last years ([72, 95, 173]), transfer process remains the most commonly performed step in the majority of the reported works dealing with graphene growth by CVD.

The standard technique suggested in literature ([119]) for carrying out graphene transfer from a metallic catalyst to an insulating substrate is the chemical etching of the metallic species involved in the process. Depending on the kind of metal used to catalyze the dissociation of carbon precursor molecules in the CVD process, different chemical etchant solutions must be employed at the end of the process in order to remove the metallic substrate on which graphene has been grown. The solution commonly used for Ni etching is HCl ([101]), while $FeCl_3$ is the solution usually employed for Cu removal ([115]).

Apart from the choice of the chemical reactant, a chemical etching transfer process is always composed by the following steps (in this sense the process is quite standard):

1. spinning of as many layers as needed of Poly(methyl-methacrylate) (PMMA) on graphene (usually a number of layers corresponding to a final PMMA membrane thickness of $\sim$ 1–2 µm is chosen, but thicker membranes are allowed);

2. soak of the PMMA/graphene/catalyst/SiO_2/Si sample in the (usually diluted) chemical etchant solution for chemical etching process;

3. fishing of the PMMA/graphene membrane floating in the chemical solution, at the end of the etching process (that has completely removed, in principle, the catalytic substrate), with a new cleaned SiO_2/Si wafer;

4. removal of the PMMA present on top of graphene with acetone (sometimes acetone vapours are used instead of or simultaneously with acetone).

These steps are schematically illustrated in Figure 107.

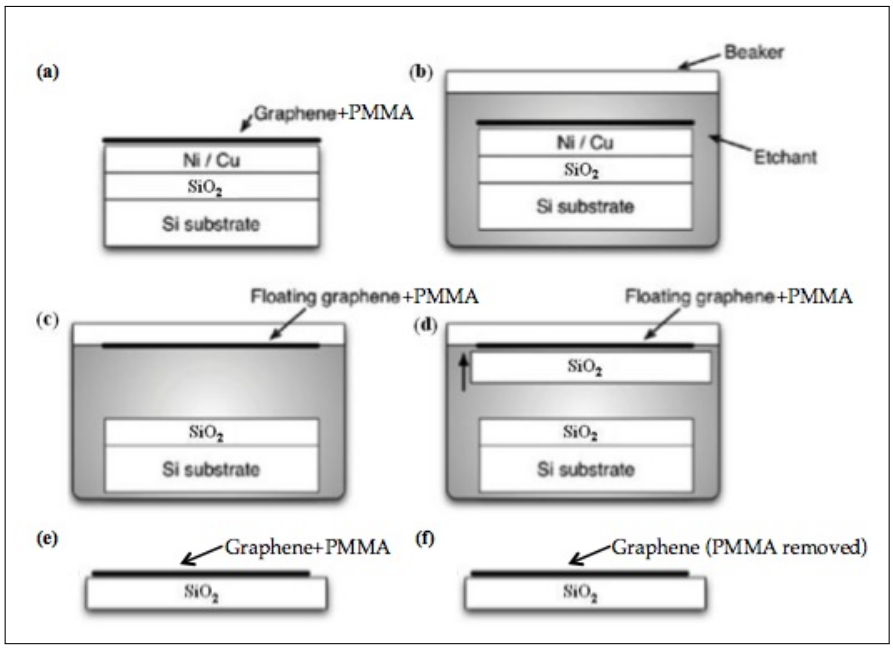

Figure 107: Graphene transfer process. Schematic view of the standard process usually implemented to transfer graphene from the metallic catalyst to an insulating substrate. The process is based on the chemical etching of the metal used during the CVD process. Transfer proceeds as follows: (a) a thin (1–2 µm) protective PMMA membrane is spun onto graphene; (b) the whole sample is soaked for many hours into the chemical etchant solution, contained in a proper beaker (the choice of the etchant depends upon the kind of metal catalyst: HCl diluted solution is usually employed for Ni etching, while $FeCl_3$ solution is employed for Cu etching); (c) once the metallic catalyst has been completely removed from the sample through the chemical etching process, the PMMA/-graphene membrane will float into the solution; (d) the solution is then properly diluted (to better see the floating membrane) and the PMMA/-graphene membrane is fished by using a new SiO_2/Si substrate; (e) the graphene/PMMA membrane is in this way deposited on the desired dielectric material; (f) at the end of the process PMMA is removed with acetone and graphene has been transferred onto an insulating substrate.

The standard technique here described is the one I have also employed in my experiments at I.N.Ri.M. in order to transfer graphene from Cu (foils or films) to a new SiO_2/Si sample (with oxide thickness $\sim$ 300 nm). First of all, approximately 1.5 µm of PMMA have been deposited on graphene through a spinning and heating cycle repeated several times. Spinning has been provided by a spinner present at I.N.Ri.M. laboratories, set-up to work at 5000 rpm for 1 min when dealing with PMMA deposition. Subsequent heating of the sample has been carried out at 165 °C for 5 min by means of

an heater. After PMMA deposition, samples have been dipped in an aqueous $\sim$ 0.5 M $FeCl_3$ etching solution for $\sim$ 4h (keeping the beaker containing the samples on the heater at 45 °C to enhance etching kinetics). Once Cu has been completely etched away from the samples, I have first of all rinsed several times with water the $FeCl_3$ solution containing Cu residual and I have then picked up PMMA/graphene membranes onto $\sim$ 300 nm-SiO_2/Si substrates. PMMA has been finally removed with acetone. For the last step (i.e. PMMA removal), several techniques have been tried in order to understand which one provides a better PMMA removal: sometimes I have dropped acetone on PMMA through a µm-graduated pipette providing a fine control on acetone deposition, other times I have exposed PMMA/graphene samples to acetone vapours (obtained by keeping a beaker containing acetone on the heater) and some other times I directly carefully dipped the PMMA/graphene sample into a beaker containing acetone. I have this way understood that acetone vapours technique is quite long but ineffective for PMMA removal (at least for the PMMA thickness I have used), while sample dip in acetone is so far the technique that has provided better results (in terms of complete removal of the PMMA membrane). Some images of the full transfer process as performed at I.N.Ri.M. are shown in Figure 108.

It is important to remark that up to now the comprehensive investigation of the transfer process has not come to an end yet. I am still optimizing the whole process, by varying the several adjustable parameters (such as the molarity of the $FeCl_3$ solution, the thickness of the PMMA membrane to spin on the graphene sample, the beaker to be used to allow a non destructive and efficient PMMA/graphene fishing at the end of the chemical etching step) affecting the final quality of transferred graphene. Indeed, in all the transfer processes I have performed, I have encountered many problems and I have often damaged grown graphene, especially because of cracking occurred in the PMMA/graphene membranes during the etching and the fishing steps or because of the presence of Cu and PMMA residuals.

Finally, it is worth mentioning that some graphene transfer techniques alternative to the standard chemical etching technique have been proposed very recently: for example, a roll-to-roll transfer technique ([4]), allowing for production of large scale areas graphene layers (up to $\sim$ 30″ in lateral size) on insulating substrates, or electrochemical exfoliation based techniques, relying on the employment of polycarbonate and polystyrene as temporary graphene support polymers instead of PMMA (these polymers are chosen because of their higher flexibility, mechanical strength and solubility in organic solvents with respect to PMMA), allowing for an up-scalability of the transfer process ([113]).

3.3 CVD PROCESSES

After the review about the characterization techniques that I have used in the experiments to investigate the (eventual) presence and the quality of graphene layers grown on catalytic substrates through CVD processes (Sec. 3.1) and the detailed explanation of the process allowing to transfer grown graphene from a metallic catalyst to an insulating surface (Sec. 3.2), I report in this section the most important results that I have successfully obtained about CVD growth of graphene layers. In Sec. 3.3.1 I will describe the first attempts I have carried out in order to grow graphene on Ni films by means of a technique slightly different from CVD. Due to the poor re-

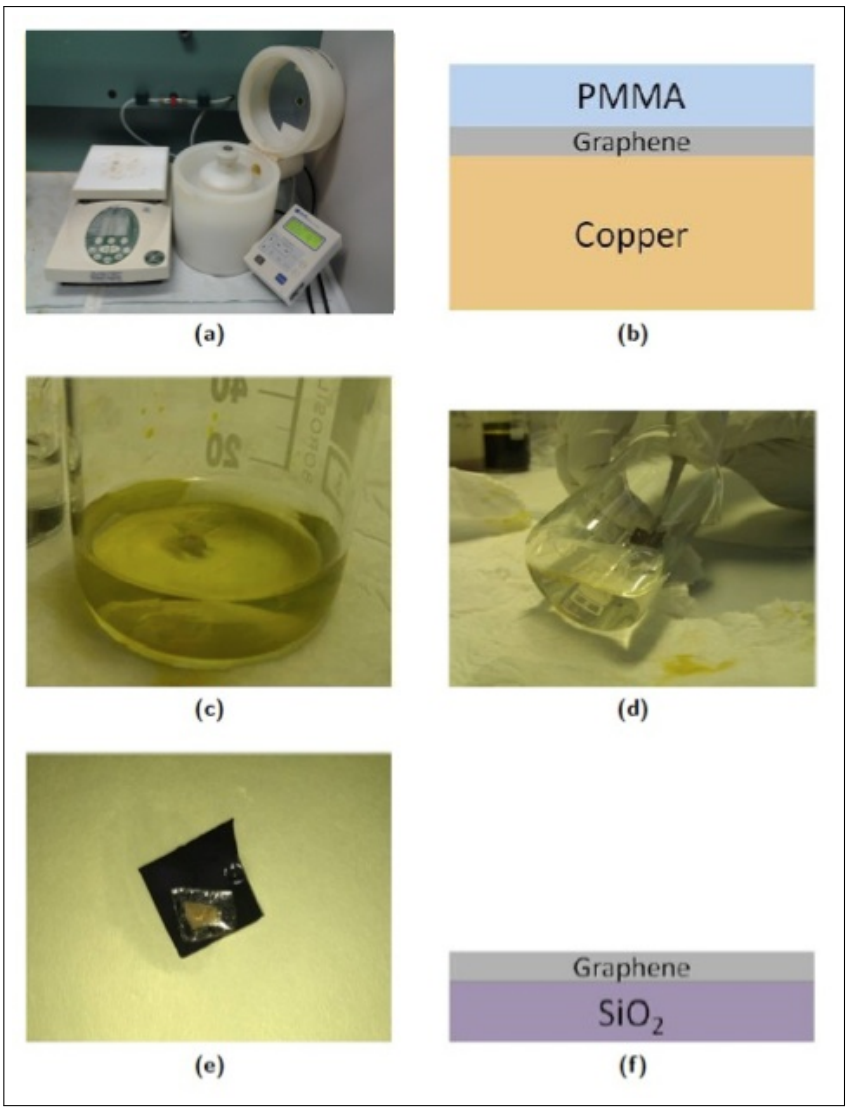

Figure 108: Graphene transfer process at I.N.Ri.M. laboratories. Picture illustrating the various steps performed at I.N.Ri.M. laboratories for graphene transfer process: (a) picture of the spinner and the heater used to deposit approximately a 1.5 µm thick PMMA membrane on top of graphene grown by CVD; (b) schematic view of graphene sample after PMMA deposition; (c) beaker containing the diluted $FeCl_3$ solution used for Cu etching and the PMMA/graphene/catalyst/SiO_2/Si sample; (d) fishing of the PMMA/graphene floating membrane at the end of the etching process (after careful rinsing of the $FeCl_3$ solution containing Cu residuals); (e) picture of the PMMA/graphene membrane transferred onto a new SiO_2/Si substrates (Cu residuals underlying the transparent membrane are clearly visible); (f) final configuration of the graphene sample, at the end of the transfer process, after PMMA removal with acetone.

sults I have obtained, I have later decided to change catalytic substrate and to use Cu instead of Ni in CVD processes: therefore, in Sec. 3.3.2, I will report the first successful results related to few-layer graphene deposition on top of Cu foils. Finally, in Sec. 3.3.3, I will describe interesting results concerning graphene growth onto Cu thin films and, more in detail, concerning an etching effect that occurred during the Raman characterization that I have carried out on my samples after the CVD processes (these results have been recently published in [145]). In the case of thin films, as described in Chapter 2, CVD processes are affected by the problem of the catalytic substrate dewetting occurring during the thermal cycle bringing to graphene deposition. Nonetheless, working a lot on the free parameters characterizing the CVD thermal cycles (mainly deposition temperature, deposition time and cooling-down rate), I succeeded in synthesizing few-layer graphene also on top of Cu thin films. However, in the case of the Cu thin films, the more interesting results do not concern the successful deposition *per se*, but a laser induced etching effect (locally reducing the number of graphene layers present on top of the metallic surface) that I have discovered while characterizing my samples with Raman analysis: according to me (and to the people who worked with me to obtain this result), this effect has a precise physical explanation that suggests to continue the investigation of the etching technique in order to find possible improvements and applications broadening its employment. As a consequence, Sec. 3.3.3 will be mainly devoted to the explanation of the etching effect, more than to the detailed description of the CVD process allowing me to successfully grow graphene on top of Cu thin film.

3.3.1 CVD on Ni

Inspired by a work reported in literature ([101]), describing a successful CVD growth of graphene onto Ni films, I have decided to employ this catalytic substrate to carry out my first CVD processes. To be more precise, I wanted to test a slightly different deposition procedure, with respect to standard CVD, based on diffusion into Ni of C atoms provided by a solid source instead of a gas precursor (Figure 109). The idea was to employ amorphous SiC samples, obtained through carbon implantation inside Si substrates, as the solid source providing C atoms needed for graphene growth: hence, while in CVD processes C atoms are provided by dissociation at high temperature of a carbon precursor in gas phase, in my process C atoms are provided by sublimation upon heating of amorphous SiC in solid phase. C atoms released during the SiC heating process (performed in the RTA system used also for CVD processes) would have been later subjected to diffusion through a Ni thin film previously deposited onto the amorphous SiC substrate (diffusion through Ni occurs for the same reasons it occurs in CVD processes, i.e. the solid solubility of C atoms in Ni). The process requires therefore to perform three steps: implantation of C atoms in Si, deposition of Ni thin film on amorphous SiC and completion of a thermal cycle similar to those employed in CVD processes to allow diffusion through Ni (during the heating step of the thermal cycle) and precipitation/crystallization on Ni surface (during the coolin-down step) of C atoms provided by amorphous SiC. Hence, the only difference of the proposed process with respect to an usual CVD process is represented by the C precursor, but the physical principles governing graphene formation are practically identical for both the processes. Indeed, successful graphene growth processes carried out with

methods similar to the one here proposed (in which the only difference is in the choice of the solid source providing C) have been also proposed in literature ([6, 66, 202]).

First of all I have tried to develop a simple model describing the diffusion of C atoms inside Ni, occurring during heating of the sample, and the subsequent precipitation/crystallization on Ni surface of the atoms due to system cooling.

For what concerns the diffusion process, I have worked in 1D assuming the Ni film to be uniform and homogeneous all over the surface and the C diffusion to occur homogeneously everywhere in the Ni film. Moreover, for the sake of simplicity, I have not considered Ni thermal expansion in the calculations. C atoms diffusion process is governed by Fick's Law [48], connecting the rate of flow of the diffusing substance with the concentration gradient causing the flow. Fick's Law (when no chemical reactions are occurring in the diffusor medium) can be expressed (in 1D) through the following diffusion equation:

$$\frac{\partial c\left(x,t\right)}{\partial t} = D\frac{\partial^2 c\left(x,t\right)}{\partial x^2} \tag{76}$$

where $c\left(x,t\right)$ is the concentration of the diffusing substance at point x of the diffusor medium and time t, expressed in $\mathrm{mol\,m^{-3}}$, while D is the *diffusion coefficient* (here considered independent of the concentration c and of the position x, although this assumption may not hold in general) of the diffusing substance into the diffusor medium and expressed in $\mathrm{m^2\,s^{-1}}$. The solution of equation 76 for $0 \leq x < \infty$ (I am therefore assuming to deal with a diffusor medium extending in an half-plane) with initial and boundary conditions (corresponding to a constant finite concentration of diffusing substance present at the boundary $x = 0$ at any time and to an inital -at $t = 0$- zero concentration of diffusing substance inside the medium)

$$c\left(x,0\right) = 0, \quad c\left(0,t\right) = c_0 \tag{77}$$

is the known *complementary error function* given by ([168])

$$c\left(x,t\right) = c_0\left[1 - \mathrm{erf}\left(\frac{x}{2\sqrt{Dt}}\right)\right] \tag{78}$$

with

$$\mathrm{erf}\left(\frac{x}{2\sqrt{Dt}}\right) = \frac{2}{\sqrt{\pi}}\int_0^{\frac{x}{2\sqrt{Dt}}} e^{-u^2}\,\mathrm{d}u. \tag{79}$$

If the concentration $c\left(0,t\right)$ of the diffusing substance at the boundary $x = 0$ at any time is not a constant c_0 but, more in general, a function $g(t)$, so that the initial and boundary conditions are given by

$$c\left(x,0\right) = 0, \quad c\left(0,t\right) = g(t), \tag{80}$$

the solution of the diffusion equation 76 is ([168])

$$c\left(x,t\right) = \frac{2}{\sqrt{\pi}}\int_{\frac{x}{2\sqrt{Dt}}}^{\infty} g\left(t - \frac{x^2}{4Du^2}\right) e^{-u^2}\,\mathrm{d}u. \tag{81}$$

In my specific model I have assumed to deal with a Ni film (the diffusor medium) of thickness $d_{\mathrm{Ni}} = 200\,\mathrm{nm}$ (I have fixed this thickness following [101]) extending from $-100\,\mathrm{nm}$ to $100\,\mathrm{nm}$ and with a linear heating step

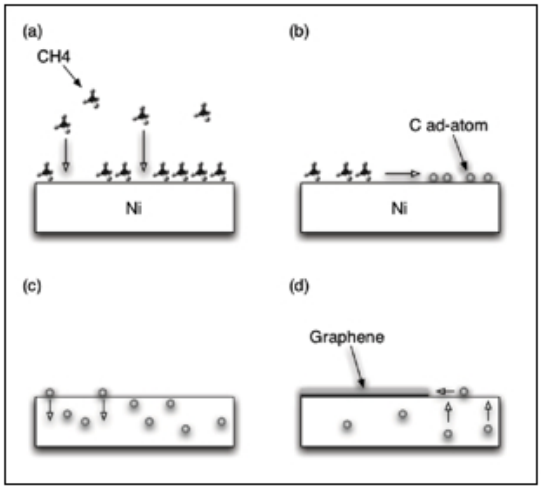

(a)

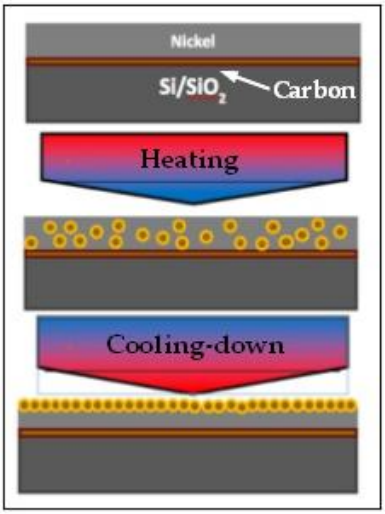

(b)

Figure 109: Graphene growth on Ni films by a solid carbon source. Comparison between a typical CVD process performed on Ni film through a carbon precursor in gas phase and a process providing the carbon precursor by a solid source (in my case amorphous SiC): (a) in a typical CVD process (described in details in Chapter 1) graphene growth occurs by the dissociation at high temperature of the carbon precursor molecules, the diffusion of free C atoms inside Ni film and the subsequent precipitation and crystallization of C atoms on Ni surface during the cooling-down process; (b) in the method I have proposed, graphene growth occurs through diffusion inside the Ni film of C atoms provided, during the heating step, by a carbon solid source on which Ni has been deposited: the carbon source is pictorially represented by the thin orange layer between Ni and the SiO_2/Si substrate and it is obtained, for example, by C implantation inside SiO_2/Si (although other solid source are allowed). C atoms diffused inside Ni segregate and crystallize on Ni surface during the subsequent cooling-down process.

bringing the temperature from $T_0 = 30\,\text{celsius} = 303.15\,\text{K}$ up to $T_{\text{fin}} = 800\,^\circ\text{C} = 1073.15\,\text{K}$ in $t\text{heating} = 20\,\text{s}$, so that

$$T(t) = T_0 + \alpha t, \quad \alpha = \frac{T_{\text{fin}} - T_0}{t_{\text{heating}}} = 38.5\,^\circ\text{C}\,\text{s}^{-1}. \tag{82}$$

The diffusion coefficient $D_{\text{C;Ni}}$ of carbon in Ni, to be inserted into equation 76, is known already from '50s to be temperature-dependent, increasing exponentially with temperature: its behaviour, according to [90], is reported in Figure 110a. Since in my model the temperature is a function of time through 82, the diffusion coefficient itself becomes time-dependent and the solution of equation76 is not anymore so simple. Moreover, the maximum concentration of carbon present at the boundary $x = -100\,\text{nm}$ at any time and at a certain temperature T is proportional to the solid solubility $S_{\text{C;Ni}}$ of carbon in Ni at temperature T: indeed, by definition, solid solubility (an adimensional quantity) expresses in weight % (so in g of diffusing substance -the "solute"- per 100 g of diffusor medium -the "solvent") the maximum concentration of diffusing substance allowed, at a certain temperature, to be interstitially present inside the diffusor medium. Again, solubility has been evaluated, in the same work by [90], to depend exponentially on temperature (its behaviour is illustrated in Figure 110b) and therefore, in my case, on time.

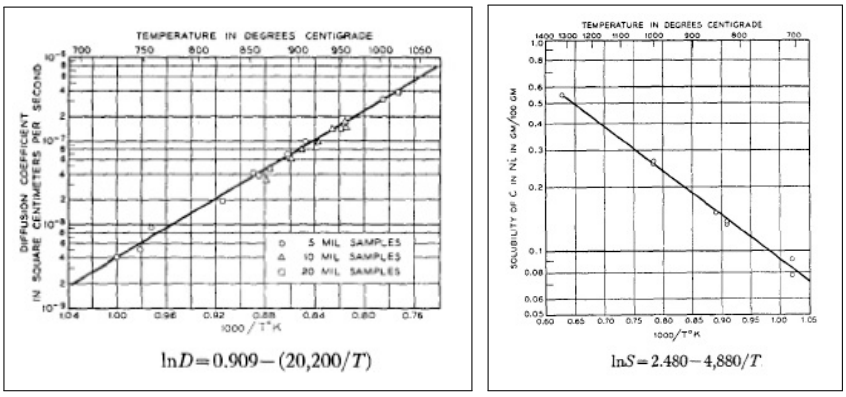

(a) (b)

Figure 110: Diffusion coefficient and solid solubility of carbon in Ni. (a) Graph showing the exponential dependence of the diffusion coefficient $D_{\text{C;Ni}}$ of carbon in Ni (expressed in $\text{cm}^2\,\text{s}^{-1}$) on the temperature (expressed in °C), in logarithmic scale. The law relating diffusion coefficient and temperature is also explicitly written. (b) Graph showing the exponential dependence of the solid solubility $S_{\text{C;Ni}}$ of carbon in Ni (expressed as g of carbon per 100 g of Ni) on the temperature (expressed in °C), in logarithmic scale. The law relating solubility and temperature is also explicitly written. Both adapted from [90].

After conversion of $D_{\text{C;Ni}}[T(t)]$, as reported in Figure 110, in the right SI units, we therefore have:

$$D_{\text{C;Ni}}[T(t)] = Ae^{-\frac{E_{\text{act}}}{T(t)}} \tag{83}$$

$$S_{\text{C;Ni}}[T(t)] = Be^{-\frac{E_{\text{act}_2}}{T(t)}} \tag{84}$$

with

$$A = e^{0.909} \cdot 10^{-4} \mathrm{m}^2\,\mathrm{s}^{-1} \qquad E_{act} = 20200,$$
$$B = e^{2.480} \qquad E_{act_2} = 4880.$$

Therefore, in my model, I must solve equation 76 with a time-dependent diffusion coefficient $D_{C;Ni}\left[T\left(t\right)\right]$ given by 83 and with initial and boundary conditions[4]

$$\begin{aligned} & c\left(x,0\right) = 0 \quad \forall x \in \left(-100\,\mathrm{nm}, 100\,\mathrm{nm}\right] \\ & c\left(x = -100\,\mathrm{nm}, t\right) = 10 S_{C;Ni}\left[T\left(t\right)\right] \rho_{Ni} / M_C \\ & \left.\frac{\partial c\left(x,t\right)}{\partial x}\right|_{x=100\,\mathrm{nm}} = 0 \end{aligned} \tag{85}$$

where $\rho_{Ni} \approx 8908\,\mathrm{kg\,m^{-3}}$ is the Ni density and $M_C \approx 12.0107\,\mathrm{g\,mol^{-1}}$ is the molar mass of carbon. The boundary condition at $x = 100\,\mathrm{nm}$ is simply expressing the fact that there is no external flow of carbon atoms from the Ni surface: in other wors, once C atoms reach the Ni surface, they are not allowed to diffuse out of it.

The solution of the diffusion equation, with the time-dependent diffusion coefficient and the boundary conditions described above, has been evaluated numerically by means of a specific software at finite elements, *COMSOL Multiphysics*. The solutions $c\left(x,t\right)\ \forall x \in \left[-100\,\mathrm{nm}, 100\,\mathrm{nm}\right]$ and $\forall t \in \left[0, 18\,\mathrm{s}\right]$, obtained by imposing the conditions 85 and expressing the carbon concentration in Ni at any depth x and at any time t, are shown in Figure 111.

I have performed this numerical simulation aiming to understand before which time interval, assuming to increase linearly the temperature of the RTA system by means of the heating ramp 82, I should have stopped heating the sample in order to avoid the diffusion of carbon atoms onto the Ni surface (i.e. to avoid obtaining a concentration $c\left(x = 100\,\mathrm{nm}, \tilde{t}\right) \neq 0$ at the boundary $x = 100\,\mathrm{nm}$ -the Ni surface- at a certain time $\tilde{t}$ falling inside the heating step time interval) already during the heating step. Indeed, it is known from CVD processes performed on Ni substrates that, in order to obtain high quality graphene, C atoms crystallization on top of the catalytic surface must occur only during the cooling-down step and the precipitation of the atoms onto Ni surface during the heating step should be avoided ([101]).

The first idea was therefore to perform other numerical simulations of the diffusion process by changing for example Ni thickness and by choosing heating ramps to model the increase in temperature different from 82 and to compare the theoretical expected results with experimental observations; then, to simulate also the (more complex) crystallization process involving C atoms precipitated on top of the Ni surface after the cooling-down process. The problem is that I faced a lot of troubles in depositing the Ni films onto the amorphous SiC substrates, especially in treating it with thermal

4 In order to convert the solubility from g of C per 100 g of Ni, as expressed in 84, into a molar concentration $c\left(x,t\right)$ expressed in mol of C per m^3 of Ni+C, as required by the software I have used to solve equation 76, I have assumed that $V_{solution} \simeq V_{solvent}$, i.e. $V_{Ni+C} \simeq V_{Ni}$ (equivalently $m_{Ni+C} \simeq m_{Ni}$), so that molar concentration is simply obtained from molality through multiplication by Ni density. Indeed, molality is obtained from 84 simply by converting g of C into mol of C (through the molar mass M_C) and 100 g of Ni into kg of Ni. The proposed approximation is acceptable because it introduces an error in the results much lower than errors introduced by other approximations employed in my model (for example errors introduced by neglecting Ni thermal expansion).

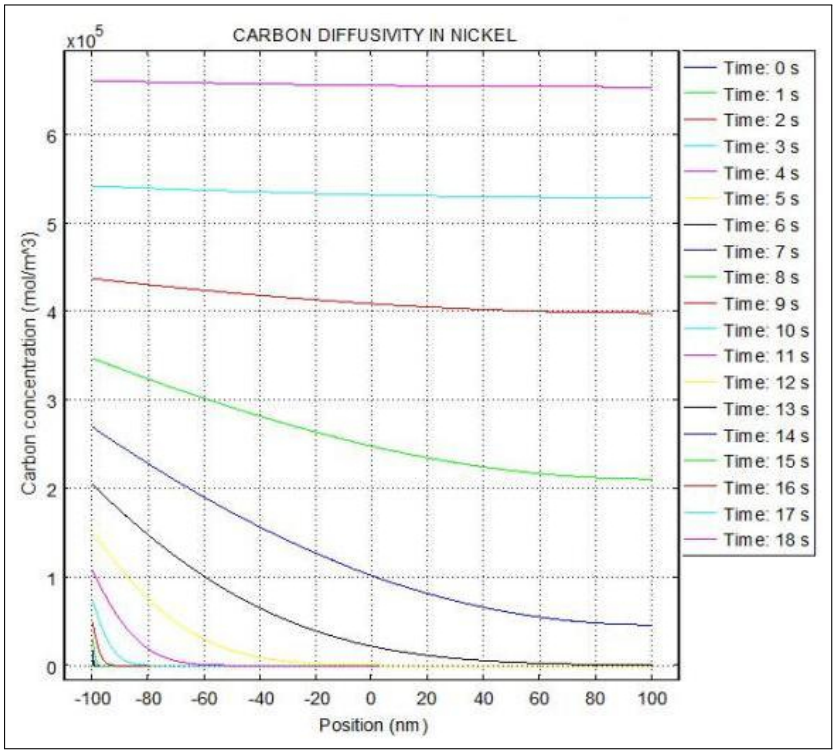

Figure 111: Concentration of C atoms into a Ni thin film at different times. Results of the numerical simulation performed with *COMSOL Multiphysics* in order to solve equation 76 with the time-dependent diffusion coefficient of carbon in Ni 83 and initial and boundary conditions 85. Each curve in the graph shows the concentration of carbon at any different depth $x \in [-100\,\text{nm}, 100\,\text{nm}]$ into the Ni film at a certain fixed time; it is clear that with the heating ramp chosen, given by 82, carbon atoms reach the Ni surface already 18 s after the beginning of the heating process.

processes. Only one time I succeeded in performing a full thermal cycle on a Ni sample heating the sample up to $T = 800\,°C$ and I could characterize with XPS analysis the sample after the process in order to check for the eventual presence of carbon onto the Ni surface. Results of XPS analysis, confirming the presence of carbon after the thermal process, are shown in Figure 112.

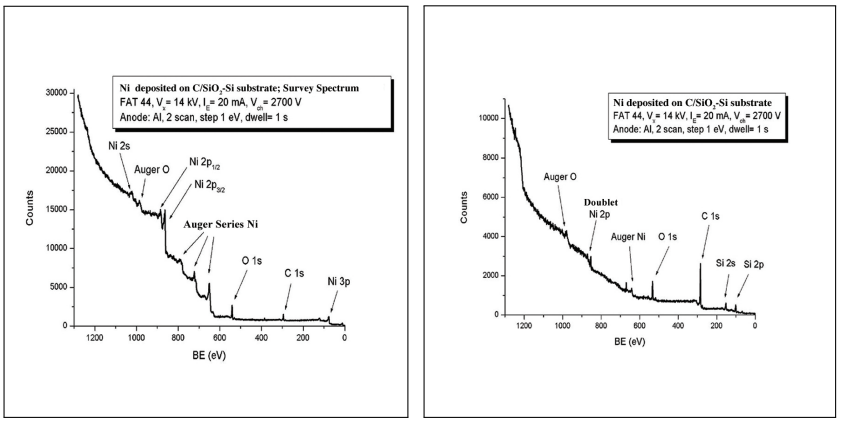

(a) (b)

Figure 112: XPS analysis on Ni thin films before and after a thermal process at $T = 800\,°C$. Comparison of XPS spectra acquired on a $d_{Ni} = 200\,nm$ thick Ni film subjected to thermal cycle for growing graphene from a solid source (amorphous SiC): (a) spectrum acquired before performing the process. No clear C peak is visible; (b) spectrum acquired on the same sample after performing the thermal process bringing the temperature up to $T = 800\,°C$. C peak (denoted in the picture "C 1s") is definitely increased, meaning that C atoms diffused from the underlying amorphous SiC substrate onto Ni surface during the process. Nonetheless, atoms on the surface did not probably crystallize in graphene lattice, but remained in amorphous form. The diffusion of C atoms has likely occurred mainly through Ni grain boundaries.

Because of all these problems and since in the meanwhile I have decided to perform (standard) CVD processes also on Cu substrates, obtaining more successful results, I have postponed and later definitely abandoned the research about graphene growth on Ni films from a solid source.

3.3.2 CVD on Cu foils

Graphene deposition on Cu foils has been obtained with standard CVD processes performed in the RTA system present at I.N.Ri.M. laboratories and already described in Sec. 2.3.1. CH_4 has been always employed as carbon precursor in gas phase for graphene growth, while *not commercially available*, but simply everyday life Cu foils (Figure 113), $\sim 1\,mm$ in thickness and properly cut in square pieces $\sim 1\,cm^2$, have been chosen as catalytic substrates to activate dissociation of CH_4 molecules and graphene crystallization on Cu surface. All the Cu samples subjected to subsequent CVD processes, this way prepared, have been cleaned through sonication cycles in acetone (5 min) and isopropanol (5 min). Some of them have undergone also a lapping process, meant to reduce the impurities and the roughness

of the Cu surface and to improve, more in general, the whole quality of the substrates.

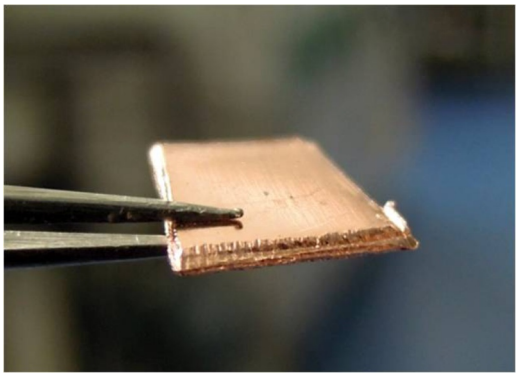

Figure 113: Cu foils for CVD growth of graphene at I.N.Ri.M.. Picture of the bulk Cu foils employed at I.N.Ri.M. for graphene deposition by CVD. The foils are not the usual commercially available Cu foils reported in literature ([16, 17, 96]), but rather everyday life Cu bars. Before undergoing CVD processes, Cu has been properly shaped in square pieces (with surface area $\sim 1\,cm^2$) and cleaned under sonication in acetone and isopropanol for $\sim 10\,min$; some samples have been also lapped, to reduce surface roughness and impurities.

The CVD processes tested on Cu foils can be summarized, according to the deposition temperatures T_{dep} of the thermal cycles and to the results obtained, as reported in Table 7. I will now briefly discuss these results; a detailed description of the processes and of the difficulties encountered during graphene depositions can be found in [29].

T (°C)	Results	
	SEM	**Raman**
800, 850	Regular structures	No clear features of graphene
900	Regular structures, wrinkles	Mainly few-layers graphene
985	Fusion of Cu and Si (no SiO_2)	

Table 7: Summary of CVD processes performed on various Cu foils. Table showing the various CVD processes performed on Cu foils (both lapped and not lapped), divided according to the deposition temperature T_{dep} fixed in each of them, and the results obtained characterizing the samples with SEM and Raman analyses. Only in the case of $T_{dep} = 900\,°C$ I have succeed in growing few-layer graphene on top of the surface.

As shown in Table 7, the CVD processes carried on Cu foils can be divided into three categories, that I will now describe:

1. **CVD processes at $T_{dep} = 985\,°C$**
   First CVD processes on Cu foils have been performed at high temperature, $T_{dep} = 985\,°C$. These processes were meant to test only the processes, performing an annealing of the samples: therefore, no CH_4 was flowing in the RTA system during this kind of thermal cycles and the processes are not really CVD cycles aiming to grow graphene on

top of Cu, but rather annealing cycles to improve the quality of the samples and to acquire experience.
The thermal cycle performed is summarized as follows (the process is shown also in Figure 114 for major clarity):

- pre-vacuum step, $\Delta t = 60\,\text{s}$;
- room temperature up to 400 °C, $\Delta t = 60\,\text{s}$, no gas flowing;
- 400 °C–400 °C, $\Delta t = 10\,\text{s}$, no gas flowing;
- 400 °C–985 °C, $\Delta t = 60\,\text{s}$, 40 sccm H_2;
- 985 °C–985 °C, $\Delta t = 60\,\text{s}$, 40 sccm H_2;
- 985 °C down to room temperature, $\Delta t = 60\,\text{s}$, no gas flowing;
- final purge of the system in N_2.

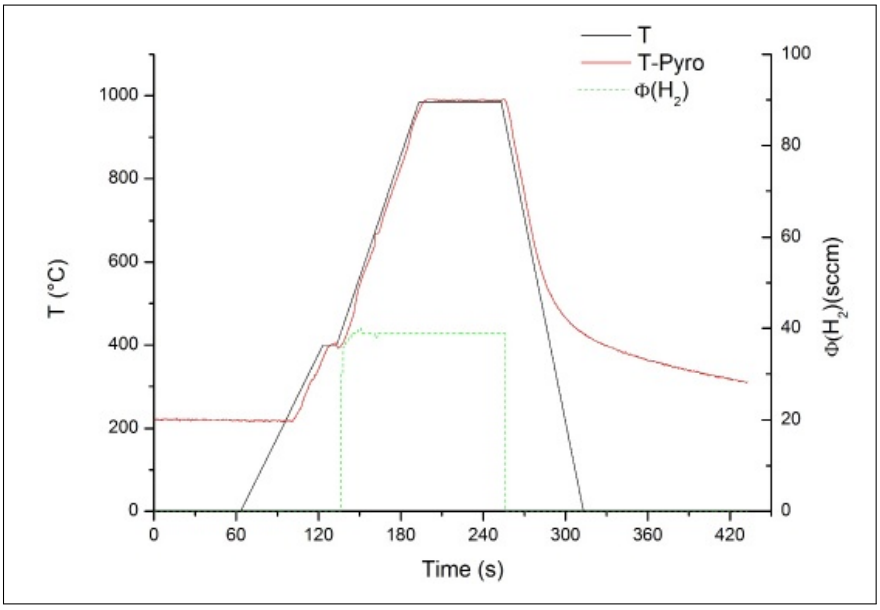

Figure 114: Thermal cycle for annealing of Cu foils at $T_{dep} = 985\,°C$. Schematic view of the thermal cycle carried out to perform the annealing of the Cu foil under H_2 flow at $T_{dep} = 985\,°C$. In the image both the set-up temperature (chosen by the user) and the temperature read by the pyrometer are shown (in black and in red respectively); H_2 is flowing in the system only during the heating and the maximum temperature steps. While H_2 is flowing, the pressure measured in the reaction chamber of the RTA system is $p_{H_2=40\ \text{sccm}} \sim 1.33\,\text{mbar}$.

It is important to mention that, while performing these processes, the Cu samples have been put directly on the Si face (and not on the SiO_2 face, having an oxide layer thermally grown on Si) of the sample-holder (a 4" Si wafer, as already explained in Sec. 2.3.1, having a lapped Si face -with only a very thin, negligible, native oxide layer grown on it- and a SiO_2 face -with a thicker thermally grown oxide layer on it), according to the standard configuration illustrated in Figure 115 and Figure 78a (since the temperature of the sample is detected by the thermocouple and the pyrometer present in the RTA system on the back of the sample-holder, I am assuming from now on, also for the processes performed on Cu films described in Sec. 3.3.3, the Cu sample to be in thermal equilibrium with the sample-holder during all the process).

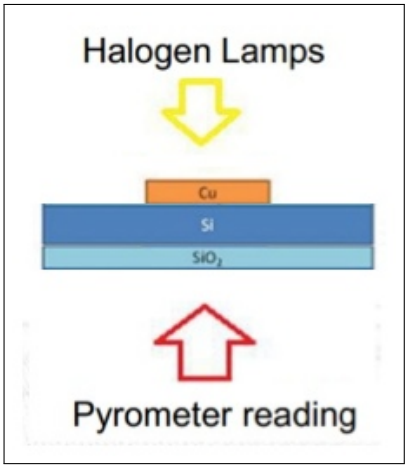

Figure 115: **Sample-holder configuration for annealing of Cu foils.** Schematic view of the sample-holder configuration employed for annealing processes of Cu foils performed in the RTA system: in these processes the Cu foils were directly in contact with the Si face of the sample-holder, a 4″ Si wafer. Because of the problems explained in the text, I have later decided to put the Cu samples always on the SiO_2 face of the face rather than on the Si one.

Once the process has been performed, I have discovered that Cu completely melted during the thermal cycle together with the underlying portion of the Si sample-holder directly in contact with it (the sample-holder after annealing process appeared as illustrated in Figure 116). At the beginning this fact has been quite puzzling, since the melting temperature of Cu, as single species, is $T_{Cu} \sim 1085\,°C$, much higher than the temperature reached in the annealing process here described. However, a careful study allowed me to understand that the problem was relying on the presence of the Si substrate underlying Cu: indeed, as reported in literature ([139]), Cu and Si form a solid binary mixed phase when put directly together, characterized by a melting temperature ranging from $\sim 800\,°C$ to $\sim 860\,°C$ (Figure 71). Therefore, at the annealing temperature $T_{dep} = 985\,°C$ reached during the process I have performed, Cu and Si have mixed forming such a binary phase and starting to melt together. Since the temperature needed to avoid the formation of the stable binary phase between Cu and Si is too low ($T \lesssim 800\,°C$) to allow CH_4 dissociation during CVD thermal cycles, for the CVD processes I have later carried out on Cu foils and Cu thin films, I have decided to simply put Cu samples on the SiO_2 face, rather than on the Si face, of the Si sample-holder (preventing this way, thanks to the insulating oxide layer, the mixing of the two species);

2. **CVD processes at $T_{dep} = 800\,°C$ and $850\,°C$**
   After having understood the problem causing Cu melting of samples thermally treated at high temperature, I have performed other CVD processes on Cu foils, put this time on the SiO_2 face of the Si wafer used as sample-holder in the RTA system, characterized by deposition temperatures $T_{dep} = 800\,°C$ and $T_{dep} = 850\,°C$.
   The thermal cycles performed are characterized by the following parameters:
   - pre-vacuum step, $\Delta t = 300\,s$;

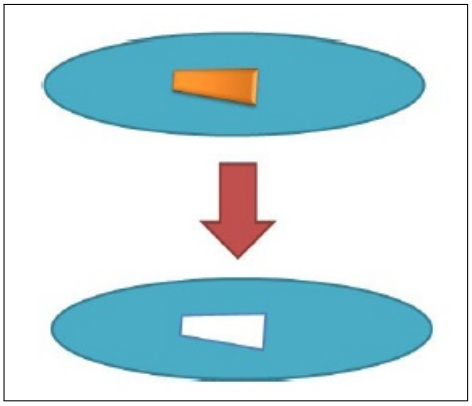

Figure 116: Cu foil after annealing process at $T_{dep} = 985\,°C$. Schematic view illustrating how appeared the Si sample-holder present in the RTA system before (*top*) and after (*bottom*) having carried out the annealing process at $T_{dep} = 985\,°C$ on Cu foils directly in contact with the Si face of the Si wafer. Because of the Cu-Si mixing, bringing to the formation of a new stable solid phase between the two species, characterized by a melting temperature $800\,°C \gtrsim T_{Cu+Si} \lesssim 850\,°C$, Cu was completely melted during the process, together with the portion of Si wafer underlying it, leaving a hole in the sample-holder.

- room temperature up to 300 °C, $\Delta t = 60\,s$, no gas flowing;
- 300 °C–800 °C (850 °C), $\Delta t = 1200\,s$, 40 sccm H_2;
- 800 °C–800 °C (850 °C), $\Delta t = 60\,s$, 40 sccm H_2;
- 800 °C–800 °C (850 °C), $\Delta t = 120\,s$, 5 sccm CH_4 + 40 sccm H_2;
- 800 °C (850 °C) down to room temperature, $\Delta t = 300\,s$, 40 sccm H_2;
- final purge of the system in N_2.

The same thermal cycle has been carried out both on lapped and not lapped Cu samples (Figure 117 shows typical images of the Cu foils employed in the CVD processes before performing the thermal cycles), to search for an eventual influence of the Cu substrate quality (in terms of roughness of the Cu surface) on the quality of the graphene layers grown on the metallic catalyst at the end of the CVD process.

After thermal treatment the samples have been first of all analysed at SEM, allowing a fast characterization highlighting any eventual change occurred during the CVD process on the substrate surface. Indeed, all the samples subjected to CVD process showed clear regular structures and wrinkles on the surface (Figure 118), similar to those detected also on Cu foils subjected to thermal cycles at $T_{dep} = 900\,°C$ (Figure 120): these structures can be attributed both to graphene layers eventually grown on the Cu surface during the processes, or to preferential crystallographic orientations of the Cu lattice. Thus, SEM analysis does not allow to provide a not ambiguous answer about the presence of graphene layers on top of Cu foils subjected to CVD thermal cycles at $T_{dep} = 800\,°C$ and $T_{dep} = 850\,°C$.

To clearly understand if graphene has been grown or not on the Cu surface, the samples have been subjected to Raman characterization. Raman spectra have been acquired on different spots, randomly chosen, directly on the Cu samples (without transferring graphene to an

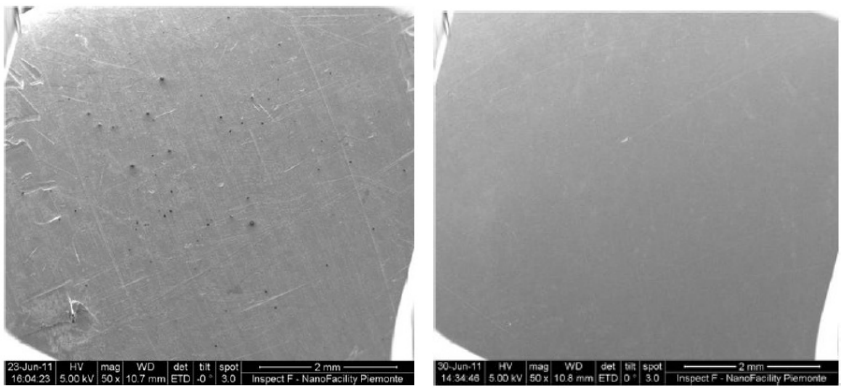

(a) (b)

Figure 117: Cu foils before CVD processes. SEM images showing different Cu foils used to carry out CVD processes, before undergoing any thermal cycle: (a) Cu foil not subjected to lapping treatment, showing high roughness and many impurities; (b) Cu foil subjected to lapping treatment: surface roughness is clearly reduced with respect to (a) and the sample appears less dirty.

insulating SiO_2 substrate) by using laser light at $\lambda = 514\,\text{nm}$: under no circumstances the G and 2D peaks associated to the presence of graphene on a certain substrate have been found in the spectra, meaning that graphene has not been deposited on Cu during the CVD processes performed at these temperatures.

We can therefore conclude that deposition temperatures lower than 900 °C, together with a quite low CH_4 flow (5 sccm) and a deposition time of 2 min, do not allow a successful growth of graphene by CVD performed onto Cu foils: the deposition temperature, the deposition time and the CH_4 flow are too low to supply the dissociation of the right amount of CH_4 molecules, needed to successfully deposit graphene on Cu. A possible way out to this problem is to increase the deposition temperature, leaving the other parameters unchanged (the route I have decided to follow), or to change CH_4 flow and deposition time to check if a deposition temperature of 800 °C or 850 °C is high enough to allow the dissociation of the carbon precursor molecules;

3. **CVD processes at $T_{dep} = 900\,°C$**
Since CVD processes performed at $T_{dep} = 800\,°C$ and $T_{dep} = 850\,°C$ had not given the expected results, i.e. graphene growth on top of Cu, I have decided to carry out new CVD processes by increasing deposition temperature up to $T_{dep} = 900\,°C$, without changing any other parameter.
Thermal cycles' parameters have been therefore set-up as follows (the thermal cycle is illustrated also in Figure 119):
   - pre-vacuum step, $\Delta t = 300\,s$;
   - room temperature up to 300 °C, $\Delta t = 60\,s$, no gas flowing;
   - 300 °C–900 °C, $\Delta t = 1200\,s$, 40 sccm H_2;
   - 900 °C–900 °C, $\Delta t = 60\,s$, 40 sccm H_2;
   - 900 °C–900 °C, $\Delta t = 120\,s$, 5 sccm CH_4 + 40 sccm H_2;
   - 900 °C down to room temperature, $\Delta t = 300\,s$, 40 sccm H_2;

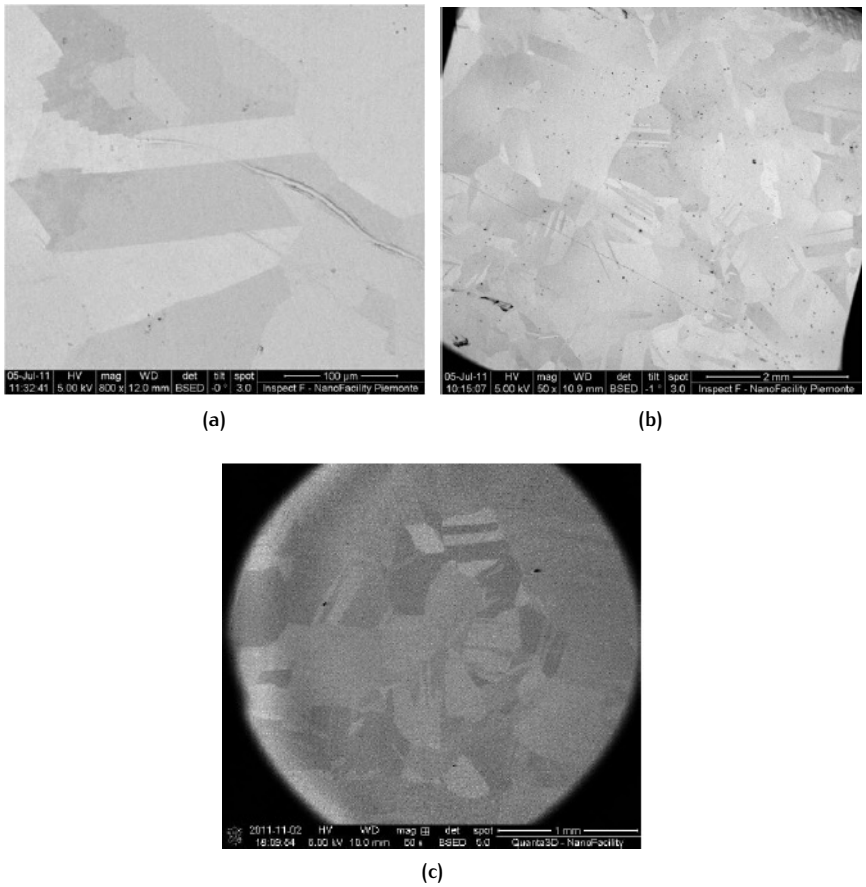

Figure 118: Cu foils after CVD processes at $T_{dep} = 800\,°C$ and $T_{dep} = 850\,°C$. SEM images of Cu foils subjected to CVD processes at different deposition temperatures: (a) magnified view of a region of a *not lapped* sample after thermal treatment at $T_{dep} = 800\,°C$: regular geometrical structures, characterized by specific angles, are clearly visible on the surface (they can be due to graphene layers present on top of Cu or to preferential crystallographic orientations of the Cu lattice); (b) full view of another *not lapped* sample, referring this time to a thermal treatment at $T_{dep} = 850\,°C$: regular structures similar to those magnified in (a) are still visible and characterize the whole Cu surface; (c) image of a *lapped* Cu sample subjected to thermal treatment at $T_{dep} = 800\,°C$: also in this case, although the initial substrate has been prepared in a different way (being this time lapped), the regular structures on the surface are visible.

- final purge of the system in N_2.

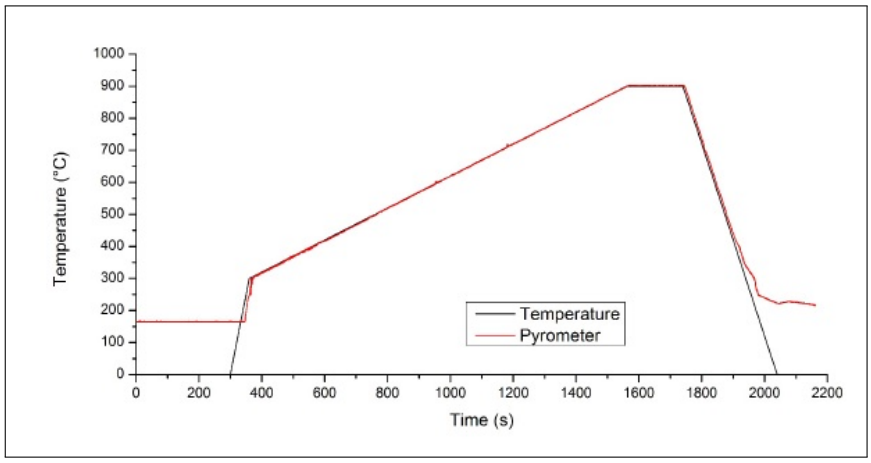

(a)

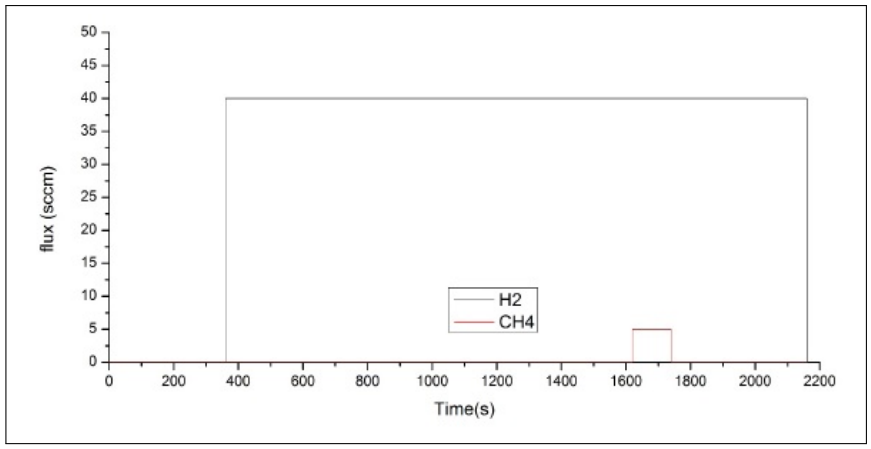

(b)

Figure 119: Thermal cycle for CVD processes on Cu foils at $T_{dep} = 900\,°C$. Schematic view of the thermal cycle carried out to perform CVD processes on Cu foils (both lapped and not lapped) at $T_{dep} = 900\,°C$: (a) set-up temperature (chosen by the user) and temperature read by the pyrometer, in black and in red respectively; (b) gas flowing during the process: H_2 is flowing in the system during the heating, the deposition and the cooling-down steps. While H_2 is flowing, the pressure measured in the reaction chamber of the RTA system is $p_{H_2=40\ sccm} \sim 1.28\,mbar$; during the deposition step, with both H_2 and CH_4 flowing in the chamber, the pressure is $p_{H_2=40\ sccm+CH_4=5\ sccm} \sim 1.33\,mbar$.

Some Cu samples undergoing CVD processes have been again polished with lapping treatment, while some other samples have been employed without performing any polishing lapping procedure on them (SEM images of the foils before undergoing any thermal treatment are shown in Figure 117). In order to avoid problems due to the interaction between Cu and Si, the samples have been put again on the SiO_2 face of the Si sample-holder.

At the end of the CVD processes, the samples have been first of all characterized at SEM. As in the case of thermal cycles performed at $T_{dep} = 800\,°C$ and $T_{dep} = 850\,°C$, also in this case geometrical structures showing regular shapes are grown on Cu surfaces (both lapped

and not lapped) during the processes (Figure 120a, Figure 120b, Figure 120c); moreover, wrinkles have been found in correspondence of Cu grain boundaries (Figure 120d), probably because of the different thermal coefficients of Cu and C, bringing to a different reaction of the two materials to the cooling-down process. Also in this case I cannot be sure, *a priori*, about the origin of these structures: further characterization of the samples is therefore needed.

To investigate the nature of the structures grown on Cu surfaces during CVD processes and to check for the eventual presence of graphene layers, Raman spectroscopy has been carried out on one (previously lapped) sample subjected to thermal cycle at $T_{dep} = 900\,°C$. First spectra have been acquired directly on Cu. In particular, by looking at the Cu surface through the optical microscope integrate in the Raman instrument, a region of the sample showing a slightly different contrast between adjacent zones (that I will call "zone *A*" and "zone *B*") has been identified (Figure 121).

Raman spectra have been acquired on both zone *A* and zone *B*, by employing both the laser wavelengths $\lambda = 514\,nm$ (Figure 122a) and $\lambda = 442\,nm$ (Figure 122b) (although by changing the laser wavelength, also the spots chosen inside both the zones *A* and *B* to acquire the spectra have been changed). The spectra clearly show that while in zone *B* no clear signature of graphene- or graphite-like structures is visible (for both laser wavelengths), in zone *A* the G and 2D peaks at the typical Raman shifts characterizing graphene have been detected (again for both laser wavelengths). Raman shifts of these peaks, for what concerns the spectra acquired in zone *A* of the sample, have been summarized in Table 8. Because of the relative intensities of the G and 2D peaks and of the Raman shift (much higher than $2700\,cm^{-1}$) and FWHM of the 2D peak it is possible in any case to infer that I have not grown monolayer graphene, but rather few-layer graphene (although an exact estimation of the possible number of graphene layers deposited onto the surface is lacking). Moreover, a quite pronounced D peak is also visible in the spectra, meaning that defects probably induced by the substrate and by grain boundaries are affecting the graphene crystal structure. Finally, it is worth pointing out that, by looking at the spectra, it is clear how much pronounced is the background plasmon emission of Cu when using "green laser light" (514 nm) with respect to the case of the "blue laser light" (442 nm): this observation explains why, in performing characterization of graphene samples directly on the Cu underlying substrate, I have later preferred to employ the blue laser wavelength.

Because of the quite encouraging results obtained, a graphene transfer process has been performed (as described in Sec. 3.2, with the only difference that in this case I have deposited only $\sim 200\,nm$ of PMMA on graphene) on the (lapped) Cu sample on which Raman characterization has provided a clear evidence of graphene present on the sample surface after the CVD process at $T_{dep} = 900\,°C$. Graphene transferred onto a new insulating SiO_2/Si substrate has appeared in an optical microscope image as in Figure 123.

Various Raman spectra have been acquired on transferred graphene, by employing laser wavelength at 514 nm (since in this case the spectra have been acquired on an insulating surface and not directly on Cu,

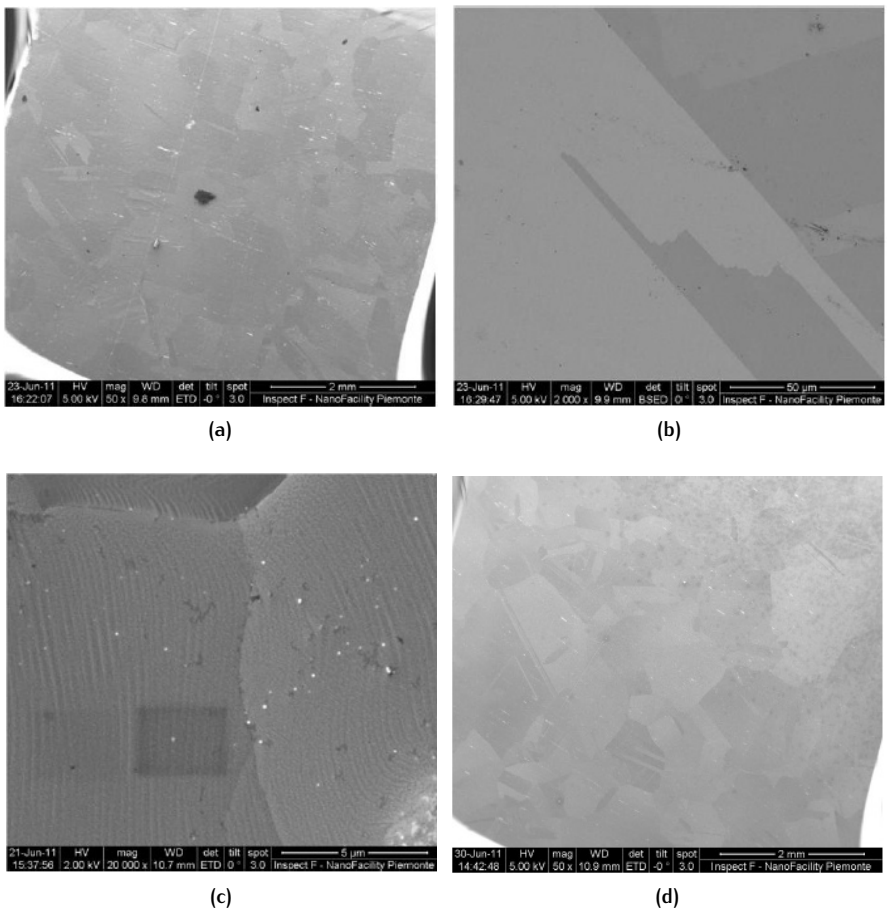

Figure 120: Cu foils after CVD processes at $T_{\mathbf{dep}} = 900\,^{\circ}\mathrm{C}$. SEM images showing the Cu samples subjected to CVD process at $T_{\mathrm{dep}} = 900\,^{\circ}\mathrm{C}$ after the thermal treatment: (a) full view of a sample not treated with lapping procedure, showing regular geometrical structures grown on the surface during the thermal cycle and absent before performing the CVD process; (b) magnified view of a region of the same sample, highlighting the geometry and the edges of the structures grown on the Cu surface; (c) magnified view of another region of the same sample showing wrinkles developed in correspondence of an underlying Cu grain boundaries. It is worth noting that the edges of the wrinkled structure grown on the substrate are characterized by angles of $\sim 120°$, proper of the graphene hexagonal lattice; (d) full view of another Cu sample subjected to CVD process at $T_{\mathrm{dep}} = 900\,^{\circ}\mathrm{C}$, in this case previously treated with lapping procedure. The same geometrical structures characterized the surface shown in (a) are visible also in this case.

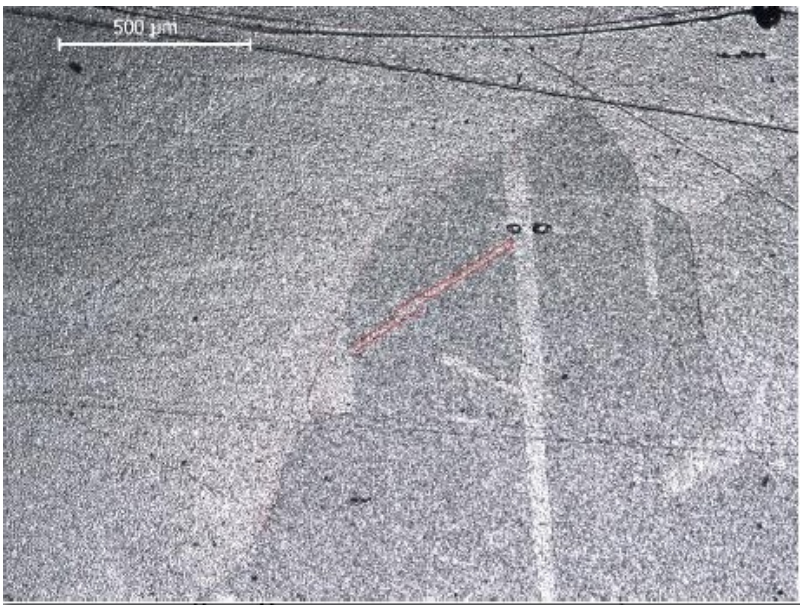

Figure 121: **Region of Cu foil characterized with Raman spectroscopy.** Optical microscope image of the region of the Cu sample chosen for Raman characterization: zone *A* lies inside the area marked in red, zone *B* is immediately outside. The area marked in red extends for hundreds of micm.

Laser wavelength (nm)	**514**			**442**		
Peak	**D**	**G**	**2D**	**D**	**G**	**2D**
Raman shift (cm^{-1})	1351	1584	2696	1351	1580	2736

Table 8: **Shift of D, G, 2D peaks for Raman spectra acquired with laser wavelengths** 442 nm **and** 514 nm **on Cu foils.** Summary of the Raman shifts of the D, G and 2D peaks visible in the Raman spectra shown in Figure 122a and Figure 122b, related to the acquisitions performed with both laser wavelengths (442 nm and 514 nm) on spots lying inside zone *A* of the Cu foil.

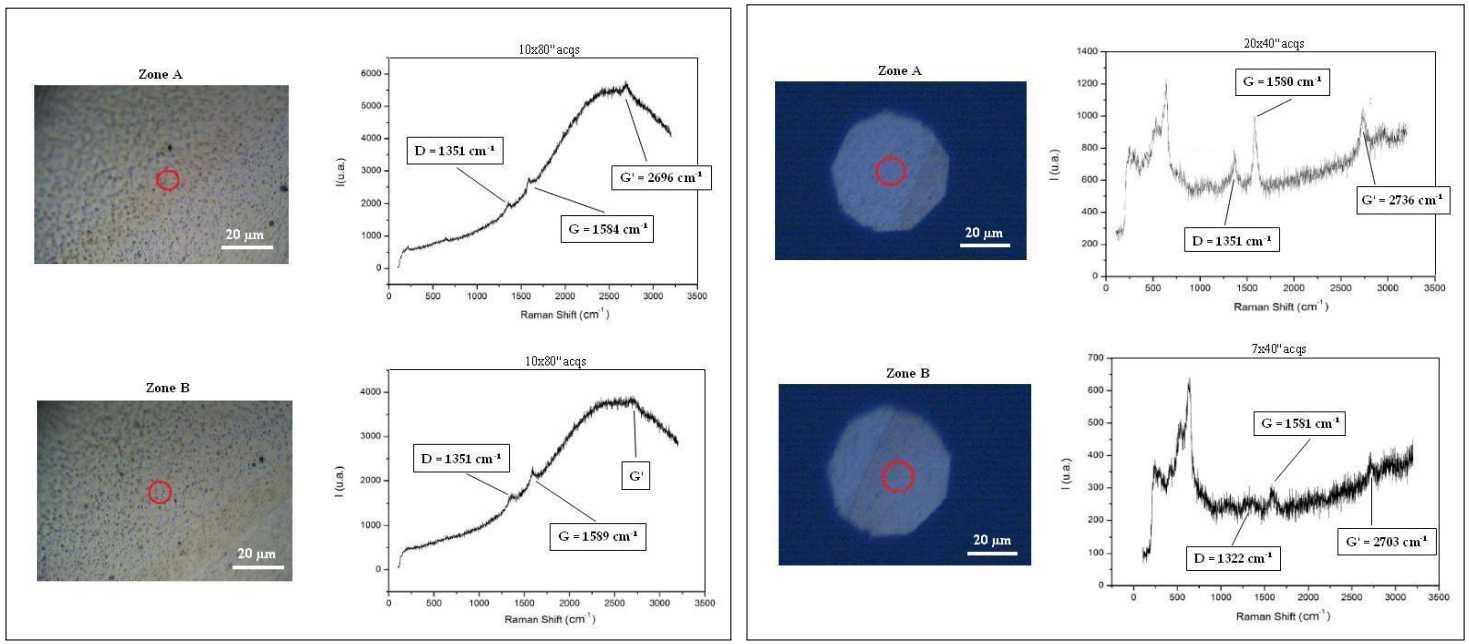

Figure 122: Raman spectra acquired on Cu foils after CVD process at $T_{dep} = 900\,°C$. Results of Raman spectroscopy performed on a lapped Cu foil after CVD process at $T_{dep} = 900\,°C$: (a) Raman spectra referring to acquisitions performed with laser wavelength $\lambda = 514\,nm$, laser power $P = 0.05\,mW$ and exposure time $\Delta t = 800\,s$. On the left, optical images of the spots randomly chosen to acquire the spectra. On top, the spectrum acquired in the spot lying into zone A of the sample, showing the typical features of (defected) graphene (the G peak at Raman shift $\sim$ 1580cm and the 2D peak -called G$'$ in the image- at Raman shift $\sim 2700\,cm^{-1}$); on the bottom, the spectrum acquired in an adjacent spot, lying in zone B, showing instead less pronounced features linked to the presence of graphene on top of the surface; (b) Raman spectra referring to acquisitions performed with laser wavelength $\lambda = 442\,nm$, laser power $P = 0.1\,mW$ and exposure times $\Delta t = 800\,s$ for zone A and $\Delta t = 280\,s$ for zone B. On the left, optical images of the spots randomly chosen to acquire the spectra. Again, as for the 514 nm laser wavelength, spectrum acquired in the spot of zone A (on top), different from the spot chosen previously for the "green laser light" acquisition, shows clear features of graphene structures grown on Cu during the CVD process; the spectrum acquired in the adjacent spot lying in zone B (on the bottom) has instead few characteristics related to the presence of graphene. It is worth noting that with the "blue laser light" ($\lambda = 442\,nm$) the background emission due to Cu substrate is highly reduced with respect to the case of the "green laser light" (this result perfectly agrees with studies reported in literature, [28]). By the way, in all cases I have not been able to establish with certainty the number of graphene layers grown in zone A of the sample during the CVD process: nonetheless, I am sure about their presence, as testified by the Raman spectra here reported.

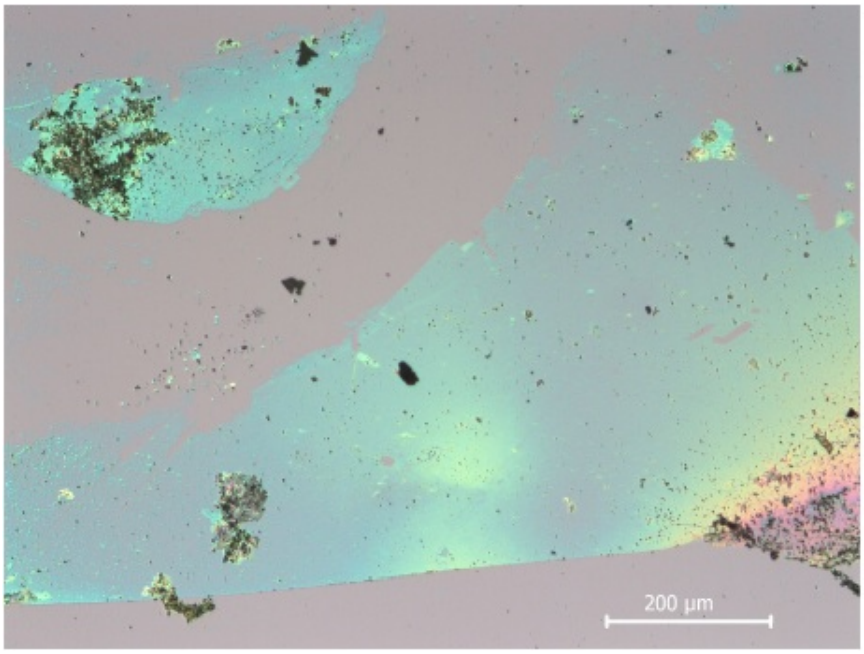

Figure 123: **Optical microscope image of graphene transferred to SiO_2/Si substrate**. Optical image showing the SiO_2/Si surface after graphene transfer: graphene flakes appear quite irregular and their presence is testified by the typical optical contrast owned by graphene layers deposited onto 300 nm thick SiO_2 substrates when subjected to optical microscopy characterization.

there have been not anymore problems related to background emission of the substrate and "green laser light" could be safely used), laser power $P = 0.25\,\text{mW}$ and exposure time of the sample to laser light $\Delta t = 720\,\text{s}$. Results of first acquisitions are shown in Figure 124a and are related to spectra acquired on three adjacent spots (called *A*, *B*, *C*), characterized by different optical contrasts. While on spots *A* and *C* only the G and D peaks, related to the presence of (defected) carbon structures (graphite or amorphous C), are visible, but no evident 2D peak related to the presence of graphene is present, the spectrum acquired on spot B shows all the two peaks (G and 2D) related to graphene and also the D peak associated to defects: Raman shifts and FWHM of these peaks have been summarized in Table 9. In particular, an intense background has been detected underlying D and G peaks: this background may be probably attributed to some amorphous carbon structures grown on Cu during the CVD process. Because of the background, a right evaluation of the I_G/I_{2D} ratio, useful to estimate the number of graphene layers grown on the surface, is quite difficult: in any case, a $I_G > I_{2D} \sim 1.4$ has been evaluated, meaning that I am dealing with multilayer graphene, characterized by a number of layers exceeding ~ 20 ([31]) .The number of graphene layers really present on top of the surface is in any case probably lower than 20, since the background underlying the G peak is affecting a lot the right value of the I_G/I_{2D} ratio. Finally, another spectrum has been acquired (whit same laser wavelength, laser power and exposure time) on a different spot of transferred graphene (Figure 124b): in this case the 2D peak has much higher intensity with respect to peak G and is much

sharper with respect to the spectrum acquired on the previous spot *B*. The I_G/I_{2D} ratio, ~ 0.8 (considering also the background underlying the G peak), together with the Raman shift and the FWHM of the 2D peak (reported in Table 9 with the positions and FWHM of D and G peaks), is a clear signal that I have succeeded in growing also few-layer graphene (characterized by a number of layers ~ 6, according to [31]; nonetheless it is worth pointing out that the ratio between 2D and G peaks intensities is deeply affected and probably overestimated, also in this case, because of the background underlying the G peak -therefore a lower number of graphene layers may be present on the spot analysed) and not only amorphous carbon or multilayer (i.e. with a number of layers $\gtrsim 20$) graphene.

Acquisition	Figure 124a, spot *B*			Figure 124b		
Peak	**D**	**G**	**2D**	**D**	**G**	**2D**
Raman shift (cm^{-1})	1352	1598	2692	1351	1594	2691
FWHM (cm^{-1})	30	38	43	41	39	39
I_G/I_{2D}		1.4			0.8	

Table 9: Shift, FWHM and intensities ratio of D, G, 2D peaks for Raman spectra acquired on transferred graphene. Summary of the Raman shifts, FWHM and intensities ratio of D, G and 2D peaks, related to the Raman spectra shown in Figure 124a - spot *B* and in Figure 124b. A comparison of the results show that in both cases graphene has grown on the surface during the CVD process, but it is characterized by a lower number of layers on the spot shown in Figure 124b.

From the results discussed above, we can conclude that CVD processes have been more successfully performed on Cu foils than on Ni films: on the former I have indeed succeeded in finding a thermal cycle, characterized by deposition temperature $T_{dep} = 900\,°C$, allowing for the deposition of few-layer graphene on top of Cu (Raman characterization on transferred graphene has shown that in some regions of the sample a number of graphene layers as small as ~ 6, or perhaps even smaller, has been grown). Besides this important result, by performing other thermal cycles at different deposition temperatures (higher and lower than 900 °C) I could gain further interesting insights about the optimization of the whole CVD process. From thermal cycles carried out at deposition temperatures $T_{dep} < 900\,°C$ I could indeed learn that these temperatures are too low in order to activate the dissociation of CH_4 molecules, needed to grow graphene; on the other side, thermal cycles performed at deposition temperature $T_{dep} > 900\,°C$ allowed me to realize that Cu and Si, at these high temperatures, form a solid stable binary mixed phase, melting together and making unfeasible the deposition of graphene. This latter point is important because it provides the indication that although deposition of Cu films directly onto a Si substrate, and not over a SiO_2 substrate, would be better to favour an oriented monocrystalline film growth, an insulating layer must be intercalated between Cu and Si if a thermal treatment at temperatures higher than 850 °C shall be performed onto the samples: the insulating layer prevents indeed the melting of the two species.

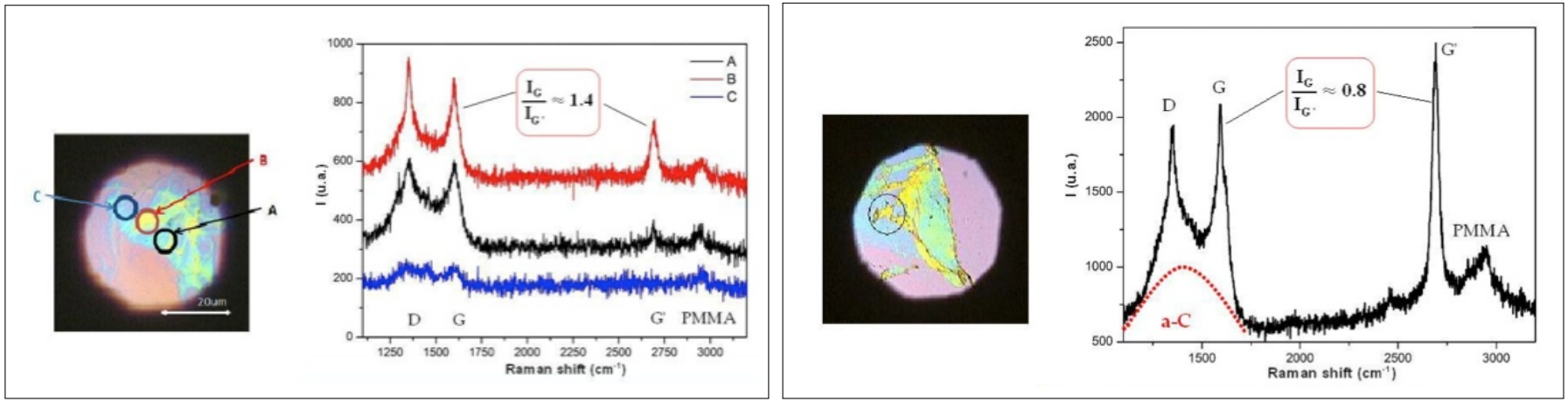

(a) (b)

Figure 124: **Raman spectra acquired on transferred graphene after CVD process at $T_{dep} = 900\,°C$.** Results of Raman spectroscopy performed on graphene grown by CVD at $T_{dep} = 900\,°C$ and transferred onto a SiO_2/Si substrate. All the spectra have been acquired with laser wavelength at 514 nm, laser power $P = 0.25\,mW$ and exposure time $\Delta t = 720\,s$: (a) on the left, the optical image of the spots randomly chosen on a certain region of the sample to acquire the spectra. On the right, the spectra acquired on spots *A*, *B* and *C*. While in *A* and *C* the spectra show clear D and G peaks related to the presence of (defected) carbon structures (graphite or amorphous C), but no evident 2D peak related to the presence of graphene, in *B* the typical G and 2D peaks of graphene are visible in the spectrum. The ratio between their intensities is > 1, meaning that I am probably dealing with multilayer graphene (with a number of graphene layers exceeding ~ 20); (b) on the left, the optical image of the spot randomly chosen on another region of the sample to acquire the spectrum. On the right the associated Raman spectrum, showing this time clearer features related to the presence of few-layer graphene onto the characterized surface. The position of the 2D peak, its sharpness and the I_G/I_{2D} ratio are compatible with a number of layers ~ 6. All the spectra in (a) and (b) are characterized by an intense background underlying the D and G peaks, probably due to amorphous carbon deposited onto the surface during the CVD process. The background affects the right evaluation of the I_G/I_{2D} ratio, resulting in an overestimation of its value. Finally, a small peak at $\sim 2900\,cm^{-1}$ is also visible in all the spectra: this peak can be attributed to residual PMMA left on the substrate after the graphene transfer process and the cleaning in acetone.

3.3.3 CVD on Cu films

Having acquired some experience about graphene deposition thanks to the CVD processes successfully performed onto Cu foils, I have decided to move on and to change substrate, substituting Cu foils with Cu thin films. I have devoted the entire Chapter 2 to the explanation of the common problems (related to dewetting effects) arising when performing thermal cycles at temperatures higher than $\sim$ 900–950 °C on Cu films thinner than $\sim$ 500 nm evaporated onto SiO_2/Si substrates: these problems deeply limit the possibility of growing graphene by CVD on very thin films and I have already explained in Sec. 2.4 how it is possible to get a better control on them by exploiting the properties of the RTA system used for CVD processes. I have also shown in Sec. 2.3.2 the results of a CVD process that I have performed at a nominal deposition temperature $T_{dep} = 850\,°C$ on a $d_{Cu} = 500\,nm$ thick Cu film: we have seen that at this temperature dewetting of the Cu film did not occur (Figure 82a), but at the same time no signature of graphene had been found on top of the Cu surface, as clearly revealed by the Raman spectrum acquired on the sample after the CVD process, showing no sharp 2D peak at $\sim 2700\,cm^{-1}$ (Figure 82b).

However, at the end of Sec. 2.4 I have already mentioned that, thanks to the dewetting studies I have performed, I could define a (small) range of temperatures and of Cu film thicknesses allowing for graphene growth by CVD, preventing at the same time film dewetting: in this section I will therefore report the results of such a process, that brought to successfully grow few-layer graphene on top of a Cu film. The CVD process has been performed on samples prepared by e-beam evaporation of $d_{Cu} = 500\,nm$ thick Cu film on top of a p-type $\langle 100 \rangle$ oriented Si wafer ($\sim 1\,cm^2$) with $\sim$ 300 nm thermal SiO_2. The e-beam evaporation procedure has been described in detail in Sec. 2.2.2. The SEM images of the samples after Cu deposition have been reported in Figure 65a, Figure 65b and clearly show a uniform coverage of the SiO_2 surface characterized by an expected Cu polycrystalline structure with grains ranging from $\sim$ 70 nm to $\sim$ 130 nm as typical size. Moreover, also STM analysis, scanning an area of $\sim 10^{-2}\,\mu m^2$, has been performed on the pristine (i.e. as deposited) Cu films and the results have been shown in Figure 67. The STM characterization allowed me in particular to evaluate the roughness of the Cu surface (Figure 67a). The resulting RMS, extrapolated by analysing the acquired data, of $\sim$ 2 nm (an order of magnitude higher than single layer graphene thickness, $\sim$ 3.3 Å), together with the topographic behaviours obtained for certain scanning directions (Figure 67b), showing among others height variations as small as few angstroms, makes ineffective the use of Atomic Force Microscopy (AFM) to detect any change in the number of graphene layers eventually present on Cu: the changes in height produced by the latter effect would be hardly distinguishable from topographic changes due to the roughness of the substrate's surface. Finally, also XRD analysis has been performed on the as deposited Cu films, with the instrumental configuration explained in Sec. 2.2.2 and with the results shown in Figure 66, showing two preferential crystallographic orientation: $\langle 111 \rangle$ and $\langle 220 \rangle$, with the former having higher intensity than the latter.

Cu samples, after careful cleaning in acetone and isopropanol, has been subjected to the thermal cycle shown in Figure 125 and summarized as follows (samples have been put on the Si sample-holder in the RTA system according to the standard configuration shown in Figure 77a):

- pre-vacuum step, $\Delta t = 900\,s$;

- room temperature up to 500 °C, $\Delta t = 150$ s, no gas flowing;
- 500 °C–725 °C, $\Delta t = 300$ s, 40 sccm H_2;
- 725 °C–725 °C, $\Delta t = 300$ s, 40 sccm H_2;
- 725 °C–725 °C, $\Delta t = 300$ s, 10 sccm CH_4;
- 725 °C–450 °C, $\Delta t = 390$ s, no gas flowing;
- 450 °C–270 °C, $\Delta t = 60$ s, no gas flowing;
- 270 °C down to room temperature with a final purge of the system in N_2.

Therefore, the CVD process is composed by four main steps:

1. a fast heating step, increasing the temperature up to 500 °C, carried out in vacuum ($p_{\text{chamber}} = 1.2 \times 10^{-2}$ mbar);
2. a subsequent annealing step (10 min long), bringing the system to 725 °C, performed under flow of 40 sccm H_2 ($p_{\text{chamber}} = 1.65$ mbar). As already explained in Chapter 1 and Sec. 2.3.2, the purpose of this step is to improve the quality of the Cu film, by increasing the size of the grains present on its surface and, consequently, by inducing a low defective growth of graphene due to the reduced number of grain boundaries;
3. a deposition step, aiming to grow graphene, performed by flowing ultrahigh purity CH_4, with a flow rate of 10 sccm, for 5 min ($p_{\text{chamber}} = 3.3 \times 10^{-1}$ mbar), without any H_2 flow. I have already reported in Sec. 2.3.2 that the rôle played by H_2 flowing during the deposition step of the CVD processes performed to grow graphene has been long debated in literature. In this case I have decided to avoid H_2 flowing in the chamber together with CH_4 during step deposition step, following [177] in which H_2 has been reported to be detrimental for the final quality of graphene sheets when using Cu thin films;
4. a cooling-down step divided in three sub-steps: a first one (at a rate of ~ 42 °C min^{-1}), down to 450 °C in gas-free conditions, a faster one by switching the heaters off (at a rate of ~ 180 °C min^{-1}), till to ~ 270 °C, again in vacuum conditions and a final one carried out in nitrogen atmosphere, to purge the system, down to room temperature.

It is worth mentioning that the deposition temperature $T_{\text{dep}} = 725$ °C here reported is only the nominal temperature read by the old thermocouple present in the RTA system at the time I have performed the CVD process, having some malfunctioning (as already explained in Sec. 2.3.1): I have later established, by means of a new thermocouple, that probably the thermocouple here employed was underestimating the temperature of the system of ~ 150 °C. As a consequence, the real deposition temperature should be $T_{\text{dep}} \sim 875$ °C.

After performing the CVD process, the samples subjected to the thermal treatment have been first characterized by SEM and XRD analyses in order to investigate a change in granulometry and crystallographic orientation of the Cu surface, due to high temperature annealing under hydrogen flow.
SEM image reported in Figure 126a shows that Cu surface reorganized itself at the temperature reached during graphene deposition: an increase of grain

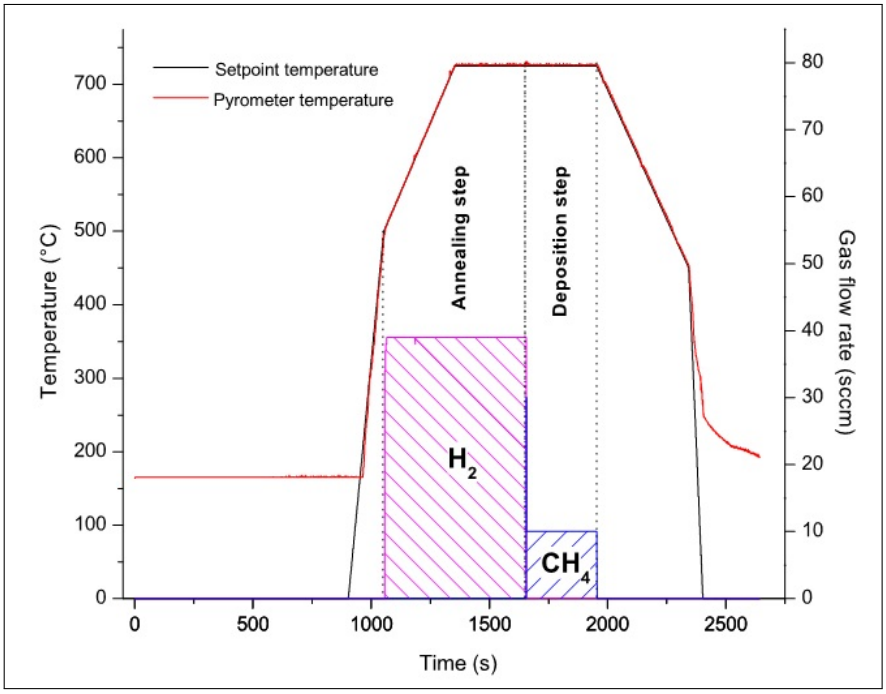

Figure 125: Thermal cycle for graphene deposition on Cu films. Illustration of the thermal process performed for CVD growth of graphene on top of a $d_{Cu} = 500\,nm$ thick Cu film at (nominal) deposition temperature $T_{dep} = 725\,°C$: during the deposition step only CH_4 is flowing in the reaction chamber of the RTA system.

average size (from $\sim 100\,nm$ to $\sim 3\,\mu m$) is observed, as expected, due to the annealing process (a similar increase in grains size hd been already observed on Cu samples with thickness $d_{Cu} = 500\,nm$ subjected to CVD process at the nominal deposition temperature $T_{dep} = 850\,°C$, as reported in Sec. 2.3.2 and shown in Figure 82a). Cu still covers uniformly the sample surface, meaning that the temperature during the annealing and deposition processes was low enough and the growth time short enough to prevent dewetting effects on the catalytic film. Nevertheless, early stage formation of Cu droplets is observed (Figure 126b).

XRD analysis performed on my samples, in contrast to what observed in other works ([177]), shows (Figure 127, to be compared with Figure 66, acquired on the pristine as deposited Cu surface) changes in the preferential crystallographic orientation of the grains present on the sample surface after CVD process, involving both $\langle 111 \rangle$ and $\langle 220 \rangle$ directions, with a decrease in the $I_{\langle 111 \rangle}/I_{\langle 220 \rangle}$ intensity ratio after the thermal treatment. This fact can probably be ascribed to the fast cooling-down rate chosen for the experiment.

For the results I want to show in this section, the most important characterization tool used to investigate the property of the samples surface after the CVD process has been Raman spectroscopy. Raman analysis, as already pointed out in Sec. 3.1.1, has been performed with He-Cd blue laser at wavelength $\lambda = 442\,nm$, avoiding in this way background plasmon emission of Cu when excited e.g. by green light (a detailed study of the correlation between the laser wavelength used to characterized graphene layers directly on a Cu surface, without transfer process to an insulating substrate such as SiO_2, and the intensity of background plasmon emission of Cu has been re-

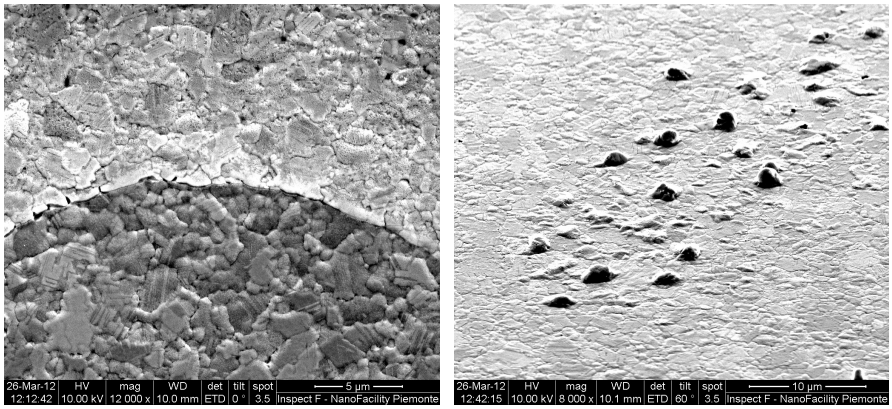

(a) (b)

Figure 126: CVD process at $T_{dep} = 725\,°C$ on $d_{Cu} = 500\,nm$ Cu thick film. SEM images of a 500 nm thick Cu sample at the end of the CVD process performed at nominal $T_{dep} = 725\,°C$: (a) dewetting is not fully occurred and Cu covers almost the whole SiO_2/Si substrates. The metallic surface is still characterized by a polycrystalline structure, but the average size of the grains ($\sim 3\,\mu m$) is increased with respect to the grains size evaluated on pristine films of same thickness just after the deposition (Figure 65b); (b) Cu droplets formation starts to appear on top of the surface, meaning that Cu dewetting is nonetheless starting to occur.

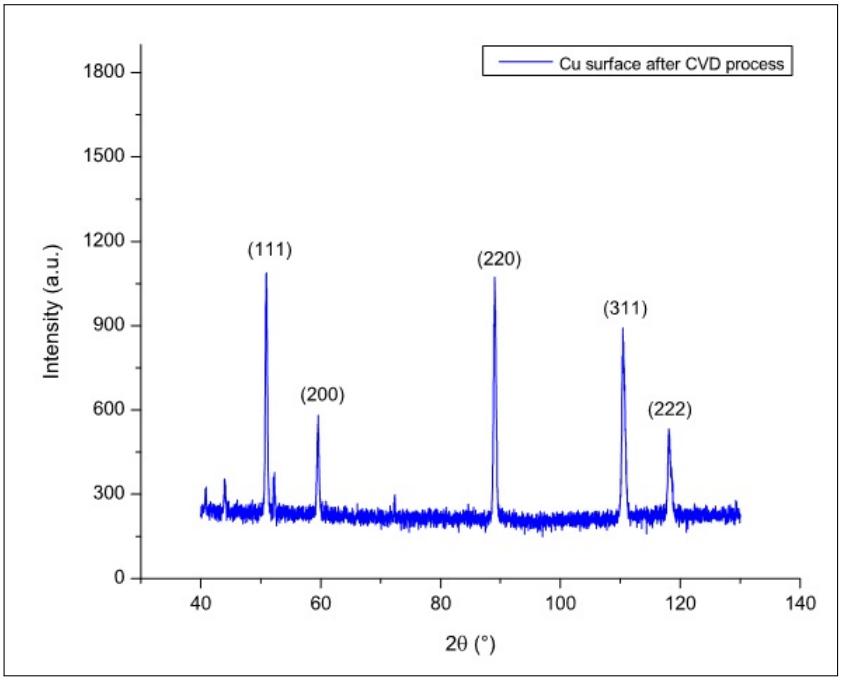

Figure 127: XRD analysis of a $d_{Cu} = 500\,nm$ thick Cu surface after CVD process at $T_{dep} = 725\,°C$. XRD spectrum illustrating the main crystallographic directions characterizing the crystal domains structure of the 500 nm thick Cu film shown in Figure 126: relative intensities of the $\langle 111 \rangle$ and $\langle 220 \rangle$ crystallographic orientations are completely changed with respect to the XRD spectrum acquired on the same sample just before carrying out the CVD process (see Figure 66). The spectrum has been acquired with an incident angle $\Omega = 0.8°$ with the XRD instrument described in Sec. 2.1.3.

ported in [28, 119]). For the acquisition I have used laser power both at 1 mW and 0.1 mW, by varying consequently the exposure time of the samples to laser irradiation (in order to keep the amount of energy $E = Pt$ transferred from laser light to samples fixed).

However, the effect of the background plasmon emission of Cu on the shape of the Raman spectra directly acquired on Cu has been explicitly evaluated to be more sure about the results: to do so, Raman spectra have been acquired through successive acquisitions (the laser beam has been shuttered between successive acquisitions) performed on two different spots A and B of a pristine 500 nm thick Cu film, identical to those employed for the CVD process here reported but not subjected to thermal treatment, using laser power $P = 0.1\,\text{mW}$ and $P = 1\,\text{mW}$ respectively (the background spectra obtained are shown in Figure 128 and Figure 129). The obtained average spectra, acquired on spot A with laser power $P = 0.1\,\text{mW}$ and on spot B with laser power $P = 1\,\text{mW}$, have been then subtracted respectively from the spectrum shown in Figure 131 and from two of the four spectra shown in Figure 132a (more precisely, from the spectra associated to the second and third acquisitions), acquired at laser power $P = 0.1\,\text{mW}$ and $P = 1\,\text{mW}$ respectively, on a Cu sample of the same thickness but subjected to CVD process. The resulting spectra are shown in Figure 130 and show in all cases (so, for both laser powers) a perfect agreement between the shape of the Raman spectra directly acquired on Cu samples after CVD process and the Raman spectra acquired on pristine Cu films of the same thickness not subjected to thermal treatment.

From now on, for what concerns the Raman spectra directly acquired on Cu samples subjected to CVD processes, I will show only the spectra as originally obtained (not flat), without subtracting the background spectrum due to plasmon emission of the Cu underlying surface, since it has been clarified the origin of the not flat shape of the original spectra and since subtraction of the background spectrum does not change the physical principles involved in what follows.

The first spectrum (shown in Figure 131) acquired directly on Cu sample after carrying out the CVD process described in Figure 125 has been obtained by setting the laser at low power (i.e 0.1 mW) and by exposing the sample to laser light for $\Delta t = 800\,\text{s}$. The obtained spectrum shows three prominent peaks[5]:

1. the D peak at $\sim 1370\,\text{cm}^{-1}$, associated to a defect induced inter-valley scattering (as explained in Sec. 3.1.1);

2. the G peak at $\sim 1597\,\text{cm}^{-1}$, associated to the presence of carbon structures on the Cu surface;

5 Usually the Raman shift of G and 2D peaks proper of graphene structures reported in literature ([47]) are slightly redshifted with respect to the values I have obtained ($\sim 1580\,\text{cm}^{-1}$ for the G peak and $\sim 2690\,\text{cm}^{-1}$ for the 2D peak). For what concerns the G peak, the slightly higher value of Raman shift I have found is likely due to some doping effect inducing charge carriers into graphene from the underlying substrate, resulting in an up- or down-shifting of the graphene Fermi level (so, the Dirac point): as explained in Sec. 3.1.1, G peak Raman shift is sensitive to doping, since any time graphene Fermi level is changing, a blueshift in the G peak position is detected. For what concerns the 2D peak Raman shift, the reason of the slightly higher value may be instead attributed to the laser wavelength I have used to perform Raman analysis, to the fact that I have acquired Raman spectra directly on Cu surface and to the fact that I am not dealing with monolayer graphene: indeed, in [28] it has been shown how 2D peak position for monolayer graphene grown by CVD on Cu is affected by the laser light wavelength (so, the laser energy) employed to acquire Raman spectra directly on the Cu surface. The values for the 2D peak Raman shift shown in that work are fully compatible with the ones I have experimentally measured.

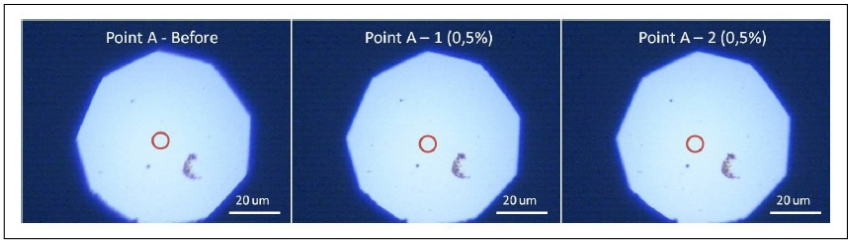

(a)

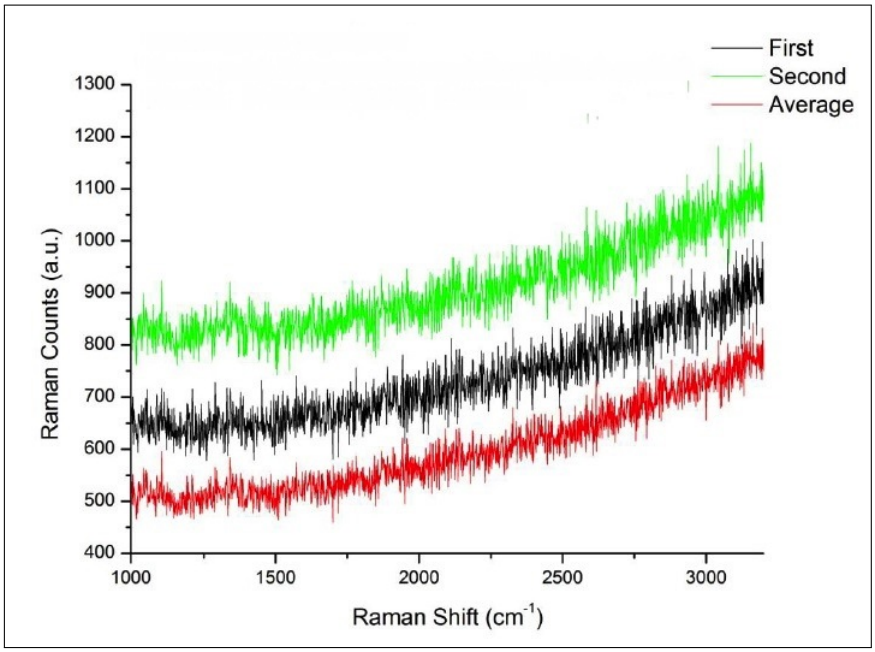

(b)

Figure 128: Raman spectra acquired on pristine 500 nm **thick Cu film at low laser power (**0.1 mW**).** Raman spectroscopy performed on the same spot A of a 500 nm thick Cu film not subjected to CVD process. Acquisitions have been performed with laser power 0.1 mW (0.5% of the full laser power of the instrument) and each one has lasted $\Delta t = 800$ s (the laser source has been switched on, counting also the time intervals between successive acquisitions, for a total time $t = 3300$ s). (a) Optical images showing the spot A of the surface subjected to Raman spectroscopy, at the beginning (before acquisition of the spectra) and after each acquisition. No significant changes of the spot are visible. (b) Raman spectra acquired during two successive acquisitions on spot A and average spectrum obtained from the previous ones. The behaviour of the spectrum (not flat) is due to background plasmon emission of Cu.

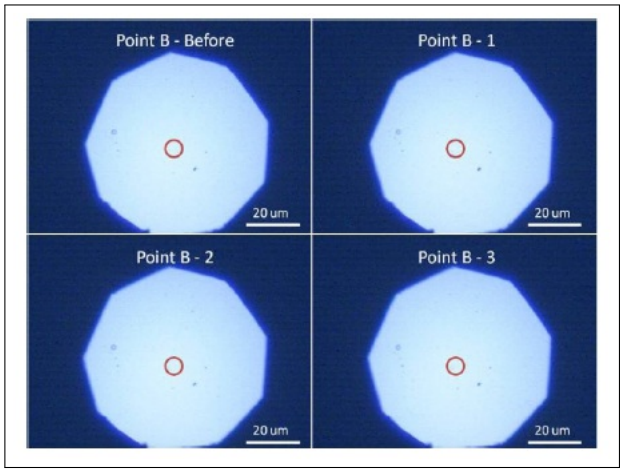

(a)

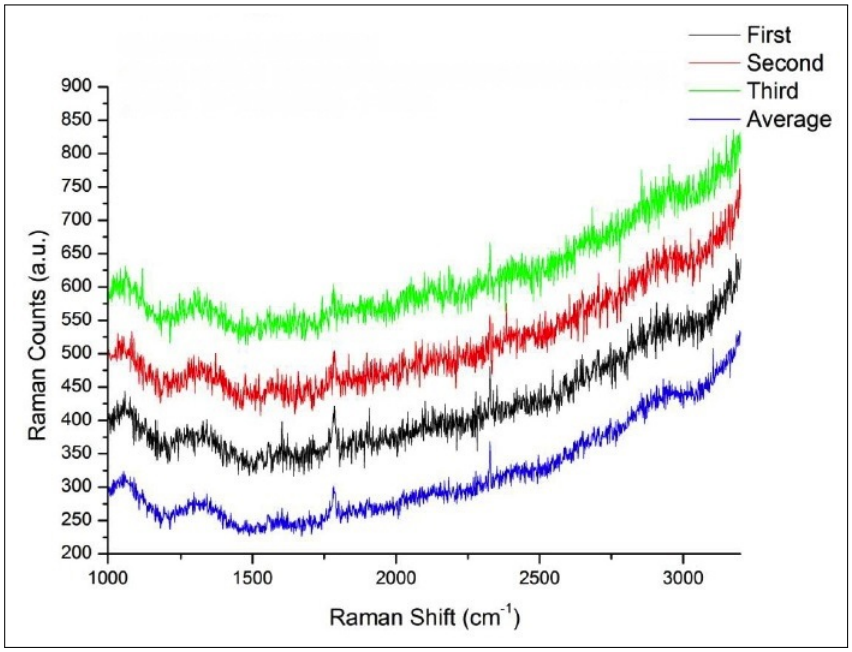

(b)

Figure 129: **Raman spectra acquired on pristine** 500 nm **thick Cu film at high laser power (**1 mW**).** Raman spectroscopy performed on the same spot B (different from the spot A of Figure 128) of a 500 nm thick Cu film not subjected to CVD process. Acquisitions have been performed with laser power 1 mW (5% of the full laser power of the instrument) and each one has lasted $\Delta t = 80$ s (the laser source has been switched on, counting also the time intervals between successive acquisitions, for a total time $t = 570$ s). (a) Optical images showing the spot B of the surface subjected to Raman spectroscopy, at the beginning (before acquisition of the spectra) and after each acquisition. No significant changes of the spot are visible. (b) Raman spectra acquired during three successive acquisitions on spot B and average spectrum obtained from the previous ones. The behaviour of the spectrum (not flat) is again due to background plasmon emission of Cu.

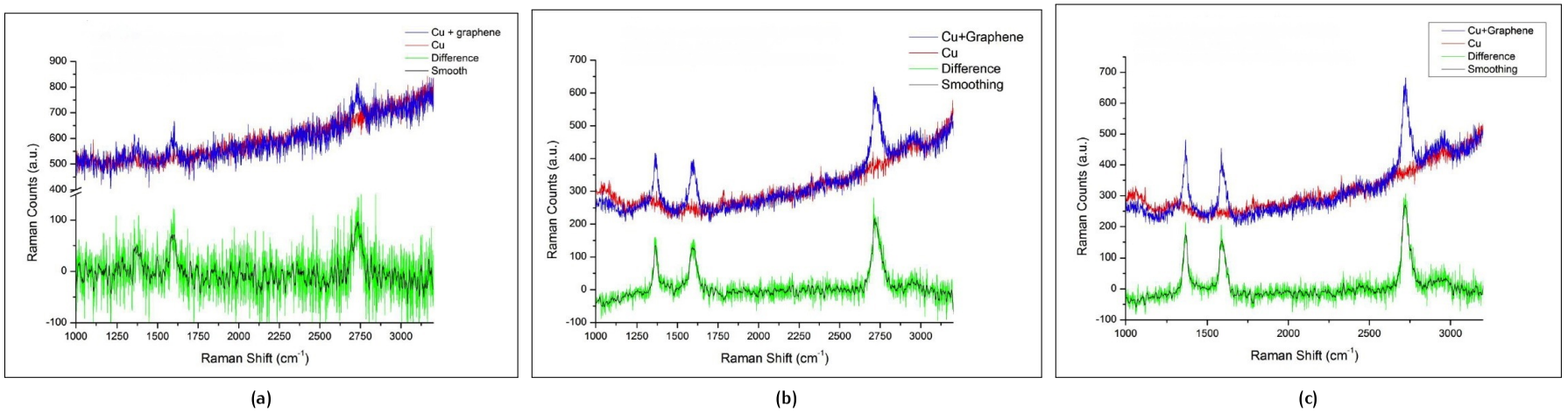

Figure 130: Background plasmon emission in Raman spectra acquired directly on Cu. Comparison among the average Raman spectra shown in Figure 128, Figure 129 and Raman spectra directly acquired on Cu samples subjected to CVD processes: (a) for the case of Raman analysis performed with low laser power ($P = 0.1\,\text{mW}$): average spectrum of Figure 128 has been compared to the Raman spectrum shown in Figure 131. A perfect agreement between the background emissions of the Cu surface in the two cases is clearly visible; (b) for the case of Raman analysis performed with high laser power ($P = 1\,\text{mW}$): average spectrum of Figure 129 has been compared to the Raman spectrum associated to the second acquisition shown in Figure 132a. A perfect agreement between the background emissions of the Cu surface in the two cases is again clearly visible; (c) again for the case of Raman analysis performed with high laser power ($P = 1\,\text{mW}$): average spectrum of Figure 129 has been compared this time to the Raman spectrum associated to the third acquisition shown in Figure 132a. A perfect agreement between the background emissions of the Cu surface in the two cases is clearly visible also in this case.

3. the 2D peak at $\sim 2707\,\mathrm{cm}^{-1}$, characterized by FWHM $\simeq 56.6\,\mathrm{cm}^{-1}$ associated to presence of graphene-like structures on the underlying sample.

The ratio between the G peak and 2D peak intensities has been evaluated to be $\frac{I_G}{I_{2D}} \simeq 0.74$: this value (much greater than 1/3), together with the position and the FWHM of the 2D peak, clearly shows that graphene is certainly grown on the Cu surface during the CVD process but, at the same time, it is not monolayer.

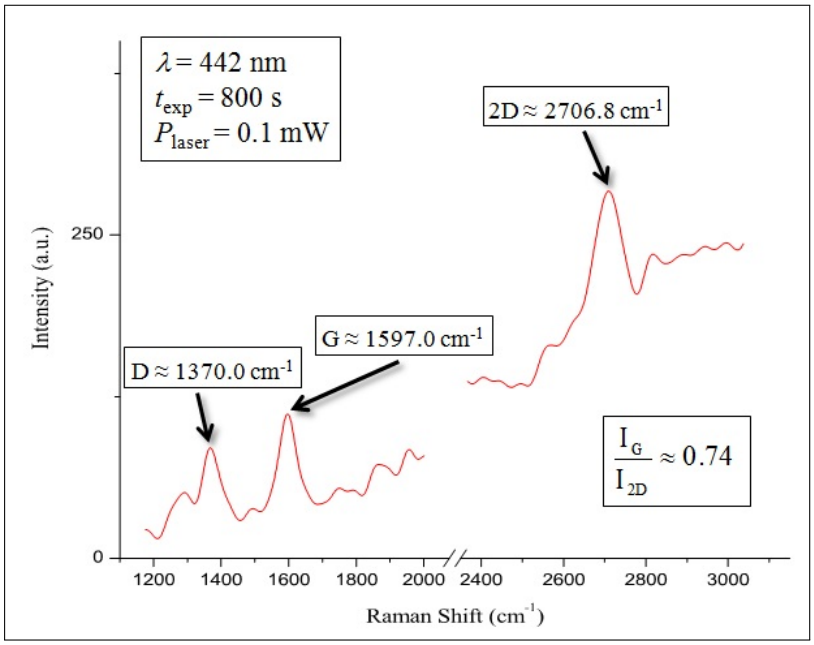

Figure 131: Raman spectrum of CVD graphene on 500 nm **thick Cu film at low laser power and long acquisition time.** First Raman spectrum of not transferred CVD graphene grown on 500 nm thick Cu, acquired with laser power $P = 0.1\,\mathrm{mW}$ for $\Delta t = 800\,\mathrm{s}$. The G and 2D peaks typical of graphene are clearly visible, together with the D peak associated to defects present in the graphene crystal structure. The value of the I_G/I_{2D} is compatible with few-layer graphene, rather than monolayer graphene.

After having acquired the first Raman spectrum, I have decided to repeat four times the acquisition (again directly on the Cu sample without graphene transfer) in the same spot of the Cu surface (of the order of $1\,\mu\mathrm{m}^2$), but this time at higher laser power (1 mW) and reduced exposure time ($\Delta t = 80\,\mathrm{s}$) and I have this way obtained the spectra shown in Figure 132a. Three prominent peaks are still visible, as previously it was for the spectrum acquired at lower laser power:

1. the D peak at $\sim 1340\,\mathrm{cm}^{-1}$, associated to defects in the graphene lattice structure;
2. the G peak at $\sim 1594\,\mathrm{cm}^{-1}$, due to the presence of carbon atoms in hexagonal crystalline structure;
3. the 2D peak at Raman shift varying between $\sim 2698\,\mathrm{cm}^{-1}$ and $\sim 2710\,\mathrm{cm}^{-1}$, strictly related to mono- or few-layer graphene present on top of the Cu surface.

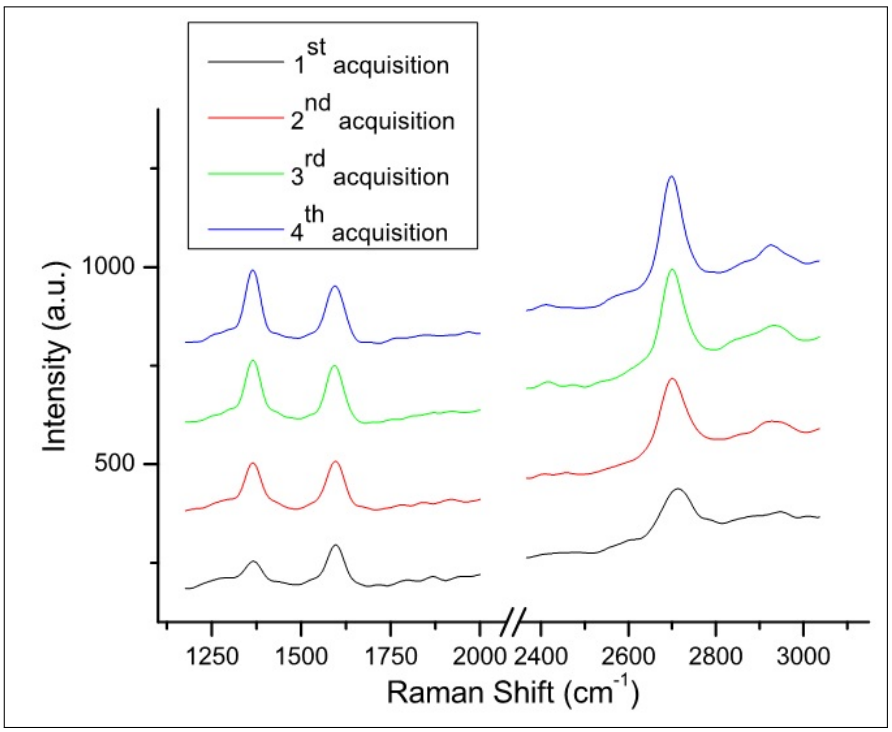

(a)

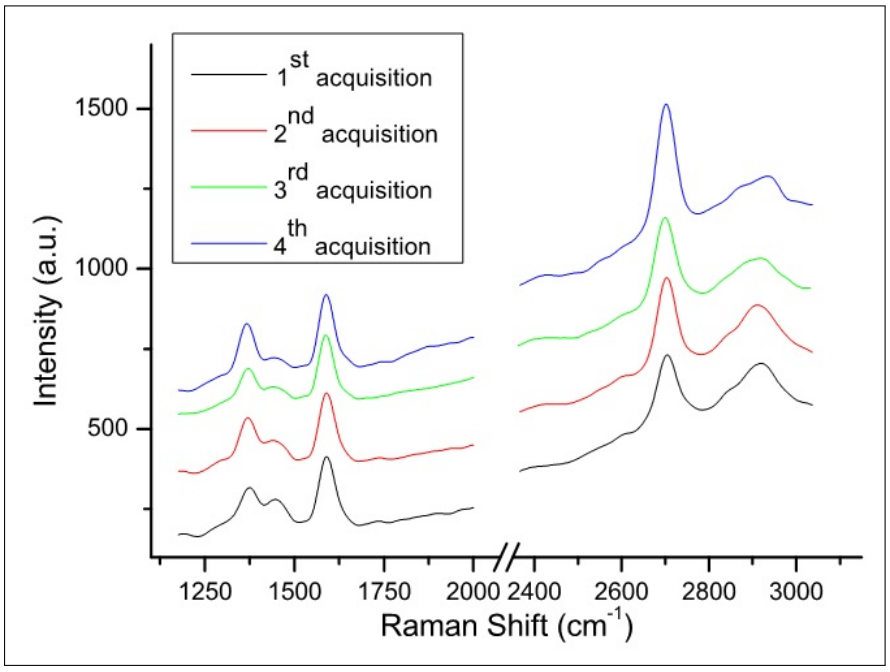

(b)

Figure 132: **Raman spectrum of CVD graphene on** 500 nm **thick Cu film at high laser power and fast acquisition time.** Raman spectra of CVD graphene grown on 500 nm thick Cu film acquired on the same spot at following time intervals (all the acquisitions have been performed at laser power $P = 1$ mW and exposure time $\Delta t = 80$ s): (a) in the case of acquisitions performed directly onto the Cu substrate; (b) in the case of acquisitions performed after graphene transfer onto an insulating SiO_2 substrate.

It is possible to notice in particular that while the G peak shape and position are unaffected by laser exposure (only a slight increase in intensity is worthy of note), the D and 2D peaks change significantly their structure. The careful analysis of both the position and the FWHM of the 2D peak for all spectra is reported in Table 10 and Figure 133a.

Acq.	*Graphene on Cu*			*Graphene on SiO_2*		
	Raman Shift (cm^{-1})	**FWHM** (cm^{-1})	I_G/I_{2D}	**Raman Shift** (cm^{-1})	**FWHM** (cm^{-1})	I_G/I_{2D}
1	2711.4	70.0	0.86	2704.0	40.3	1.01
2	2701.3	60.0	0.60	2702.7	37.7	0.79
3	2699.8	49.2	0.56	2699.0	43.8	0.80
4	2698.2	46.6	0.46	2701.1	38.7	0.61

Table 10: 2D peak position and sharpness and I_G/I_{2D} ratio evolution for successive Raman acquisitions at high laser power. Comparison of the position and FWHM of 2D peaks of subsequent Raman acquisitions (performed at high laser power, $P = 1\,mW$) as extracted by a single Lorentzian fit of the spectra shown in Figure 132, Figure 133 and evolution of the I_G/I_{2D} ratio. Uncertainties of the order of $0.01 - 0.04\%$ for the 2D peak Raman shifts and of $3 - 6\%$ for 2D peak FHWMs have been estimated. The results concerning transferred graphene onto insulating SiO_2/Si substrates are affected by higher uncertainties because of pronounced secondary peaks (possibly due to residual PMMA used for graphene transfer) present in the Raman spectra (see Figure 132b), making the fit procedure less accurate.

The results show a significant evolution in the 2D peak shape: this fact may be attributed to some change in the graphene-like structure grown on Cu. The evolution here reported is compatible with a decrease in the number of graphene layers present on the Cu substrate, as suggested by the lowering in the Raman shift position of the peaks centre and by the sharpening of the 2D peaks observed while the exposure to laser light is increased in time. This interpretation is confirmed by the evaluation of the I_G/I_{2D} ratio of the four spectra: the ratio is decreasing as expected for a decrease in the number of graphene layers ([47, 72, 110, 154]), as shown in Table 10. However, these results do not permit to make a clear quantitative estimation of the number of graphene layers present on the Cu substrate before and after the exposition to the laser light during Raman analysis, because they do not completely agree with the typical values reported in literature for position and FWHM of 2D peak of mono-, bi- and few-layer graphene.

A possible phenomenological model to explain this effect, as discussed also in [62], is based on the observation that the laser beam at high power provides an amount of heat sufficient to locally etch away, in presence of oxygen atmosphere, outermost graphene layers grown during CVD process on top of Cu. Although it is known that suspended monolayer graphene shows a room temperature thermal conductivity of up to $\sim 5000\,W\,m^{-1}\,K^{-1}$ ([5]), the effect of such a huge value can be significantly reduced in the system I have employed because of the decrease in the surface area of graphene flakes occurring while increasing number of layers (said $A^{(i)}$ the area of the

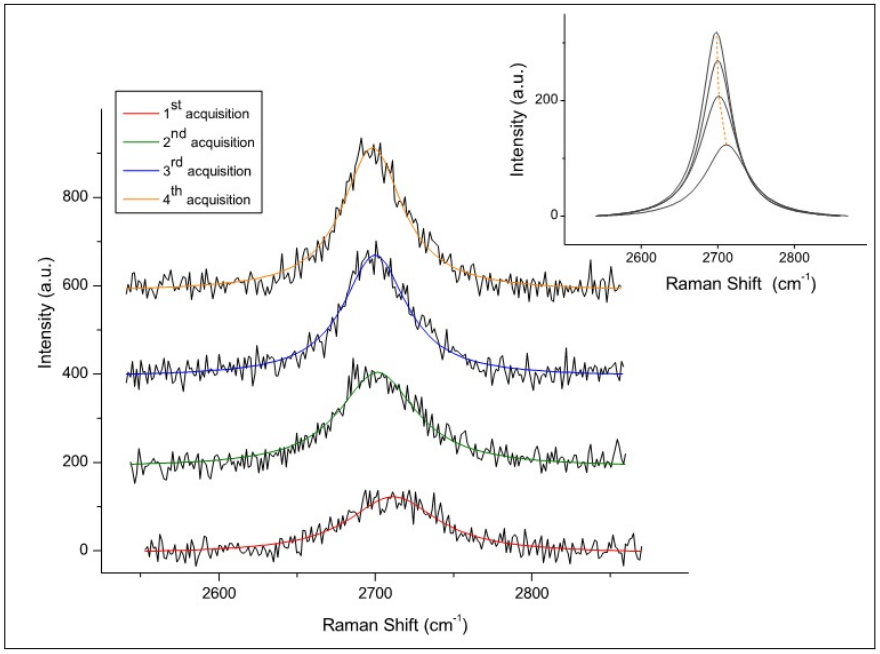

(a)

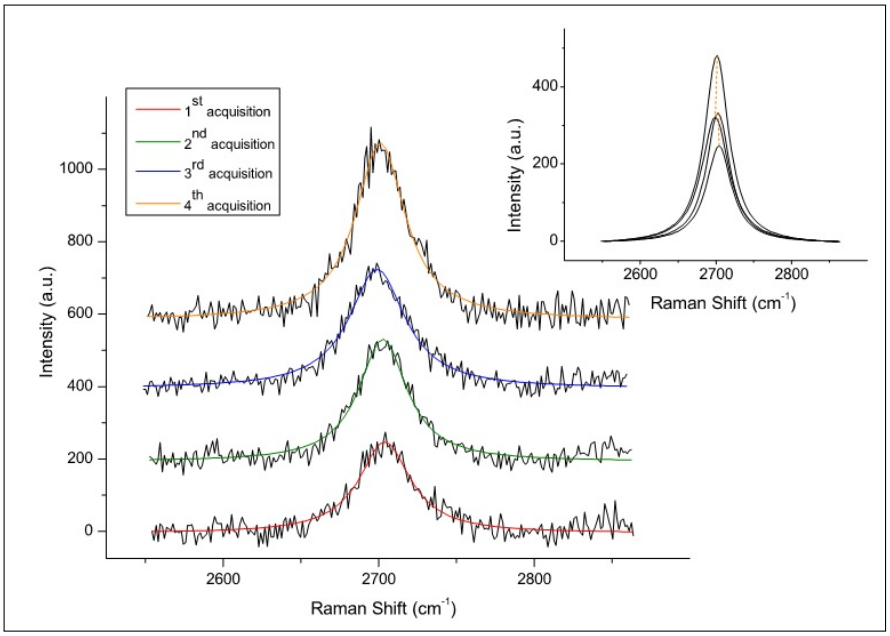

(b)

Figure 133: 2D peak evolution with number of Raman acquisitions. Behaviour of position and shape of 2D peak of the Raman spectra acquired in the same spot of the sample at high laser power ($P = 1\,\mathrm{mW}$) and fast exposure time ($\Delta t = 80\,\mathrm{s}$): (a) for acquisitions directly performed onto Cu substrate; (b) for acquisitions performed after graphene transfer onto an insulating SiO_2 substrate. In the insets of both pictures, the change in position and intensity of the single Lorentzian curves used to fit the 2D peak of the spectra is shown. A clear increase in intensity, decrease in FWHM and lowering in Raman shift of the 2D peak is visible in both the pictures and it is more pronounced in the case of Raman spectra acquired directly on Cu samples (so for not transferred graphene).

surface covered by the i-th graphene flake and $A^{(Cu)}$ the area of the underlying Cu grain, $A^{(n)} > A^{(n-1)} > \ldots > A^{(2)} > A^{(1)} > A^{(Cu)}$). Moreover, Raman mapping performed on different spots of the Cu film subjected to CVD process shows different regions with different number of layers on the same sample, corroborating the hypothesis of a terraces-like structure characterizing all the substrate. This fact implies that in-plane heat dissipation through outer graphene layers is largely suppressed by finite-size effects and out-of-plane heat transfer (much lower than the previous one) becomes the dominant heat transfer channel, resulting in a local overheating and subsequent etching of the layers (the model is schematically represented in Figure 134). On the contrary, the innermost graphene layer directly bound to the Cu surface is protected from this effect by the presence of the substrate acting as heat sink. Indeed, as I have reported in Sec. 3.1.1, it has been reported ([16]) that Cu lowers the thermal conductivity of CVD monolayer graphene grown on it: a significant change in the enhancement of the temperature and in the G peak shifting as a function of the absorbed laser power by using Cu instead of SiO_2 as a substrate has been reported in this work, as I have shown in Figure 102b. As a consequence, graphene-on-Cu and Cu systems have comparable thermal conductivities and the effect of the substrate is not anymore negligible: being Cu a good heat conductor, it provides in turn the dominant contribution to heat dissipation and allows for a more efficient heat exchange through the substrate with respect to the case of transferred graphene onto SiO_2.

At such photon energies other mechanisms, like molecular desorption of chemical species, cannot be *a priori* excluded, but they can hardly affect the Raman signature and they can be detected only through electrical measurements ([174]).

Moreover, it would have been interesting to directly estimate the eventual change in temperature of my sample, and therefore of the graphene layers, among successive acquisitions of Raman spectra. This result can be obtained by exploiting two standard techniques: by employing confocal micro-Raman spectroscopy to extrapolate the temperature of the sample from the dependence of the G peak Raman shift on excitation laser power (and therefore on sample temperature) or by employing a Raman instrument equipped for the detection of both Stokes and anti-Stokes Raman modes (the ratio between the intensities of the peak corresponding to the same pair of resonant vibrational states, detected in Stokes and anti-Stokes regimes, is indeed proportional to the temperature of the sample subjected to Raman analysis, according to relation 73). Unfortunately, I.N.Ri.M. laboratories are not equipped with confocal micro-Raman spectroscopy instruments: to exploit this technique I should deeply modify the RTA system that I use to perform CVD process, in order to equip the system itself with a micro-Raman spectroscopy instrument, but I have not planned to engineer such a modification in the near future. For what concerns the detection of Stokes and anti-Stokes regimes during Raman spectroscopy, I could not access this feature during my measurements since modern commercially available Raman instruments (as the one I have employed to perform Raman characterization on my samples) are fabricated in a way allowing only the detection of Stokes regime: as a consequence, I could not compare the two regimes in order to infer the temperature of the sample during Raman analysis. It has been recently decided to equip I.N.Ri.M. laboratories with a monochromator (to be mounted on a Raman instrument) allowing detection of both Stokes and anti-Stokes regimes during the acquisition of Raman spectra, but I am still

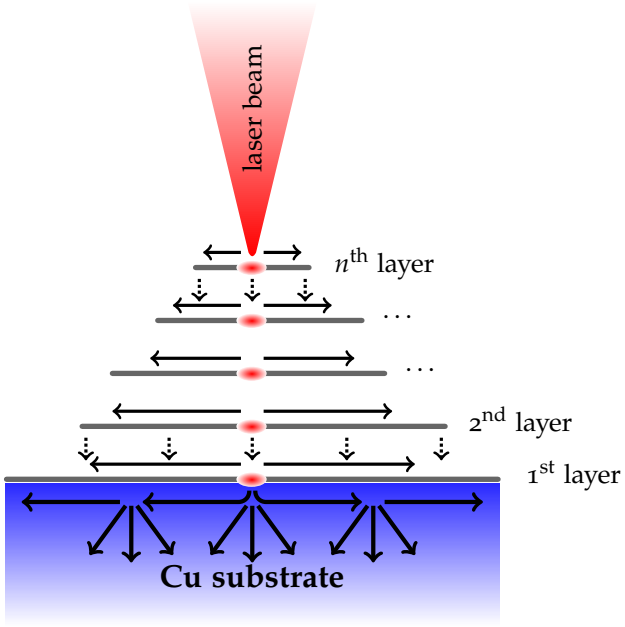

Figure 134: **Phenomenological model for local overheating and etching of multilayer graphene grown by CVD on Cu thin films.** Schematic model representing the possible origin of local overheating and etching of outermost graphene layers grown on Cu films. The heat provided by the focused laser beam is dissipated through in-plane (horizontal arrows) and out-of-plane (vertical arrows) channels. Though the in-plane channel is dominant in graphene, the finite size of outer layers makes out-of-plane dissipation significant and reduces the in-plane contribution, thus causing local overheating and subsequent etching of the layers. The innermost layer is instead prevented from etching by the presence of the Cu substrate acting as heat sink.

configuring and arranging the full system. As a consequence, up to now I am not able to give an estimate of the temperature reached by graphene layers upon heating induced by exposure to the laser beam used during Raman characterization of the Cu samples subjected to CVD processes.

The fact that the G peak position is almost unaffected by the laser irradiation can be explained as a result of two competing effects: the local enhancement of temperature (due to overheating), bringing to a redshift of the G peak ([16, 18], see Figure 102) and the decrease in the number of graphene layers (due to etching), resulting instead in a blueshift of the G peak ([193], see Figure 100).
The unexpected unaltered intensity of the G peak (that should decrease as the number of graphene layers decreases, as illustrated in Figure 101) can be explained in two ways. A first effect, applying to Raman measurements performed both on transferred and not transferred graphene samples, relies on the increase in temperature of graphene layers upon laser irradiation, likely resulting in an effect similar to what observed in experiments concerning the evolution of graphene Raman signature upon controlled annealing at high temperatures ([130]). As pointed out in this work, the G peak intensity is not changing between few- and monolayer graphene sheets after the annealing process, meaning that in these experimental conditions G peak intensity cannot be regarded as a fingerprint to distinguish number of graphene layers. A second reasoning, applying only on graphene samples over Cu, relies on the roughness of the Cu surface, determining a light trapping effect close to the substrate's surface that results in an enhanced number of multiple reflections of the laser light between Cu and graphene layers: as a consequence, the number of C atoms detected by the unfocused beam is always comparable to the number of C atoms present in multilayer graphene, although the number of graphene layers is decreasing. As reported in [131] and shown in Figure 101 the G band intensity for a number of graphene layers exceeding ~ 15 is in this case decreasing by increasing number of layers and then constant, as observed in my spectra.

The origin of the prominent D peak (increasing in intensity as the number of acquisitions increases) is not completely clear yet: it can be attributed to the acquisition of the spectra on a point of the sample lying on a grain boundary of the Cu substrate (resulting in a change of the crystallographic orientation of graphene flake through it) or to defects (terrace boundaries) produced in graphene crystal structure by the laser etching.

After having obtained these results directly onto Cu substrates, I have decided to transfer graphene (with the procedure described in Sec. 3.2) to an insulating SiO_2/Si substrate and to perform again the same kind of Raman characterization (i.e. using the same experimental setup with laser wavelength $\lambda = 442\,\text{nm}$, laser power $P = 1\,\text{mW}$ and exposure time $\Delta t = 80\,\text{s}$), in order to check if the effect detected on Cu could be measured also on transferred graphene. As a result, Raman analysis performed on transferred graphene samples confirms the behaviour observed in the spectra acquired on graphene/Cu substrates, although less pronounced. A similar evolution in shape and position of the peaks is obtained for subsequent spectrum acquisitions, as shown in Figure 132b and Figure 133b.

In summary, I have reported here a possible way to locally etch graphene layers based on laser heating released during Raman analysis. Graphene structure (crystallization degree and number of layers) evolution can be monitored and inferred by looking directly at the Raman spectra acquired on the metallic catalyst sample. The technique I am proposing is suitable in

particular for etching layers of graphene grown by CVD on a catalytic metal. In my case I have reported results obtained with Cu and I have explained in detail how it is possible, by lightening the sample with incident laser light at quite high power ($\gtrsim 1\,\mathrm{mW}$) for short time periods ($\sim 80\,\mathrm{s}$), to produce a clear sharpening and lowering of the 2D peak position in the acquired Raman spectra, together with a decrease in the I_G/I_{2D} ratio: we have seen that these results are compatible with a decrease in the number of graphene layers grown on the metallic substrate. Moreover, I have reported also that D peak increases in intensity as function of the laser exposure, meaning an increasing of defects in the graphene structure. I believe that the method here presented can be easily applied to other metallic substrates: since the technique deeply relies on the dispersion of the heat provided by laser irradiation through the substrate, the most important feature required for the substrate is its high thermal conductivity.

The technique can be very useful since some catalysts, like Cu, are very promising for CVD synthesis of graphene because of the expected self-limited mono-layered growth of this material on them, but experimentally it is found that a few-layered structure is often grown. Laser etching here reported can therefore provide an *in situ* technique to get rid of this problem. However, laser can also have an active rôle in inducing unwanted defects, such as vacancies in pristine graphene films: for this reason the proposed method shall be further developed. I finally envisage the application of the photo-etching process here reported to large areas if efficient and uniform illumination conditions, as those used in the RTA system at I.N.Ri.M., are employed.

In conclusion, in this chapter I have reported the results I have obtained about the main subject of the Ph.D. research: the growth of graphene by CVD onto various catalytic substrates. First of all, I have shown some theoretical models I have developed to predict the behaviour governing the diffusion of C atoms released from a solid source (amorphous SiC) into Ni thin films ($d_{Ni} = 200\,\mathrm{nm}$). Nonetheless, I have encountered many troubles in evaporating and undergoing thermal cycles on Ni films deposits onto the amorphous SiC substrate and therefore only one time I have succeeded in carrying out a CVD process on Ni. I could only characterize the resulting surface with XPS analysis, that showed indeed the presence of carbon atoms on top of the Ni film at the end of the thermal treatment: since C atoms diffusion through Ni is enhanced in correspondence of grain boundaries, deposited C atoms are likely organized in amorphous or graphitic-like structures grown mainly close to Ni grain boundaries. With the acquired data I cannot establish if graphene has been really synthesized on Ni, but I am quite unconfident about this occurrence.
I have then reported the more successful results I have obtained on Cu substrates. At the beginning I have worked with not commercial foils ($d_{Cu} \sim 1\,\mathrm{mm}$) properly cleaned (and in some case also lapped) and after some tests I have found a proper CVD process, performed in the RTA system present at I.N.Ri.M. laboratories at deposition temperature $T_{dep} = 900\,^{\circ}\mathrm{C}$, allowing for deposition of graphene-like structures on top of Cu. This time I could characterize the samples with Raman analysis (using laser wavelength at $\lambda = 514\,\mathrm{nm}$ and $\lambda = 442\,\mathrm{nm}$), this way having a clear fingerprint of the presence of mainly few-layer graphene onto Cu: the same features, proper of few-layer graphene present on top of the underlying substrate, have been detected in Raman spectra acquired on graphene transferred (with a standard technique based on chemical etching of the metallic catalyst) onto a

new insulating SiO_2/Si substrate.
After having improved this way my experience about CVD processes on Cu substrates and about the choice of the values to be assigned at the parameters governing CVD thermal cycles, I have employed Cu thin films of various thickness (ranging from $\sim 250\,nm$ and $\sim 500\,nm$) instead of foils for growing graphene. Indeed, only by working with deposited films graphene can match the requirements of nowadays accepted and known device fabrication technology; on the other hand, CVD processes carried out on Cu films are still quite messy because of dewetting problems involving the catalytic substrate, limiting a massive and standardized graphene production (I have widely discussed these problems in Chapter 2). Nonetheless, by varying deposition conditions (deposition temperature, deposition time and gas mixture flowing in the reaction chamber of the RTA system during the deposition step of the CVD thermal cycle), I have finally found a CVD process allowing to successfully grow graphene on top of a $d_{Cu} = 500\,nm$ thick Cu film (on thinner films I have always faced a pronounced dewetting of the Cu substrate forbidding the deposition of graphene), at the nominal deposition temperature $T_{dep} = 725\,°C$ (I have also explained in the text that, because of thermocouple malfunctions encountered while reading the temperature of the system during CVD processes, this nominal temperature is probably underestimating the real temperature of the process of $\sim 150\,°C$).
However, the most interesting result has arisen while characterizing with Raman spectroscopy (always performed, in this case, at laser wavelength $\lambda = 442\,nm$ to avoid a pronounced background plasmon emission of Cu excited with laser light) the sample subjected to the successful CVD thermal cycle. Indeed, by focusing the laser beam on a certain spot of the sample, by choosing a quite high laser power (1 mW) and by acquiring Raman spectra on the same spot in subsequent acquisitions, each one lasting 80 s, I have not only found the characteristic graphene G and 2D peaks in the spectra, but I have also reported a clear evolution of the 2D peak shape (sharpening and increasing in intensity) and of the I_G/I_{2D} ratio, compatible with a (local) decrease in the number of graphene layer present on top of the Cu surface. I have explained how this effect can be ascribed to local overheating and subsequent etching of outermost graphene layers grown on Cu during the CVD process, locally induced by the laser beam employed for Raman characterization. Although suspended graphene is known to have a superior in-plane thermal conductivity, its value is likely reduced on my sample because of the presence of the Cu substrate and because of a terraces-like graphene structure limiting a lot in-plane heat dissipation in favour of an out-of-plane dissipation (that, for few-layer graphene, is known to be much lower than the in-plane one). Nonetheless, the graphene layer directly in contact with the Cu surface is prevented from etching because of the presence of the metallic substrate acting as an heat sink and providing the dominant contribution to heat dissipation: therefore, the innermost layer is not subjected to an high overheating resulting in a local etching. Moreover, same results have been found also characterizing transferred graphene (although the evolution of the 2D peak is in this case less pronounced probably because of the lower thermal conductivity of the SiO_2/Si substrate with respect to the Cu substrate), meaning that the effect should be quite robust.
My findings are quite interesting because they provide a useful technique to obtain monolayer graphene on top of Cu (at least locally) in a post-CVD treatment of the sample and not necessarily during the CVD process. Although CVD growth on top of Cu should be theoretically self-limited and

should stop after one layer of graphene has been grown on the underlying surface, experiments show that often this is not the case and few-layer graphene growth is reported: for this reason, an etching technique as the one I have proposed may provide a way to successfully grow monolayer graphene on top of Cu. Moreover, I envisage the possibility of employing the technique also on other (conducting) catalytic substrates and over larger areas: the latter point can be achieved by exploitation of the properties of the RTA system, allowing for a fast heating, in oxygen atmosphere, of all the sample subjected to the CVD process (since the technique is based on a overheating of graphene layers, I think that the heating source -a laser beam or halogen lamps- should not be a crucial factor for the etching effect). Further investigations on these points are underway.
The results of my research, together with other details about the etching technique here described, have been published in [145].

CONCLUSIONS

Graphene is a revolutionary material for many research fields and industrial applications, ranging from Nanoelectronics, to Optoelectronics, Photonics, Spintronics, Chemical Harvesting and also Metrology: it is nowadays regarded as one of the most promising materials to substitute Si in future electronic devices. It owes much of its success to the astonishing transport properties hold by its charge carriers, behaving as massless Dirac relativistic fermions with Fermi velocity $v_F \sim 10^{-6}\,m\,s^{-1}$: this peculiarity, not found in any other semiconductor employed in nanoelectronic industry, deeply relies on the honeycomb (hexagonal) crystalline arrangement of carbon atoms in graphene and contributes to other remarkable properties of this exactly 2D material (such as an anomalous Quantum Hall Effect, a weak localization, a perfect tunneling through rectangular potential barriers). Although living entirely on a surface, charge carriers do not suffer from surface contaminations, showing instead incredibly high mobilities (up to $200\,000\,cm^2\,V^{-1}\,s^{-1}$ for freestanding mechanically exfoliated graphene) even at room temperature. Moreover, an ambipolar Electric Field Effect, switching continuously charge carriers from electrons to holes by varying an external gate potential V_g, has been surprisingly demonstrated also in graphene, although, unlike other semiconductors (like Si or GaAs), no band gap is present in its electronic band structure: such a discovery, paired with the ease of making ohmic contacts, has sparked hopes to conceive graphene-based Field Effect Transistors for future nanoscale electronics, going beyond the fundamental limitations of Si-based electronics.

Nonetheless, to match the nowadays accepted and developed paradigms of device fabrication technologies and the requirements of electronic industries, an efficient, scalable, non destructive and cost-effective method to grow monolayer graphene over large scale areas is definitely needed. Moreover, such a technique should leave the remarkable properties of this material almost entirely unaffected during the growth process, in order to fully exploit them in applications. The enormous efforts performed in the last years, inspired by the search of new methods for synthesizing graphene, led to the optimization of some really powerful techniques: in particular, the epitaxial growth of graphene by thermal sublimation of crystalline SiC, the Chemical Vapour Deposition (CVD) of graphene on various catalytic substrates and, recently, the reduction of chemically synthesized graphene oxides, are regarded as the most promising routes towards the deposition of graphene for industrial purposes. All of these methods have positive peculiar aspects and have been demonstrated to allow the growth high quality graphene, suitable for post-deposition electrodes gating and integration in circuitry, but they show also some drawbacks: the research for a final answer to the request for a feasible graphene growth technique is therefore still challenging researchers and industries worldwide.

In this thesis I have reported the results of the research carried out at I.N.Ri.M. laboratories, focused on the optimization of the CVD technique for the growth of large scale area monolayer graphene on catalytic thin films. I have presented first of all the attempts made for growing graphene on Ni films by a carbon solid source (a slightly different technique with respect to CVD, relying by the way on the same physical principles), re-

sulted in many problems encountered while depositing the metallic catalyst onto the amorphous SiC substrate. I have this way explained why I have decided to change the catalytist employed for CVD processes, from Ni to Cu: the latter provides indeed, at least in principle, a self-limited graphene deposition, stopped after one layer of material is grown on the surface, and an easiest graphene transfer to other substrates. I have later presented the CVD thermal cycles that brought to successful depositions of few-layer graphene on top of Cu foils. Nonetheless, in order to make significant improvements on the CVD technique, aiming to a useful exploitation and integration of graphene grown by means of such a method in electronic devices, the employment of Cu thin films is required. Unfortunately, the use of Cu thin films e-beam evaporated onto SiO_2/Si substrates in CVD processes performed at temperatures $\gtrsim 900\,^{\circ}C$ is not straightforward: indeed, I have demonstrated (confirming other results already reported in literature) that Cu films with thickness $d_{Cu} \lesssim 500\,nm$, at these temperatures, dewet unavoidably from the underlying substrate, deeply changing their morphology and forming droplets limiting and in much cases forbidding the possibility of growing graphene. This problem is strictly related to the adhesion energy between Cu and SiO_2/Si, becoming lower, at high temperatures, than cohesive forces among Cu atoms: a possible way out of this problem is therefore represented by the enhancement the sticking coefficient of Cu with the substrate. For this reason, I have investigated the effects on the adhesion of Cu to the substrate obtained by intercalating a Cr buffer layer between Cu and the SiO_2/Si surface and by depositing Cu by means of an IBAD-Electron Beam Physical Vapour Deposition technique: up to now, I have not detected any significant change in the response of the Cu samples under thermal treatment at high temperature, that still dewet from the underlying substrate, but further investigations have been planned for the future.

Besides searching routes for enhancing Cu adhesion to SiO_2, I have also developed a useful *in situ* technique allowing for a qualitative real-time control of dewetting effects occurring on the Cu surface undergoing thermal processes in Low Vacuum conditions. As described in the thesis, the technique relies on the properties of the Rapid Thermal Annealing (RTA) system used to deposit graphene by CVD at I.N.Ri.M. and, in particular, on the physical laws governing the functioning of the pyrometer detecting the temperature into the RTA system and its calibration procedure. Although the technique does not provide yet a satisfactory quantitative analysis of the dewetting phenomenon, a qualitative tool allowing a better control on the morphology of the substrates involved in CVD processes is, according to my opinion, a right step towards the optimization and standardization of the whole method: it allows indeed to find the right conditions (in terms of catalyst thickness and CVD deposition temperature) to perform graphene synthesis avoiding undesired dewetting effects. The next purpose will be represented by an implementation of the technique extending its use also to situations in which gas is flowing in the RTA reaction chamber, more resembling the conditions characterizing CVD thermal cycles.

Thanks to the developed technique, I could find a range of Cu film thicknesses and deposition temperatures allowing me to successfully deposit graphene on a 500 nm thick Cu substrate. However, also in this case, as already happened on Cu foils, deposited graphene has resulted to be thicker than a single layer (as inferred with Raman spectroscopy characterization). This experimental evidence is quite messy and a method ensuring the pos-

sibility of getting monolayer graphene would be high desirable. Besides optimizing CVD growth parameters, a possible efficient way to get monolayer graphene may be represented by the development of a proper post-deposition technique providing the etching of the undesired graphene layers grown on the catalytic substrate during the process. By analysing the results of the Raman characterization performed on my samples, I have then suggested a possible practical realization of such a technique: it is based on the local etching of outermost graphene layers present on Cu surface due to overheating induced on graphene by laser employed at sufficiently high power during Raman spectroscopy. I have also envisaged the possibility of extending the etching effect from the local spot on which laser is focused to the whole sample by means of a uniform heat source, as the one present in the RTA system at I.N.Ri.M..

We can therefore conclude that I have developed two techniques improving the capabilities of growing graphene by CVD on Cu films: on one hand, one technique allows to control Cu dewetting, thus making possible to carry out CVD processes on this kind of catalytic substrate, on the other hand the second technique allows to obtain monolayer graphene, at least locally, once the CVD process has been performed.

Nonetheless, I have still to make many progress towards a full exploitation of both the techniques and, more in general, of the whole CVD process. For the future research I have therefore planned some improvements, summarized as follows:

- extend the possibility of controlling Cu dewetting to conditions more resembling the conditions occurring while depositing graphene by CVD, i.e. with gas flowing in the RTA reaction chamber;
- investigate methods to enhance Cu adhesion to the underlying substrate, thus preventing Cu dewetting;
- check the possibility of developing a technique allowing graphene etching on the whole Cu sample, and not only locally, after having carried out the CVD process;
- improve the quality and the average size of graphene flakes grown by CVD on Cu reducing the grain boundaries present on the substrate;
- perform electrical characterization on graphene grown by CVD, by fabrication of graphene-based devices like Quantum Hall bars.

The last two points deserve further explanations.

For what concerns the grain boundaries present on Cu substrates after e-beam evaporations, affecting the crystal structure and the size of graphene flakes, these are due to the island Volmer-Weber growth mode governing Cu atoms nucleation and coalescence on top of SiO_2 surface: being SiO_2 amorphous, it does not allow a monocrystalline film growth. As a result, I have demonstrated in my e-beam evaporations onto SiO_2/Si substrates that Cu is always characterized by a polycrystalline nature, with grains of $\sim$ 100 nm as average size (when deposited directly onto SiO_2 without intercalated buffer layers of a different material). A possibility to grow crystalline Cu oriented in a specific crystallographic orientation is represented by the employment of crystalline Si instead of amorphous SiO_2 as target substrate for Cu deposition: in particular, it has been reported in literature and I have very recently demonstrated, as explained in the thesis, that Si$\langle 110 \rangle$

allows to grow monocrystalline Cu with crystallographic orientation $\langle 111 \rangle$ (the best orientation for graphene deposition by CVD, as reported in many works). Nonetheless, by growing Cu directly on Si another problem is faced, namely the formation at high temperature of a solid binary phase between the two species, characterized by a melting temperature ranging from 800 °C to 850 °C: therefore, evaporation of Cu on Si ensures a layer Frank-van der Merwe growth mode (so, a monocrystalline ordered growth) but precludes the possibility of performing CVD processes for graphene growth on Cu.

By the way, I have planned to investigate a possible route to come out from this apparently unsolvable problem. The idea, as described in the text, is to exploit the peculiar features of porous Si, namely the memory of its crystallographic orientation for Si substrates deposited on it and the ease to carry out oxidation processes with chemical and electrochemical techniques, to grow single crystalline oriented Cu$\langle 111 \rangle$ thin films onto insulating oxide layers, this way suitable for CVD processes. This route, if successfully implemented, may allow important improvements towards an effective exploitation of CVD on Cu thin films.

The second point, concerning the fabrication of graphene-based devices such as Quantum Hall bars, is of great importance both for graphene characterization and for metrological applications. It has been indeed reported that the exploitation of Quantum Hall effect in graphene could bring to a new definition of the electrical resistance standard, a very important task of nowadays metrological research: being I.N.Ri.M. the Italian Institute devoted to the realization of primary standards for the basic and derived units of the International System, a quite natural interest about the use of graphene not only for industrial applications, but also for metrological purposes has arisen. To fully realize this task, I have planned first of all to optimize the graphene transfer process, searching also for alternative transfer methods with respect to the usual chemical etching technique widely proposed in literature. Quantum Hall devices will be then patterned and fabricated by means of Electron Beam lithography, a technique for which I.N.Ri.M. has the required instruments and has developed a good expertise through the years.

To conclude, in the three years of my Ph.D. research, I have acquired a lot of experience about the employment of techniques concerning thin film deposition (the e-beam evaporation technique), graphene growth (the CVD technique) and film characterization (in particular the Scanning Electron Microscopy and the Raman spectroscopy techniques), contributing to the results reported in this thesis. I have acquired also an important expertise from a theoretical and modeling point of view, in particular for what concerns statistical data analysis. The results I have obtained can be safely considered useful steps towards the exploitation of CVD as a possible route for graphene growth, in particular on Cu thin films. While research on other catalytic metals or on Cu foils is now quite established, the research about Cu films, at the best of my knowledge, is still in its infancy: so, results obtained in this direction are well liked.

A final answer about the standardization of the whole CVD process on Cu films is far from being obtained and many steps sill require an optimization and a deep investigation, but the great improvements achieved during the years about CVD processes justify regarding this technique as the most promising one to grow high quality monolayer graphene, over large scale areas, for nanotechnologies applications.

BIBLIOGRAPHY

[1] D. S. L. Abergel, V. Apalkov, J. Berashevich, K. Ziegler, and T. Chakraborty. "*Properties of graphene: a theoretical perspective*". Adv. Phys. **59** (2010), 261–482 (cit. on pp. 12, 16, 41).

[2] N. W. Ashcroft and N. D. Mermin. *Solid State Physics*. Brooks/Cole, 1976 (cit. on pp. 12, 73).

[3] P. Avouris and F. Xia. "*Graphene applications in electronics and photonics*". MRS Bull. **37** (2012), 1225–1234 (cit. on p. xxi).

[4] S. Bae, H. Kim, Y. Lee, X. Xu, J.-S. Park, Y. Zheng, J. Balakrishnan, T. Lei, H. R. Kim, Y. I. Song, Y.-J. Kim, K. S. Kim, B. Özyilmaz, J.-H. Ahn, B. H. Hong, and S. Iijima. "*Roll-to-roll production of 30-inch graphene films for transparent electrodes*". Nat. Nanotechnol. **5** (2010), 574–578 (cit. on pp. 48, 53, 56, 152).

[5] A. A. Balandin, S. Ghosh, W. Bao, I. Calizo, D. Teweldebrhan, F. Miao, and C. N. Lau. "*Superior Thermal Conductivity of Single-Layer Graphene*". Nano Lett. **8** (2008), 902–907 (cit. on pp. xxii, 185).

[6] L. Baraton, Z. He, C. S. Lee, J.-L. Maurice, C. S. Cojocaru, A.-F. Gourgues-Lorenzon, Y. H. Lee, and D. Pribat. "*Synthesis of few-layered graphene by ion implantation of carbon in nickel thin films*". Nanotechnology **22** (2011), 085601(1–5) (cit. on p. 155).

[7] N. C. Bartelt and K. F. McCarty. "*Graphene growth on metal surfaces*". MRS Bull. **37** (2012), 1158–1165 (cit. on p. 53).

[8] D. M. Basko. "*Calculation of the Raman G peak intensity in monolayer graphene: role of Ward identities*". New J. Phys. **11** (2009), 095011(1–12) (cit. on pp. 135, 136).

[9] F. Bassani and G. Pastori Parravicini. *Electronic States and Optical Transitions in Solids*. Ed. by R. A. Ballinger. International Series of Monographs in the Science of the Solid State, Vol. 8. Oxford: Pergamon Press, 1975 (cit. on p. 12).

[10] C. Bena and G. Montambaux. "*Remarks on the tight-binding model of graphene*". New J. Phys. **11** (2009), 095003(1–15) (cit. on pp. 12, 17, 18).

[11] D. S. Bethune, C. H. Klang, M. S. de Vries, G. Gorman, R. Savoy, J. Vazquez, and R. Beyers. "*Cobalt-catalysed growth of carbon nanotubes with single-atomic-layer walls*". Nature **363** (1993), 605–607 (cit. on p. 3).

[12] S. Bhattacharjee, M. Maiti, and K. Sengupta. "*Theory of tunneling conductance of graphene normal metal-insulator-superconductor junctions*". Phys. Rev. B **76** (2007), 184514(1–7) (cit. on p. 41).

[13] J. D. Bjorken and S. D. Drell. *Relativistic Quantum Mechanics*. New York: McGraw-Hill, 1964 (cit. on p. 26).

[14] K. I. Bolotin, F. Ghahari, M. D. Shulman, H. L. Stormer, and P. Kim. "*Observation of the fractional quantum Hall effect in graphene*". Nature **462** (2009), 196–199 (cit. on pp. 34, 37).

[15] D. W. Boukhvalov, M. I. Katsnelson, and A. I. Lichtenstein. "*Hydrogen on graphene: Electronic structure, total energy, structural distortions and magnetism from first-principles calculations*". Phys. Rev. B **77** (2008), 035427(1–7) (cit. on p. 16).

[16] W. Cai, A. L. Moore, Y. Zhu, X. Li, S. Chen, L. Shi, and R. S. Ruoff. "*Thermal Transport in Suspended and Supported Monolayer Graphene Grown by Chemical Vapor Deposition*". Nano Lett. **10** (2010), 1645–1651 (cit. on pp. 48, 56, 146, 161, 187, 189).

[17] W. Cai, Y. Zhu, X. Li, R. D. Piner, and R. S. Ruoff. "*Large area few-layer graphene/graphite films as transparent thin conducting electrodes*". Appl. Phys. Lett. **95** (2009), 123115(1–3) (cit. on pp. 56, 161).

[18] I. Calizo, A. A. Balandin, W. Bao, F. Miao, and C. N. Lau. "*Temperature Dependence of the Raman Spectra of Graphene and Graphene Multilayers*". Nano Lett. **7** (2007), 2645–2649 (cit. on pp. 144, 146, 189).

[19] A. Calogeracos and N. Dombey. "*History and physics of the Klein paradox*". Contemp. Phys. **40** (1999), 313–321 (cit. on p. 38).

[20] G. Cao. *NANOSTRUCTURES & NANOMATERIALS - Synthesis, Properties & Applications*. Imperial College Press, 2004 (cit. on p. 59).

[21] H. Cao, Q. Yu, L. A. Jauregui, J. Tian, W. Wu, Z. Liu, R. Jalilian, D. K. Benjamin, Z. Jiang, J. Bao, S. S. Pei, and Y. P. Chen. "*Electronic transport in chemical vapor deposited graphene synthesized on* Cu*: Quantum Hall effect and weak localization*". Appl. Phys. Lett. **96** (2010), 122106(1–3) (cit. on pp. 48, 56).

[22] R. Casalbuoni. *Quantum Field Theory*. Lecture Notes. Università di Firenze, 1997 (cit. on p. 25).

[23] A. H. Castro Neto, F. Guinea, and N. M. R. Peres. "*Drawing conclusions from graphene*". Phys. World **19** (2006), 33–37 (cit. on p. 2).

[24] A. H. Castro Neto, F. Guinea, N. M. R. Peres, K. S. Novoselov, and A. K. Geim. "*The electronic properties of graphene*". Rev. Mod. Phys. **81** (2009), 109–162 (cit. on pp. 9, 12, 14, 20–23, 36, 41).

[25] G. Cicero. *LEED technique*. Lecture Notes. In: Physics of Surfaces and Interfaces. Politecnico di Torino, 2011 (cit. on p. 71).

[26] G. Cicero. *XPS and ESCA technique*. Lecture Notes. In: Physics of Surfaces and Interfaces. Politecnico di Torino, 2011 (cit. on pp. 148, 149).

[27] J. Coraux, A. T. N'Diaye, C. Busse, and T. Michely. "*Structural Coherency of Graphene on* (111)". Nano Lett. **8** (2008), 565–570 (cit. on p. 48).

[28] S. D. Costa, A. Righi, C. Fantini, Y. Hao, C. Magnuson, L. Colombo, R. S. Ruoff, and M. A. Pimenta. "*Resonant Raman spectroscopy of graphene grown on copper substrates*". Solid State Commun. **152** (2012), 1317–1320 (cit. on pp. 56, 138, 139, 171, 179).

[29] L. Croin. "Deposizione di grafene su larga area su substrati di rame". Master Degree thesis. Università degli Studi di Torino, 2011 (cit. on p. 161).

[30] S. Das Sarma, S. Adam, E. H. Hwang, and E. Rossi. "*Electronic transport in two-dimensional graphene*". Rev. Mod. Phys. **83** (2011), 407–470 (cit. on pp. 26, 41).

[31] A. Das, B. Chakraborty, and A. K. Sood. "*Raman spectroscopy of graphene on different substrates and influence of defects*". Bull. Mater. Sci. **31** (2008), 579–584 (cit. on pp. 141, 172, 173).

[32] W. A. de Heer, C. Berger, X. Wu, P. N. First, E. H. Conrad, X. Li, T. Li, M. Sprinkle, J. Hass, M. L. Sadowski, M. Potemski, and G. Martinez. "*Epitaxial graphene*". Solid State Commun. **143** (2007), 92–100 (cit. on p. 46).

[33] W. A. de Heer, C. Berger, X. Wu, M. Sprinkle, Y. Hu, M. Ruan, J. A. Stroscio, P. N. First, R. Haddon, B. Piot, C. Faugeras, M. Potemski, and J.-S. Moon. "*Epitaxial graphene electronic structure and transport*". J. Phys. D: Appl. Phys. **43** (2010), 374007(1–13) (cit. on p. 47).

[34] C. Di, D. Wei, G. Yu, Y. Liu, Y. Guo, and D. Zhu. "*Patterned Graphene as Source/Drain Electrodes for Bottom-Contact Organic Field-Effect Transistors*". Adv. Mater. **20** (2008), 3289–3293 (cit. on p. 48).

[35] N. Dombey and A. Calogeracos. "*Seventy years of the Klein paradox*". Phys. Rep. **315** (1999), 41–58 (cit. on pp. 38, 39).

[36] M. S. Dresselhaus. *Transport Properties of Solids*. Lecture Notes. In: - SOLID STATE PHYSICS - PART 1. Massachusetts Institute of Technology, 2001. URL: http://web.mit.edu/course/6/6.732/www/6.732-pt1.pdf (cit. on p. 12).

[37] M. S. Dresselhaus and G. Dresslhaus. "Light Scattering in Graphite Intercalation Compounds". *Light Scattering in Solids III*. Ed. by M. Cardona and G. Güntherodt. Berlin Heidelberg: Springer, 1982. Chap. 2, pp. 3–57 (cit. on p. 145).

[38] D. Du, Y. Yang, and Y. Lin. "*Graphene-based materials for biosensing and bioimaging*". MRS Bull. **37** (2012), 1290–1296 (cit. on p. xxi).

[39] X. Du, I. Skachko, A. Barker, and E. Y. Andrei. "*Approaching ballistic transport in suspended graphene*". Nat. Nanotechnol. **3** (2008), 491–495 (cit. on p. xxii).

[40] X. Du, I. Skachko, F. Duerr, A. Luican, and E. Y. Andrei. "*Fractional quantum Hall effect and insulating phase of Dirac electrons in graphene*". Nature **462** (2009), 192–195 (cit. on pp. 34, 37).

[41] A. Einstein. "*Über einen die Erzeugung und Verwandlung des Lichtes betreffenden heuristischen Gesichtspunkt*". Ann. Phys. (Berlin) **322** (1905), 132–148 (cit. on p. 145).

[42] K. V. Emtsev, A. Bostwick, K. Horn, J. Jobst, G. L. Kellogg, L. Ley, J. L. McChesney, T. Ohta, S. A. Reshanov, J. Röhrl, E. Rotenberg, A. K. Schmid, D. Waldmann, H. B. Weber, and T. Seyller. "*Towards wafer-size graphene layers by atmospheric pressure graphitization of silicon carbide*". Nat. Mater. **8** (2009), 203–207 (cit. on p. 46).

[43] W. Ensinger. "*Ion sources for ion beam assisted thin-film deposition*". Rev. Sci. Instrum. **63** (1992), 5217–5233 (cit. on pp. 68, 69).

[44] G. Etxebarria, M. Gomez-Uranga, and J. Barrutia. "*Tendencies in scientific output on carbon nanotubes and graphene in global centers of excellence for nanotechnology*". Scientometrics **91** (2012), 253–268 (cit. on pp. 7, 8).

[45] J. W. Evans, P. A. Thiel, and M. C. Bartelt. "*Morphological evolution during epitaxial thin film growth: Formation of* 2D *islands and* 3D *mounds*". Surf. Sci. Rep. **61** (2006), 1–128 (cit. on p. 78).

[46] N. Ferralis, R. Maboudian, and C. Carraro. "*Evidence of Structural Strain in Epitaxial Graphene Layers on* 6H − SiC(0001)". Phys. Rev. Lett. **101** (2008), 156801(1–4) (cit. on p. 145).

[47] A. C. Ferrari, J. C. Meyer, V. Scardaci, C. Casiraghi, M. Lazzeri, F. Mauri, S. Piscanec, D. Jiang, K. S. Novoselov, S. Roth, and A. K. Geim. "*Raman Spectrum of Graphene and Graphene Layers*". Phys. Rev. Lett. **97** (2006), 187401(1–4) (cit. on pp. 138, 141, 179, 185).

[48] A. Fick. "*Ueber Diffusion*". Ann. Phys. (Berlin) **170** (1855), 59–86 (cit. on p. 155).

[49] M. Freitag and J. C. Tsang. "Raman Spectroscopy of Carbon Nanotubes and Graphene Materials and Devices". *Handbook of Instrumentation and Techniques for Semiconductor Nanostructure Characterization*. Ed. by R. Haight, F. M. Ross, and J. B. Hannon. Vol. 2. World Scientific, 2011. Chap. 11, pp. 479–523 (cit. on pp. 133, 135, 141, 144, 145).

[50] W. Friedrich, P. Knipping, and M. von Laue. "*Interferenz-Erscheinungen bei Röntgenstrahlen*". Sitzungsberichte der Mathematisch-Physikalischen Classe der Königlich-Bayerischen Akademie der Wissenschaften zu München **1912** (1912), 303 (cit. on p. 72).

[51] J. M. Garcia, R. He, M. P. Jiang, J. Yan, A. Pinczuk, Y. M. Zuev, K. S. Kim, P. Kim, K. Baldwin, K. W. West, and L. N. Pfeiffer. "*Multilayer graphene films grown by molecule beam deposition*". Solid State Commun. **150** (2010), 809–811 (cit. on p. 54).

[52] A. K. Geim and K. S. Novoselov. "*The rise of graphene*". Nat. Mater. **6** (2007), 183–191 (cit. on pp. 11, 24, 41).

[53] S. Gentiluomo. "Deposizione di strati sottili di rame mediante PVD per la sintesi del grafene". Bachelor Degree thesis. Università degli Studi di Torino, 2011 (cit. on p. 78).

[54] F. Giannazzo and V. Raineri. "*Graphene: Synthesis and nanoscale characterization of electronic properties*". Riv. Nuovo Cimento **35** (2012), 267–304 (cit. on p. xxii).

[55] A. J. M. Giesbers, G. Rietveld, E. Houtzager, U. Zeitler, R. yang, K. S. Novoselov, A. K. Geim, and J. C. Maan. "*Quantum resistance metrology in graphene*". Appl. Phys. Lett. **93** (2008), 222109(1–3) (cit. on p. 35).

[56] S. M. Girvin. *The Quantum Hall Effect: Novel Excitations and Broken Symmetries*. arXiv:cond-mat/9907002v1 [cond-mat.mes-hall]. 1999. URL: http://arxiv.org/pdf/cond-mat/9907002v1.pdf (cit. on p. 33).

[57] M. O. Goerbig. "*Electronic properties of graphene in a strong magnetic field*". Rev. Mod. Phys. **83** (2011), 1193–1243 (cit. on p. 34).

[58] M. O. Goerbig. *Quantum Hall Effects*. arXiv:0909.1998v2 [cond-mat.mes-hall]. 2009. URL: http://arxiv.org/pdf/0909.1998v2.pdf (cit. on pp. 30, 31, 33–35).

[59] *Graphene Fundamentals and Functionalities*. MRS Bull. **37**, pages 1119–1328. 2012 (cit. on p. 43).

[60] C. R. M. Grovenor, H. T. G. Hentzell, and D. A. Smith. "*THE DEVELOPMENT OF GRAIN STRUCTURE DURING GROWTH OF METALLIC FILMS*". Acta metall. **32** (1984), 773–781 (cit. on p. 78).

[61] A. Gupta, G. Chen, P. Joshi, S. Tadigadapa, and P. C. Eklund. "*Raman Scattering from High-Frequency Phonons in Supported n-Graphene Layer Films*". Nano Lett. **6** (2006), 2667–2673 (cit. on pp. 141, 143).

[62] G. H. Han, S. J. Chae, E. S. Kim, F. Güneş, I. H. Lee, S. W. Lee, S. Y. Lee, S. C. Lim, H. K. Jeong, M. S. Jeong, and Y. H. Lee. "*Laser Thinning for Monolayer Graphene Formation: Heat Sink and Interference Effect*". ACS Nano **5** (2011), 263–268 (cit. on p. 185).

[63] G. H. Han, F. Güneş, J. J. Bae, E. S. Kim, S. J. Chae, H.-J. Shin, J.-Y. Choi, D. Pribat, and Y. H. Lee. "*Influence of Copper Morphology in Forming Nucleation Seeds for Graphene Growth*". Nano Lett. **11** (2011), 4144–4148 (cit. on p. 90).

[64] A. Hansen and F. Ravndal. "*Klein's Paradox and Its Resolution*". Phys. Scripta **23** (1981), 1036–1042 (cit. on pp. 38, 39).

[65] J. Hass, W. A. de Heer, and E. H. Conrad. "*The growth and morphology of epitaxial multilayer graphene*". J. Phys-Condens. Mat. **20** (2008), 323202(1–27) (cit. on p. 46).

[66] J. Hofrichter, B. N. Szafranek, M. Otto, T. J. Echtermeyer, M. Baus, A. Majerus, V. Geringer, M. Ramsteiner, and H. Kurz. "*Synthesis of Graphene on Silicon Dioxide by a Solid Carbon Source*". Nano Lett. **10** (2010), 36–42 (cit. on p. 155).

[67] M. Hotokka. *Raman spectroscopy*. Lecture Notes. In: Molecular spectroscopy. Abo Akademi University, 2010. URL: http://users.abo.fi/mhotokka/mhotokka/lecturenotes/ms04.d/ms04-raman-eng.pdf (cit. on p. 133).

[68] W. S. Hummers Jr. and R. E. Offeman. "*Preparation of Graphitic Oxide*". J. Am. Chem. Soc. **80** (1958), 1339 (cit. on p. 44).

[69] S. Iijima. "*Helical microtubes of graphitic carbon*". Nature **354** (1991), 56–58 (cit. on p. 3).

[70] S. Iijima and T. Ichihashi. "*Single-shell carbon nanotubes of 1-nm diameter*". Nature **363** (1993), 603–605 (cit. on p. 3).

[71] F. P. Incropera, D. P. DeWitt, T. L. Bergman, and A. S. Lavine. *Principles of Heat and Mass Transfer*. 7th Edition - International Student Version. John Wiley & Sons, 2012 (cit. on p. 100).

[72] A. Ismach, C. Druzgalski, S. Penwell, A. Schwartzberg, M. Zheng, A. Javey, J. Bokor, and Y. Zhang. "*Direct Chemical Vapor Deposition of Graphene on Dielectric Surfaces*". Nano Lett. **10** (2010), 1542–1548 (cit. on pp. 48, 53, 56, 150, 185).

[73] G. G. Jernigan, B. L. VanMil, J. L. Tedesco, J. G. Tischler, E. R. Glaser, A. Davidson III, P. M. Campbell, and D. Kurt Gaskill. "*Comparison of Epitaxial Graphene on* Si*-face and* C*-face* 4H SiC *Formed by Ultrahigh Vacuum and RF Furnace Production*". Nano Lett. **9** (2009), 2605–2609 (cit. on p. 47).

[74] H. Jiang, T. J. Klemmer, J. A. Barnard, W. D. Doyle, and E. A. Payzant. "*Epitaxial growth of* Cu(111) *films on* Si(110) *by magnetron sputtering: orientation and twin growth*". Thin Solid Films **315** (1998), 13–16 (cit. on p. 92).

[75] Z.-Y. Juang, C.-Y. Wu, C.-W. Lo, W.-Y. Chen, C.-F. Huang, J.-C. Hwang, F.-R. Chen, K.-C. Leou, and C.-H. Tsai. "*Synthesis of graphene on silicon carbide substrates at low temperature*". Carbon **47** (2009), 2026–2031 (cit. on p. 47).

[76] C. L. Kane and E. J. Mele. "*Quantum Spin Hall Effect in Graphene*". Phys. Rev. Lett. **95** (2005), 226801(1–4) (cit. on p. 19).

[77] T. Kaplas, D. Sharma, and Y. Svirko. "*Few-layer graphene synthesis on a dielectric substrate*". Carbon **50** (2012), 1503–1509 (cit. on p. 109).

[78] M. I. Katsnelson. *Graphene - Carbon in Two Dimensions*. Cambridge University Press, 2012 (cit. on pp. 12, 41).

[79] M. I. Katsnelson, K. S. Novoselov, and A. K. Geim. "*Chiral tunnelling and the Klein paradox in graphene*". Nat. Phys. **2** (2006), 620–625 (cit. on pp. 40, 41).

[80] M. Kaviany. *Principles of Heat Transfer*. John Wiley & Sons, 2002 (cit. on p. 100).

[81] M. W. Keller. "*Current status of the quantum metrology triangle*". Metrologia **45** (2008), 102–109 (cit. on p. xxiii).

[82] H. K. Kim, C. Mattevi, M. Reyes Calvo, J. C. Oberg, L. Artiglia, S. Agnoli, C. F. Hirjibehedin, M. Chhowalla, and E. Saiz. "*Activation Energy Paths for Graphene Nucleation and Growth on* Cu". ACS Nano **6** (2012), 3614–3623 (cit. on p. 52).

[83] K. S. Kim, Y. Zhao, H. Jang, S. Y. Lee, J. M. Kim, K. S. Kim, J.-H. Ahn, P. Kim, J.-Y. Choi, and B. H. Hong. "*Large-scale pattern growth of graphene films for stretchable transparent electrodes*". Nature **457** (2009), 706–710 (cit. on p. 48).

[84] C. Kittel. *Introduction to Solid State Physics*. 8th Edition. John Wiley & Sons, 2004 (cit. on pp. 14, 73, 93).

[85] O. Klein. "*Die Reflexion von Elektronen an einem Potentialsprung nach der relativistischen Dynamik von Dirac*". Z. Phys. **53** (1929), 157–165 (cit. on p. 35).

[86] D. Kondo, S. Sato, K. Yagi, N. Harada, M. Sato, M. Nihei, and N. Yokoyama. "*Low-Temperature Synthesis of Graphene and Fabrication of Top-Gated Field Effect Transistors without Using Transfer Processes*". Appl. Phys. Expr. **3** (2010), 025102(1–3) (cit. on p. 48).

[87] P. Kosiński, P. Maślanka, J. Sławińska, and I. Zasada. "QED_{2+1} *in Graphene: Symmetries of Dirac Equation in* $2+1$ *Dimensions*". Prog. Theor. Phys. **128** (2012), 727–739 (cit. on p. 25).

[88] D. V. Kosynkin, A. L. Higginbotham, A. Sinitskii, J. R. Lomeda, A. Dimiev, B. Katherine Price, and J. M. Tour. "*Longitudinal unzipping of carbon nanotubes to form graphene nanoribbons*". Nature **458** (2009), 872–876 (cit. on p. 54).

[89] H. W. Kroto, J. R. Heath, S. C. O'Brien, R. F. Curl, and R. E. Smalley. "C_60*: Buckminsterfullerene*". Nature **318** (1985), 162–163 (cit. on p. 3).

[90] J. J. Lander, H. E. Kern, and A. L. Beach. "*Solubility and Diffusion Coefficient of Carbon in Nickel: Reaction Rates of Nickel-Carbon Alloys with Barium Oxide*". J. Appl. Phys. **23** (1952), 1305–1309 (cit. on p. 157).

[91] G. Landsberg and L. Mandelstam. "*Eine neue Erscheinung bei der Lichtzerstreuung in Krystallen*". Naturwissenschaften **16** (1928), 557–558 (cit. on p. 130).

[92] R. B. Laughlin. "*Anomalous Quantum Hall Effect: An Incompressible Quantum Fluid with Fractionally Charged Excitations*". Phys. Rev. Lett. **50** (1983), 1395–1398 (cit. on p. 32).

[93] C. Lee, X. Wei, J. W. Kysar, and J. Hone. "*Measurement of the Elastic Properties and Intrinsic Strength of Monolayer Graphene*". Science **321** (2008), 385–388 (cit. on p. xxii).

[94] Y. Lee, S. Bae, H. Jang, S. Jang, S.-E. Zhu, S. H. Sim, Y. I. Song, B. H. Hong, and J.-H. Ahn. "*Wafer-Scale Synthesis and Transfer of Graphene Films*". Nano Lett. **10** (2010), 490–493 (cit. on pp. 48, 56).

[95] M. P. Levendorf, C. S. Ruiz-Vargas, S. Garg, and J. Park. "*Transfer-Free Batch Fabrication of Single Layer Graphene Transistors*". Nano Lett. **9** (2009), 4479–4483 (cit. on pp. 48, 53, 56, 150).

[96] X. Li, W. Cai, J. An, S. Kim, J. Nah, D. Yang, R. Piner, A. Velamakanni, I. Jung, E. Tutuc, S. K. Banerjee, L. Colombo, and R. S. Ruoff. "*Large-Area Synthesis of High-Quality and Uniform Graphene Films on Copper Foils*". Science **324** (2009), 1312–1314 (cit. on pp. 48, 56, 161).

[97] X. Li, W. Cai, L. Colombo, and R. S. Ruoff. "*Evolution of Graphene Growth on* Ni *and* Cu *by Carbon Isotope Labeling*". Nano Lett. **9** (2009), 4268–4272 (cit. on pp. 49, 56).

[98] C. H. Liebert and R. D. Thomas. *SPECTRAL EMISSIVITY OF HIGHLY DOPED SILICON*. NASA Technical Note D-4303. 1968 (cit. on p. 117).

[99] K. K. Likharev and A. B. Zorin. "*Theory of Bloch-wave oscillations in small Josephson junctions*". J. Low Temp. Phys. **59** (1985), 347–382 (cit. on pp. xxiii, xxiv).

[100] J. Liu, Y. Xue, M. Zhang, and L. Dai. "*Graphene-based materials for energy applications*". MRS Bull. **37** (2012), 1265–1272 (cit. on p. xxi).

[101] W. Liu, C.-H. Chung, C.-Q. Miao, Y.-J. Wang, B.-Y. Li, L.-Y. Ruan, K. Patel, Y.-J. Park, J. Woo, and Y.-H. Xie. "*Chemical vapor deposition of large area few layer graphene on* Si *catalyzed with nickel films*". Thin Solid Films **518** (2010), S128–S132 (cit. on pp. 48, 51, 53, 150, 154, 155, 158).

[102] R. Loudon. "*The Raman Effect in Crystals*". Adv. Phys. **13** (1964), 423–482 (cit. on p. 133).

[103] R. Loudon. "*Theory of the first-order Raman effect in crystals*". Proc. R. Soc. Lond. A **275** (1963), 218–232 (cit. on p. 135).

[104] C.-S. Lu. "*Mass determination with piezoelectric quartz crystal resonators*". J. Vac. Sci. Technol. **12** (1975), 578–583 (cit. on p. 60).

[105] C.-S. Lu and O. Lewis. "*Investigation of film-thickness determination by oscillating quartz resonators with large mass load*". J. Appl. Phys. **43** (1972), 4385–4390 (cit. on p. 60).

[106] Z. Luo, T. Yu, Z. Ni, S. Lim, H. Hu, J. Shang, L. Liu, Z. Shen, and J. Lin. "*Electronic Structures and Structural Evolution of Hydrogenated Graphene Probed by Raman Spectroscopy*". J. Phys. Chem. C **115** (2011), 1422–1427 (cit. on p. 145).

[107] S. Luryi and E. Suhir. "*New approach to the high quality epitaxial growth of lattice-mismatched materials*". Appl. Phys. Lett. **49** (1986), 140–142 (cit. on p. 92).

[108] A. H. MacDonal. *Introduction to the Physics of the Quantum Hall Regime*. arXiv:cond-mat/9410047v1. 1994. URL: http://arxiv.org/pdf/cond-mat/9410047v1.pdf (cit. on p. 33).

[109] L. M. Malard, M. H. D. Guimarães, D. L. Mafra, M. S. C. Mazzoni, and A. Jorio. "*Group-theory analysis of electrons and phonons in N-layer graphene systems*". Phys. Rev. B **79** (2009), 125426(1–8) (cit. on p. 7).

[110] L. M. Malard, M. A. Pimenta, G. Dresselhaus, and M. S. Dresselhaus. "*Raman spectroscopy in graphene*". Phys. Rep. **473** (2009), 51–87 (cit. on pp. 133, 134, 140–143, 145, 185).

[111] R. Martel, V. Derycke, C. Lavoie, J. Appenzeller, K. K. Chan, J. Tersoff, and Ph. Avouris. "*Ambipolar Electrical Transport in Semiconducting Single-Wall Carbon Nanotubes*". Phys. Rev. Lett. **87** (2001), 256805(1–4) (cit. on p. 4).

[112] D. Martoccia, P. R. Willmott, T. Brugger, M. Björck, S. Günther, C. M. Schlepütz, A. Cervellino, S. A. Pauli, B. D. Patterson, S. Marchini, J. Wintterlin, W. Moritz, and T. Greber. "*Graphene on* Ru(0001)*: A* 25×25 *Supercell*". Phys. Rev. Lett. **101** (2008), 126102(1–4) (cit. on p. 48).

[113] M. Matis, U. Kosidlo, F. Tonner, C. Glanz, and I. Kolaric. "Electrochemical Exfoliation: A Cost-Effective Approach to Produce Graphene Nanoplatelets in Bulk Quantities". *GRAPHITE, GRAPHENE AND THEIR POLYMER NANOCOMPOSITES*. Ed. by P. Mukhopadhyay and R. K. Gupta. CRC Press, 2012. Chap. 4, pp. 139–168 (cit. on p. 152).

[114] A. Mattausch and O. Pankratov. "*Ab Initio Study of Graphene on* SiC". Phys. Rev. Lett. **99** (2007), 076802(1–4) (cit. on p. 46).

[115] C. Mattevi, H. Kim, and M. Chhowalla. "*A review of chemical vapor deposition of graphene on copper*". J. Mater. Chem. **21** (2011), 3324–3334 (cit. on pp. 53, 109, 150).

[116] E. McCann and V. I. Fal'ko. "*Landau-Level Degeneracy and Quantum Hall Effect in a Graphite Bilayer*". Phys. Rev. Lett. **96** (2006), 086805(1–4) (cit. on p. 34).

[117] C. F. McConville, D. P. Woodruff, S. D. Kevan, M. Weinert, and J. W. Davenport. "*Electronic structure of the* (2×2)C *p* 4*g carbidic phase on* Ni{100}". Phyis. Rev. B **34** (1986), 2199–2206 (cit. on p. 5).

[118] N. D. Mermin. "*Crystalline Order in Two Dimensions*". Phys. Rev. **176** (1968), 250–254 (cit. on p. 6).

[119] C. Miao, C. Zheng, O. Liang, and Y.-H. Xie. "Chemical Vapor Deposition of Graphene". *Physics and Applications of Graphene - Experiments*. Ed. by S. Mikhailov. Rijeka: InTech, 2011. Chap. 3, pp. 37–54 (cit. on pp. 50, 53, 150, 179).

[120] J. Millman and C. C. Halkias. *Microelettronica*. Bollati Boringhieri, 1982 (cit. on p. xix).

[121] T. M. G. Mohiuddin, A. Lombardo, R. R. Nair, A. Bonetti, G. Savini, R. Jalil, N. Bonini, D. M. Basko, C. Galiotis, N. Marzari, K. S. Novoselov, A. K. Geim, and A. C. Ferrari. "*Uniaxial strain in graphene by Raman spectroscopy: G peak splitting, Grüneisen parameters, and sample orientation*". Phys. Rev. B **79** (2009), 205433(1–8) (cit. on p. 145).

[122] M. Monthioux and V. L. Kuznetsov. "*Who should be given the credit for the discovery of carbon nanotubes?*" Carbon **44** (2006), 1621–1623 (cit. on p. 3).

[123] G. E. Moore. "*Cramming more components onto integrated circuits*". Electronics **38** (1965). URL: http://download.intel.com/museum/Moores_Law/Articles-Press_Releases/Gordon_Moore_1965_Article.pdf (cit. on p. xix).

[124] E. Moreau, S. Godey, F. J. Ferrer, D. Vignaud, X. Wallart, J. Avila, M. C. Asensio, F. Bournel, and J.-J. Gallet. "*Graphene growth by molecule beam epitaxy on the carbon-face of* SiC". Appl. Phys. Lett. **97** (2010), 241907(1–3) (cit. on p. 54).

[125] S. V. Morozov, K. S. Novoselov, M. I. Katsnelson, F. Schedin, D. C. Elias, J. A. Jaszczak, and A. K. Geim. "*Giant Intrinsic Carrier Mobilities in Graphene and Its Bilayer*". Phys. Rev. Lett. **100** (2008), 016602(1–4) (cit. on pp. 22, 24).

[126] G. Murthy and R. Shankar. "*Hamiltonian theories of the fractional quantum Hall effect*". Rev. Mod. Phys. **75** (2003), 1101–1158 (cit. on p. 33).

[127] R. R. Nair, P. Blake, A. N. Grigorenko, K. S. Novoselov, T. J. Booth, T. Stauber, N. M. R. Peres, and A. K. Geim. "*Fine Structure Constant Defines Visual Transparency of Graphene*". Science **320** (2008), 1308 (cit. on p. xxii).

[128] K. Nakada, M. Fujita, G. Dresselhaus, and M. S. Dresselhaus. "*Edge state in graphene ribbons: Nanometer size effect and edge shape dependence*". Phys. Rev. B **54** (1996), 17954–17961 (cit. on p. 19).

[129] O. Nakagoe, N. Takagi, and Y. Matsumoto. "*Thermal decomposition of acetylene on* Pt(111) *studied by scanning tunneling microscopy*". Surf. Sci. **514** (2002), 414–419 (cit. on p. 48).

[130] Z. H. Ni, H. M. Wang, Y. Ma, J. Kasim, Y. H. Wu, and Z. X. Shen. "*Tunable Stress and Controlled Thickness Modification in Graphene by Annealing*". ACS Nano **2** (2008), 1033–1039 (cit. on p. 189).

[131] Z. H. Ni, Y. Y. Wang, T. Yu, and Z. X. Shen. "*Raman Spectroscopy and Imaging of Graphene*". Nano Res. **1** (2008), 273–291 (cit. on pp. 141, 144, 189).

[132] C. Nordling, E. Sokolowski, and K. Siegbahn. "*Precision Method for Obtaining Absolute Values of Atomic Binding Energies*". Phys. Rev. **105** (1957), 1676–1677 (cit. on p. 147).

[133] K. S. Novoselov, A. K. Geim, S. V. Morozov, D. Jiang, M. I. Katsnelson, I. V. Grigorieva, S. V. Dubonos, and A. A. Firsov. "*Two-dimensional gas of massless Dirac fermions in graphene*". Nature **438** (2005), 197–200 (cit. on p. 34).

[134] K. S. Novoselov, A. K. Geim, S. V. Morozov, D. Jiang, Y. Zhang, S. V. Dubonos, I. V. Grigorieva, and A. A. Firsov. "*Electric Field Effect in Atomically Thin Carbon Films*". Science **306** (2004), 666–669 (cit. on pp. xxi, xxii, 6, 22, 43).

[135] K. S. Novoselov, Z. Jiang, Y. Zhang, S. V. Morozov, H. L. Stormer, U. Zeitler, J. C. Maan, G. S. Boebinger, P. Kim, and A. K. Geim. "*Room-Temperature Quantum Hall Effect in Graphene*". Science **315** (2007), 1379 (cit. on pp. 35, 36).

[136] K. S. Novoselov, E. McCann, S. V. Morozov, V. I. Fal'ko, M. I. Katsnelson, U. Zeitler, D. Jiang, F. Schedin, and A. K. Geim. "*Unconventional quantum Hall effect and Berry's phase of* 2π *in bilayer graphene*". Nat. Phys. **2** (2006), 177–180 (cit. on p. 34).

[137] A. N. Obraztsov, E. A. Obraztsov, A. V. Tyurnina, and A. A. Zolotukhin. "*Chemical vapor deposition of thin graphite films of nanometer thickness*". Carbon **45** (2007), 2017–2021 (cit. on p. 48).

[138] R. S. Ohl. *Light-sensitive electric device*. U.S. Patent. Filed May 27^{th}, 1941. Granted June 25^{th}, 1946 (cit. on p. xix).

[139] R. W. Olesinski and G. J. Abbaschian. "*The* Cu – Si *(Copper-Silicon) system*". J. Phase Equilib. **7** (1986), 170–178 (cit. on pp. 92, 94, 163).

[140] T. Otsuji, S. A. Boubanga Tombet, A. Satou, H. Fukidome, M. Suemitsu, E. Sano, V. Popov, M. Ryzhii, and V. Ryzhii. "*Graphene materials and devices in terahertz science and technology*". MRS Bull. **37** (2012), 1235–1243 (cit. on p. xxi).

[141] N. M. R. Peres. "*Colloquium: The transport properties of graphene: An introduction*". Rev. Mod. Phys. **82** (2010), 2673–2700 (cit. on pp. 22, 41).

[142] N. M. R. Peres, F. Guinea, and A. H. Castro Neto. "*Electronic properties of disordered two-dimensional carbon*". Phys. Rev. B **73** (2006), 125411(1–23) (cit. on p. 41).

[143] M. E. Peskin and D. V. Schroeder. *An Introduction to Quantum Field Theory*. Westview Press, 1995 (cit. on p. 38).

[144] M. Piazzi. *Everything (?) you always wanted to know about GRAPHENE . . . or maybe not*. Ph.D. II year seminar. 2012. URL: http://dottorato.ph.unito.it/Studenti/Pretesi/XXV/piazzi.pdf (cit. on p. 38).

[145] M. Piazzi, L. Croin, E. Vittone, and G. Amato. "*Laser-induced etching of few-layer graphene synthesized by Rapid-Chemical Vapour Deposition on Cu thin films*". SpringerPlus **1** (2012), 52(1–12) (cit. on pp. 154, 192).

[146] W. E. Pickett. ""Tight Binding" Method: Linear Combination of Atomic Orbitals (LCAO)". Lecture notes. 2006. URL: http://yclept.ucdavis.edu/course/241/TB.pdf (cit. on p. 12).

[147] F. Piquemal and G. Genevès. "*Argument for a direct realization of the quantum metrological triangle*". Metrologia **37** (2000), 207–211 (cit. on p. xxiii).

[148] M. Planck. *The Theory of Heat Radiation*. Ed. by M. Masius. Translated - 2nd Edition. P. Blakiston's Son & Co., 1914 (cit. on p. 100).

[149] E. Pop, V. Varshney, and A. K. Roy. "*Thermal properties of graphene: Fundamentals and applications*". MRS Bull. **37** (2012), 1273–1281 (cit. on p. xxi).

[150] M. Prato. "Un sistema automatico per l'evaporazione mediante cannone elettronico di film sottili in UHV". Bachelor Degree thesis. Università degli Studi di Torino, 2012 (cit. on p. 66).

[151] A. A. Radzig and B. M. Smirnov. *Reference Data on Atoms, Molecules, and Ions*. Springer Series in Chemical Physics, Vol. 31. Berlin: Springer-Verlag, 1985 (cit. on p. 1).

[152] C. V. Raman and K. S. Krishnan. "*A new type of secondary radiation*". Nature **121** (1928), 501–502 (cit. on p. 130).

[153] M. Regmi, M. F. Chisholm, and G. Eres. "*The effect of growth parameters on the intrinsic properties of large-area single layer graphene grown by chemical vapor deposition on* Cu". Carbon **50** (2012), 134–141 (cit. on pp. 48, 56).

[154] A. Reina, X. Jia, J. Ho, D. Nezich, H. Son, V. Bulovic, M. S. Dresselhaus, and J. Kong. "*Large Area, Few-Layer Graphene Films on Arbitrary Substrates by Chemical Vapor Deposition*". Nano Lett. **9** (2009), 30–35 (cit. on pp. 48, 185).

[155] M. Ruan, Y. Hu, Z. Guo, R. Dong, J. Palmer, J. Hankinson, C. Berger, and W. A. de Heer. "*Epitaxial graphene on silicon carbide: Introduction to structured graphene*". MRS Bull. **37** (2012), 1138–1147 (cit. on p. 47).

[156] S. Sahoo and S. Das. "*Fractional quantum Hall effect in graphene*". Indian J. Pure Ap. Phys. **47** (2009), 658–662 (cit. on p. 34).

[157] R. Saito, G. Dresselhaus, and M. S. Dresselhaus. *Physical Properties of Carbon Nanotubes*. London: Imperial College Press, 1998 (cit. on pp. 12, 145).

[158] R. Saito, M. Hofmann, G. Dresselhaus, A. Jorio, and M. S. Dresselhaus. "*Raman spectroscopy of graphene and carbon nanotubes*". Adv. Phys. **60** (2011), 413–550 (cit. on p. 145).

[159] M Sasaki, Y Yamada, Y Ogiwara, S Yagyu, and S Yamamoto. "*Moiré contrast in the local tunneling barrier height images of monolayer graphite on* Pt(111)". Phys. Rev. B **61** (2000), 15653–15656 (cit. on p. 48).

[160] G. Sauerbrey. "*Verwendung von Schwingquarzen zur Wägung dünner Schichten und zur Mikrowägung*". Z. Phys. **155** (1959), 206–222 (cit. on p. 61).

[161] H. Scherer and B. Camarota. "*Quantum metrology triangle experiments: a status review*". Meas. Sci. Technol. **23** (2012), 124010(1–13) (cit. on p. xxiii).

[162] F. Schopfer and W. Poirier. "*Graphene-based quantum Hall effect metrology*". MRS Bull. **37** (2012), 1255–1264 (cit. on p. xxi).

[163] P. Seneor, B. Dlubak, M.-B. martin, A. Anane, H. Jaffres, and A. Fert. "*Spintronics with graphene*". MRS Bull. **37** (2012), 1245–1254 (cit. on p. xxi).

[164] W. Shockley. "*The Theory of p-n Junctions in Semiconductors and p-n Junction Transistors*". **28** (1949), 435–489 (cit. on p. xix).

[165] V. Singh, D. Joung, L. Zhai, S. Das, S. I. Khondaker, and S. Seal. "*Graphene based materials: Past, present and future*". Prog. Mater. Sci. **56** (2011), 1178–1271 (cit. on pp. 7, 8, 43–45).

[166] J. C. Slater and G. F. Koster. "*Simplified LCAO Method for the Periodic Potential Problem*". Phys. Rev. **94** (1954), 1498–1524 (cit. on p. 12).

[167] A. Smekal. "*Zur Quantentheorie der Dispersion*". Naturwissenschaften **11** (1923), 873–875 (cit. on p. 130).

[168] I. N. Sneddon. *Elements of Partial Differential Equations*. International Student Version. Kōgakusha: McGraw-Hill Book Company, 1957 (cit. on p. 155).

[169] C. Soldano, A. Mahmood, and E. Dujardin. "*Production, properties and potential of graphene*". Carbon **48** (2010), 2127–2150 (cit. on pp. 43, 46, 47).

[170] M. Sprinkle, D. Siegel, Y. Hu, J. Hicks, A. Tejeda, A. Taleb-Ibrahimi, P. Le Févre, F. Bertran, S. Vizzini, H. Enriquez, S. Chiang, P. Soukiassian, C. Berger, W. A. de Heer, A. Lanzara, and E. H. Conrad. "*First Direct Observation of a Nearly Ideal Graphene Band Structure*". Phys. Rev. Lett. **103** (2009), 226803(1–4) (cit. on pp. 46, 47).

[171] A. Srivastava, C. Galande, L. Ci, L. Song, C. Rai, D. Jariwala, K. F. Kelly, and P. M. Ajayan. "*Novel Liquid Precursor-Based Facile Synthesis of Large-Area Continuous, Single, and Few-Layer Graphene Films*". Chem. Mater. **22** (2010), 3457–3461 (cit. on p. 56).

[172] D. E. Starr, E. M. Pazhetnov, A. I. Stadnichenko, A. I. Boronin, and S. K. Shaikhutdinov. "*Carbon films grown on* Pt(111) *as supports for model gold catalysts*". Surf. Sci. **600** (2006), 2688–2695 (cit. on p. 48).

[173] C.-Y. Su, A.-Y. Lu, C.-Y. Wu, Y.-T. Li, K.-K. Liu, W. Zhang, S.-Y. Lin, Z.-Y. Juang, Y.-L. Zhong, F.-R. Chen, and L.-J. Li. "*Direct Formation of Wafer Scale Graphene Thin Layers on Insulating Substrates by Chemical Vapor Deposition*". Nano Lett. **11** (2011), 3612–3616 (cit. on pp. 48, 56, 107, 150).

[174] P. Z. Sun, M. Zhu, K. L. Wang, M. L. Zhong, J. Q. Wei, D. H. Wu, Y. Cheng, and H. W. Zhu. "*Photoinduced molecular desorption from graphene films*". Appl. Phys. Lett. **101** (2012), 053107(1–4) (cit. on pp. 145, 187).

[175] I. Sunagawa. "*Growth and Morphology of Crystals*". Forma **14** (1999), 147–166 (cit. on p. 78).

[176] S. M. Sze and K. K. Ng. *Physics of Semiconductor Devices*. 3^{rd} Edition. John Wiley & Sons, 2006 (cit. on p. xix).

[177] L. Tao, J. Lee, H. Chou, M. Holt, R. S. Ruoff, and D. Akinwande. "*Synthesis of High Quality Monolayer Graphene at Reduced Temperature on Hydrogen-Enriched Evaporated Copper* (111) *Films*". ACS Nano **6** (2012), 2319–2325 (cit. on pp. 48, 56, 105, 106, 176, 177).

[178] C. V. Thompson. "*Solid-State Dewetting of Thin Films*". Annu. Rev. Mater. Res. **42** (2012), 399–434 (cit. on p. 96).

[179] M. J. Thomson and B. H. J. McKellar. "*The solution of the Dirac equation for a high square barrier*". Am. J. Phys. **59** (1991), 340–346 (cit. on p. 38).

[180] N. Tombros, C. Jozsa, M. Popinciuc, H. T. Jonkman, and B. J. van Wees. "*Electronic spin transport and spin precession in single graphene layers at room temperature*". Nature **448** (2007), 571–574 (cit. on p. xxii).

[181] A. W. Tsen, L. Brown, M. P. Levendorf, F. Ghahari, P. Y. Huang, R. W. Havener, C. S. Ruiz-Vargas, D. A. Muller, P. Kim, and J. Park. "*Tailoring Electrical Transport Across Grain Boundaries in Polycrystalline Graphene*". Science **336** (2012), 1143–1146 (cit. on p. 90).

[182] D. C. Tsui, H. L. Stormer, and A. C. Gossard. "*Two-Dimensional Magnetotransport in the Extreme Quantum Limit*". Phys. Rev. Lett. **48** (1982), 1559–1562 (cit. on p. 32).

[183] F. Tuinstra and J. L. Koenig. "*Raman Spectrum of Graphite*". J. Chem. Phys. **53** (1970), 1126–1130 (cit. on p. 145).

[184] A. Tzalenchuk, S. Lara-Avila, A. Kalaboukhov, S. Paolillo, M. Syväjärvi, R. Yakimova, O. Kazakova, T. J. B. M. Janssen, V. Fal'ko, and S. Kubatkin. "*Towards a quantum resistance standard based on epitaxial graphene*". Nat. Nanotechnol. **5** (2010), 186–189 (cit. on pp. xxiv, 35).

[185] J. Vaari, J. Lahtinen, and P. Hautojärvi. "*The adsorption and decomposition of acetylene on clean and* K*-covered* Co(0001)". Catal. Lett. **44** (1997), 43–49 (cit. on p. 48).

[186] A. J. Van Bommel, J. E. Crombeen, and A. Van Tooren. "*LEED and Auger electron observations of the* SiC(0001) *surface*". Surf. Sci. **48** (1975), 463–472 (cit. on p. 5).

[187] F. Varchon, R. Feng, J. Hass, X. Li, B. Ngoc Nguyen, C. Naud, P. Mallet, J.-Y. Veuillen, C. Berger, E. H. Conrad, and L. Magaud. "*Electronic Structure of Epitaxial Graphene Layers on SiC: Effect of the Substrate*". Phys. Rev. Lett. **99** (2007), 126805(1–4) (cit. on p. 46).

[188] J. A. Venables, G. D. T. Spiller, and M. Hanbücken. "*Nucleation and growth of thin films*". Rep. Prog. Phys. **47** (1984), 399–459 (cit. on p. 78).

[189] L. Vicarelli, M. S. Vitiello, D. Coquillat, A. Lombardo, A. C. Ferrari, W. Knap, M. Polini, V. Pellegrini, and A. Tredicucci. "*Graphene field-effect transistors as room-temperature terahertz detectors*". Nat. Mater. **11** (2012), 865–871 (cit. on p. xxi).

[190] I. Vlassiouk, M. Regmi, P. Fulvio, S. dai, P. Datskos, G. Eres, and S. Smirnov. "*Role of Hydrogen in Chemical Vapor Deposition Growth of Large Single-Crystal Graphene*". ACS Nano **5** (2011), 6069–6076 (cit. on p. 106).

[191] K. von Klitzing, G. Dorda, and M. Pepper. "*New Method for High-Accuracy Determination of the Fine-Structure Constant Based on Quantized Hall Resistance*". Phys. Rev. Lett. **45** (1980), 494–497 (cit. on p. 27).

[192] P. R. Wallace. "*The Band Theory of Graphite*". Phys. Rev. **71** (1947), 622–634 (cit. on pp. 5, 12, 14).

[193] H. Wang, Y. Wang, X. Cao, M. Feng, and G. Lan. "*Vibrational properties of graphene and graphene layers*". J. Raman Spectrosc. **40** (2009), 1791–1796 (cit. on pp. 141, 143, 189).

[194] H. Wang, J. You, L. Wang, M. Feng, and Y. Wang. "*Theory of the evolution of* 2D *band in the Raman spectra of monolayer and bilayer graphene with laser excitation energy*". J. Raman Spectrosc. **41** (2010), 125–129 (cit. on p. 139).

[195] K.-A. Wang, A. M. Rao, P. C. Eklund, M. S. Dresselhaus, and G. Dresselhaus. "*Observation of higher-order infrared modes in solid* C_{60} *films*". Phys. Rev. B **48** (1993), 11375–11380 (cit. on p. 133).

[196] X. Wang, Q. Li, J. Xie, Z. Jin, J. Wang, Y. Li, K. Jiang, and S. Fan. "*Fabrication of Ultralong and Electrically Uniform Single-Walled Carbon Nanotubes on Clean Substrates*". Nano Lett. **9** (2009), 3137–3141 (cit. on p. 3).

[197] Y. Y. Wang, Z. H. Ni, Z. X. Shen, H. M. Wang, and Y. H. Wu. "*Interference enhancement of Raman signal of graphene*". Appl. Phys. Lett. **92** (2008), 043121(1–3) (cit. on p. 141).

[198] Y. Y. Wang, Z. H. Ni, T. Yu, Z. X. Shen, H. M. Wang, Y. H. Wu, W. Chen, and A. Thye Shen Wee. "*Raman Studies of Monolayer Graphene: The Substrate Effect*". J. Phys. Chem. C **112** (2008), 10637–10640 (cit. on p. 142).

[199] D. Wei, Y. Liu, Y. Wang, H. Zhang, L. Huang, and G. Yu. "*Synthesis of* N*-Doped Graphene by Chemical Vapor Deposition and Its Electrical Properties*". Nano Lett. **9** (2009), 1752–1758 (cit. on p. 56).

[200] J. Wintterlin and M.-L. Bocquet. "*Graphene on metal surfaces*". Surf. Sci. **603** (2009), 1841–1852 (cit. on p. 53).

[201] J. D. Wood, S. W. Schmucker, A. S. Lyons, E. Pop, and J. W. Lyding. "*Effects of Polycrystalline Cu Substrate on Graphene Growth by Chemical Vapor Deposition*". Nano Lett. **11** (2011), 4547–4554 (cit. on p. 92).

[202] M. Xu, D. Fujita, K. Sagisaka, E. Watanabe, and N. Hanagata. "*Production of Extended Single-Layer Graphene*". ACS Nano **5** (2011), 1522–1528 (cit. on p. 155).

[203] J. Yan, Y. Zhang, P. Kim, and A. Pinczuk. "*Electric Field Effect Tuning of Electron-Phonon Coupling in Graphene*". Phys. Rev. Lett. **98** (2007), 166802(1–4) (cit. on pp. 135, 137).

[204] T.-Y. Yang, J. Balakrishnan, F. Volmer, A. Avsar, M. Jaiswal, J. Samm, S. R. Ali, A. Pachoud, M. Zeng, M. Popinciuc, G. Güntherodt, B. Beschoten, and B. Özyilmaz. "*Observation of Long Spin-Relaxation Times in Bilayer Graphene at Room Temperature*". Phys. Rev. Lett. **107** (2011), 047206(1–4) (cit. on p. xxii).

[205] L. Zhao, K. T. Rim, H. Zhou, R. He, T. F. Heinz, A. Pinczuk, G. W. Flynn, and A. N. Pasupathy. "*Influence of copper crystal surface on the CVD growth of large area monolayer graphene*". Solid State Commun. **151** (2011), 509–513 (cit. on p. 92).

PUBLICATIONS & TALKS, SCHOOLS, WORKSHOPS, ...

Publications

1. M. Piazzi, L. Croin, E. Vittone, G. Amato, *"Laser-induced etching of few-layer graphene synthesized by Rapid-Chemical Vapour Deposition on Cu thin films"*. SpringerPlus **1** (2012), 52(1–10).

Communications at conferences

Talks

1. M. Piazzi, L. Croin, F. Gregori, G. Amato, *"Rapid-CVD of Few-Layer Graphene on Dewetting Cu Catalyzing Films"*; "GrapHEL - A European Conference/Workshop on the Synthesis, Characterization and Applications of Graphene", Mykonos (Greece), September 27th–30th, 2012;

2. M. Piazzi, *"GRAPHENE PRODUCTION... towards the dream of a flat-land"*; Department of Physics - University of Turin, Turin (Italy), October 21st, 2010.

Posters

1. M. Piazzi, L. Croin, E. Enrico, G. Amato, *"Rapid-CVD of few layer graphene on Si-substrates catalyzed with Cu"*; National School on The Physics of the Matter 2011 - International School of Solid State Physics - "Quantum Phenomena in Graphene, other Low-Dimensional Materials, and Optical Lattice", Majorana Centre, Erice - Trapani (Italy), July 26th–August 6th, 2011.

Schools, conferences, workshops

Graphene subject

1. "Graphene Week Conference 2012", Delft (Netherlands), June 5th–10th, 2012;

2. "GraphITA - A Multidisciplinary and Intersectorial European Workshop on Synthesis, Characterization and Technological Exploitation of Graphene", Gran Sasso National Laboratories, Assergi - L'Aquila (Italy), May 15th–18th, 2011;

3. *Mathematica* Summer School on Theoretical Physics - 2nd Edition: *"Condensed Matter and Two-dimensional physics"*, Oporto Physics Department, Oporto (Portugal), July 11th–16th, 2010.

Other subjects

1. Workshop: "Spectroscopic Ellipsometry", Nanostructured Interfaces and Surfaces (NIS) Centre of Excellence, Turin (Italy), October 16th, 2012;

2. International Conference: "The Time-Machine Factory", Regional Museum of Natural Sciences, Turin (Italy), October 14^{th}–19^{th}, 2012;

3. International School: "Italian School on Magnetism", Department of Physics "A. Volta" - University of Pavia, Pavia (Italy), February 5^{th}–10^{th}, 2012;

4. International Conference: "Chimica e sostenibilità: il problema energetico", Sala dei Mappamondi - Academy of Sciences, Turin (Italy), September 20^{th}, 2011;

5. European Forum: *"ESOF 2010 - EuroScience Open Forum"*, Lingotto Conference and Exhibition Centre, Turin (Italy), July 2^{nd}–7^{th}, 2010;

6. Workshop: "News in foundations of Quantum Mechanics", Istituto Nazionale di Ricerca Metrologica (I.N.Ri.M.), Turin (Italy), July 2^{nd}, 2010;

7. "nanoforum" - VI Edition, Politecnico of Turin, Turin (Italy), June 16^{th}–17^{th}, 2010.